frontiers | Research Topics

Weather disasters in the south china sea and surrounding regions: Observations, theories, data assimilation, and numerical forecasting

Edited by
Jianjun Xu, Julian Wang, Sheng Chen and Chunlei Liu

Coordinated by
Jingchao Long

Published in
Frontiers in Earth Science

ISSN 1664-8714
ISBN 978-2-8325-3259-1
DOI 10.3389/978-2-8325-3259-1

About Frontiers

Frontiers is more than just an open access publisher of scholarly articles: it is a pioneering approach to the world of academia, radically improving the way scholarly research is managed. The grand vision of Frontiers is a world where all people have an equal opportunity to seek, share and generate knowledge. Frontiers provides immediate and permanent online open access to all its publications, but this alone is not enough to realize our grand goals.

Frontiers journal series

The Frontiers journal series is a multi-tier and interdisciplinary set of open-access, online journals, promising a paradigm shift from the current review, selection and dissemination processes in academic publishing. All Frontiers journals are driven by researchers for researchers; therefore, they constitute a service to the scholarly community. At the same time, the *Frontiers journal series* operates on a revolutionary invention, the tiered publishing system, initially addressing specific communities of scholars, and gradually climbing up to broader public understanding, thus serving the interests of the lay society, too.

Dedication to quality

Each Frontiers article is a landmark of the highest quality, thanks to genuinely collaborative interactions between authors and review editors, who include some of the world's best academicians. Research must be certified by peers before entering a stream of knowledge that may eventually reach the public - and shape society; therefore, Frontiers only applies the most rigorous and unbiased reviews. Frontiers revolutionizes research publishing by freely delivering the most outstanding research, evaluated with no bias from both the academic and social point of view. By applying the most advanced information technologies, Frontiers is catapulting scholarly publishing into a new generation.

What are Frontiers Research Topics?

Frontiers Research Topics are very popular trademarks of the *Frontiers journals series*: they are collections of at least ten articles, all centered on a particular subject. With their unique mix of varied contributions from Original Research to Review Articles, Frontiers Research Topics unify the most influential researchers, the latest key findings and historical advances in a hot research area.

Find out more on how to host your own Frontiers Research Topic or contribute to one as an author by contacting the Frontiers editorial office: frontiersin.org/about/contact

Weather disasters in the south china sea and surrounding regions: Observations, theories, data assimilation, and numerical forecasting

Topic editors

Jianjun Xu — Guangdong Ocean University, China

Julian Wang — National Oceanic and Atmospheric Administration (NOAA), United States

Sheng Chen — Northwest Institute of Eco-Environment and Resources, Chinese Academy of Sciences (CAS), China

Chunlei Liu — Guangdong Ocean University, China

Topic Coordinator

Jingchao Long — Guangdong Ocean University, China

Citation

Xu, J., Wang, J., Chen, S., Liu, C., Long, J., eds. (2023). *Weather disasters in the south china sea and surrounding regions: Observations, theories, data assimilation, and numerical forecasting*. Lausanne: Frontiers Media SA.

doi: 10.3389/978-2-8325-3259-1

Table of contents

frontiers | Frontiers in Earth Science

TYPE Original Research
PUBLISHED 10 January 2023
DOI 10.3389/feart.2022.1050858

OPEN ACCESS

EDITED BY
Jianjun Xu,
Guangdong Ocean University, China

REVIEWED BY
Jie Cao,
Nanjing University of Information Science and Technology, China
Cheng Sun,
Beijing Normal University, China

*CORRESPONDENCE
Lifang Sheng,
shenglf@ouc.edu.cn

SPECIALTY SECTION
This article was submitted to Interdisciplinary Climate Studies, a section of the journal Frontiers in Earth Science

RECEIVED 22 September 2022
ACCEPTED 28 December 2022
PUBLISHED 10 January 2023

CITATION
Feng J, Huang Y, Wang F, Guo F, Li W, Wang W, Teng S, Xing F, Sun J, Zhou Y and Sheng L (2023), Distribution and evolution of hydrometeors in the stratiform cloud with embedded convection in the autumn ITCZ precipitation in Xisha: Case study. *Front. Earth Sci.* 10:1050858. doi: 10.3389/feart.2022.1050858

Distribution and evolution of hydrometeors in the stratiform cloud with embedded convection in the autumn ITCZ precipitation in Xisha: Case study

Jie Feng[1,2], Yanbin Huang[2], Fei Wang[1], Feiyan Guo[3], Wanju Li[1], Wencai Wang[1], Shiwen Teng[1], Fenghua Xing[2], Jiaming Sun[1], Yu Zhou[2] and Lifang Sheng[1,2,4]*

[1]College of Oceanic and Atmospheric Sciences, Ocean University of China, Qingdao, China, [2]Key Laboratory of South China Sea Meteorological Disaster Prevention and Mitigation of Hainan Province, Haikou, China, [3]Qingdao Meteorological Bureau, Qingdao, China, [4]Key Laboratory of Physical Oceanography, Ocean University of China, Qingdao, China

In autumn, the clouds over the South China Sea contain more cloud water and cloud ice. Intertropical Convergence Zone sometimes can strengthen and move north, causing heavy precipitation in the northern South China Sea. To reveal the distribution and evolution of hydrometeors in the Intertropical Convergence Zone precipitation clouds, a rainfall process occurred in Xisha and surrounding regions on 16 October 2021 was analyzed by utilizing S-band dual-polarization weather radar data and fuzzy logic algorithm. The classified hydrometeors showed that drizzle, rain, and dry snow were the three most abundant types, while dry crystal was less, indicating deposition and aggregation were more active in the marine environment with sufficient water vapor. The relative content of drizzle and dry snow changed oppositely to that of rain particles, suggesting the coalescence of drizzle and the transformation of dry snow were important processes affecting the formation of rain particles. The precipitation clouds were characterized by stratiform clouds with embedded convections. The strong updraft in the convective clouds transported liquid water upward, thus dry snow could collide with supercooled water and rime to form graupel, then graupel melted to form large raindrops below the 0°C layer. However, compared with continental convective clouds, the riming was weaker. In the stratiform clouds, the ascending motion was weak, no graupel was generated, and the 0°C-layer bright band indicated that dry snow could directly contribute to the small raindrops by melting. This study revealed the evolution of hydrometeors in the Intertropical Convergence Zone precipitation clouds and found that the increase in raindrop size in convective clouds was caused by the combined effects of stronger coalescence and riming.

KEYWORDS

hydrometeors, dual-polarization radar, fuzzy logic algorithm, Xisha, ITCZ precipitation clouds

1 Introduction

Microphysical processes include the mutual transformation between water vapor and various hydrometeors in clouds. Liquid hydrometeors are mainly located below the 0°C layer, while ice hydrometeors are mainly distributed above the 0°C layer (Fan et al., 2010; Zhu and Guo, 2014). Due to the complexity of ice hydrometeors in shape, size, and density, they can be further classified as ice crystals, snow, graupel, and hail, etc. The growth and evolution of these hydrometeors include condensation, coalescence, deposition, freezing, riming, aggregation, and melting, etc. (Sheng et al., 2013). Among them, riming and aggregation are important growth processes of ice hydrometeors. Riming means that ice crystals grow by colliding with supercooled water and then freezing, and aggregation refers to multiple ice crystals stick together to form snow or larger ice crystals (Zhou et al., 2016). These processes are affected by the thermal and dynamic conditions in clouds, and they also have important feedback on the cloud dynamics, ultimately affect the rainfall area, intensity, and the accumulated amount of precipitation (Hua and Liu, 2016; Lee et al., 2018; Hou et al., 2020).

In warm clouds, hydrometeors grow through condensation and coalescence, the latter is the main mechanism for raindrop formation (Zhou et al., 2017; Chen and Li, 2022). However, the diversity of ice hydrometeors increases the complexity of microphysical processes in cold clouds. In general, the riming process controls the formation of cold cloud precipitation. As the products of riming, the melting of graupel and hail below the 0°C layer is an important source of raindrops in cold rain, and the increase in graupel density implies the enhancement of precipitation rate (Cheng et al., 2010; Ribaud et al., 2019; Cao et al., 2021; Zhang et al., 2021). In the area with insufficient supercooled water, ice hydrometeors mainly grow through deposition, while abundant supercooled water can enhance riming, which promotes the conversion of ice crystals to graupel, resulting in a low concentration of ice crystals in a warm front cloud system, but high in cold front (Qi et al., 2019; Zhu and Guo, 2014). Even under the same weather system, the intensity of riming is different in different stages or types of clouds (Zhao and Lei, 2014; Hou et al., 2021).

In addition to the coalescence of cloud droplets and the melting of graupel, the formation of raindrops is also affected by the melting of snow. From radar observation, there is sometimes a strong echo band near the 0°C layer, which is called the "0°C-layer bright band". Zhang et al. (2000) summarized the reasons for its formation as follows: the melting effect of ice crystals or snowflakes, the collision and aggregation effect of particles, and the velocity and shape effect after the melting of ice crystals or snowflakes. From the above, it can be seen that the melting of snow provides an important source of raindrops. However, previous studies have also shown that snow in the clouds was far above the 0°C layer, which made it unable to make a direct contribution to the ground rainfall, but could indirectly affect the precipitation by riming to graupel (He et al., 2010; Zhang et al., 2021). Therefore, how snow affects the raindrop formation needs to be further analyzed.

Previous research on cloud microphysics and precipitation mainly focused on North China, Pearl River Delta, and Yangtze River Delta, but relatively little on marine areas. Xisha is located in the northwest region of the South China Sea (SCS). In autumn, cold air often interacts with tropical disturbances in the northward moving Intertropical Convergence Zone (ITCZ) to form precipitation (Li et al., 2016; Wang et al., 2021). Both satellite and ground-based observations demonstrated that precipitation peaked in autumn over most parts of the SCS, especially in September and October, with 58% heavy rainfall caused by non-typhoon systems, of which ITCZ was an important member (Li et al., 2006; Xiao et al., 2013; Li et al., 2016; Feng et al., 2017). So far, many studies have focused on the thermal and dynamic analysis of such precipitations, with less attention paid to microphysics, especially on the distribution and evolution of hydrometeors (Zhao et al., 2011; Feng et al., 2017; Wang et al., 2021). The dual-polarization weather radar can transmit and receive horizontal and vertical electromagnetic waves to obtain the size, shape, phase state, density, and spatial orientation of particles in clouds, then the classification of hydrometeors can be realized combined with algorithms (Liu and Chandrasekar, 2000; Liu et al., 2005; Paulitsch et al., 2009). Based on the observation data of S-band dual-polarization weather radar and fuzzy logic algorithm, this paper classifies the hydrometeors in the clouds during an autumn ITCZ precipitation process in the northwestern SCS and analyzes the distribution and evolution of these particles.

This paper is organized as follows. Section 2 describes the data and methods used in the study. Section 3 introduces the precipitation event. Section 4 presents the hydrometeor classification and evolution during the rainfall. The distribution of hydrometeors in different cloud types is analyzed in Section 5. Conclusion are summarized in Section 6.

2 Data and methods

2.1 Data

Reanalysis data including geopotential height, air temperature, meridional wind, zonal wind, specific humidity, and mean sea level pressure, with a spatial resolution of 0.25° × 0.25° and a temporal resolution of 1 h, were obtained from European Center for Medium-Range Weather Forecasts (ERA5 | ECMWF) to analyze the atmospheric circulation of the precipitation event. The sounding data, surface meteorological elements, and S-band dual-polarization weather radar data were all provided by Sansha Meteorological Station on Yongxing Island (112.33°E, 16.83°N). The sounding data were used to analyze the stratification state of atmosphere and determine the altitudes of the specific temperature layers. To better capture the vertical structure of atmosphere during the precipitation process, a 6-h intensive sounding observation was conducted. Surface meteorological elements include temperature, precipitation, wind speed, and wind direction, with a temporal resolution of 1 h. The S-band dual-polarization weather radar can emit horizontal and vertical electromagnetic waves with a wavelength of 10 cm. The radar operates in volume coverage pattern 21 (i.e., scanning is completed within 6 min for nine elevation angles: 0.5°, 1.5°, 2.4°, 3.3°, 4.3°, 6.0°, 9.9°, 14.6°, and 19.5°), and its radial resolution is 250 m. The polarization parameters of radar include reflectivity Z, differential reflectivity Z_{DR}, specific differential phase K_{DP}, and copular correlation coefficient ρ_{HV}. They have been business corrected, and radial five points smoothing was applied to reduce the random disturbance.

Reflectivity Z represents the sum of the sixth power of the diameters of all hydrometeors in a unit volume, in dBZ, the formula is as follows:

$$\mathbf{Z} = \mathbf{10}\boldsymbol{lg}\left(\frac{\int_0^{\infty} \boldsymbol{n}(\boldsymbol{D})\boldsymbol{D}^{\mathbf{6}}\boldsymbol{dD}}{\boldsymbol{Z_1}}\right) \quad (1)$$

here $\boldsymbol{n}(\boldsymbol{D})$ represents the number of particles with a diameter between $\boldsymbol{D}$ and $\boldsymbol{D}+\boldsymbol{dD}$ in a unit volume, $Z_1 = 1.0\,mm^6\,m^{-3}$ (Yu et al., 2006). Reflectivity Z reflects the size and number density of particles in the observed target (Yu et al., 2006). Details of other radar polarization parameters are provided in the supplementary material.

2.2 Radar quantitative precipitation estimate

The relationship between rain rate $\mathbf{R}$ ($\mathbf{mm\,h^{-1}}$) and radar reflectivity factor $\boldsymbol{Z_0}$ ($\boldsymbol{mm^6\,m^{-3}}$) is the basis of quantitative precipitation estimation, and the relationship varies with region, season and rainfall type (Part and Barros 2009; Zeng et al., 2019). Based on the onboard disdrometer dataset, Zeng et al. (2019) gave the Z_0-R relationship for precipitation in October in the SCS, which can be expressed as:

$$\boldsymbol{Z_0} = \mathbf{339}\boldsymbol{R}^{\mathbf{1.46}} \quad (2)$$

In this study, the relationship was used for rainfall estimation.

2.3 Fuzzy logic algorithm

There is no clear boundary between the polarization parameters of different hydrometeors, the fuzzy logic algorithm divides the polarization parameters into various levels so that the particles can be identified according to the flexible classification principle (Liu and Chandrasekar, 2000). Liu and Chandrasekar (2000) used neural network learning to determine the constant parameter values in the algorithm. Since then, the algorithm has been further optimized (Cao et al., 2005; Park et al., 2009; Song et al., 2021). At present, this method has been widely used to classify hydrometeors based on radar observation (Dolan et al., 2013; Wu et al., 2018). The process of the algorithm includes the following four steps: fuzzification, inference, aggregation and defuzzification.

2.3.1 Fuzzification

Fuzzification transforms the polarization parameter value into the possibility (also known as a fuzzy set) of being judged as a certain hydrometeor type by constructing a membership function. In the membership function, the observed parameters are independent variables and the fuzzy set is a dependent variable. A one-to-one membership function was applied between each hydrometeor type and each polarization parameter, 10 types of hydrometeors (drizzle, rain, dry snow, dry crystal, wet snow, dry graupel, wet graupel, small hail, large hail, rain hail) could be distinguished, and four parameters (Z, Z_{DR}, K_{DP}, ρ_{HV}) were used in this study. As for the type of membership function, the asymmetric trapezoidal function given by Park et al. (2009) was used, and the expression is as follows:

$$\boldsymbol{T}(\boldsymbol{x},\boldsymbol{X_1},\boldsymbol{X_2},\boldsymbol{X_3},\boldsymbol{X_4}) = \begin{cases} \mathbf{0}, & \boldsymbol{x} < \boldsymbol{X_1} \\ \dfrac{\boldsymbol{x}-\boldsymbol{X_1}}{\boldsymbol{X_2}-\boldsymbol{X_1}}, & \boldsymbol{X_1} \le \boldsymbol{x} < \boldsymbol{X_2} \\ \mathbf{1}, & \boldsymbol{X_2} \le \boldsymbol{x} < \boldsymbol{X_3} \\ \dfrac{\boldsymbol{X_4}-\boldsymbol{x}}{\boldsymbol{X_4}-\boldsymbol{X_3}}, & \boldsymbol{X_3} \le \boldsymbol{x} < \boldsymbol{X_4} \\ \mathbf{0}, & \boldsymbol{x} \ge \boldsymbol{X_4} \end{cases} \quad (3)$$

where $\boldsymbol{x}$ is the value of radar polarization parameter, $\boldsymbol{X_1}, \boldsymbol{X_2}, \boldsymbol{X_3}, \boldsymbol{X_4}$ are constant parameters, which control the shape of the function. The constant parameters for the 10 hydrometeor types (Table 1) used in this study were referred to the results given by Cao et al. (2005) and the temperature thresholds given by Li et al. (2017).

2.3.2 Inference and aggregation

The membership function value $\boldsymbol{T_{ij}}$ corresponding to the polarization parameter j (j = 1, 2, 3, 4) and the hydrometeor type i (i = 1, 2, 3, …, 10) can be obtained through fuzzification. The processing of inference and aggregation enables each hydrometeor type to have aggregated value $\boldsymbol{RS_i}$ at each observation point. Cao et al. (2005) pointed out that there was no significant difference in the results of $\boldsymbol{RS_i}$ by multiplying or adding the function values with unequal weights. The multiplication formula is as follows:

$$\boldsymbol{RS_i} = \prod_{j=1}^{4} \boldsymbol{T_{ij}} \quad (4)$$

2.3.3 Defuzzification

For each point, there should be 10 aggregated values, the defuzzification aims to select the type with the largest **RS** from them and take it as the classification result.

Although the fuzzy logic algorithm can only identify the dominant hydrometeor type, and the classification results are affected by the quality of radar data and temperature profile (Dolan et al., 2013). It is still an effective method to investigate the spatial and temporal distribution of hydrometeors in clouds, and the uncertainty can be reduced by statistical analysis.

3 Overview of the precipitation event

3.1 Radar reflectivity and precipitation estimation

From the evening to the night of 16 October 2021, there were thunderstorms occurred in Xisha and surrounding regions. The precipitation on Yongxing Island was concentrated from 19:00 to 20:00 (UTC+8, the same below), with the hourly rainfall of 11.3 mm (Figure 1A). Due to the "Cone of Silence", it is difficult to study the cloud directly above the radar, and to reduce the influence of radar scanning field on statistics, a fixed square region (Region 1, 111.6°E–111.9°E, 16.8°N–17.1°N, a size that can contain a complete

TABLE 1 Parameters of the membership functions for 10 hydrometeor types.

		Drizzle	Rain	Dry snow	Dry crystal	Wet snow	Dry graupel	Wet graupel	Small hail	Large hail	Rain hail
Z (dBZ)	X_1	0	23	0	0	0	38	39	48	53	45
	X_2	0	27	0	0	0	40	42	50	56	50
	X_3	22	58	35	25	43	50	54	60	70	70
	X_4	28	63	41	32	46	52	56	62	70	70
Z_{DR} (dB)	X_1	−.2	.1	−.2	−.3	−.3	−.6	−.8	−.6	−2	−1.2
	X_2	.2	.6	.2	.2	.2	−.4	−.4	−.4	−2	−.8
	X_3	.8	3.8	.5	5	2.6	.8	2.6	.4	−.8	.8
	X_4	1.2	4.3	.7	5	3.2	1.2	3.2	.6	−.2	1.2
K_{DP} (° km^{-1})	X_1	−.3	−.4	−.1	.3	−.2	−.8	−.4	−.8	−1.2	−.8
	X_2	0	.2	.2	.5	.3	−.4	0	−.5	−.8	.2
	X_3	0	12	.5	1.5	2.0	.4	2.0	.5	.8	12
	X_4	.3	12	.8	1.8	2.3	.8	2.2	.8	1.2	12
ρ_{HV}	X_1	.96	.92	.92	.90	.75	.92	.90	.90	.92	.82
	X_2	.98	.97	.97	.96	.84	.97	.97	.97	.97	.92
	X_3	1	1	1	1	.93	1	1	1	1	1
	X_4	1	1	1	1	.98	1	1	1	1	1
T (°C)		>0	>−10	<0	<0	<5	<0	<5	>−25	>−15	>−10

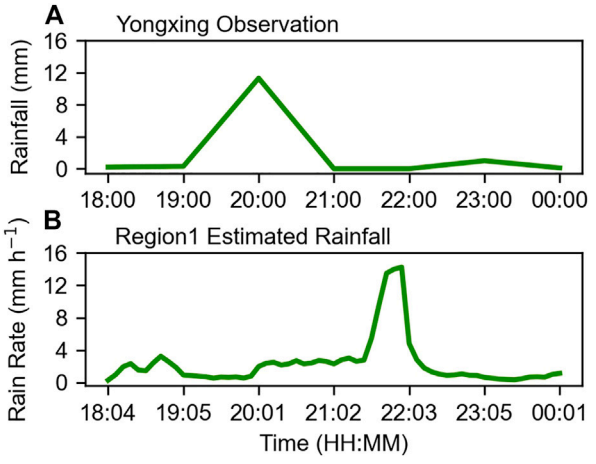

FIGURE 1
Time series of **(A)** hourly rainfall (units: mm) observed on Yongxing Island and **(B)** rain rate (units: mm h^{-1}) of Region 1 obtained by radar quantitative precipitation estimation on 16 October 2021 (UTC + 8, the same below).

convective cell) in the west was selected for further analysis, instead of tracking the clouds. Mean rainfall of Region 1 estimated by Eq. (2) is shown in Figure 1B, and radar reflectivity during the rainfall period are shown in Figure 2. The black square in Figure 2 denotes Region 1, and radar reflectivity depicts that the precipitation clouds were mixture of convective and stratiform clouds. Scattered convective bubbles with high reflectivity were embedded in broad stratiform clouds with low reflectivity. Under the prevailing east wind, the clouds system kept moving westward, and the Region 1 was successively affected by different clouds. At 20:01, the strong echo belt from northeast to southwest was located in the east of Region 1, then it moved westward and weakened at 20:31. At 21:17, the rear enhanced convective clouds moved to the eastern edge of Region 1, making the rainfall begin to increase. And at 21:43, Rigion 1 was almost covered by convective clouds, the strongest rainfall occurred, with the rate increasing from less than 4 mm h^{-1} to more than 14 mm h^{-1}. Later, as the convective clouds moved out and decayed, the echo over Region 1 weakened and the mean rain rate dropped to less than 2 mm h^{-1}, the rainfall tended to end.

3.2 Atmospheric circulation

Figure 3 delineates large-scale circulation at 17:00 on 16 October. At 200 hPa, the northern SCS was controlled by the South Asian High, and there was a divergence in the upper level (Figure 3A). The East Asian Trough at 500 hPa in the middle and high latitudes was located in the east of 120°E (Figure 3B). The continental high corresponding to the upper trough carried strong cold air southward (Figure 3D). The ridge of Western Pacific Subtropical High at 500 hPa was located near 28°N and extended west to 95°E. Therefore, the warm and humid airflow on the southwest side of the subtropical high was conducive to the transport of water vapor and the development of ascending motion. In the lower layers (700 hPa and below), ITCZ controlled the northern SCS and a tropical depression formed in the ITCZ.

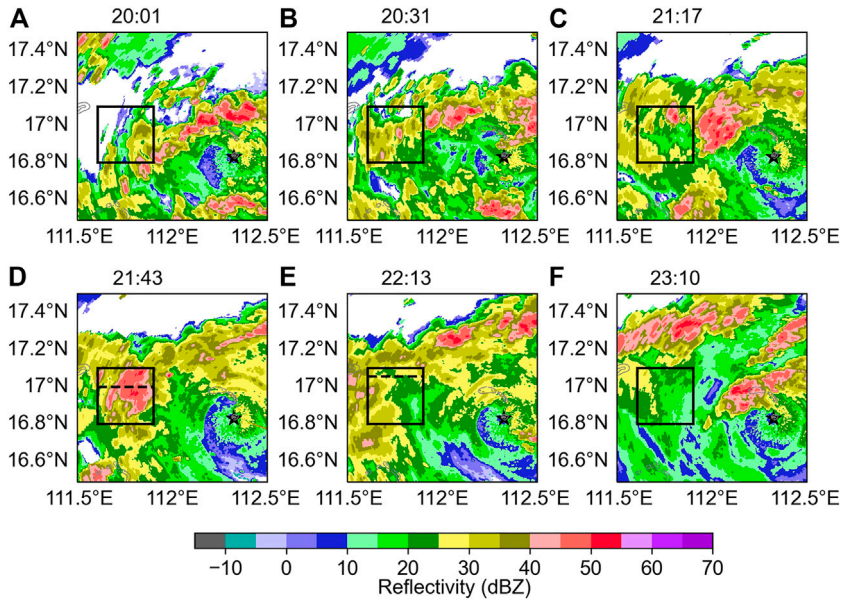

FIGURE 2
Distribution of composite reflectivity (units: dBZ) at **(A)** 20:01, **(B)** 20:31, **(C)** 21:17, **(D)** 21:43, **(E)** 22:13, and **(F)** 23:10 on 16 October. The black square denotes Region 1 (the same below).

Lander (1996) pointed out that ITCZ was located south of 10°N in October, compared with its climatological position, both wind convergence and the maximum outgoing longwave radiation during the event were around 15°N, indicating a northward shift of ITCZ (shown in Supplementary Figures S1, S2). Yongxing Island was located in the north of the depression, the northeast and the southeast airflow converged to form a low-level easterly jet, which provided sufficient water vapor flux for the occurrence of the rainfall (Figure 3C). The continuous southward movement of the continental high increased the pressure gradient in the north of the tropical depression and further intensified the dynamic field. The above analysis indicates that the rainfall was affected by the interactions of multiple systems, including the continental high, the Western Pacific Subtropical High, and the tropical depression in the ITCZ. In autumn, several heavy precipitation events in Xisha were caused by this synoptic situation, so the case was representative to some extent (Feng et al., 2015; Li et al., 2016).

3.3 Atmospheric stratification

As shown in Figure 4, the temperature profile, dew point temperature profile, and Convective Available Potential Energy (CAPE) in the skew T-lnP diagram were all "narrow and long" at 19:00 on 16 October, indicating there was plenty water vapor from bottom to top, which was favorable for the formation and development of the rainfall. The CAPE reached 3018.3 J kg^{-1}, and the convective inhibition (CIN) was 0, these were thermodynamic factors triggering convection. The lifting condensation level (LCL) was around 150 m, which was responsible for the condensation of water vapor, and the release of latent heat further promoted the development of convection. The 0°C layer was located near 5060 m, and the thick warm cloud layer provided an ample area for the development of warm rain. From the sounding data, the corresponding altitudes of 5°C, 0°C, −10°C, −15°C, and −25°C layers were 4,240, 5,060, 7,160, 8,110, and 9,600 m respectively, which were used to classify hydrometeors in fuzzy logic algorithm. Easterly winds prevailed during the rainfall, the wind speed exceeded 20 m s^{-1} from 800 to 920 hPa, and the vertical wind shear was 15.2 m s^{-1} from 0 to 6 km. High CAPE, low LCL, and moderate deep vertical wind shear were all favorable conditions for the development of the convection.

The dew point temperature form bottom to top decreased significantly at 01:00 on 17 October, demonstrating that the relative humidity decreased, because the rainfall consumed a certain amount of water vapor. Moreover, the convective instability energy below 700 hPa was reduced, but the CAPE was still high (2860.61 J kg^{-1}), which provided energy for the rainfall on 17 October.

4 Classification and statistical analysis of hydrometeors

4.1 Hydrometeor classification

To verify the accuracy of algorithm results, the correlation coefficient between the time series of mean rain rate in Region 1 and the time series of particles classified as rain was calculated. The correlation was up to .93, which was statistically significant at the 95% confidence level, indicating that the classification results of the fuzzy logic algorithm were reasonable.

Figure 5 shows the hydrometer distribution at 4.3° elevation at the same time as Figure 2. It can be seen that the distribution of hydrometeors depended on the temperature inside the clouds. Liquid hydrometeors (rain and drizzle) were mainly located below the 0°C layer, and the greater the reflectivity, the larger the raindrops. Only a few rain particles were transported upward to form

10.3389/feart.2022.1050858

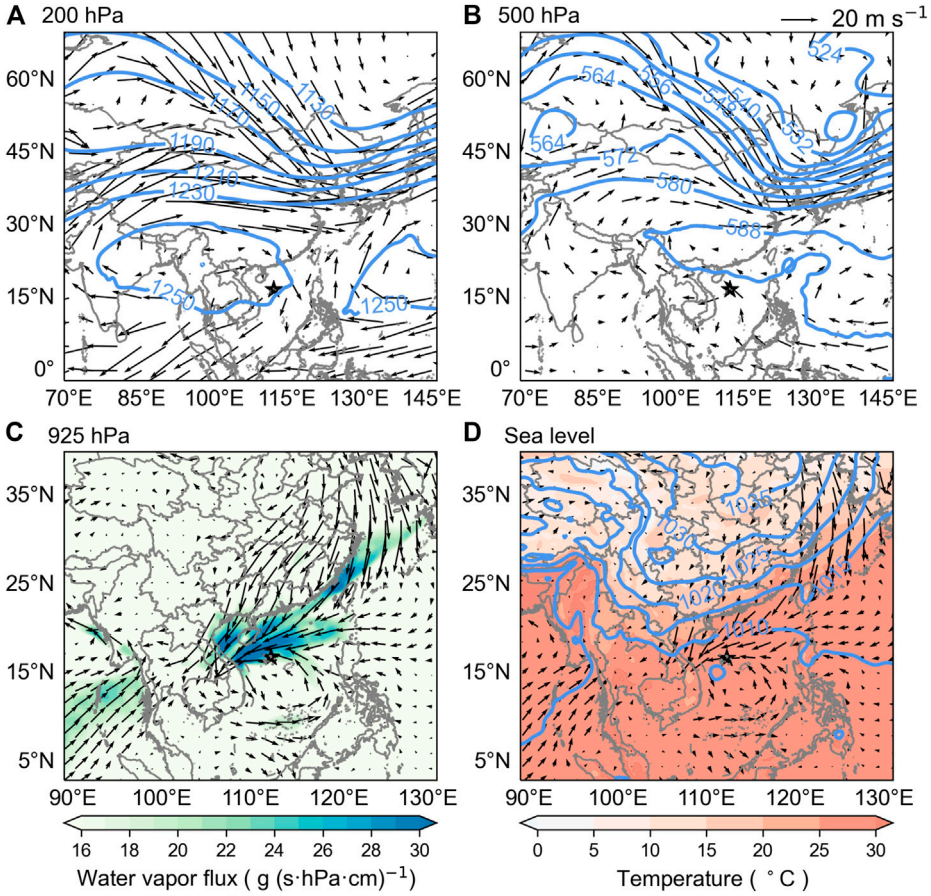

FIGURE 3
Large-scale circulation at 17:00 on 16 October 2021. **(A)** Geopotential height (blue contours, units: dagpm) and wind field at 200 hPa; **(B)** Geopotential height (blue contours, units: dagpm) and wind field at 500 hPa; **(C)** Water vapor flux [shading, units: g (s·hPa·cm)$^{-1}$] and wind field at 925 hPa; **(D)** Mean sea level pressure (blue contours, units: hPa), 2 m temperature (shading, units: °C) and 10 m wind field. The black star represents Sansha meteorological station (the same below).

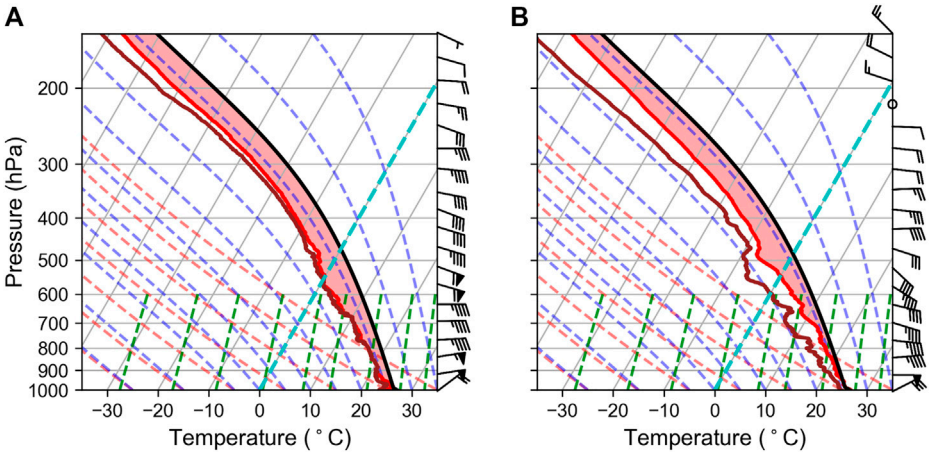

FIGURE 4
The skew T-lnP diagram of Sansha meteorological station at 19:16 on 16 October **(A)**, and 01:18 on 17 October **(B)**. The brown and red solid lines are the dew point temperature and temperature profile, respectively.

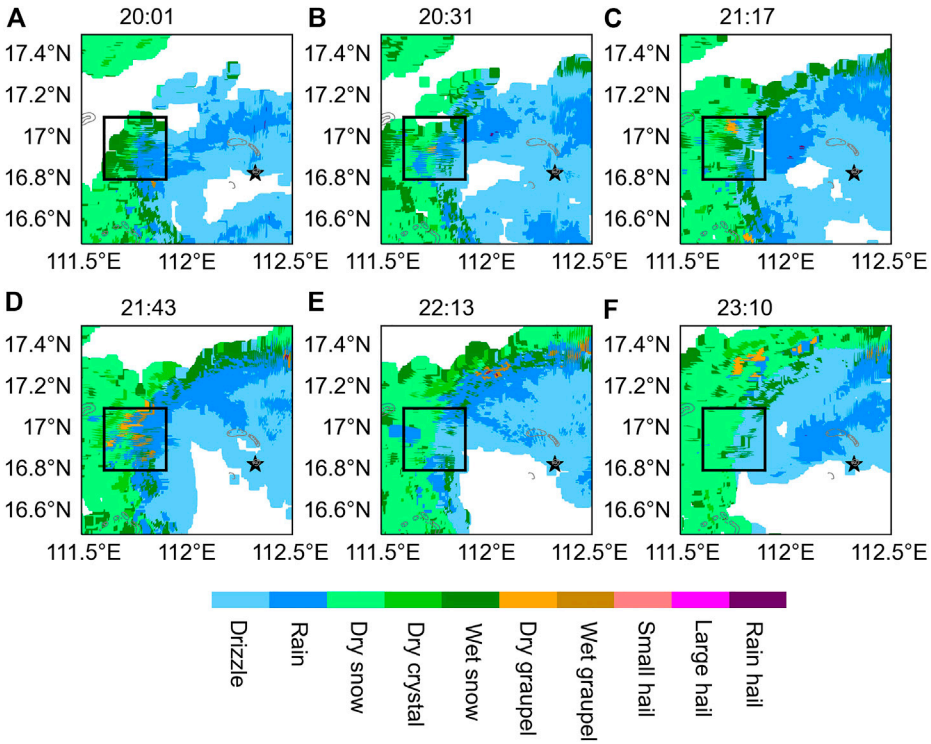

FIGURE 5
Distribution of hydrometeors at 4.3° elevation **(A)** 20:01, **(B)** 20:31, **(C)** 21:17, **(D)** 21:43, **(E)** 22:13, and **(F)** 23:10 on 16 October.

TABLE 2 The relative content of each hydrometeor type in Region 1 and its correlation with rain particles.

Type	Percentage %	Correlation coefficient
Drizzle	9.42~75.39	−.46[a]
Rain	.35~53.54	—
Dry snow	0~52.59	−.54[a]
Dry crystal	0~4.55	.34
Wet snow	0~15.32	−.24
Dry graupel	0~1.72	.61[a]
Wet graupel	0~1.93	.69[a]

[a]Indicates the value passes 95% significance test.

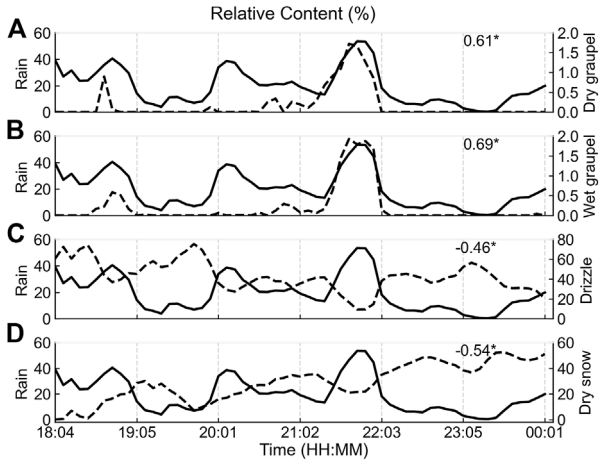

FIGURE 6
Time series of the relative content of rain, dry graupel, wet graupel, drizzle, and dry snow in Region 1. The black solid line represents rain particles, the black dashed line in **(A–D)** represents dry graupel, wet graupel, drizzle, and dry snow, respectively. The number shows their correlation coefficient, and * indicates the value passes 95% significance test.

supercooled water above the 0°C layer, where ice hydrometeors dominated, among which dry snow was the main type, mixed with wet snow and a small amount of dry crystal. The transition zone was located near the 0°C layer, where liquid and ice hydrometeors coexisted, in which wet snow was abundant, and graupel scattered in the strong echo area.

4.2 Statistical characteristics of hydrometeors

To explore the evolution of hydrometeors during the rainfall process and their impact on the raindrop formation, the relative content of particles was counted, and the correlations between rain particles and other types of hydrometeor were calculated (Table 2). The three most types were drizzle (9.42%–75.39%), rain (0.35%–53.54%) and dry snow (0%–52.59%), followed by wet snow (0%–15.32%) and dry crystal (0%–4.55%), dry graupel and wet graupel

TABLE 3 Percentage of reflectivity in the convective and stratiform clouds.

	0~10 dBZ (%)	10~20 dBZ (%)	20~30 dBZ (%)	30~40 dBZ (%)	>40 dBZ (%)
Convective	9.13	13.73	28.28	26.92	21.97
Stratiform	25.66	36.18	33.63	4.54	0.00

(0%–1.72%, 0%–1.93%) were the least, and there were almost no hails (small hail, large hail, rain hail). Abundant liquid and ice hydrometeors indicated that both warm and cold cloud played an important role in the rainfall.

Figure 6 shows the time series of the relative content of rain, dry graupel, wet graupel, drizzle, and dry snow. Although the content of dry graupel and wet graupel was small, their relative content showed a consistent change with rain particles, with a correlation coefficient of .61 and .69 respectively (Figures 6A, B), which meant graupel could enhance the ground rainfall (Hua and Liu, 2016). However, due to the low quantity of graupel, its melting was not the main source of rain particles. Figure 6C shows that the increase of rain particles was accompanied by the decrease of drizzle, the opposite trends indicated that the coalescence played an important role in this event. As a kind of giant cloud condensation nuclei with great hygroscopicity, high sea salt aerosol concentration in marine environment can accelerate the conversion of cloud water to rain water, promoting rain formation (Rosenfeld, 2018; Jiang et al., 2019). Compared with the previous research (Li et al., 2017), the dry snow over the Xisha area was rich while the dry crystal was less. This might be because the moist marine environment was conducive to deposition and aggregation, making the generation of snow easy. In addition, as shown in Figure 6D, at 18:04, the relative content of dry snow approached 0%, then it gradually increased with time, and had the strongest negative correlation with rain particles (with a correlation coefficient of −.54). This suggested that the initial rain particles were formed by the collision of drizzle, and then the increasing dry snow also had an important contribution to rain formation. When the focus region was enlarged to Region 2 (Supplementary Figure S3), it was found that the above rule was still valid, but the relative content of dry snow was more negatively correlated with rain particles (−.83, shown in Supplementary Figure S4), which further indicated that during the rainfall dry snow had an important contribution to rain formation.

5 Radar reflectivity and hydrometeors distribution in different clouds

Under the prevailing east wind, the precipitation cloud system kept moving westward, and the development and dissipation of clouds changed rapidly. To study the distribution and evolution of hydrometeors in different cloud types, convective clouds at 21:43 (Figure 2D) on 16 October and stratiform clouds at 22:13 (Figure 2E) in Region 1 were selected. Table 3 shows the percentage of reflectivity with different intensities in the two cloud types. There were strong echoes in the convective clouds, 48.89% of which exceeded 30 dBZ, while reflectivity of the stratiform clouds was mainly below 30 dBZ, and only 4.54% was greater than that.

5.1 Radar reflectivity and hydrometeors distribution in convective clouds

Radar composite reflectivity and hydrometeors distribution of the convective clouds at 21:43 on 16 October are shown in Figures 2D, 5D respectively. From the classification results at 4.3° elevation in Figure 5D, it can be seen that hydrometeors below the 0°C layer were large rain particles and mixed with wet snow and wet graupel, while above the 0°C layer were mainly dry snow and mixed with dry graupel. A section along the dashed lines in Figure 2D was chosen to analyze the vertical characteristics of the convective clouds, the results are shown in Figure 7, in which the two black horizontal dashed lines represent the 0°C and − 38°C isotherms respectively. The convective clouds were fully developed with the echo top height of 11 km, and the reflectivity greater than 40 dBZ was below the 0°C layer (Figure 7A). Figure 7B shows that graupel existed near the 0°C layer with reflectivity greater than 40 dBZ, which was consistent with the results of Wu et al. (2018). According to the spatial distribution of particles, it can be inferred that the sources of graupel mainly included the automatic conversion of snow to graupel, freezing of rain to graupel when colliding with snow or collected by snow. The melting of ice hydrometeors was an important source of ground rainfall. In the strong convection areas, snow can rime to form graupel, and graupel can further melt to form large raindrops (Wu et al., 2018).

5.2 Radar reflectivity and hydrometeors distribution in stratiform clouds

With the removal of convective system, Region 1 was covered by stratiform clouds at 22:13 on 16 October, the echo intensity obviously weakened (Figure 2E). Hydrometeors below the 0°C layer was small size drizzle, and there was no graupel existed (Figure 5E). The section analysis shows that the echo distribution was flat and conformed to the characteristics of stratiform clouds (Figure 8A). Compared with the convective clouds, the echo top height decreased. The reflectivity greater than 30 dBZ was mainly below the 0°C layer, and a 0°C-layer bright band generated. Above the 0°C layer, dry snow dominated, mixed with a small amount of dry crystal (Figure 8B). According to the formation of bright bands and the distribution of particles, it could be speculated that the formation of the bright band was mainly caused by the melting of snow and the change of particle velocity and shape after melting, which indicated that snow could directly affect ground rainfall in the stratiform clouds by melting. In addition, the existence of the bright band also suggested that the ascending motion in the clouds was weak, creating favorable conditions for the melting of snow.

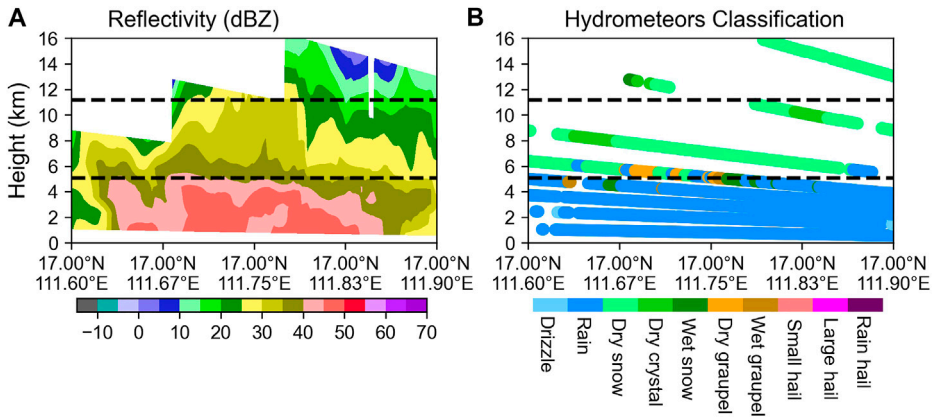

FIGURE 7
Distribution of **(A)** radar reflectivity (units: dBZ) and **(B)** hydrometeors at 4.3° elevation in the convective clouds at 21:43 on 16 October along the section in Figure 2D. The black dashed line represents 0°C and −38°C isotherms, respectively.

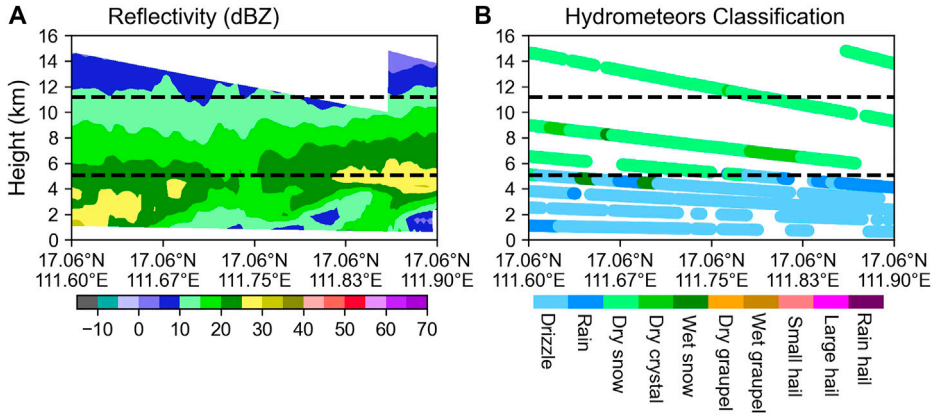

FIGURE 8
Distribution of **(A)** radar reflectivity (units: dBZ) and **(B)** hydrometeors at 4.3° elevation in the stratiform clouds at 22:13 on 16 October along the section in Figure 2E. The black dashed line represents 0°C and −38°C isotherms, respectively.

5.3 Distribution of hydrometeors at different heights

During this tropical marine rainfall, the particles grew through deposition and aggregation above the 0°C layer, and rimed in the supercooled water zone; the rimed particles fell below the 0°C layer and melted, finally forming raindrops through condensation and coalescence growth. This was a typical "seeding-feeding" structure (Hong and Zhou, 2005; He et al., 2015). To explore the effect of ice hydrometeors on raindrop formation and their evolution in different cloud types, the relative content of hydrometeors was analyzed (Table 4). Among them, supercooled water refers to rain particles that existed above the 0°C layer. The relative content of all kinds of hydrometeors was significantly different. In the upper layer where the temperature was lower than −20°C, there were only three type hydrometeors: dry snow, dry crystal, and wet snow. Among them, dry snow was the most, accounting for 10.35% and 19.19% of the total in the convective and stratiform clouds respectively, and 6.81% and 11.44% of them were located above the −38°C layer. It is generally considered that − 38°C is the threshold temperature for homogeneous nucleation of particles, the result shows that homogeneous nucleation could happen above marine area, then dry snow was formed through active deposition and aggregation. In the middle layer of 0 to −20°C, the amount of supercooled water in the convective clouds was more than that in the stratiform clouds (4.18% and 1.28% respectively), the reason was that the ascending motion was more vigorous in the convective clouds, so the liquid hydrometeors in the lower layer was transported to the middle layer. The increase in supercooled water is in favor of rimming. Therefore, dry snow in the convective clouds was consumed and graupel was generated, while no graupel appeared in the stratiform clouds in either the middle or lower layer. This showed that the "seeding-feeding" phenomenon in the convective bubbles was more active. However, compared with the results on continental convective clouds of Li et al. (2017), the content of graupel was less, suggesting that the riming in the marine convective clouds was weaker, this might be attributed to lower anthropogenic aerosol concentration. As an important source of cloud condensation nuclei,

TABLE 4 The relative content of hydrometeors in different layers of the convective and stratiform clouds.

	Type	Convective (%)	Stratiform (%)
Upper layer (<−20°C)	Dry snow	10.35	19.19
	Dry crystal	1.49	.30
	Wet snow	1.26	.52
Middle layer (0 to −20°C)	Supercooled water	4.18	1.28
	Dry snow	11.60	21.32
	Dry crystal	2.37	1.69
	Wet snow	.57	.55
	Dry graupel	1.27	.00
	Wet graupel	.25	.00
Lower layer (>0°C)	Wet snow	2.13	2.12
	Wet graupel	1.63	.00
	Drizzle	9.55	44.29
	Rain	53.34	8.74

high anthropogenic aerosol concentration can reduce the size of cloud droplets (Albrecht, 1989). On the one hand, it can reduce the efficiency of converting cloud water to rain water and the collision between ice crystals and supercooled water; on the other hand, the decrease in the coalescence efficiency increases the liquid water content, providing more cloud water for riming and freezing (Cheng et al., 2010). Cao et al. (2021) and Xiao et al. (2016) also found that high anthropogenic aerosol concentration could ultimately increase surface rainfall by strengthen riming. In the lower layer where the temperature was higher than 0°C, there were mainly liquid types: drizzle and rain. Compared with the stratiform clouds, the size of raindrops in the convective clouds was larger, mainly because of the following two reasons. Firstly, ice hydrometeors in the upper layer in the convective clouds, such as dry snow, could form graupel by riming in the supercooled water zone, and then the graupel melt to form larger size liquid phase particles. Secondly, the stronger updraft in the convective clouds prevented the raindrops of small size from falling to the ground, so the smaller raindrops suspended in the air were easily collected by the larger ones (Seela et al., 2018; Bao et al., 2020).

6 Conclusion

One autumn rainfall caused by the northward movement of ITCZ in Xisha and surrounding regions on 16 October 2021 was analyzed by using S-band dual-polarization weather radar data and fuzzy logic algorithm, to explore the microphysics mechanisms. The conclusions are as follows:

1) The rainfall event was caused by the interactions of the Western Pacific Subtropical High, the continental high, and the tropical depression in the ITCZ. The atmosphere was thermally unstable, with low LCL, large CAPE, and moderate vertical wind shear.
2) Radar quantitative precipitation estimation showed the peak mean rain rate of Region 1 was 14.3 mm h^{-1}. Drizzle, rain, and dry snow were the three most types in the precipitation clouds. Below the 0°C layer, there were mainly liquid hydrometeors, and the greater the reflectivity, the larger the particles. Dry snow was dominant above the 0°C layer, sufficient water vapor in the marine environment promoted the deposition and aggregation growth of ice particles, making the dry snow more than dry crystal. The transition zone was located around the 0°C layer where liquid and ice hydrometeors coexisted, with graupel scattered in the strong echo region (>40 dBZ).
3) The relative content of dry graupel and wet graupel showed consistent trends with rain particles, which confirmed the generation of graupel could enhance surface rainfall, but the melting of it was not the main source of raindrops because of its low content. The opposite trend between drizzle, dry snow and rain particles indicated that the coalescence growth and transformation of snow made great contributions to the ground rainfall.
4) In the stratiform clouds, dry snow mainly melted to small raindrops because of insufficient supercooled water. The vigorous vertical development in the convective clouds transported liquid water above the 0°C layer to form supercooled water, then dry snow could rime to form graupel, and large raindrops were generated by graupel melting. The stronger riming and coalescence growth in the convective clouds made the raindrops larger than that of stratiform clouds. Compared with continental convective clouds, the riming in marine environment was weaker, which might be attributed to lower anthropogenic aerosol concentration.

Data availability statement

The original contributions presented in the study are included in the article/Supplementary Material, further inquiries can be directed to the corresponding author.

Author contributions

JF conceived the idea, processed the data, plotted figures, and wrote the manuscript. YH and FX provided the observed data and gave guidance on the data processing. FG, ST, YH, and FW improved the manuscript. FW, WL, WW, JS, and YZ contributed to the study design. LS gave scientific research guidance and revised the manuscript.

Funding

This study is supported by the National Natural Science Foundation of China (Grant No. 41975008) and the Key Laboratory of South China Sea Meteorological Disaster Prevention and Mitigation of Hainan Province (Grant No. SCSF201906).

Acknowledgments

The authors would like to thank ECMWF for providing the free dataset; to Python for the computing and plotting techniques; to editor and reviewers for their efforts and constructive comments that have improved the manuscript.

Conflict of interest

The authors declare that the research was conducted in the absence of any commercial or financial relationships that could be construed as a potential conflict of interest.

Publisher's note

Supplementary material

The Supplementary Material for this article can be found online at: https://www.frontiersin.org/articles/10.3389/feart.2022.1050858/full#supplementary-material

References

Albrecht, B. A. (1989). Aerosols, cloud microphysics, and fractional cloudiness. *Science* 245, 1227–1230. doi:10.1126/science.245.4923.1227

Bao, X., Wu, L., Zhang, S., Li, Q., Lin, L., Zhao, B., et al. (2020). Distinct raindrop size distributions of convective inner-and outer-rainband in typhoon maria (2018). *J. Geophys. Res. Atmos.* 125 (14), e2020JD032482. doi:10.1029/2020JD032482

Cao, J., Liu, L., and Ge, R. (2005). A study of fuzzy logic method in classification of hydrometeors based on polarimetric radar measurement. *Chin. J. Atmos. Sci.* 29 (5), 827–836. doi:10.3878/j.issn.1006–9895.2005.05.15

Cao, Q., Jiang, B., Shen, X., Lin, W., and Chen, J. (2021). Microphysics effects of anthropogenic aerosols on urban heavy precipitation over the Pearl River Delta, China. *Atmos. Res.* 253, 105478. doi:10.1016/j.atmosres.2021.105478

Chen, Z., and Li, Y. (2022). formation and hydrometeor type evolution of a typical warm precipitation based on cloud radar and precipitation radar data. *Trans. Atmos. Sci.* 45 (1), 87–98. doi:10.13878/j.cnki.dqkxxb.20210819001

Cheng, C.-T., Wang, W.-C., and Chen, J.-P. (2010). Simulation of the effects of increasing cloud condensation nuclei on mixed-phase clouds and precipitation of a front system. *Atmos. Res.* 96 (2–3), 461–476. doi:10.1016/j.atmosres.2010.02.005

Dolan, B., Rutledge, S. A., Lim, S., Chandrasekar, V., and Thurai, M. (2013). A robust C-band hydrometeor identification algorithm and application to a long-term polarimetric radar dataset. *J. Appl. Meteorol. Climatol.* 52 (9), 2162–2186. doi:10.1175/JAMC–D–12–0275.1

Fan, Y., Guo, X., Zhang, D., Fu, D., Chen, J., and Ma, Y. (2010). Airborne particle measuring system measurement on structure and size distribution of stratocumulus during august to september in 2004 over beijing and its surrounding areas. *Chin. J. Atmos. Sci.* 34 (6), 1187–1200. doi:10.3878/j.issn.1006–9895.2010.06.12

Feng, W., Fu, S., and Zhao, F. (2015). Circulation of extreme rainstorm and its anomalous characteristics during post-flood period of the last decade in hainan Island. *Meteorol. Mon.* 41 (2), 143–152. doi:10.7519/j.issn.1000-0526.2015.02.002

Feng, W., Wu, W., Zhao, F., and Zhou, L. (2017). Comparative analysis of circulation feature and dynamic structure of the rainstorms with different intensity during the autumn flood season in hainan Island. *J. Meteorological Sci.* 37 (6), 784–796. doi:10.3969/2016jms.0077

He, H., Gao, Q., Liu, X., Zhou, W., and Jia, X. (2015). Numerical simulation of the structure characteristics and precipitation mechanism of stratiform clouds with embedded convections. *Chin. J. Atmos. Sci.* 39 (2), 315–328. doi:10.3878/j.issn.1006–9895.1404.14102

He, Y., Xiao, H., and Lü, D. (2010). Analysis of hydrometeor distribution characteristics in stratiform clouds using polarization radar. *Chin. J. Atmos. Sci.* 34 (1), 23–34. doi:10.3878/j.issn.1006–9895.2010.01.03

Hong, Y., and Zhou, F. (2005). A numerical simulation on study of precipitation formation mechanism of "Seeding-Feeding" cloud system. *Chin. J. Atmos. Sci.* 29 (6), 885–896. doi:10.3878/j.issn.1006–9895.2005.06.05

Hou, T., Lei, H., He, Y., Yang, J., Zhao, Z., and Hu, Z. (2021). Aircraft measurements of the microphysical properties of stratiform clouds with embedded convection. *Adv. Atmos. Sci.* 38 (6), 966–982. doi:10.1007/s00376–021–0287–8

Hou, T., Lei, H., Hu, Z., Yang, J., and Li, X. (2020). Simulations of microphysics and precipitation in a stratiform cloud case over northern China: Comparison of two microphysics schemes. *Adv. Atmos. Sci.* 37 (1), 117–129. doi:10.1007/s00376–019–8257–0

Hua, C., and Liu, Q. (2016). Sensitivity of landing typhoon structure and precipitation to varying cloud microphysical processes. *J. Trop. Meteorol.* 22 (3), 341–351. doi:10.16555/j.1006–8775.2016.03.008

Jiang, B., Lin, W., Li, F., and Chen, J. (2019). Sea-salt aerosol effects on the simulated microphysics and precipitation in a tropical cyclone. *J. Meteor. Res.* 33 (1), 115–125. doi:10.1007/s13351–019–8108–z

Lander, M. A. (1996). Specific tropical cyclone track types and unusual tropical cyclone motions associated with a reverse-oriented monsoon trough in the western north pacific. *Weather Forecast* 11 (2), 170–186. doi:10.1175/1520-0434(1996)011<0170:stctta>2.0.co;2

Lee, H., Baik, J.-J., and Khain, A. P. (2018). Turbulence effects on precipitation and cloud radiative properties in shallow cumulus: An investigation using the WRF-LES model coupled with bin microphysics. *Asia Pac. J. Atmos. Sci.* 54, 457–471. doi:10.1007/s13143–018–0012–4

Li, X., Zhou, Y., Xiao, H., Wu, W., Zhai, L., Guo, F., et al. (2017). Synthesis and biological evaluation of a series of bile acid derivatives as FXR agonists for treatment of NASH. *Chin. J. Atmos. Sci.* 41 (6), 1246–1251. doi:10.1021/acsmedchemlett.7b00318

Li, Y., Li, X., Feng, W., and Chen, Y. (2016). Investigation of the synoptic situation associated with autumnal non-TC heavy precipitation in Xisha. *Meteorol. Mon.* 42 (8), 934–943. doi:10.7519/j.issn.1000–0526.2016.08.003

Li, Y., Lu, R.-Y., and He, J.-H. (2006). Tropical large-scale atmospheric circulation and sea surface temperature corresponding to autumn precipitation in hainan Island. *Chin. J. Atmos. Sci.* 30 (5), 1034–1042. doi:10.3878/j.issn.1006-9895.2006.05.29

Liu, H., and Chandrasekar, V. (2000). Classification of hydrometeors based on polarimetric radar measurements: Development of fuzzy logic and neuro-fuzzy systems, and *in situ* verification. *J. Atmos. Ocean. Technol.* 17 (2), 140–164. doi:10.1175/1520–0426(2000)017<0140:COHBOP>2.0.CO;2

Liu, L., Zhang, P., Xu, Q., Kong, F., and Liu, S. (2005). A model for retrieval of dual linear polarization radar fields from model simulation outputs. *Adv. Atmos. Sci.* 22 (5), 711–719. doi:10.1007/BF02918714

Park, H., Ryzhkov, A. V., Zrnic, D. S., and Kim, K.-E. (2009). The hydrometeor classification algorithm for the polarimetric WSR-88d: Description and application to an MCS. *Weather Forecast* 24 (3), 730–748. doi:10.1175/2008WAF2222205.1

Part, O. P., and Barros, A. P. (2009). Exploring the transient behavior of Z–R relationships: Implications forRadar rainfall estimation. *J. Appl. Meteorology Climatol.* 48 (10), 2127–2143. doi:10.1175/2009JAMC2165.1

Paulitsch, H., Teschl, F., and Randeu, W. L. (2009). Dual-polarization C-band weather radar algorithms for rain rate estimation and hydrometeor classification in an alpine region. *Adv. Geosci.* 20, 3–8. doi:10.5194/adgeo–20–3–2009

Qi, P., Guo, X., Lu, G., Duan, Y., Li, B., Wu, Z., et al. (2019). Aircraft measurements of a stable stratiform cloud with embedded convection in eastern taihang mountain of north China: Characteristics of embedded convection and melting layer structure. *Chin. J. Atmos. Sci.* 43 (6), 1365–1384. doi:10.3878/j.issn.1006–9895.1901.18220

Ribaud, J.-F., Machado, L. A. T., and Biscaro, T. (2019). X-band dual-polarization radar-based hydrometeor classification for Brazilian tropical precipitation systems. *Atmos. Meas. Tech.* 12 (2), 811–837. doi:10.5194/amt–12–811–2019

Rosenfeld, D. (2018). "Chapter 6—Cloud-aerosol-precipitation interactions based of satellite retrieved vertical profiles of cloud microstructure," in *Remote sensing of aerosols, clouds, and precipitation*. Editors T. Islam, Y. Hu, A. Kokhanovsky, and J. Wang (Elsevier), 129–152.

Seela, B. K., Janapati, J., Lin, P.-L., Wang, P. K., and Lee, M.-T. (2018). Raindrop size distribution characteristics of summer and winter season rainfall over north taiwan. *J. Geophys. Res. Atmos.* 123 (20602–11), 11, 602–611, 624. doi:10.1029/2018JD028307

Sheng, P., Mao, J., Li, J., Mo, Z., Zhang, A., Sang, J., et al. (2013). *Atmospheric physics*. Beijing: Peking University Press.

Song, W. T., Li, Y. Y., Huang, H., and Zhu, K. F. (2021). Hydrometeors classification and its application based on S-band dual polarization radar data. *Trans. Atmos. Sci.* 44 (2), 209–218. doi:10.13878/j.cnki.dqkxxb.20200318001

Wang, F., Sheng, L., An, X., Liu, Q., Zhou, H., Zhang, Y., et al. (2021). Controls on the northward movement of the ITCZ over the South China sea in autumn: A heavy rain case study. *Adv. Atmos. Sci.* 38 (10), 1651–1664. doi:10.1007/s00376–021–0445–z

Wu, D., Zhao, K., Kumjian, M. R., Chen, X., Huang, H., Wang, M., et al. (2018). Kinematics and microphysics of convection in the outer rainband of typhoon nida (2016) revealed by polarimetric radar. *Mon. Weather Rev.* 146 (7), 2147–2159. doi:10.1175/MWR–D–17–0320.1

Xiao, C., Yuan, W., Li, J., and Yu, R. (2013). Preliminary study of autumn rain in the South China sea. *Clim. Environ. Res.* 18 (6), 693–700. doi:10.3878/j.issn.1006–9585.2013.12163

Xiao, H., Yin, Y., Chen, Q., and Zhao, P. (2016). Impact of aerosol and freezing level on orographic clouds: A sensitivity study. *Atmos. Res.* 176–177, 19–28. doi:10.1016/j.atmosres.2016.02.014

Yu, X., Yao, X., Xiong, T., Zhou, X., Wu, H., Deng, B., et al. (2006). *Doppler weather radar principle and business application*. Beijing: China Meteorological Press.

Zeng, Q., Zhang, Y., Lei, H., Xie, Y., Gao, T., Zhang, L., et al. (2019). Microphysical characteristics of precipitation during pre-monsoon, monsoon, and post-monsoon periods over the South China sea. *Adv. Atmos. Sci.* 36 (10), 1103–1120. doi:10.1007/s00376-019-8225-8

Zhang, M., Deng, X., Zhu, R., Ren, Y., and Xue, H. (2021). The impact of aerosol vertical distribution on a deep convective cloud. *Atmosphere* 12 (6), 675. doi:10.3390/atmos12060675

Zhang, P., Du, B., and Dai, T. (2000). *Radar meteorology*. Beijing: China Meteorological Press.

Zhao, F., Wang, F., and Feng, W. (2011). Preliminary study on circulation characteristics and mechanism of rainstorm in autumn of hainan Island. *Chin. J. Trop. Agric.* 31 (5), 50–57.

Zhao, Z., and Lei, H. (2014). Observed microphysical structure of nimbostratus in northeast cold vortex over China. *Atmos. Res.* 142 (1), 91–99. doi:10.1016/j.atmosres.2013.09.008

Zhou, Y., Zhao, P., Da, X., Wu, W., Li, X., and Zhai, L. (2016). *Physics of clouds and precipitation*. Beijing: China Meteorological Press.

Zhou, Y., Zhao, P., and Xiao, H. (2017). *Warm cloud*. Beijing: China Science Publishing & Media LTD.

Zhu, S., and Guo, X. (2014). Ice crystal habits, distribution and growth process in stratiform clouds with embedded convection in North China: Aircraft measurements. *Acta Meteor. Sinica* 72 (2), 366–389. doi:10.11676/qxxb2014.013

frontiers | Frontiers in Earth Science

TYPE Original Research
PUBLISHED 10 January 2023
DOI 10.3389/feart.2022.1085136

OPEN ACCESS

EDITED BY
Chunlei Liu,
Guangdong Ocean University, China

REVIEWED BY
Yu Zhang,
Guangdong Ocean University, China
Jian-Feng Gu,
University of Reading, United Kingdom

*CORRESPONDENCE
Yu Du,
duyu7@mail.sysu.edu.cn

SPECIALTY SECTION
This article was submitted to Interdisciplinary Climate Studies, a section of the journal Frontiers in Earth Science

RECEIVED 31 October 2022
ACCEPTED 15 December 2022
PUBLISHED 10 January 2023

CITATION
Shen Y and Du Y (2023), Sensitivity of boundary layer parameterization schemes in a marine boundary layer jet and associated precipitation during a coastal warm-sector heavy rainfall event.
Front. Earth Sci. 10:1085136.
doi: 10.3389/feart.2022.1085136

Sensitivity of boundary layer parameterization schemes in a marine boundary layer jet and associated precipitation during a coastal warm-sector heavy rainfall event

Yian Shen[1,2] and Yu Du[1,3,4]*

[1]School of Atmospheric Sciences, Sun Yat-sen University, and Southern Marine Science and Engineering Guangdong Laboratory (Zhuhai), Zhuhai, China, [2]Huzhou Meteorological Bureau, Huzhou, China, [3]Guangdong Province Key Laboratory for Climate Change and Natural Disaster Studies, Sun Yat-Sen University, Zhuhai, China, [4]Key Laboratory of Tropical Atmosphere-Ocean System, Sun Yat-Sen University, Ministry of Education, Zhuhai, China

The sensitivity of planetary boundary layer (PBL) parameterization schemes in a marine boundary layer jet and associated precipitation is investigated in this study. Six PBL parameterization schemes in the Weather Research and Forecasting Model, including YSU, MYJ, MYNN, ACM2, BouLac, and UW schemes, are examined in simulating a marine boundary layer jet (BLJ) over South China Sea and associated coastal precipitation during a warm-sector heavy rainfall event (19–20 May 2015) near the coast of South China. The results show that YSU, MYJ, MYNN, and BouLac schemes can generally reproduce the coastal warm-sector heavy rainfall with 6-h accumulated precipitation exceeding 50 mm, but not for the ACMs and UW schemes. No convection initiation occurs in the ACM2 run, while rainfall is located to further north with weaker intensity in the UW run. Meanwhile, weakest and strongest BLJs are simulated in the ACM2 and UW runs, respectively. In the ACM2 run, the weaker BLJ with the maximum wind speed less than 17 m s^{-1} induces weaker convergence and lifting in the upwind side of the coastal terrain as well as less water vapor transport to the coastal area, which thus inhibit convection initiation. On the contrary, the too strong BLJ in the UW run with large area of wind speed greater than 18 m s^{-1} causes the northward movement of convection along with cold pools, and rainfall moves further north accordingly. The differences in BLJs' strength among PBL schemes are attributed to varying simulated low-level vortex on the northern side of the BLJ through veering ageostrophic winds. The intensity of the simulated low-level vortex is affected by variations in boundary layer mixing over land and associated vertical temperature stratification under different PBL schemes.

KEYWORDS

warm-sector heavy rainfall, PBL schemes, low-level jet, South China, numerical simulation

1 Introduction

The pre-summer rainy season over southern China (April—June) is the first rainy season on the mainland of China, which contributes approximately half of the annual precipitation (Luo et al., 2017) and causes severe floods or mudslides and large economic and human losses (Zhou et al., 2003). Heavy rainfall during the pre-summer rainy season often occurs near the front or in the warm sector hundreds of kilometers away from the front, which are regarded as frontal heavy rainfall and warm-sector heavy rainfall, respectively (Ding, 1994; Luo et al., 2017). Differences and similarities between the two types of heavy rainfall in South China are found in their initiation and maintenance mechanisms (Luo, 2017).

Previous studies have documented that the southerly marine boundary layer jet (BLJ), as one type of low-level jet (LLJ), play an important role in warm-sector heavy rainfall (Luo et al., 2017; Du and Chen, 2018; Zhang and Meng, 2018). Du and Chen (2018), Du and Chen (2019a), Du and Chen (2019b), Du et al. (2020a) and Du et al. 2022) demonstrated that the spatial structure and temporal evolution of the BLJ exert a significant influence on the convection initiation and development of warm-sector heavy rainfall. Based on statistical analysis (Wu et al., 2020; Li and Du, 2021), most warm-sector heavy rainfall cases are accompanied by the LLJs. Zhang and Meng (2018) used ensemble sensitivity analyses to examine the controlling factors of a persistent warm-sector rainfall event over southern China, and found that the LLJ was essential in rainfall intensity. In addition, the LLJs interacting with local terrain at the coastal area and the cold pools are important for the initialization and maintenance of warm-sector heavy rainfall over southern China (Wu and Luo, 2016; Du et al., 2020b).

Lack of obvious synoptic-scale forcings (e.g., a front or shear line), the formation mechanisms of warm-sector heavy rainfall over southern China have not been well understood compared to frontal heavy rainfall, and thus its quantitative precipitation forecast (QPF) skill remains rather low (Luo, 2017; Luo et al., 2017). Ensemble-based analyses showed that warm-sector rainfall events have a large ensemble spread, which indicated their limited practical predictability (Du and Chen, 2018; Zhang and Meng, 2018; Wu et al., 2020). Zhang and Meng (2019) demonstrated that the quantitative precipitation forecasting skill in warm-sector heavy rainfall associated with a LLJ was generally lower than that without LLJ.

The formation of LLJs is attributed to inertial oscillation driven by turbulent vertical mixing in the boundary layer (Blackadar, 1957), diurnal thermal contrast (Holton, 1967) and their combination (Du and Rotunno, 2014). Since PBL schemes in the numerical simulation parameterize the vertical turbulent transport of momentum and heat, different PBL schemes may produce varying boundary layer structures and thus affect the simulated performance of LLJs (Salmond and McKendry, 2005; Steeneveld et al., 2008; Steeneveld, 2014). Smith et al. (2018) evaluated the WRF model's ability to simulate nocturnal LLJs through three common boundary layer parameterization schemes, and found Quasi-Normal Scale Elimination (QNSE) run performed slightly better than Yonsei University (YSU) runs and the Mellor–Yamada Nakanishi Niino (MYNN) runs. Storm et al. (2009) demonstrated that different PBL schemes have the capability to capture some essential characteristics of the observed LLJs, such as location and timing, while the simulated LLJ wind speeds were sensitive to the PBL schemes.

A warm-sector heavy rainfall event occurred during 19–20 May 2015 at coast of South China with the maximum daily rainfall reaching 542 mm (Wu and Luo, 2016), which was one of the most intense heavy rain events during the pre-summer rainy season of that year (Luo et al., 2017). The ensemble forecasts from the European Center for Medium-Range Weather Forecasts (ECMWF) initialized at 0000 UTC 19 May or 1200 UTC 19 May completely missed this warm-sector rainfall event over the east coastal area of Guangdong Province (Shen et al., 2020). Wu and Luo (2016) analyzed this coastal warm-sector rainfall event by observations and documented that a mesoscale boundary, formed between the cold dome and the warm-and-moist air from the ocean (marine BLJ), caused the formation and maintenance of the quasi-linear-shaped MCS. Wu et al. (2020) further studied this same case by ensemble-based sensitivity analysis on the practical and intrinsic predictability and demonstrated that a stronger low-level southerly wind (marine BLJ) over the sea and a considerable surface cooling over the northern mountains were favorable for the warm-sector convection initiation. However, how the strength of simulated upstream marine BLJ influences the simulated warm-sector heavy rainfall event in the WRF model worth further study, and the response of the BLJ over the South China Sea to the planetary boundary layer (PBL) parameterization schemes is still not clear.

The objective of the current study is to examine the sensitivity of planetary boundary layer parameterization schemes in simulating warm-sector heavy rainfall over southern China associated with a marine boundary layer jet. Data and methodology used in the present study are provided in Section 2. Section 3 briefly introduces the warm-sector rainfall event we studied. The relationships between the BLJ and coastal warm-sector rainfall under different PBL schemes are investigated in Section 4. Section 5 presents the sensitivity of PBL parameterization schemes on the BLJ. Finally, concluding remarks and discussion are given in Section 6.

2 Data and method

2.1 Observational data

The radar reflectivity obtained from the S-band weather radar in Shanwei, Guangdong (station number: Z9660; the red

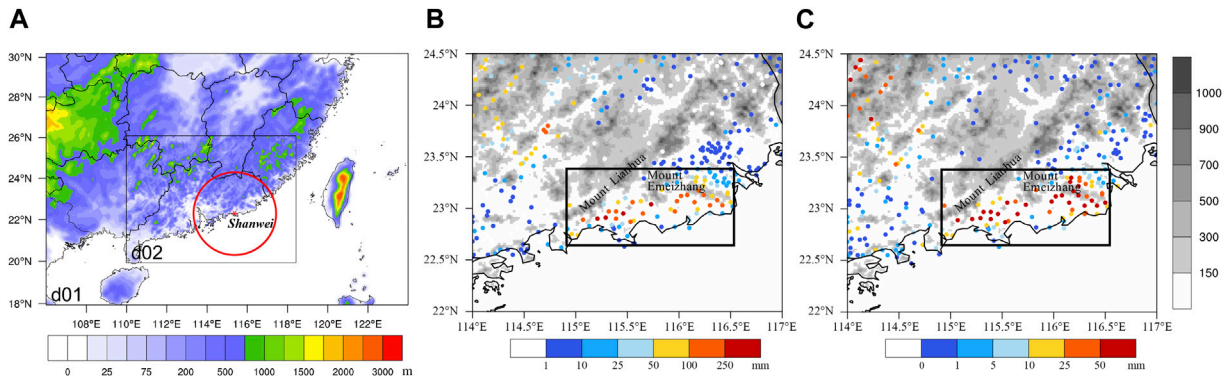

FIGURE 1
(A) Domain configurations of D01 and D02 and terrain height (units: m, shaded). The circle with a radius of 230 km is centered at the S-band weather radar in Shanwei; **(B)** Horizontal distribution of accumulated rainfall (mm, colored dots) during 1200 UTC 19 to 0000 UTC 20 May 2015 based on surface observations from surface weather stations; **(C)** Horizontal distribution of 6-h accumulated rainfall (mm, colored dots) during 1500 UTC 19 to 2100 UTC 20 May 2015. The location of colored dots represents the location of these weather stations. Grey shading represents topography height (m), and Mount Lianhua and Mount Emeizhang are labeled.

asterisk marked in Figure 1A) is utilized to illustrate the convection initiation and upscale growth in the warm-sector heavy rainfall event. The precipitation amount at 1-h intervals from 289 surface weather stations in the analysis domain (Figures 1B, C) are used, and these weather stations are densely distributed over southern China.

2.2 Numerical model

The Weather Research and Forecasting (WRF) Model (WRF-ARW, version 4.0) was applied in this study to simulate the warm-sector heavy-rainfall event. The model is initialized at 1200 UTC 18 May 2015 with the initial and lateral boundary conditions every 6 h from National Center for Environmental Prediction (NCEP) FNL operational global analysis data with spatial resolutions of 1°. Two model domains D01 and D02, with a horizontal grid spacing of 12 km and 4 km respectively, are shown in Figure 1A. The inner domain (D02) is one-way nested within an outer domain (D01). The vertical grid in the WRF Model employs 50 pressure levels, and the pressure of the model top is 50 hPa.

The physical parameterizations used in both two domains include the Thompson microphysics scheme (Thompson et al., 2008), the Rapid Radiative Transfer Model for Global Climate Models (RRTMG) longwave and shortwave radiation schemes (Iacono et al., 2008), and the unified Noah land surface model scheme (Livneh et al., 2011). The Kain–Fritsch convection parameterization scheme (Kain, 2004) is used in D01 but not applied in D02. This model configuration is commonly used in this area and achieves good performance in simulating heavy rainfall events (Du and Chen, 2019a).

The PBL parameterization schemes and associated surface layer schemes are varied in the simulations. Six PBL schemes were applied to examine the sensitivity of the PBL schemes, including 1) the Mellor-Yamada-Janjic PBL Scheme (MYJ) (Janjić, 2002), 2) the Yonsei University PBL Scheme (YSU) (Hong et al., 2006), 3) Mellor–Yamada Nakanishi Niino (MYNN) Level 2.5 PBL Scheme (Nakanishi and Niino, 2006), 4) Asymmetric Convection Model 2 PBL Scheme (ACM2) (Pleim, 2007a; Pleim, 2007b), 5) Bougeault-Lacarrere PBL Scheme (BouLac) (Bougeault and Lacarrere, 1989), and 6) University of Washington (UW) Boundary Layer Scheme (Bretherton and Park, 2009). MYJ scheme is applied with associated MYJ surface layer scheme, while the other five PBL schemes are used with revised MM5 Monin-Obukhov surface layer scheme (Jiménez et al., 2012). MYJ scheme, MYNN2.5 scheme, BouLac scheme and UW scheme are local schemes, while YSU scheme and ACM2 scheme are non-local scheme. Considering YSU scheme is widely used to simulate warm-sector heavy rainfall events and boundary layer jet over Southern China (Zhang and Meng, 2019; Dong et al., 2020; Du et al., 2014; Du et al., 2020), and the warm-sector heavy rainfall event we studied was well simulated with YSU scheme, the YSU scheme is regarded as a control run in the present study.

2.3 Momentum balance analysis

The momentum balance analysis is conducted to investigate the controlling forcings that cause the difference of simulated LLJ by various boundary layer schemes. The horizontal momentum equation can be written as

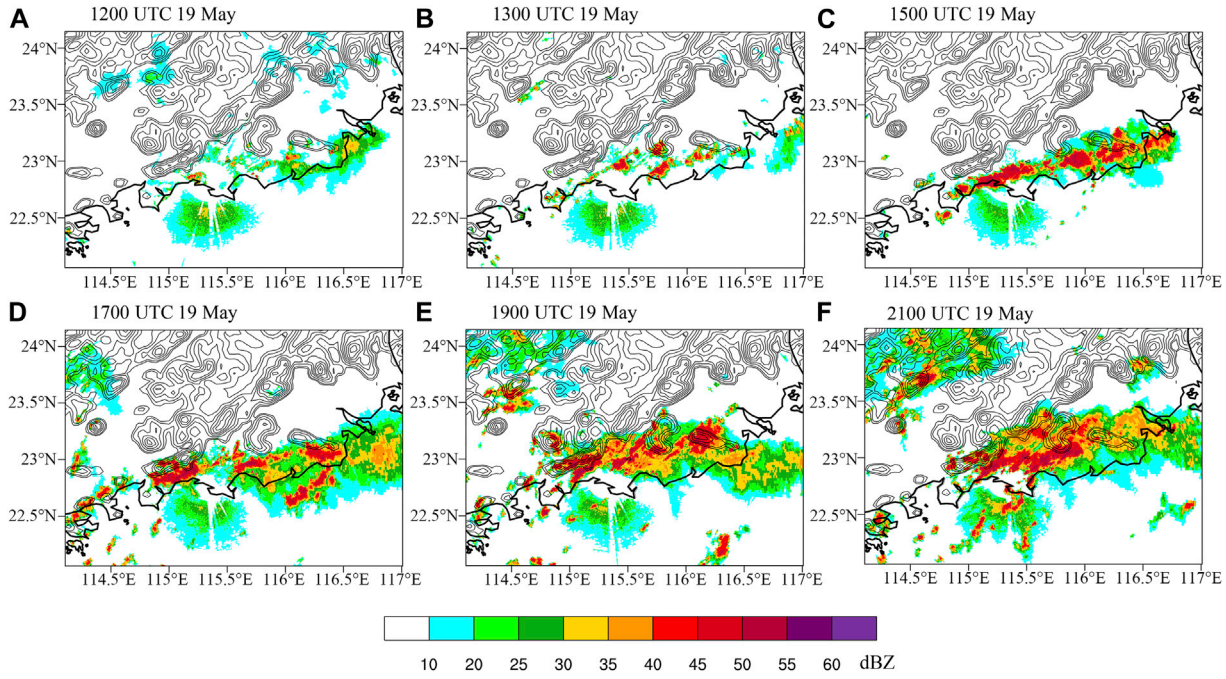

FIGURE 2
(A–F) Temporal evolution of composite radar reflectivity (unit: dBZ, shaded) from the S-band radar from 1200 UTC 19 May to 2100 UTC 19 May. Contour lines represent topography height in an interval of 100 m.

$$\frac{\partial u}{\partial t} = \left(-u\frac{\partial u}{\partial x} - v\frac{\partial u}{\partial y}\right) + f\left(v - v_g\right) + F_x \tag{2.1}$$

$$\frac{\partial v}{\partial t} = \left(-u\frac{\partial v}{\partial x} - v\frac{\partial v}{\partial y}\right) - f\left(u - u_g\right) + F_y \tag{2.2}$$

term I term II term III term IV

Where the local acceleration of the x and y wind component (term I) could be decomposed into horizontal advection (term II), the Coriolis force acting on ageostrophic wind (term III), and the residual in the x and y directions (term IV).

Since the LLJ's direction is not along the x or y direction, the horizontal momentum from (x, y) coordinates are transformed into right-hand coordinates (x', y'), with the y' axis pointing to the LLJ's direction (Zhang et al., 2003; Du et al., 2014). In this way, the wind speed in the y' axis direction could be written as

$$v' = u\sin\varphi + v\cos\varphi \tag{2.3}$$

where φ is the angle between the y' axis and the y axis.

The momentum balance in the y' direction (along the LLJ's direction) can be written as:

$$\text{Term I} = \frac{\partial u}{\partial t}\sin\varphi + \frac{\partial v}{\partial t}\cos\varphi \tag{2.4}$$

$$\text{Term II} = \left(-u\frac{\partial u}{\partial x} - v\frac{\partial u}{\partial y}\right)\sin\varphi + \left(-u\frac{\partial v}{\partial x} - v\frac{\partial v}{\partial y}\right)\cos\varphi \tag{2.5}$$

$$\text{Term III} = f\left(v - v_g\right)\sin\varphi - f\left(u - u_g\right)\cos\varphi \tag{2.6}$$

$$\text{Term IV} = F_x\sin\varphi + F_y\cos\varphi \tag{2.7}$$

3 Case overview

On 19–20 May 2015, a warm-sector heavy rainfall event occurred along the coastal area of Guangdong province (Figure 1B and Figure 2). This heavy rainfall was mainly maintained during 1200 UTC 19 May to 0000 UTC 20 May (Wu et al., 2020), with the 12-h accumulated precipitation (1200 UTC 19-0000 UTC 20 May) exhibits a west-east-oriented precipitation area to the south of the Mount Lianhua where rainfall amounts at 21 stations exceed 100 mm (Figure 1B).

Figure 2 presents the temporal evolution of the composite radar reflectivity observed by the Shanwei S-band radar. The convection was initiated (composite radar reflectivity exceeds 35 dBZ) after sunset at around 1200 UTC 19 May (Figure 2A), and developed into a quasi-stationary well-defined nocturnal rain band along the coast and over the south of the Mount Lianhua (Figures 2B–F), leading to persistent local rainfall for more than 12 h. During this rainfall event, a boundary layer jet at 925 hPa was present over South China Sea (Shen et al., 2020), and yields a wind-speed convergence zone near the coast, where the

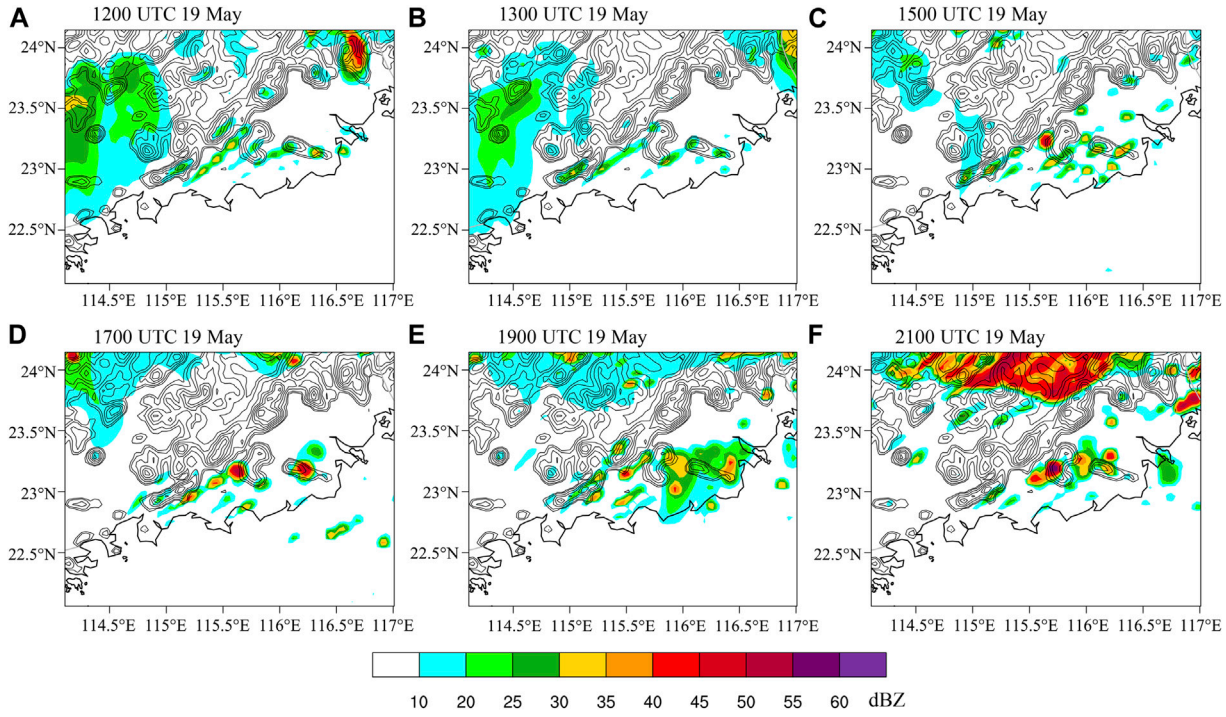

FIGURE 3
As in Figure 2, but simulated by the YSU scheme. Contour lines represent topography height in an interval of 100 m.

warm-sector heavy rainfall mainly occurs (Wu et al., 2020). More detailed descriptions on this case have been introduced by Wu and Luo (2016) and Wu et al. (2020).

4 Variations of LLJ and rainfall with PBL schemes and their relationship

Figure 3 shows the temporal evolution of simulated radar reflectivity simulated by the YSU scheme. Similar to the observations, the simulated warm-sector convection was triggered over the south of the Mount Lianhua, with the radar reflectivity greater than 30 dBZ at 1200 UTC 19 May, and then was developed and maintained near the coastal terrain. The initiation and maintenance of the warm-sector heavy rainfall can be well captured by the YSU scheme, although the simulated radar reflectivity is weaker than the observations (Figure 2).

The variations in the 6-h accumulated precipitation from 1500 UTC to 2100 UTC 19 May, which is the most obvious period of precipitation, among the six runs with different boundary layer parameterization schemes (YSU, MYJ, MYNN2.5, ACM2, BouLac, and UW) and the observations greater than 25 mm (black dots) are presented in Figure 4. The ACM2 run did not simulate the warm-sector rainfall at all without convection initiation (Figure 4D), while simulated rainfall in the UW run is much weaker and tends to further north (Figure 4F). Except for the ACM2 and UW runs, other sensitivity runs (MYJ, MYNN, and BouLac) generally reproduce the warm-sector coastal heavy rainfall as the control run with 6-h accumulated precipitation over 50 mm (Figures 4A–C, E). The equitable threat scores (ETS) with 25-mm threshold and a radius of 20 km (5 grid points) of 6-h accumulated precipitation simulated by six schemes are calculated through a neighborhood-based method (Clark et al., 2010; Zhang and Meng, 2019). If an event is observed at a grid point, this grid point is a hit if the event is forecast at any grid point within a circular radius. Unlike the traditional point-to-point criteria, the neighborhood-based criteria avoids the punishment of small displacement errors in decent forecasts (Ebert 2008; Squitieri and Gallus 2016). Result shows that the ETS of YSU scheme (0.75) is not only significantly greater than that of ACM2 scheme (0.0) and UW scheme (0.0), but also slightly higher than the ETS of MYJ scheme (0.44), MYNN scheme (0.30) and BouLac scheme (0.52). Therefore, the simulation by YSU scheme is reasonable to select as the control run in this study.

Previous studies have documented that the warm-sector heavy rainfall over southern China is closely related to the marine BLJ (Zhang and Meng, 2018; Wu et al., 2019; Zhang

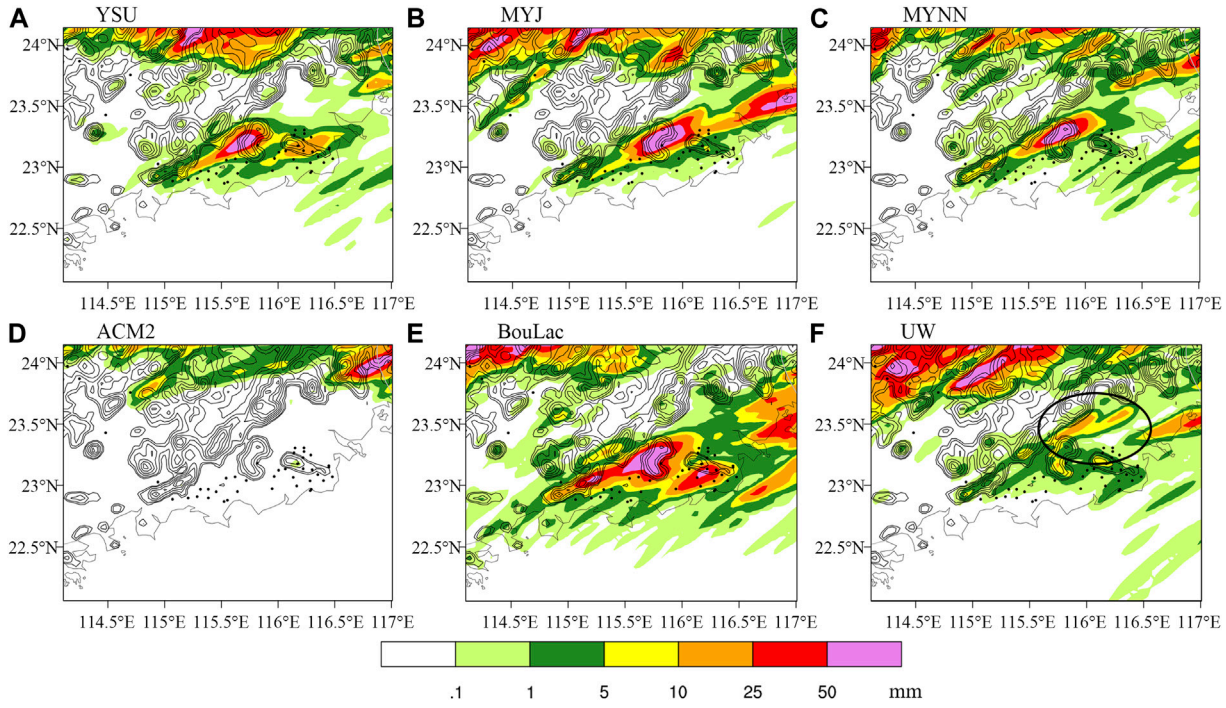

FIGURE 4
The simulated 6-h accumulated rainfall amount (shaded, mm) form 1500 UTC to 2100 UTC 19 May in the **(A)** YSU, **(B)** MYJ, **(C)** MYNN, **(D)** ACM2, **(E)** BouLac and **(F)** UW run. Black dots represent observed 6-h accumulated rainfall greater than 25 mm.

and Meng, 2019; Du et al., 2020a). Therefore, variations in the 950-hPa horizontal wind field simulated by different boundary layer parameterization schemes are examined (Figure 5). All sensitivity runs with different boundary layer schemes can successfully simulate the BLJ over South China Sea with wind speed greater than 12 m s^{-1} but with different intensity. Among those sensitivity experiments, the ACM2 run simulates the weakest BLJ with the maximum wind speed less than 17 m s^{-1} (Figure 5D), while the UW run simulates the strongest BLJ with the wind speed over large area greater than 18 m s^{-1} (Figure 5F). The coastal heavy rainfall was not well reproduced in the both runs (ACM2 and UW, Figure 4).

The temporal evolution of area-averaged wind speed among different PBL schemes is further presented in Figure 6. Since the location of low-level jet varies in different PBL schemes, the analysis region (black box in Figure 5) was selected to cover the center of maximum wind speed as much as possible in all schemes. Similarly, the simulated BLJ intensity undergoes strongest or weakest during the most analysis period in the UW (black line in Figure 6) or ACM2 (red line in Figure 6) runs, respectively. Next, we will explore whether the strongest or weakest BLJs simulated by the UW scheme and the ACM2 scheme leads to their poor ability to simulate the initiation and maintenance of warm-sector heavy rainfall event. Therefore, the following research mainly focus on the comparison of YSU scheme, ACM2 scheme and UW scheme in details.

In order to investigate the reasons of the poor ability to simulate the initiation and maintenance of the warm-sector heavy rainfall between the ACM2 and UW runs, the difference of specific humidity at 950 hPa in the ACM2 scheme or the UW scheme and the YSU scheme are compared in Figure 7. Compared with the YSU run, the specific humidity over the south side of coastal terrain in the ACM2 run is apparently smaller by 1.5 g kg^{-1} (Figure 7A), which is not favorable for convection initiation. On the contrary, the specific humidity around the coastal terrain in the UW run is larger than that in the YSU run by 0.6 g kg^{-1}, especially in the leeward slope of the coastal terrain (Figure 7B) due to the stronger upstream BLJ over the South China Sea.

Furthermore, the vertical cross section of vertical motion around the rainfall center (along the black line in Figure 7A) are shown in Figure 8 at 1300 UTC 19 May. In the YSU run, the vertical cross section shows upward motions on the windward slope of coastal terrain (Figure 8A), and turn to downward motion near the mountain top and leeward slope. The difference in meridional wind and vertical motion between the ACM2 run and control run (Figure 8B) shows that the low-level meridional winds in the ACM2 run is weaker than those in the YSU scheme at around 22.8°N–23.2°N, leading to the weaker upward motion near the coastal area (Figure 8B). The

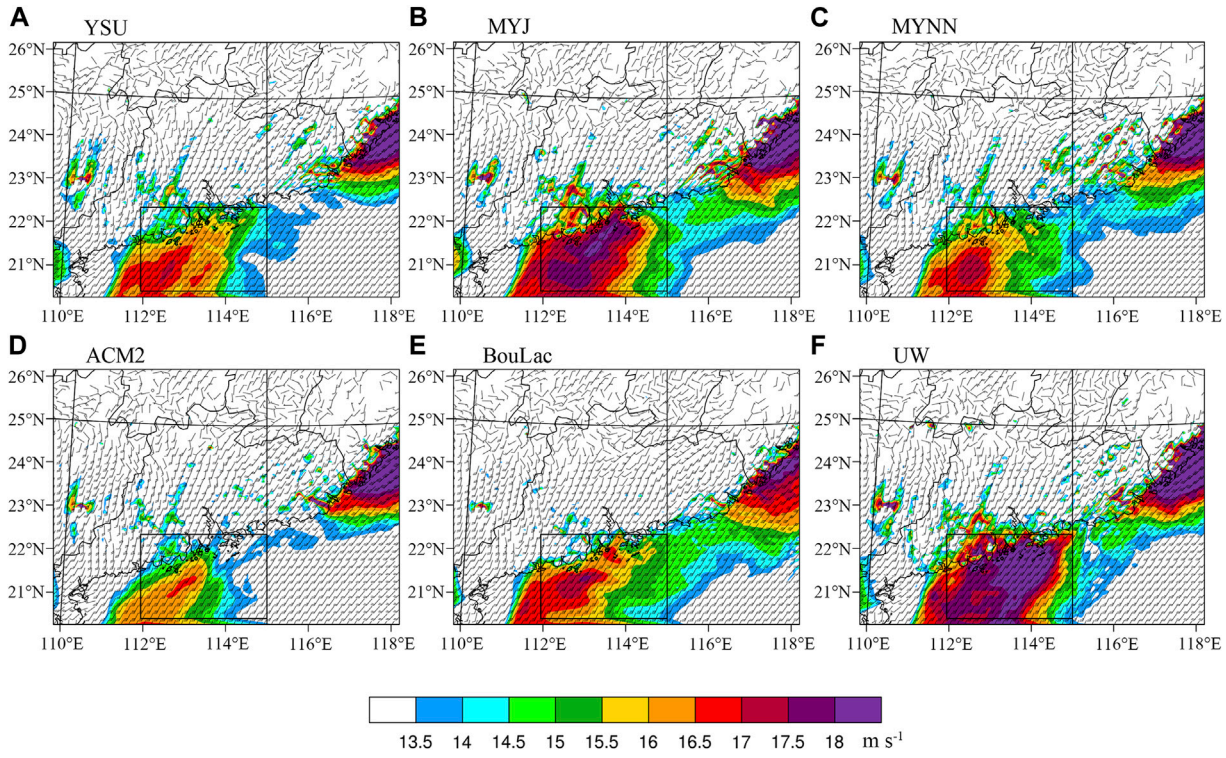

FIGURE 5
The 950-hPa horizontal wind field simulated by the **(A)** YSU, **(B)** MYJ, **(C)** MYNN, **(D)** ACM2, **(E)** BouLac and **(F)** UW scheme.

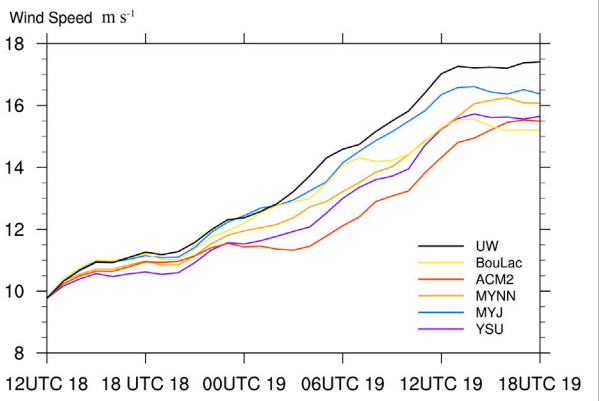

FIGURE 6
Temporal evolution of area-averaged 950-hPa wind speed over the black box in Figure 5A of different boundary layer schemes form 1200 UTC 18 May to 1800 UTC 19 May.

upward motions in the ACM2 run are located over the sea at around 22.5°N–22.8°N (Figure 8B), where downward motions occur in the YSU run (Figure 8A). On the contrary, the low-level meridional winds simulated by the UW scheme is stronger than those in the YSU run, causing stronger upward motions in the upslope of the coastal terrain at 23.2°N (Figure 8C).

The insufficient specific humidity and upward motion in the ACM2 run indicated unfavorable conditions for the initiation of warm-sector rainfall, while the sufficient water vapor and stronger upward motion in the UW run should be beneficial to convection initiation and growth. However, the precipitation simulated by the UW scheme is much weaker and occurs to further north compared to the control run. Figure 9 presents the temporal evolution of radar reflectivity simulated by the UW scheme. Compared with the YSU scheme (Figure 3), the UW run can successfully trigger convection with the maximum radar reflectivity greater than 35 dBZ at 1,200–1300 UTC 19 May (Figures 9A, B), which is even stronger than that in the YSU run. However, after 1500 UTC 19 May, the UW run could not successfully capture the development and maintenance of convection in the windward slope of coastal terrain (Figures 9C–F). At 2100 UTC 19 May, the simulated warm-sector rainfall in the UW run developed and got matured on the lee side of Mount Emeizhang, with the maximum radar reflectivity of 55 dBZ. Different from the UW run, both the radar reflectivity observed by Shanwei S-band weather radar and simulated in the YSU run show that the convection is

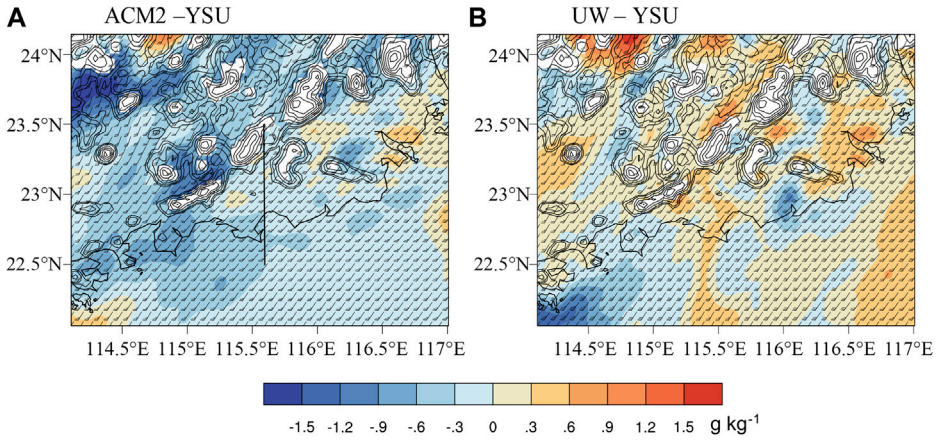

FIGURE 7
Difference of 950-hPa specific humidity at 1200 UTC 19 May between **(A)** the ACM2 scheme and YSU scheme, **(B)** the UW scheme and YSU scheme.

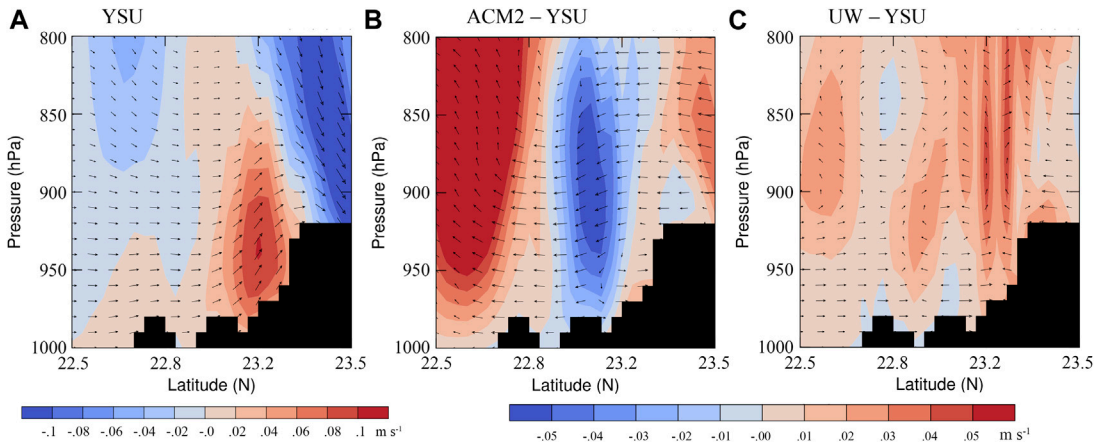

FIGURE 8
Vertical cross section of vertical motion (shading; m s^{-1}) and wind vectors (meridional wind vs. 100 × vertical motion) along the black line in Figure 7A at 1300 UTC 19 May of **(A)** the YSU scheme, **(B)** between the ACM2 scheme and YSU scheme, and **(C)** the UW scheme and YSU scheme.

maintained locally and confined along the coast, especially over the southern windward slope of Mount Emeizhang (Figures 2C–F; Figures 3C–F).

Previous studies have documented that the cold pool generated by convection (during 0500 UTC to 1100 UTC 19 May, not shown) is an important factor for the locally development and maintenance of rainstorm over the windward slope of coastal terrain (Wu and Luo, 2016). The cold pools simulated by the UW and YSU scheme are further compared in Figure 10. Cold pool is identified as thermal buoyancy, $B = g(\theta_v - \overline{\theta_v})/\overline{\theta_v}$ (Du et al., 2020b), where g is the acceleration of gravity (m^*s^{-2}), θ_v is the virtual potential temperature (K), and $\overline{\theta_v}$ is the area-averaged virtual potential temperature (K). The results show that the strength and location of the cold pools (red circles in Figure 10) in the UW and YSU runs are similar at 1200 UTC 19 May, with the thermal buoyancy over the south of the Mount Lianhua reaches $-0.03\ m\ s^{-2}$ (Figures 10A, B). However, at 2100 UTC 19 May, the cold pool simulated by the two schemes showed a significant difference. The cold pool in the YSU run still anchors over the south side of Mount Lianhua and the upwind slope of Mount Emeizhang (labeled in Figure 10), whereas the cold pool in the UW run moves to the lee side of Mount Emeizhang.

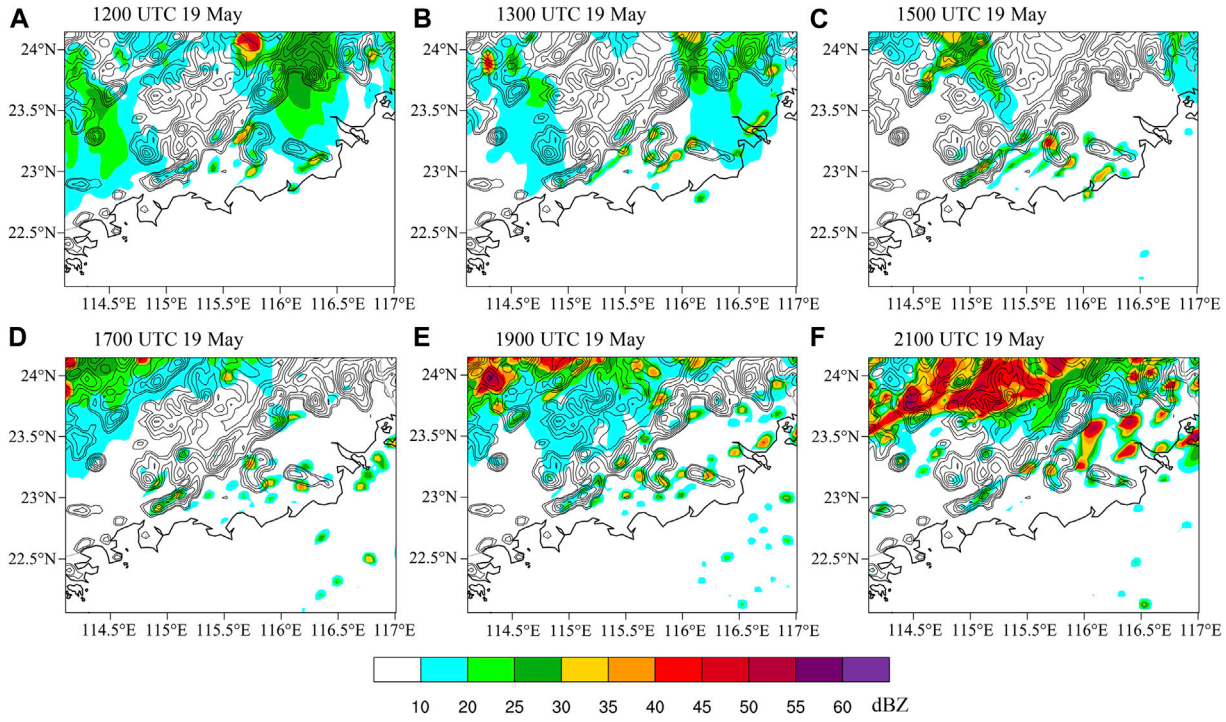

FIGURE 9
As in Figure 3, but simulated by the UW scheme.

Vertical cross sections of the thermal buoyancy and vertical motion along the black line in Figure 10 at 2100 UTC 19 May are further shown in Figure 11 to illustrate the uplift effect at the leading edge of the cold pool. In the YSU run, the south edge of the cold pool and related vertical motion expand southeastward to 23.1°N. In contrast, the south edge of the cold pool and strong upward motion simulated in the UW run are located to farther north (23.2°N). Since the BLJ in the UW run is stronger, the cold pool generated by previous convection moved to the northeastward accompanied by the southwesterly BLJ, rather than maintained locally. Therefore, at around 2100 UTC 19 May, the warm-sector heavy rainfall simulated in the UW run developed on the lee side of Mount Emeizhang.

5 Sensitivity of PBL parameterization schemes on LLJ

As mentioned in the previous section, the BLJ intensity has an important influence on the occurrence and development of the warm-sector rainfall. Thus, the sensitivity of different boundary layer parameterization schemes on the BLJ intensity will be further discussed in this section.

Figure 12 shows the 950-hPa geostrophic and ageostrophic winds at 1200 UTC 19 May simulated by different boundary layer schemes (YSU, ACM2, and UW). The geostrophic winds are obtained from the smoothed geopotential height by applying a low-pass Barnes's filter (Barnes, 1964), and the ageostrophic winds are calculated by subtracting the geostrophic winds from filtered total wind (Zeng et al., 2019; Du et al., 2020a). Due to the small area of inner domain (D02), proper filtered results cannot be obtained from D02. Thus, filtered geostrophic and ageostrophic winds are obtained from D01 instead. A low-pressure vortex (red box in Figures 12A, D) occurred over the eastern coastal area, and the BLJ was located on the southwest of the vortex. The vortex intensity is varied among the three sensitivity experiments. The vortex simulated by the UW scheme is strongest with a largest area of the geopotential height lower than 475 geopotential meters at 950 hPa, and the minimum geopotential height reaches 470 geopotential meters. The corresponding southwesterly geostrophic and nearly southerly ageostrophic wind over the southwest or south side of the vortex (especially over the South China Sea) become strongest in the UW run. On the contrary, the vortex simulated by the ACM2 scheme becomes weakest, with the minimum

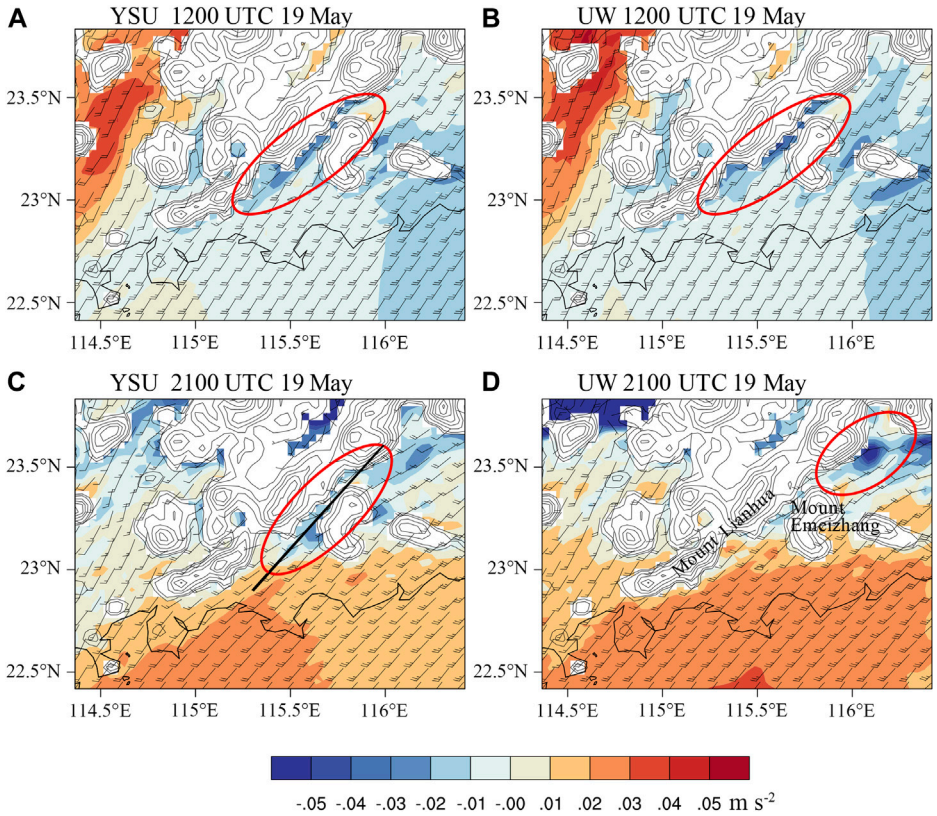

FIGURE 10
Thermal buoyancy (shaded) with wind vectors at 250 m in the **(A,C)** YSU scheme run, **(B,D)** UW scheme run at **(A,B)** 1200 UTC 19 May and **(C,D)** 2100 UTC 19 May.

geopotential height of 477.3 geopotential meters. Accordingly, the geostrophic and ageostrophic winds associated with the vortex are weakest in the ACM2 run. As for the YSU scheme, the intensity of the geostrophic wind, ageostrophic wind and vortex is between the ACM2 scheme and UW scheme.

Furthermore, the momentum budgets at 950 hPa over the BLJ region are calculated for the different sensitivity experiments, as shown in Figure 13. The local acceleration of the BLJ in the UW run (black line in Figure 13A) is apparently larger than that in the YSU run and in the ACM2 run especially during 2000 UTC 18 May to 1000 UTC 19 May (between the two dash lines in Figure 13A), and the ACM2 run presents the minimum local acceleration (red line in Figure 13A). Hence, individual terms in the horizontal momentum equation are calculated averaged over 2000 UTC 18 May to 1000 UTC 19 May. It is found that the smaller (larger) effect of Coriolis force on ageostrophic wind is one of reasons for the weaker (stronger) BLJ simulated by the ACM2 scheme (UW scheme) (Figure 13B). The veering ageostrophic winds are found in the three sensitivity experiments but with different rotation amplitudes (Figure 13C). The results above indicate the role of inertial oscillation, which makes the ageostrophic winds gradually veer to southwesterly that is the direction of the BLJ. The strongest inertial oscillation in the UW run leads to the strongest BLJ. In addition to the inertial oscillation, the horizontal advection also contributes to the difference of the BLJ intensity. Since the low-pressure vortex moves from west to east (black spots in Figures 12D–F), the effect of horizontal advection is attributed to the movement of the vortex.

The differences in the vortex intensity simulated by different boundary layer schemes might be caused by varying turbulence intensity. The vertical velocity variance σ_w^2 is used to measure the stability of the boundary layer (Bonin et al., 2015; Bonin et al., 2020). Small σ_w^2 indicates weak turbulent mixing and stable boundary layer. Figure 14 shows the evolution of σ_w^2 below 1.5 km over the land of the domain 2 calculated from vertical velocity with temporal resolutions of 6 min. During 0000–2000 UTC 19 May, σ_w^2 of the ACM2 scheme is smaller than that of the YSU scheme, indicating weaker turbulent mixing intensity of the ACM2 scheme (Figure 14B). Thus, the higher temperature near the surface layer cannot be fully mixed with the lower temperature in the upper layer during the daytime, resulting in a larger vertical temperature gradient (Figure 15A). On the contrary, σ_w^2 of the UW scheme is larger

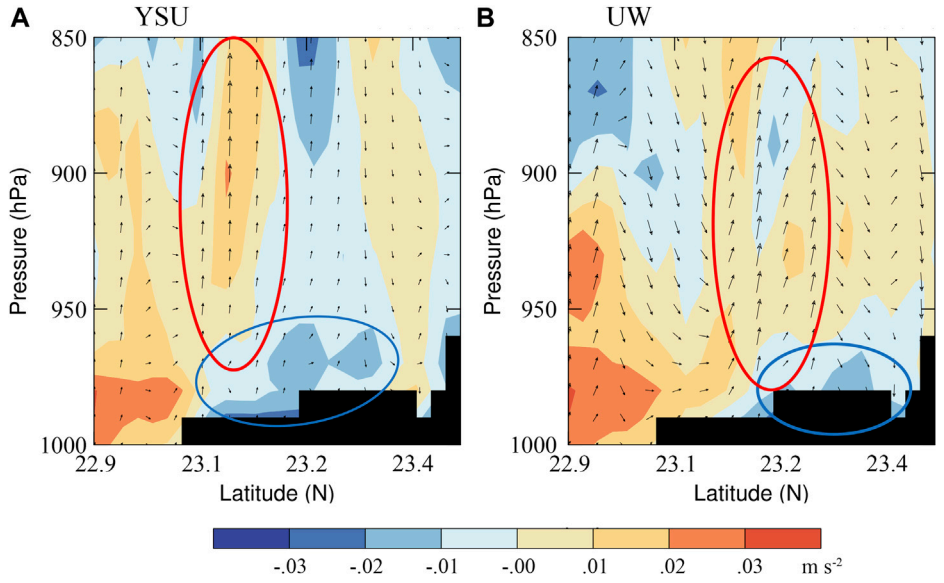

FIGURE 11
Vertical cross sections of thermal buoyancy (shading; ms^{-2}) and wind vectors (meridional wind vs. 100 times of vertical motion) at 2100 UTC 19 May in the **(A)** YSU scheme run and **(B)** UW scheme run.

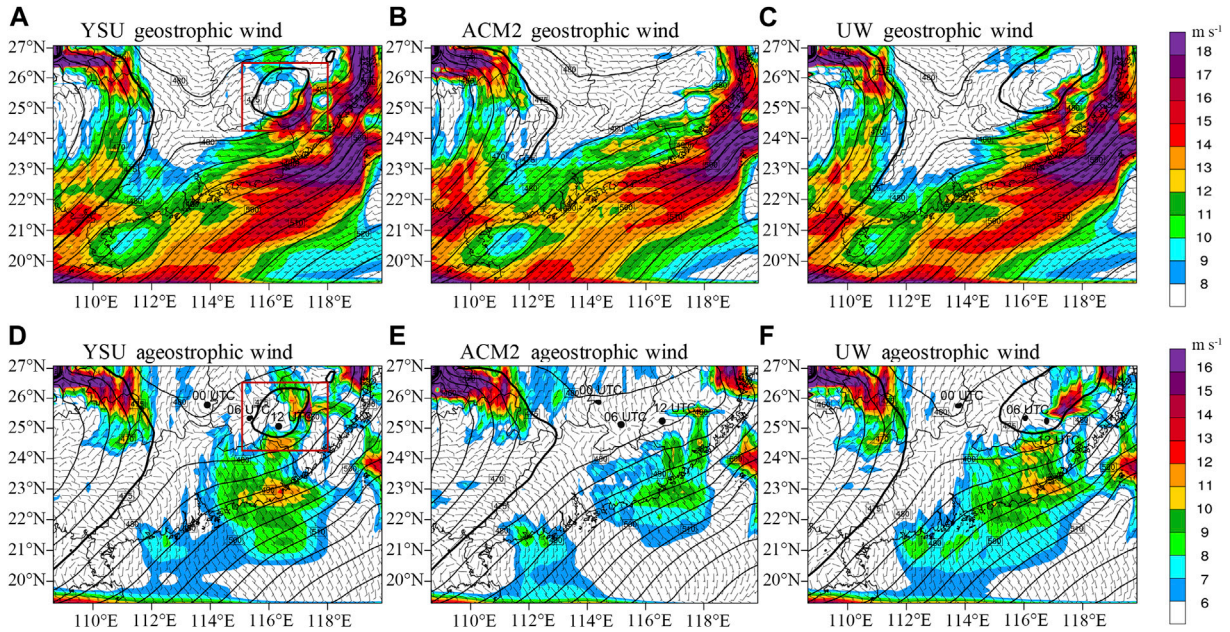

FIGURE 12
Horizontal distributions of **(A,C)** geostrophic wind and **(D–F)** ageostrophic wind velocity (shading; ms^{-1}) and wind vectors at 950 hPa at 1200 UTC 19 May in the **(A,D)** YSU scheme run, **(B,E)** ACM2 scheme run and **(C,F)** UW scheme run. Black spots in Figures 12D–F represent the minimum geopotential height of the vortex at 0000 UTC, 0600 UTC and 1200 UTC 19 May in the YSU scheme run, ACM2 scheme run and UW scheme run, respectively.

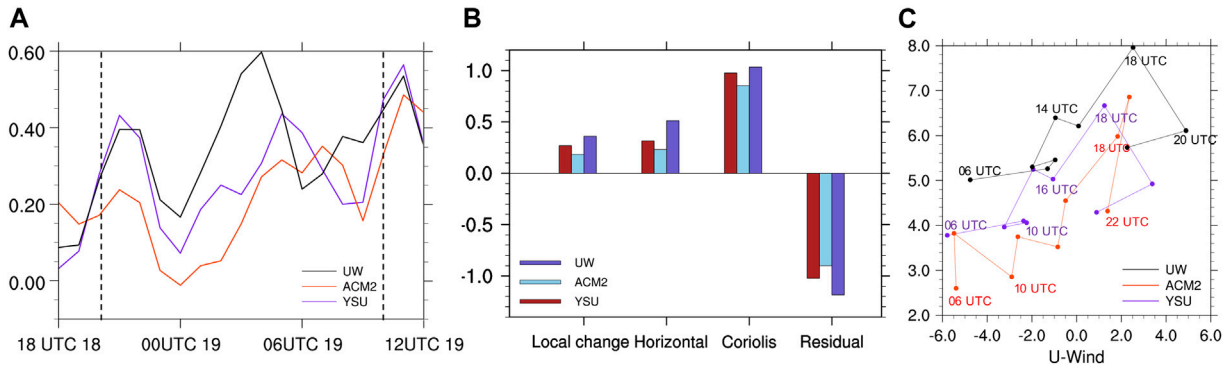

FIGURE 13
(A) Temporal evolution of the local acceleration of the BLJ (winds at 950 hPa) simulated by different PBL schemes, **(B)** individual terms in the horizontal momentum equation at the 950-hPa level averaged over 2000 UTC 18 May to 1000 UTC 19 May, and **(C)** clockwise rotation of mean 950-hPa ageostrophic wind, averaged over the black box in Figure 5A.

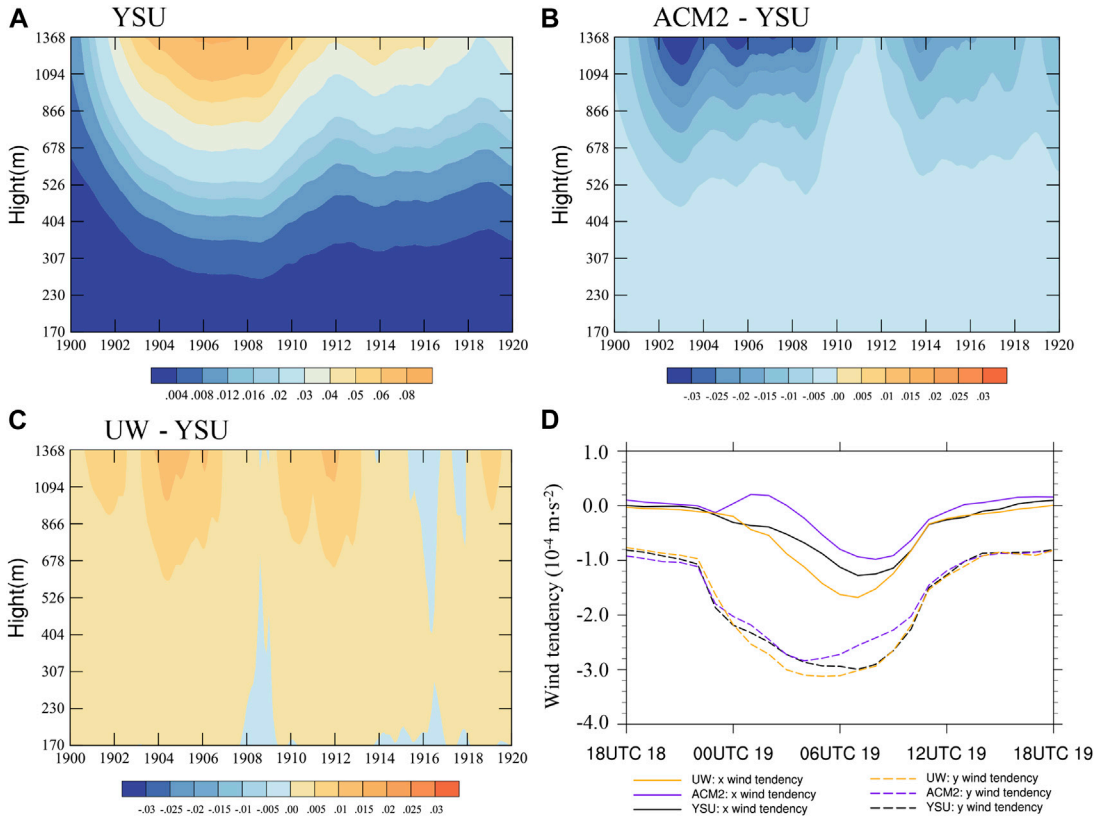

FIGURE 14
Temporal evolution of the vertical velocity variance σ_w^2 during 0000-2000 UTC 19 May in **(A)** the YSU scheme, **(B)** the differences of σ_w^2 between the ACM2 scheme and YSU scheme, and **(C)** between the UW scheme and YSU scheme; **(D)** The evolution of wind tendencies in the *x* and *y* direction due to PBL Parameterization (YSU scheme, ACM2 scheme and UW scheme) averaged over the land of domain 2 below 1 km height.

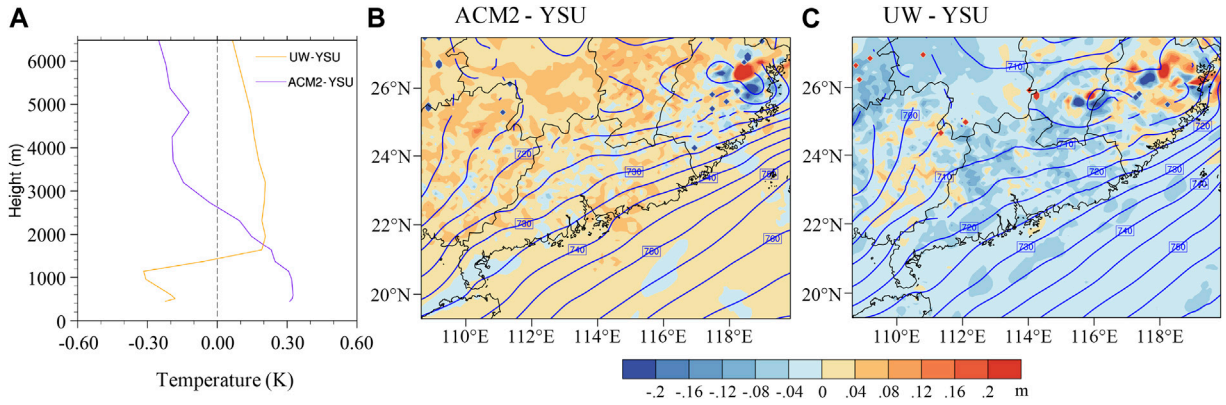

FIGURE 15
(A) Vertical profile of the difference of temperature between the ACM2 scheme and YSU scheme (purple line), and between UW scheme and YSU scheme (orange line) averaged over the low-level disturbance (red box in Figure 12D) at 0900 UTC 19 May; and the differences of $-\frac{R_d}{g}\int_{P_t}^{P_b} T_v d\ln P$ (m) at 0900 UTC 19 May **(B)** between the ACM2 scheme and YSU scheme, and **(C)** between the UW scheme and YSU scheme.

than that of the YSU scheme, indicating stronger turbulent mixing intensity (Figure 14C) and thus smaller vertical temperature gradient in the UW run (Figure 15A). Figure 15A shows that the differences of stratification are not only located in the lower levels, but only can well extend above 6 km, and the results of σ_w^2 above 1.5 km is consistent well with that below 1.5 km. Considering the reason of the PBL schemes itself, the YSU scheme is a non-local PBL scheme with an explicit treatment entrainment process at the top of the PBL (Hong et al., 2006), the ACM2 scheme is a hybrid local-nonlocal scheme with non-local upward mixing and local downward mixing, and extra considers the interaction between the lowest layer and each and every layer above (Pleim, 2007a; Pleim, 2007b). That means the PBL schemes could not only affect the lower levels below the planetary boundary layer, but also could affect the mid-to higher levels.

The wind tendencies contributed by PBL parameterization are also used to estimate turbulent mixing intensity directly. The wind tendencies in the x and y directions are averaged over the land of domain 2 below 1 km height. Figure 14D shows that the negative wind tendencies in the UW (ACM2) scheme are more (less) apparent compared to the YSU scheme, especially during the daytime (0000 UTC 19 May to 1200 UTC 19 May). The results indicate that PBL schemes produce weakest turbulent mixing in ACMs and strongest turbulent mixing in UW, which is consistent well with σ_w^2.

Furthermore, varying temperature stratification caused by the boundary layer turbulent mixing can affect the intensity of low-pressure vortex. Compared to the YSU scheme, the lower temperature at the upper layer due to the weaker turbulent mixing of the ACM2 scheme (Figure 15A) mainly accounts for the weaker low-pressure disturbance at 950 hPa simulated by ACM2 scheme. The change of geopotential height (z) can be expressed as (Markowski and Richardson, 2010):

$$\frac{\partial z(P_b)}{\partial t} - \frac{\partial z(P_t)}{\partial t} = -\frac{R_d}{g}\int_{P_t}^{P_b}\frac{\partial T_v}{\partial t} d\ln P,$$

where p_t and p_b are pressure levels at the top and bottom, and T_v is the virtual temperature. Assuming that $\frac{\partial z(P_t)}{\partial t} \approx 0$, the equation then can be simplified as $\frac{\partial z(P_b)}{\partial t} = -\frac{R_d}{g}\int_{P_t}^{P_b}\frac{\partial T_v}{\partial t} d\ln P$. Since the initial conditions $[z(P_b)]$ for different boundary layer schemes are same, the comparisons in the change of geopotential height for different boundary layer schemes can be simplified as the comparisons in $-\frac{R_d}{g}\int_{P_t}^{P_b} T_v d\ln P$, which means the change of geopotential height is closely related to the temperature stratification. The result calculated by the equation $-\frac{R_d}{g}\int_{P_t}^{P_b} T_v d\ln P$ at 0900 UTC 19 May for the different boundary layer parameterization schemes are shown in Figures 15B, C, where P_b is set to 950 hPa and P_t is set to the pressure of the model top (50 hPa).

Because of the larger (small) vertical temperature gradient in ACM2 (UW) scheme (Figure 15A), the negative change of geopotential height above 950 hPa simulated by the ACM2 (UW) scheme is less (more) than that in YSU scheme (Figures 15B, C), resulting in a weaker (stronger) low-pressure vortex simulated by the ACM2 (UW) scheme.

The reason from the PBL schemes itself might play an important role in BLJ formation. The UW scheme is characterized by the use of moist-conserved variables, an explicit entrainment closure, downgradient diffusion of momentum, and conserved scalars within turbulent layers

(Bretherton and Park, 2009), so the entrainment parameterization of the UW moist turbulence scheme and the updraft microphysics can be easily extended (Park and Bretherton, 2009), indicating stronger turbulent mixing intensity. Yang et al. (2013) also documented that the UW scheme with a moist turbulence parameterization overpredict the height of the low-level jet and the wind speed. The turbulent mixing intensity of the ACM2 scheme is relative weak in this case, so the higher temperature near the surface layer cannot be fully mixed with the lower temperature in the upper layer during the daytime, resulting in a weaker vortex and further smaller effect of Coriolis force on ageostrophic wind. According to Hong et al. (2006), the YSU scheme decreases boundary layer mixing in the mechanically induced forced convection regime, so that the excessive mixing in the mixed layer in the presence of strong winds is resolved. Jiménez et al. (2012) also documented that an increase in Prandtl number for unstable conditions is utilized the YSU scheme, which will result in weaker mixing during daytime. Under these circumstances, the turbulent mixing intensity simulated by YSU scheme is weaker than that in UW scheme in this study, resulting in weaker BLJ compared with that in UW scheme.

6 Summary and discussion

In this study, the WRF model is used to investigate the sensitivity of planetary boundary layer (PBL) parameterization schemes in simulating boundary layer jet (BLJ) over South China Sea and its downstream warm-sector heavy rainfall during 19–20 May 2015 at the coast of South China.

Six PBL parameterization schemes are examined in the present study including YSU, MYJ, MYNN, ACM2, BouLac, and UW. Expect for the ACMs and UW schemes, YSU, MYJ, MYNN, and BouLac schemes can generally simulate the warm-sector coastal heavy rainfall with 6-h accumulated precipitation exceeding 50 mm. No convection initiation is found in the ACM2 run, while simulated coastal rainfall is relatively weak and occurs to further north in the UW run.

All the six boundary layer schemes can simulate the boundary layer jet over the South China Sea with a wind speed greater than 12 m s^{-1} at 950 hPa, but with the varying jet's intensity. The ACM2 run simulates the weakest BLJ, while the UW run produces the strongest BLJ among the sensitivity experiments.

Compared with the YSU run, the weaker BLJ induces weaker convergence and lifting as well as less water vapor transport over the south side of Mount Lianhua in the ACM2 run, which are not favorable for the convection initiation and growth. On the contrary, the UW scheme can successfully simulate the convection initiation of warm-sector heavy rainfall on the south side of mountains with a maximum radar reflectivity of 35 dBZ, but the development and maintenance of convection in upwind side of Mount Emeizhang are not well preformed. The too strong BLJ in the UW run results in the northward movement of the cold pool associated with convection, and thus yields the development of convection on the leeside of Mount Emeizhang.

Variations in boundary layer mixing over land among different PBL schemes results in different vertical temperature stratification and further affects the intensity of low-pressure vortex at low levels. The weaker (stronger) mixing intensity of ACM2 scheme (UW scheme) induces the weaker (stronger) low-pressure vortex. Furthermore, the varying intensity of the low-pressure vortex with different PBL schemes causes different strength of BLJs on the south side of the vortex through veering ageostrophic wind.

The sensitivity of different PBL schemes in precipitation has been widely discussed in previous studies. The evolution of convective systems and associated rainfall is found to be highly sensitive to the PBL parameterization (Xu and Zhao, 2000; Que et al., 2016). Previous studies have also pointed out high sensitivity of simulated heavy rainfall in South China to the PBL schemes (Cai et al., 2005; Zhao, 2008; Dong et al., 2019). The different boundary layer schemes cause varying divergence fields, and further affect the rainfall forecasting performance in South China (Cai et al., 2005). However, few studies have focused on the sensitivity of the BLJ over the South China Sea to the PBL parameterization, even if it is known that the southerly marine BLJ plays an important role in warm-sector coastal heavy rainfall (Luo et al., 2017; Du and Chen, 2018; Zhang and Meng, 2018). Thus, we innovatively regard the BLJ as a bridge to explore the effects of PBL schemes on the heavy rainfall associated with BLJs. The results can also implicit the influence mechanisms of BLJs on heavy rainfall from a perspective of numerical simulations and forecasts.

In summary, the present study suggests that simulated marine boundary layer jet over the South China Sea and associated precipitation are sensitive to the PBL schemes. However, it is unreasonable to conclude that one particular scheme is better or worse than others on simulating warm-sector heavy rainfall only through a case study. Besides, the initial perturbations and lateral boundary conditions were also sensitive to heavy rainfall events. Therefore, we plan to simulate more similar warm-sector heavy rainfall events associated with a marine boundary layer jet over southern China, to statistically study which boundary layer scheme is the best on simulating warm-sector heavy rainfall event in South China.

Data availability statement

Publicly available datasets were analyzed in this study. This data can be found here: https://rda.ucar.edu/datasets/ds083.2/index.html#!description.

Author contributions

YS and YD contributed to the idea and research of the study. YS contributed to the data processing and prepared the original draft, YD edited and reviewed the manuscript. All authors have read and agreed to the submitted version.

Funding

The study was supported by the Guangdong Major Project of Basic and Applied Basic Research (2020B0301030004), the National Natural Science Foundation of China (Grant Nos. 42075006, 42122033, and 41875055), and Guangzhou Science and Technology Plan Projects (202002030346).

Conflict of interest

The authors declare that the research was conducted in the absence of any commercial or financial relationships that could be construed as a potential conflict of interest.

Publisher's note

All claims expressed in this article are solely those of the authors and do not necessarily represent those of their affiliated organizations, or those of the publisher, the editors and the reviewers. Any product that may be evaluated in this article, or claim that may be made by its manufacturer, is not guaranteed or endorsed by the publisher.

References

Barnes, S. L. (1964). A technique for maximizing details in numerical weather map analysis. *J. Appl. Meteor.* 3, 396–409. doi:10.1175/1520-0450(1964)0030396:ATFMDI.2.0.CO;2

Blackadar, A. K. (1957). Boundary layer wind maxima and their significance for the growth of nocturnal inversions. *Bull. Am. Meteorological Soc.* 38, 283–290. doi:10.1175/1520-0477-38.5.283

Bonin, T. A., Blumberg, W. G., Klein, P. M., and Chilson, P. B. (2015). Thermodynamic and turbulence characteristics of the south- ern great plains nocturnal boundary layer under differing turbulent regimes. *Boundary-Layer Meteorol.* 157, 401–420. doi:10.1007/s10546-015-0072-2

Bonin, T. A., Klein, P. M., and Chilson, P. B. (2020). Contrasting characteristics and evolution of southerly low-level jets during different boundary-layer regimes. *Boundary-Layer Meteorol.* 174 (2), 179–202. doi:10.1007/s10546-019-00481-0

Bougeault, P., and Lacarrere, P. (1989). Parameterization of orography–induced turbulence in a mesobeta–scale model. *Mon. Weather Rev.* 117, 1872–1890. doi:10.1175/1520-0493(1989)117<1872:pooiti>2.0.co;2

Bretherton, C. S., and Park, S. (2009). A new moist turbulence parameterization in the Community Atmosphere Model. *J. Clim.* 22, 3422–3448. doi:10.1175/2008JCLI2556.1

Cai, R., Wang, H., Wang, W., and Mao, S. (2005). Comparison analysis of different boundary layer parameterization schemes in the numerical simulation of torrential rain. *Guangdong Meteorol.* 01, 6–8. doi:10.3969/j.issn.1007-6190.2005.01.003

Clark, A. J., Gallus, W. A., Jr., and Weisman, M. L. (2010). Neighborhood-based verification of precipitation forecasts from convection-allowing NCAR WRF model simulations and the operational NAM. *Weather Forecast.* 25 (5), 1495–1509. Available at:https://journals.ametsoc.org/view/journals/wefo/25/5/2010waf222240. doi:10.1175/2010waf2222404.1

Ding, Y. (1994). *Monsoons over China*. Netherlands: Kluwer Academic Publishers, 419. doi:10.1007/978-94-015-8302-2

Dong, F., Zhang, L., Chen, W., Li, D., Wang, J., and Zhi, X. (2020). Role of boundary layer jet in the occurrence and development of warm-sector heavy rainfall over SouthSouth China: A case study. *IOP Conf. Ser. Earth Environ. Sci.* 603, 012023. doi:10.1088/1755-1315/603/1/012023

Dong, M., Ji, C., Chen, F., and Wang, Y. (2019). Numerical study of boundary layer structure and rainfall after landfall of typhoon fitow (2013): Sensitivity to planetary boundary layer parameterization. *Adv. Atmos. Sci.* 36 (4), 431–450. doi:10.1007/s00376-018-7281-9

Du, Y., and Chen, G. (2019b). Climatology of low-level jets and their impact on rainfall over southern China during the early-summer rainy season. *J. Clim.* 32, 8813–8833. doi:10.1175/JCLI-D-19-0306.1

Du, Y., Chen, G., Han, B., Bai, L., and Li, M. (2020b). Convection initiation and growth at the coast of SouthSouth China. Part II: Effects of the terrain, coastline, and cold pools. *Mon. Weather Rev.* 148 (9), 3871–3892. doi:10.1175/MWR-D-20-0090.1

Du, Y., Chen, G., Han, B., Mai, C., Bai, L., and Li, M. (2020a). Convection initiation and growth at the coast of SouthSouth China. Part I: Effect of the marine boundary layer jet. *Mon. Weather Rev.* 148 (9), 3847–3869. doi:10.1175/MWR-D-20-0089.1

Du, Y., and Chen, G. (2018). Heavy rainfall associated with double low-level jets over southern China. Part I: Ensemble-Based analysis. *Mon. Weather Rev.* 146, 3827–3844. doi:10.1175/MWR-D-18-0101.1

Du, Y., and Chen, G. (2019a). Heavy rainfall associated with double low-level jets over southern China. Part II: Convection initiation. *Mon. Weather Rev.* 147, 543–565. doi:10.1175/MWR-D-18-0102.1

Du, Y., and Rotunno, R. (2014). A simple analytical model of the nocturnal low-level jet over the great plains of the United States. *J. Atmos. Sci.* 71 (10), 3674–3683. doi:10.1175/JAS-D-14-0060.1

Du, Y., Shen, Y., and Chen, G. (2022). Influence of coastal marine boundary layer jets on rainfall in SouthSouth China. *Adv. Atmos. Sci.* 39, 782–801. doi:10.1007/s00376-021-1195-7

Du, Y., Zhang, Q., Chen, Y., Zhao, Y., and Wang, X. (2014). Numerical simulations of spatial distributions and diurnal variations of low-level jets in China during early summer. *J. Clim.* 27 (15), 5747–5767. doi:10.1175/JCLI-D-13-00571.1

Ebert, E. E. (2008). Fuzzy verification of high-resolution gridded forecasts: A review and proposed framework. *Meteorol. Appl.* 15, 51–64. doi:10.1002/met.25

Holton, J. R. (1967). The diurnal boundary layer wind oscillation above sloping terrain. *Tellus* 19, 199–205. doi:10.1111/j.2153.3490.1967.tb01473.x

Hong, S. Y., Noh, Y., and Dudhia, J. (2006). A new vertical diffusion package with an explicit treatment of entrainment processes. *Mon. Weather Rev.* 134, 2318–2341. doi:10.1175/MWR3199.1

Iacono, M. J., Delamere, J. S., Mlawer, E. J., Shephard, M. W., and Collins, W. D. (2008). Radiative forcing by long–lived greenhouse gases: Calculations with the AER radiative transfer models. *J. Geophys. Res. Atmos.* 113, D13103. doi:10.1029/2008JD009944

Janjić, Z. I. (2002). Nonsingular implementation of the mellor–yamada level 2.5 scheme in the NCEP meso model. *NCEP Off. Note* 437, 61.

Jiménez, P. A., Dudhia, J., González-Rouco, J. F., Navarro, J., Montávez, J. P., and García-Bustamante, E. (2012). A revised scheme for the WRF surface layer formulation. *Mon. Weather Rev.* 140, 898–918. doi:10.1175/MWR-D-11-00056.1

Kain, J. S. (2004). The Kain–Fritsch convective parameterization: An update. *J. Appl. Meteorology* 43, 170–181. doi:10.1175/1520-0450(2004)043<0170:tkcpau>2.0.co;2

Li, X., and Du, Y. (2021). Statistical relationships between two types of heavy rainfall and low-level jets in SouthSouth China. *J. Clim.* 34 (21), 8549–8566. doi:10.1175/JCLI-D-21-0121.1

Livneh, B, Restrepo, P. J., and Lettenmaier, D. P. (2011). Development of a unified land model for prediction of surface hydrology and land-atmosphere interactions. *J. Hydrometeorol.* 12, 1299–1320. doi:10.1175/2011JHM1361.1

Luo, Y. (2017). Advances in understanding the early-summer heavy rainfall over South China. *Glob. Monsoon Syst. Res. Forecast* 9, 215–226. World scientific series on asia-pacific weather and climate. World Scientific. doi:10.1142/9789813200913_0017

Luo, Y., Zhang, R., Wan, Q., Wang, B., Wong, W. K., Hu, Z., et al. (2017). The southern China monsoon rainfall experiment (SCMREX). *Bull. Am. Meteorological Soc.* 98 (5), 999–1013. doi:10.1175/BAMS-D-15-00235.1

Markowski, P., and Richardson, Y. (2010). *Mesoscale Meteorology in midlatitudes*. Wiley Blackwell. doi:10.1002/9780470682104

Nakanishi, M., and Niino, H. (2006). An improved mellor–yamada level 3 model: Its numerical stability and application to a regional prediction of advection fog. *Boundary-Layer Meteorol.* 119, 397–407. doi:10.1007/s10546-005-9030-8

Park, S., and Bretherton, C. S. (2009). The university of Washington shallow convection and moist turbulence schemes and their impact on climate simulations with the community atmosphere model. *J. Clim.* 22 (12), 3449–3469. Available at:https://journals.ametsoc.org/view/journals/clim/22/12/2008jcli2557. doi:10.1175/2008jcli2557.1

Pleim, J. E. (2007a). A combined local and nonlocal closure model for the atmospheric boundary layer. Part I: Model description and testing. *J. Appl. Meteorology Climatol.* 46, 1383–1395. doi:10.1175/JAM2539.1

Pleim, J. E. (2007b). A combined local and nonlocal closure model for the atmospheric boundary layer. Part II: Application and evaluation in a mesoscale meteorological model. *J. Appl. Meteorology Climatol.* 46, 1396–1409. doi:10.1175/JAM2534.1

Que, Lin-Jing., Que, Wei-Lun., and Feng, Jin-Ming. (2016). Intercomparison of different physics schemes in the WRF model over the Asian summer monsoon region. *Atmos. Ocean. Sci. Lett.* 9 (3), 169–177. doi:10.1080/16742834.2016.1158618

Salmond, J. A., and McKendry, I. G. (2005). A review of turbulence in the very stable nocturnal boundary layer and its implications for air quality. *Prog. Phys. Geogr.* 29, 171–188. doi:10.1191/0309133305pp442ra

Shen, Y., Du, Y., and Chen, G. (2020). Ensemble sensitivity analysis of heavy rainfall associated with three MCSs coexisting over southern China. *J. Geophys. Res. Atmos.* 125, e2019JD031266. doi:10.1029/2019JD031266

Smith, E. N., Gibbs, J. A., Evgeni, F., and Klein, P. M. (2018). WRF model study of the great plains low-level jet: Effects of grid spacing and boundary layer parameterization. *J. Appl. Meteorology Climatol.* 57, 2375–2397. doi:10.1175/JAMC-D-17-0361.1

Squitieri, B. J., and Gallus, W. A., Jr. (2016). WRF forecasts of great plains nocturnal low-level jet-driven MCSs. Part I: Correlation between low-level jet forecast accuracy and MCS precipitation forecast skill. *Weather Forecast.* 31 (4), 1301–1323. Available at:https://journals.ametsoc.org/view/journals/wefo/31/4/waf-d-15-0151_1.xml. doi:10.1175/waf-d-15-0151.1

Steeneveld, G.-J. (2014). Current challenges in understanding and forecasting stable boundary layers over land and ice. *Front. Environ. Sci.* 2, 1–6. doi:10.3389/fenvs.2014.00041

Steeneveld, G.-J., Mauritsen, T., de Bruijn, E. I. F., Vilà-Guerau de Arellano, J., Svensson, G., and Holtslag, A. (2008). Evaluation of limited-area models for the representation of the diurnal cycle and contrasting nights in CASES-99. *J. Appl. Meteorology Climatol.* 47, 869–887. doi:10.1175/2007JAMC1702.1

Storm, B., Dudhia, J., Basu, S., Swift, A., and Giammanco, I. (2009). Evaluation of the weather research and forecasting model on forecasting low-level jets: Implications for wind energy. *Wind Energy* 12 (1), 81–90. doi:10.1002/we.288

Thompson, G., Field, P. R., Rasmussen, R. M., and Hall, W. D. (2008). Explicit forecasts of winter precipitation using an improved bulk microphysics scheme. Part II: Implementation of a new snow parameterization. *Mon. Weather Rev.* 136, 5095–5115. doi:10.1175/2008MWR2387.1

Wu, M., and Luo, Y. (2016). Mesoscale observational analysis of lifting mechanism of a warm-sector convective system producing the maximal daily precipitation in China mainland during pre-summer rainy season of 2015. *J. Meteorological Res.* 30 (5), 719–736. doi:10.1007/s13351-016-6089-8

Wu, N., Ding, X., Wen, Z., Chen, G., Min, J., Lin, L., et al. (2019). Contrasting frontal and warm-sector heavy rainfalls over south China during the early-summer rainy season. *Atmos. Res.* 235, 104693. doi:10.1016/j.atmosres.2019.104693

Wu, N., Zhuang, X., Min, J., and Meng, Z. (2020). Practical and intrinsic predictability of a warm-sector torrential rainfall event in the South China monsoon region. *J. Geophys. Res. Atmos.* 125, e2019JD031313. doi:10.1029/2019JD031313

Xu, L. R., and Zhao, M. (2000). The influences of boundary layer parameterization schemes on mesoscale heavy rain system. *Adv. Atmos. Sci.* 17, 458–472. doi:10.1007/s00376-000-0036-3

Yang, Q., Berg, L. K., Pekour, M., Fast, J. D., Newsom, R. K., Stoelinga, M., et al. (2013). Evaluation of WRF-predicted near-hub-height winds and ramp events over a pacific northwest site with complex terrain. *J. Appl. Meteorology Climatol.* 52 (8), 1753–1763. Available at:https://journals.ametsoc.org/view/journals/apme/52/8/jamc-d-12-0267.1.xml. doi:10.1175/jamc-d-12-0267.1

Zeng, W., Chen, G., Du, Y., and Wen, Z. (2019). Diurnal variations of low-level winds and precipitation response to large-scale circulations during a heavy rainfall event. *Mon. Wea. Rev.* 147, 3981–4004. doi:10.1175/MWR-D-19-0131.1

Zhang, M., and Meng, Z. (2018). Impact of synoptic-scale factors on rainfall forecast in different stages of a persistent heavy rainfall event in south China. *J. Geophys. Res. Atmos.* 123 (7), 3574–3593. doi:10.1002/2017JD028155

Zhang, M., and Meng, Z. (2019). Warm-sector heavy rainfall in southern China and its WRF simulation evaluation: A low-level-jet perspective. *Mon. Weather Rev.* 147, 4461–4480. doi:10.1175/MWR-D-19-0110.1

Zhang, Q., Lau, K., Kuo, Y., and Chen, S. J. (2003). A numerical study of a mesoscale convective system over the Taiwan strait. *Mon. Weather Rev.* 131 (6), 1150–1170. doi:10.1175/1520-0493(2003)131<1150:ansoam>2.0.co;2131<1150:ANSOAM>2.0.CO;2)

Zhao, M. (2008). A review of the research on the effects of boundary layer and land surface process on heavy rain in China. *Torrential Rain Disasters* 02, 186–190. (in Chinese).

Zhou, X., Xue, J., Tao, Z., Zhao, S., Yi, Q., Su, B., et al. (2003). *Heavy rainfall experiment in SouthSouth China during pre-summer rainy season (HUAMEX)*. Beijing: China Meteorological Press, 220. (in Chinese).

frontiers | Frontiers in Earth Science

TYPE Original Research
PUBLISHED 12 January 2023
DOI 10.3389/feart.2022.1026945

OPEN ACCESS

EDITED BY
Jianjun Xu,
Guangdong Ocean University, China

REVIEWED BY
Wei Zhang,
Utah State University, United States
Cheng Sun,
Beijing Normal University, China

*CORRESPONDENCE
Lei Chen,
leichen@cug.edu.cn

SPECIALTY SECTION
This article was submitted to Interdisciplinary Climate Studies, a section of the journal Frontiers in Earth Science

RECEIVED 24 August 2022
ACCEPTED 31 October 2022
PUBLISHED 12 January 2023

CITATION
Lee R, Chen L and Ren G (2023), A comparison of East-Asia landfall tropical cyclone in recent reanalysis datasets--before and after satellite era.
Front. Earth Sci. 10:1026945.
doi: 10.3389/feart.2022.1026945

A comparison of East-Asia landfall tropical cyclone in recent reanalysis datasets--before and after satellite era

Ruyuan Lee[1,2], Lei Chen[1,2]* and Guoyu Ren[1,2,3]

[1]Department of Atmospheric Science, School of Environmental Studies, China University of Geosciences, Wuhan, Hubei, China, [2]Centre for Severe Weather and Climate and Hydro-Geological Hazards, Wuhan, China, [3]National Climate Center, Laboratory for Climate Studies, China Meteorological Administration, Beijing, China

Based on different reanalysis datasets, reconstructions of East Asia landfall tropical cyclones (TCs) were compared with observations. The 20th-century reanalysis version 3 dataset (20CRv3) received the most approval in this assessment. It performed better in terms of annual frequency. The fifth generation of atmospheric reanalysis dataset (ERA5) and Japanese 55-year reanalysis dataset (JRA55) are also recommended in this study. Nevertheless, an apparent inconsistency in reconstructed TCs before and after 1980 is visible. Temporally, after the satellite era, the underestimation on TC frequency of the National Centres for Environmental Prediction and National Centre for Atmospheric Research (NCEP/NCAR) reanalysis dataset (NCAR) and 20-century reanalysis of European Center for Medium-Range Weather Forecasts (ERA20C) has been greatly improved. The downward trend of landfalling TCs is well captured by ERA5 and ERA20C. Spatially, the underestimation of TC track discrepancy is reduced in the post-satellite era. ERA5 and 20CRv3 showed relatively consistent performance compared to the former reanalysis in pre-and post-satellite time, which might be due to their better TC treatment. Despite the essential need for high resolution, this study stressed the importance of observation and assimilation development for the reanalysis TCs.

KEYWORDS

relative vorticity, tropical cyclone, satellite era, reanalysis data, observation, East Asia

1 Introduction

Tropical cyclones (TCs) are important natural hazards in East Asia and have been of great concern to policymakers and researchers due to their large socioeconomic impacts. As TC observational data are relatively limited spatially and temporally, atmospheric reanalysis datasets play an indispensable role in TC research. Reanalysis datasets are used as an observation supplement for large-scale systems, such as monsoons (Zhou and Wu, 2019) and the El Nino Southern Oscillation (ENSO) (Zhang et al., 2018), when investigating their relationship with TCs, and the direct representation of TCs in reanalysis data is important to those studies (Scoccimarro et al., 2012). Reanalysis

data have also been used to describe the thermodynamic, dynamic, and other environmental factors that favor TC genesis (Pu et al., 2019). Some reanalysis data have even been used in historical TC research for over a century (Liu et al., 2021). Furthermore, reanalysis data act as a bridge between the model and observations. Before the tracking method and identification criteria made for TCs are adapted in models, reanalysis data can provide reliability tests for those schemes (Bengtsson et al., 2007a; Murakami and Sugi, 2010). Other than that, reanalysis data can also specify the regional model boundary conditions for the model-based future projection study of TCs (e.g., Walsh, 2015).

Investigations of reanalysis TCs have been performed in the last 2 decades. It was found that reanalysis TCs are basin-dependent in their representation of TC track, the position difference is less in eastern America and eastern China, which have the densest observations in their neighboring basins (Schenkel and Hart, 2012). By using 6 reanalysis datasets, Murakami (2014) discovered that with finer resolution and assimilation of wind data, Japanese reanalysis gives the finest and the most reasonable result in TC spatial distribution and TC structure. Their research also showed that the interannual variation in reanalysis TCs in the Western North Pacific (WNP) and North Atlantic has a high correlation with observation data. Furthermore, Hodges et al. (2017) also affirmed that reanalysis TC genesis can reach close-to-realistic annual counts through a proper identification scheme. The limited resolution of reanalysis data means that they cannot truly reproduce strong TCs (Murakami and Sugi, 2010; Strachan et al., 2013). Malakar et al. (2020) investigated the intensity, structure and evolution history of 28 TCs in the North Indian Ocean and found that the Global Forecast System reanalysis and ERA5 capture the realistic evolution of different TC cases, while its interim dataset underestimates TC intensity and intensification, and their study also stated the importance of high resolution. However, a reasonable description of TC intensity can not only be solved by increasing the resolution but also be achieved by improving data assimilation, model physical processes, and air-sea coupling (Murakami, 2014).

Previous studies gave us an increased understanding of how TC reconstruction was realized by improving reanalysis data and the TC tracking method. However, most studies do not show pre-satellite time reanalysis TC results due to considerations of inconsistency in the quality of TC data before and after the satellite era. Meanwhile, there have been many developments in East Asia landfalling TC climatology, landfalling TC's trend and variation on the scale of 60-year were investigated (e.g., Chan and Xu, 2008; Shan and Yu, 2021). Data on landfalling TCs in East Asia are considered reliable beyond 60 years, especially the more intense ones.

This paper reports a succinct TC tracking method and its application to the reconstruction of historical landfalling TCs in East Asia by using different reanalysis data, tries to figure out if there exits inconsistency before and after satellite era, and answers the question that if there is any reanalysis dataset considered to be better when we want to analyze the climate change of tropical cyclones. The remainder of this paper is organized as follows. Section 2 describes the observational and reanalysis datasets used in our work, as well as the TC tracking method used. Section 3 gives the results of the reanalysis TCs in terms of track, genesis density, duration, variability and trend of TCs before and after 1980. Section 4 provides a conclusion of this work and briefly discusses the issues to be investigated in the future.

2 Data and methods

2.1 Data

One observational and six reanalysis datasets were used in this study, including the best-track data from the International Best-Track Archive for Climate Stewardship (IBTrACS, Knapp et al., 2010), NCAR (Kalnay et al., 1996) from NCEP/NCAR, 20CRv3 (Slivinski et al., 2019) from the National Oceanic and Atmospheric Administration (NOAA), the Cooperative Institute for Research in Environmental Sciences and the U.S. Department of Energy, JRA55 (Kobayashi et al., 2015) from the Japan Meteorological Agency, the ECMWF reanalysis interim dataset (ERAI, Dee et al., 2011), ERA5 (Hersbach et al., 2020; Bell et al., 2021) and ERA20C (Poli et al., 2016). Further details are provided below.

2.1.1 Observation data

The IBTrACS project merges TC information from agencies around the world and offers various TC variables, including Universal Time Coordinate (UTC) time, longitude and latitude. This study used best-track data from the Chinese Meteorological Administration Shanghai Typhoon Institute (CMA, Ying et al., 2014), obtained from IBTrACS version 04 (Knapp et al., 2010). CMA data offer longitude, latitude, minimum central pressure (MCP), storm type and max sustained wind speed (MSW) with a 2-min average time. The MSW is the highest surface wind that occurs within the TC circulation. We used CMA's 2-min average MSW to satisfy the national standard, which states that typhoon (TY) intensity occurs when the TC's central 2-min average wind speed exceeds 32.7 m/s but is no greater than 41.4 m/s. In this study, we use TCs with a maximum intensity exceeding 32.7 m/s.

2.1.2 Reanalysis data

The assimilation method, resolution, period, and TC treatment of the six reanalysis datasets used are given in Table 1. All the reanalysis data we used are based on a temporal frequency of 6 h, and each day contains four timesteps of 00 UTC, 06 UTC, 12 UTC and 18 UTC. Five out

TABLE 1 The assimilation method, model resolution, research period and TC treatment of the NCAR, 20CRv3, JRA55, ERAI, ERA5, and ERA20C reanalysis datasets.

Name	Assimilation	Model resolution	Period	TC treatment
NCAR	3D-Var	T62 (210 km)	1949–2019	None
20CRv3	4D-Var	T254 (60 km)	1949–2015	Assimilate TC min central pressure contained ISPD dataset and special QC
JRA55	4D-Var	T319 (55 km)	1958–2019	TCR assimilation
ERAI	4D-Var	T255 (80 km)	1980–2016	None
ERA5	4D-Var	T639 (31 km)	1950–2019	Assimilate TC min central pressure contained ISPD dataset
ERA20C	4D-Var	T159 (125 km)	1949–2010	Bogus TC

of six reanalysis datasets used in this work adapt a four-dimensional variation data assimilation, which yields a more accurate large-scale flow and should produce TCs more precisely (Whitaker et al., 2009; Dee et al., 2011). Based on all these data, 20CRv3 and ERA5 assimilate the International Surface Pressure Databank (ISPD), which contains the TC minimum central pressure from IBTrACS. Furthermore, 20CR has a special treatment for TCs; it allows significant low-pressure values caused by TCs to bypass quality control (QC) in the IBTrACS data assimilation (Compo et al., 2011). In version 3, a 4D incremental analysis method replaces the digital filter so that low-pressure values of TCs are retained and yet do not cause any system instability (Slivinski et al., 2019). The measures above enable the 20CRv3 data to present a more accurate location, sea level pressure and wind distribution around the TC (Slivinski et al., 2019). ERA20C uses a method called "bogus TC" to improve TC presentation, that is, it uses information, such as TC structure and behavior obtained from observations, as well as empirical formulas and gradient wind relationships to generate more realistic TCs in the model (Ahn and Lee, 2002; Poli et al., 2016). JRA55 assimilates the retrieval data (TCR) of the TC surrounding wind profile from Dr. Michael Fiorino (from NOAA). This technology makes the former JRA25 more representative for TCs than other reanalysis data in the same period. However, when applied to JRA55, the detection rate of TCs appears to unexpectedly decline in the 2000s, which is most likely affected by the artificial weakening trend of TCR's global average wind speed (Kobayashi et al., 2015).

2.2 Methods

2.2.1 Objective tracking method

The objective tracking method for reanalysis cyclone data in this study was proposed by Hodges (1994). Objective tracking is an approach that uses appropriate meteorological fields to segment background and object points and then identifies the initial feature points, tracks them by frame to obtain a series of feature points, forming the systems' path. In this study, the tracking utilized the 850 hPa relative vorticity field and set the segmentation threshold to $1 \times 10^{-5}\ s^{-1}$, then, the initial feature point was found and a search for the next timestep's feature point was conducted within a certain radius, and the positive vorticity points of each timestep were processed in sequence. Finally, the positive vorticity point's position, time and 850 hPa relative vorticity value were stored for further verification and identification.

2.2.2 Identification scheme

At present, apart from manual identification methods, many previous works focus on the TC warm core structure. Coupled with thresholds, such as duration and low-level relative vorticity, vorticity or temperature differences between levels are widely used (Bengtsson et al., 1996; Camargo and Zebiak, 2002; Bengtsson et al., 2007b; Zhao et al., 2009; Murakami and Sugi, 2010; Bell et al., 2013; Strachan et al., 2013; Hodges et al., 2017). Alternately, the Okubo–Weiss–Zeta (OWZ) diagnostic method focuses on the environmental conditions conducive to the generation and development of TCs (Tory et al., 2013). However, there is great disagreement among the different tracking schemes, in which the determination of duration, wind speed and genesis latitude thresholds play an important role, and the difference in each scheme's focus point can also lead to disparities (Horn et al., 2014).

In this study, together with the landing criterion, we used an overall identification method similar to Hodges et al. (2017). Limitations in the track starting area were used, the initial point of the track must be in WNP basin. The applied objective tracking method has been shown to produce an extended TC life cycle including the post-TC stage in which vorticity disturbance has just emerged and the extratropical transition stage of the positive vorticity system remains (Strachan et al., 2013). To remove false alarms that are unlikely even to be attributed to tropical depressions, a longer duration of no less than 4 days (16 timesteps) was considered. Here, the duration refers to the trajectory existence time, as a longer life cycle was demonstrated in objective tracking TC, and a longer duration condition has little impact on the TCs that we focused on.

Reanalysis TC position uncertainty was considered when developing the landfall criterion. TCs were considered to be

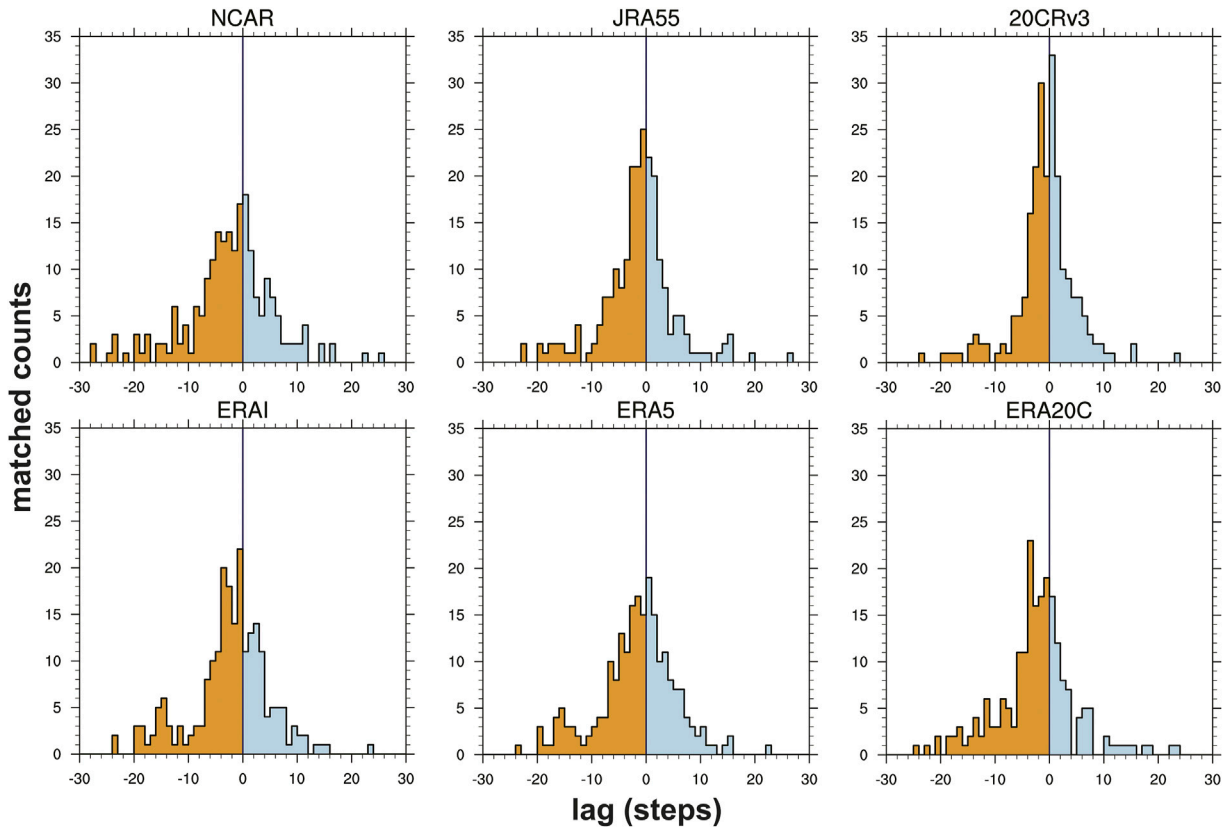

FIGURE 1
BT-RV time lag distribution for NCAR, 20CRv3, JRA55, ERAI, ERA5, and ERA20C (1980–2009). The Y-axis represents the sample number of matching tracks, and the X-axis represents the lag time (6 h a step) between the reanalysis and observed TC.

linked to landfall when the minimum distance between the coastline and its track was less than 1°. Here, we focused on five landfall regions, including China, the Philippines, Malaysia, Brunei, and Vietnam, collectively described as the East Asia area. Apart from the requirement below, a distinctive approach, namely, the west-moving requirement, was added to our identification scheme. The surrounding atmospheric circulation is the dominant factor that affects TC movement (Chan and Gray, 1982). In East Asia, tropical easterlies, monsoon throughs and subtropical highs are strongly associated with TC trajectories as part of background flows (Harr and Elsberry, 1995), and their combined effect drives TCs, showing straightforward or recurving trajectories (Chen et al., 2009). Most of the studied landfall TCs in our concerned regions are straightforward or recurving when they move out of the genesis basin, and their movement direction is mainly westward, especially at the beginning (Camargo et al., 2007). Among all the positive vorticity systems affecting East Asia, a considerable false alarm was composed of extratropical cyclones, which are dominated by westerlies and perform differently from TCs. We have captured the key difference between these two cyclones' trajectories mentioned above in East Asia, limiting the direction of motion in the early stages of cyclone generation, successfully separated extra-tropical cyclones and ensured the reliability of TC landfall processes.

The key to finding the 850 hPa RV threshold at TY intensity is to construct the connections between RV and MSW values. A TY's intensification can be accompanied by enhanced positive vorticity near its center, along with the appearance of a positive vorticity column through the middle to upper troposphere (Yu et al., 2008). To avoid the interference track such as tropical depression, we matched the best-track (BT) TCs with reanalysis TCs using the direct matching method (Hodges et al., 2017), and we found that the maximum intensity times of all six-reanalysis data TCs appeared to be early or delayed compared with the BT TCs within their matching period. The maximum intensity time lags within each dataset are shown in Figure 1. The time lag is calculated by using the observation MSW maximum timestep minus the reanalysis RV maximum timestep (in their matching period). A positive value (blue) means that the RV maximum appears early to the MSW maximum, while a

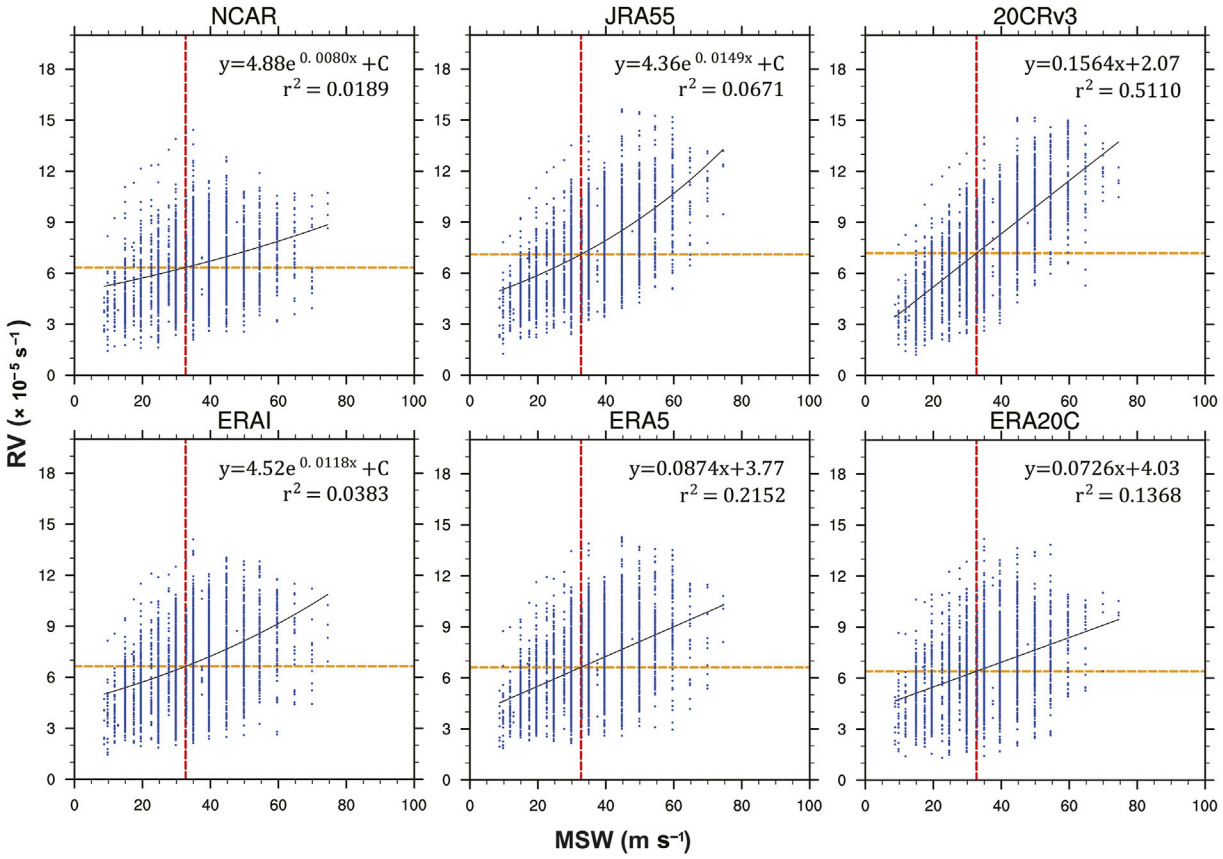

FIGURE 2
BT max sustained wind (MSW) and matching 850 hPa relative vorticity (RV) scatter (blue) (1980–2009), with the fitting function (black straight line), the TY wind speed threshold of 32.7 m/s (red dotted line), and the vorticity threshold corresponding to the typhoon wind speed threshold on the fitting function (yellow dotted line).

negative value (yellow) means a delay. The early and delayed appearance of RV maximums compared to MSW maximums are within the back and front 10 timesteps (60 h), which means there is a great chance to find an RV maximum within the back and front 60 h in the observational TC's maximum MSW.

With the discovery above, we draw the MSW maximum and time corresponding to the RV value in its surrounding 60 h, as depicted in Figure 2. To objectively find the intensity threshold, linear and e functions were used to fit those scatter points. With the highest r^2, the 20CRv3 MSW-RV relationship is reasonably explained. The high-intensity reproduction failure of ERAI is also mentioned by Malakar et al. (2020), who claimed that in the North Indian Ocean, ERAI obtained a higher number of hits for lower-intensity statements but failed to present higher-intensity statements. To find a correct threshold for reanalysis TCs, the corresponding value of RV for TY intensity was found. For simplicity, we choose $6 \times 10^{-5}\ s^{-1}$ as the final threshold. In summary, the identification criteria we developed are given as follows:

(1) The shortest distance between reanalysis TC tracks and coastlines is less than 1°.
(2) The duration of TCs must exceed 4 days.
(3) The first point of TCs must be in the WNP basin (0°–35° N, 105°–210° E).
(4) The tracks must move west from the genesis time compared to the third day (12 steps).
(5) The 850 hPa RV must reach the threshold of $6 \times 10^{-5}\ s^{-1}$ at south of 35° N.

The identification used here is highly based on the regional circulation characteristics; therefore, it is a basin-dependent method that should change accordingly when applied to other basins. The threshold of RV chosen here is based on the MSW-RV relationship, which can allocate different thresholds based on different reanalysis, despite their resolution difference. However, this study attempted to find a general threshold for TY intensity; thus, a RV threshold of $6 \times 10^{-5}\ s^{-1}$ is chosen, and therefore the TC studied following indicates tropical cyclone with max intensity exceeds TY.

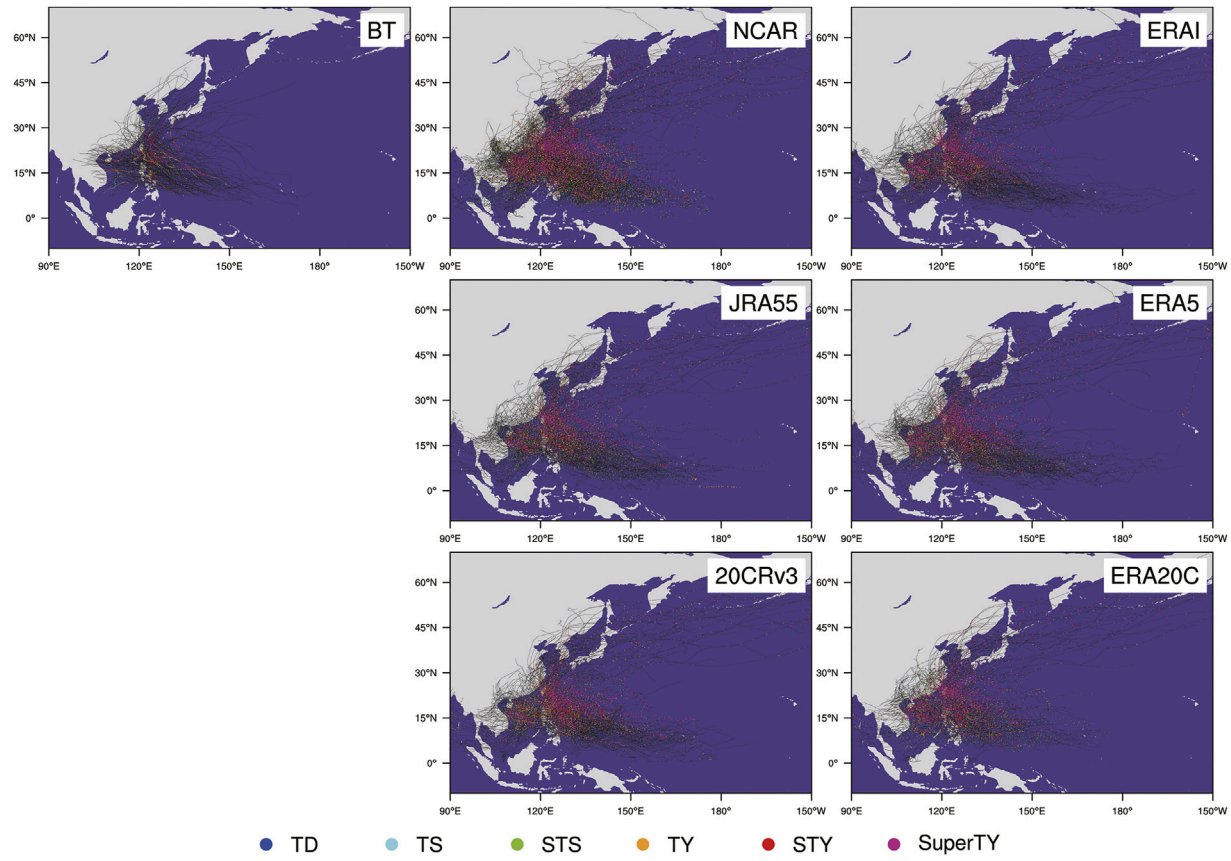

FIGURE 3
NCAR, 20CRv3, JRA55, ERAI, ERA5, ERA20C, and BT TC tracks (1980–2009) (black). Scatter in different colors indicate different intensity stages: tropical depression (TD) is blue; tropical storm (TS) is cyan; strong tropical storm (STS) is green; typhoon (TY) is yellow; strong typhoon (STY) is red; and super typhoon (Super TY) is purple.

3 Results

3.1 TC track, genesis and lifetime

Figure 3 shows the TC tracks of the observations and six reanalysis datasets. The classification of reanalysis TC intensity levels was determined according to the fitting function that was determined in subsection 2.2.2. The TY trajectories of all reanalysis data are more widely distributed, extending near the equator to the south, to the Indochina Peninsula and the Bay of Bengal to the west, and covering Northeast China, the Korean Peninsula and Japan to the north. At the same time, it is noteworthy that reanalysis TCs demonstrate the process of extratropical transition more obviously, which reminds us that it is very important to deal with the information of the extratropical transition stage when using those data to evaluate TC trajectory.

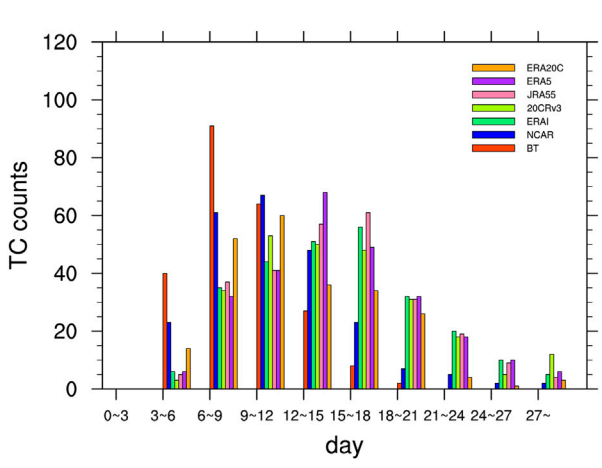

FIGURE 4
Duration in the distributions of BT TCs and NCAR, ERAI, 20CRv3, JRA55, ERA5, and ERA20C (1980–2009) TCs.

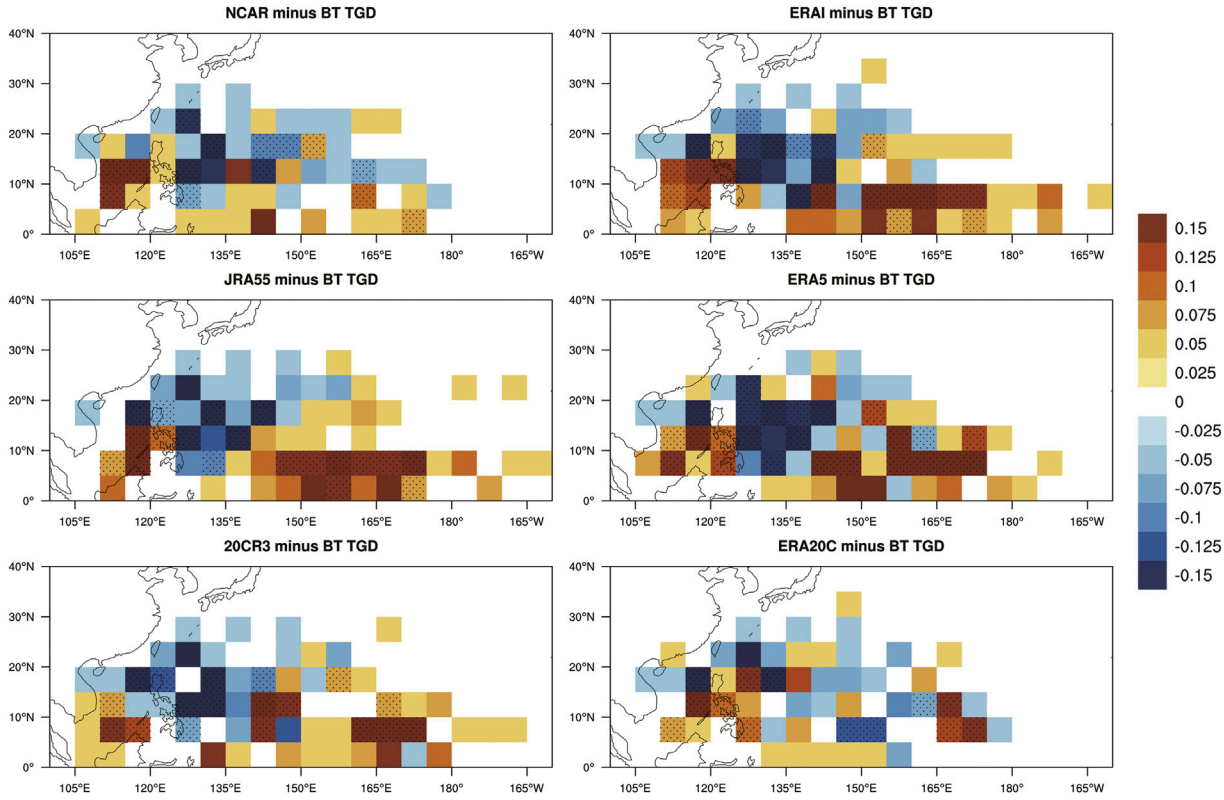

FIGURE 5
The differences between the BT TGD (TC genesis density) and NCAR, 20CRv3, JRA55, ERAI, ERA5, and ERA20C (1980–2009) TGDs. The shadow indicates that the difference is significant at the 0.05 level.

As the reanalysis TC tracks seem to be longer, as shown in Figure 3, the durations and genesis position of reanalysis and observation TCs were investigated. Characteristically, most reanalysis datasets have longer life cycles than the observations (Figure 4, red bar). The duration of observed TCs is mostly distributed at 3–12 days, while ERAI, ERA5, ERA20C, JRA55, and 20CRv3 TCs last longer than 12 days (Figure 4). As a characteristic of the tracking method itself, most reanalyzes have a consistent lifetime distribution (Hodges et al., 2017). High resolutions like ERA5 and JRA55 are linked to a longer lifetime, and course resolutions like NCAR and ERA20C can surely infect the result of the life cycle. Figure 5 shows the genesis distribution difference between reanalysis and observed TCs. The reanalysis TC generation position was closer to the equator and northern central Pacific, especially in 20CRv3, JRA55, ERAI, and ERA5, while the northern South China Sea and the Philippine Sea had a greater genesis of observed TCs. Reanalysis TC's more distant generation, longer life cycle and the extended track are coherent with the previous objective tracking results (Strachan et al., 2013; Hodges et al., 2017). No manual processing was applied to the initial tracks as we intended to retain more information from the initial tracking results.

3.2 TC detection rate

In this section, a direct method was used to evaluate the restoration of the reanalysis to the observed TCs. Similar to Hodges et al. (2017), we defined the probability of detection (POD) as the reanalysis TC matching rate reaching that of the observed TC. Additionally, the false alarm rate (FAR) was defined as the proportion of the tracks in the reanalysis data that could not be confirmed by observation data. Table 2 lists the annual count, annual hit count, POD, FAR, correlation coefficient and linear trend difference between the reconstruction series and BT series for six reanalysis TCs. In NCAR and ERA20C, the average annual reanalysis landfall TC counts reach 7.39 and 7.32, respectively, with an average BT landfall TC count of approximately 8.5, NCAR and ERA20C were the only two reanalysis datasets that underestimate the annual genesis number, while the other reanalysis datasets appear to be slightly overestimated. Overall, numerically, the

TABLE 2 The identification result, matching result, correlation coefficient (* means significant at the 0.05 level) and linear trend differences in the NCAR, 20CRv3, JRA55, ERAI, ERA5, and ERA20C TCs.

Reanalysis dataset	Period	Average annual count	Average hit count	POD	Far	Correlation coefficient	Linear trend difference
NCAR	1949–2019	7.39	4.88	0.58	0.34	0.16	0.088
20CRv3	1949–2015	8.72	5.25	0.75	0.27	0.50*	0.013
JRA55	1958–2019	9.50	6.31	0.75	0.33	0.58*	0.024
ERAI	1980–2016	8.68	5.43	0.71	0.38	0.29	0.079
ERA5	1950–2019	9.09	5.93	0.70	0.35	0.51*	0.033
ERA20C	1949–2010	7.32	5.16	0.60	0.30	0.31*	0.063

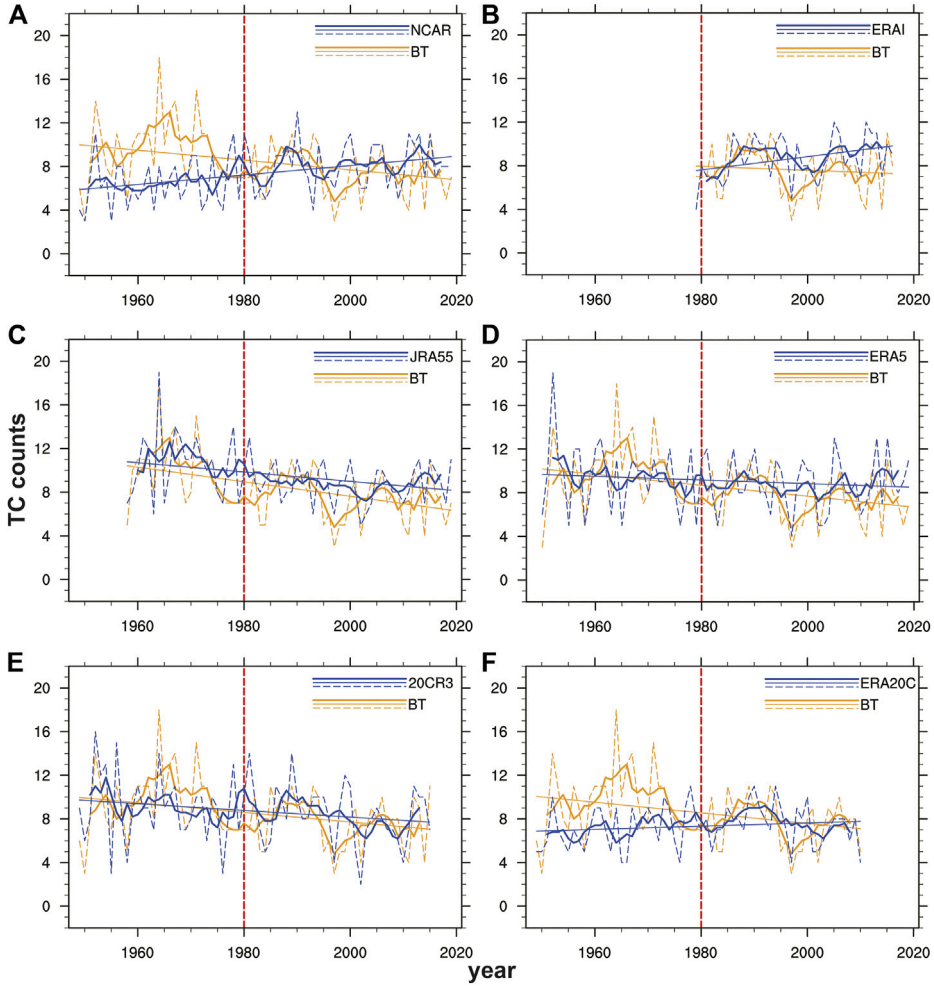

FIGURE 6
The annual variation in NCAR **(A)**, ERAI **(B)**, JRA55 **(C)**, ERA5 **(D)**, 20CRv3 **(E)**, and ERA20C **(F)** in the reference observations (dashed line). Blue means reanalysis series, and yellow means observations. The thick solid line indicates the 5-year running average, and the thin solid line indicates the linear regression fit curve. The red dash lines are the cutting line of the pre- and post-satellite era.

observed annual frequency of TCs has been practically restored. Furthermore, based on POD and FAR, 20CRv3 is the best of all reanalysis data, for it retained a high POD value when the application of the identification scheme reduced the FAR to a small enough value. Notably, JRA55 shows an equal performance for POD with 20CRv3, even though its FAR is slightly higher and

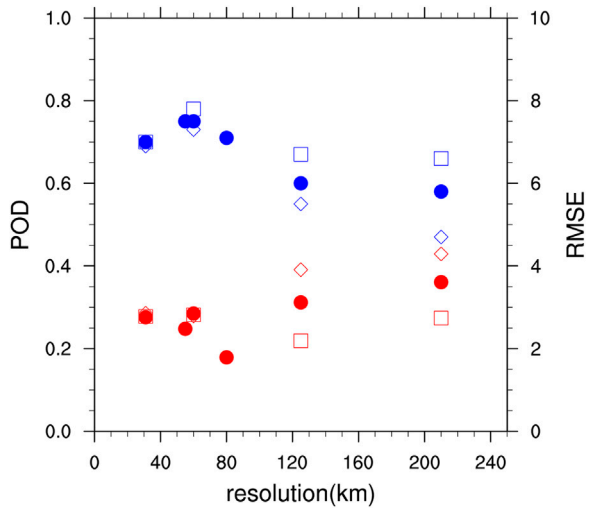

FIGURE 7
Scatter of resolution- POD (blue) and RMSE (red) relationships, solid dots indicate results for full-time periods, when squares indicate 1980–2009 and diamonds indicate 1950–1979.

can also be considered a good presentation for an actual TC. Four out of six reanalysis data PODs reach to or above 0.70, and four out of six data FARs are approximately 0.3, demonstrating that the identification used in this work can largely determine the TC characteristic. The correlation coefficients of the 20CRv3, JRA55, and ERA5 TC series compared with the observations surpassed 0.5 and appeared to be significant at the 0.05 level, while the NCAR value was 0.16 and considered statistically nonsignificant, which is supportive of the result that 20CRv3, JRA55, and ERA5 are better reanalysis datasets in terms of presenting East Asia TCs making landfall compared with the other three datasets.

3.3 TC annual variation and inconsistency in approximately 1980

Figure 6 gives the annual variation in TC counts during the reanalysis dataset's different research periods compared with those in the observations. The annual TC counts in 20CRv3, JRA55, and ERA5 have higher correlation coefficients (Table 2); together, their annual variations are closer to the observations. Similar to the observations, through their research period, 20CRv3, JRA55, and ERA5 show a downward trend, and 20CRv3 has the smallest linear trend difference from the observations (Table 2). In contrast, NCAR, ERAI, and ERA20C show an upward trend, in which NCAR and ERA20C show an upward trend mainly because they underestimated East Asia landfall TCs before 1975.

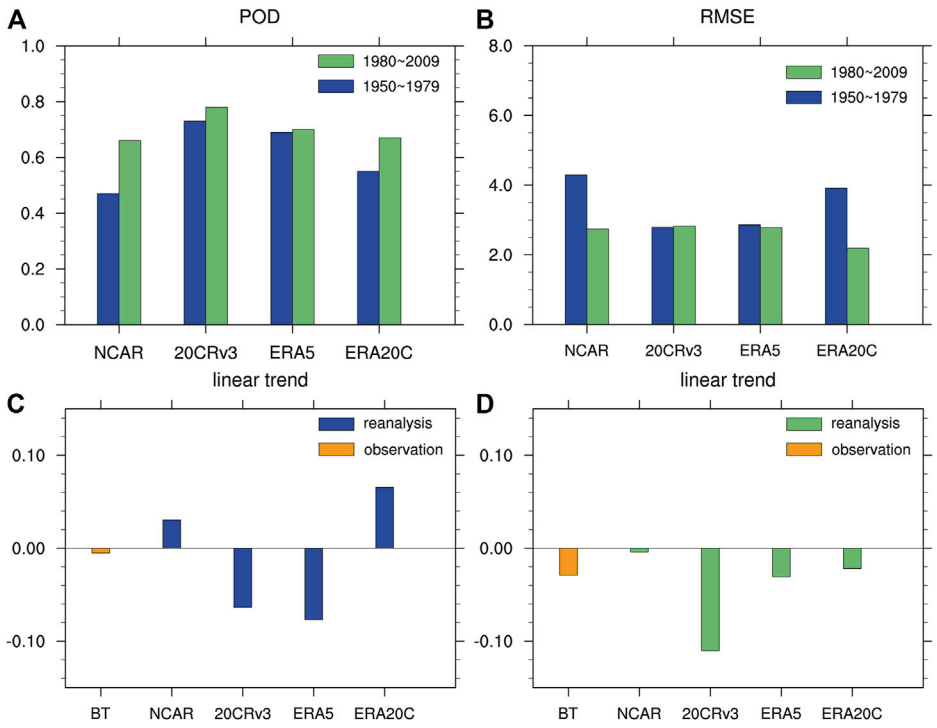

FIGURE 8
The comparison of two periods of POD **(A)** and RMSE **(B)** of NCAR, 20CRv3, ERA5, and ERA20C and their linear trend with BT TCs in 1950–1979 **(C)** and 1980–2009 **(D)**.

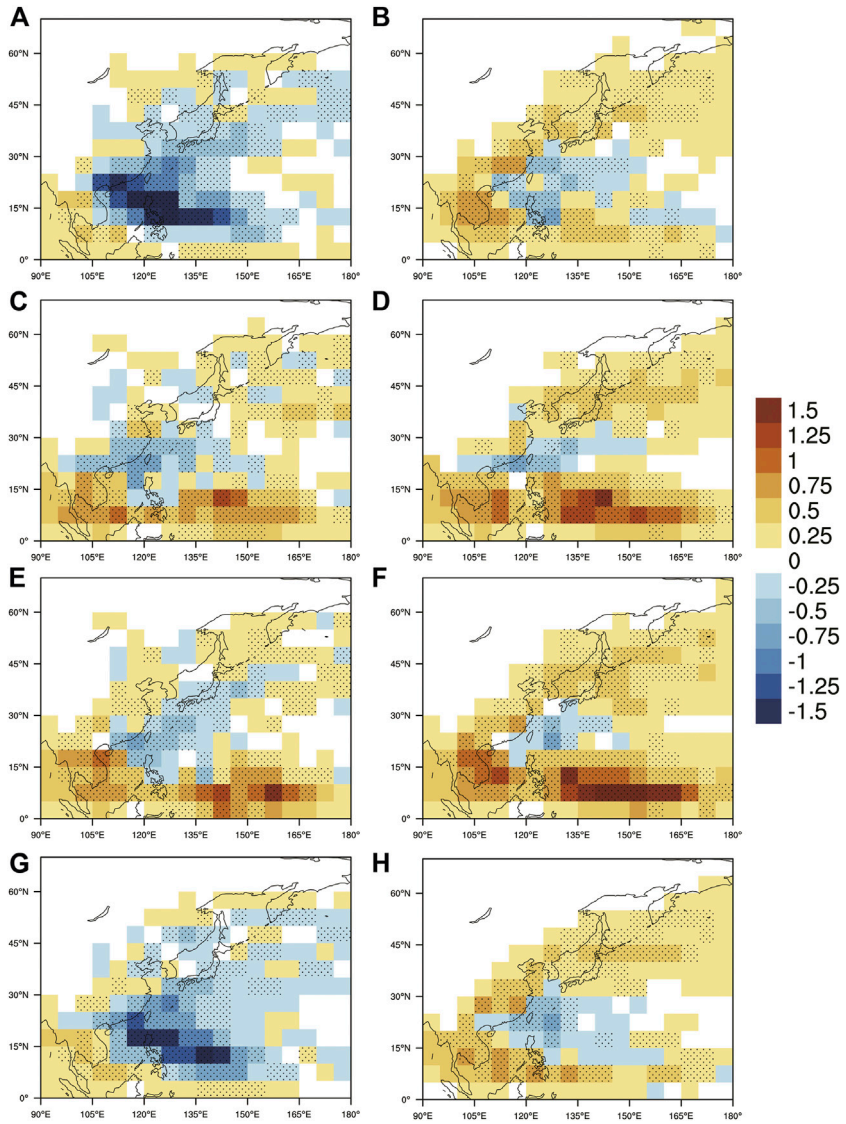

FIGURE 9
The differences between the BT TCTD and NCAR **(A,B)**, 20CRv3 **(C,D)**, ERA5 **(E,F)** and ERA20C **(G,H)** TCTDs in 1950–1979 **(A,C,E,G)** and 1980–2009 **(B,D,F,H)**. The shadow indicates that the difference is significant at the 0.05 level.

We divided the NCAR, 20CRv3, ERA5, and ERA20C TC series into two 30-year periods around 1980 to determine whether reanalysis TCs have apparent inconsistencies during the pre-satellite time and after. And as an investigation of how resolution becomes the essential background of reanalysis TCs, we performed the relationship between the POD and RMSE in Figure 7. Before 1980, NCAR and ERA20C show an obvious underestimation of the annual TC count, with maximum underestimated counts both exceeding 9 (Figure 6). At the same time, the root mean square error (RMSE) values of those two reanalysis datasets are higher, and the POD values are lower (Figure 8). ERA5 and 20CRv3 did not show an obvious underestimation; however, the observed TC has a higher count between 1960 and 1975, which explains why their linear trend shows a downward overestimation in the first 30 years (Figure 8). Most reanalysis data were more comparable to the observations after 1980, even though they were obtained in different ways. A higher POD value appears for all the reanalysis TCs; among them, the increases in NCAR and ERA20C were more obvious, and their RMSE decreased to the same level as the other two reanalysis datasets. The linear trend of 1980–2009 restored by reanalysis showed a consistent downward trend with the

observations. This downward trend was obtained more accurately in ERA5 and ERA20C. In all the reanalysis datasets, including ERAI and JRA55, the reanalysis datasets almost uniformly overestimated the low values of TC interannual variability in approximately 1998 and 2014 (Figure 6), which means that the interannual variability amplitude of reanalysis TC is smaller than that of the observation. Considering the extremely high, directly matching POD value, this overestimation may be related to the inaccurate estimation of TC intensity by the reanalysis datasets. In summary, the reanalysis datasets with higher resolutions tends to have more consistent POD and RMSE in pre- and post-satellite era. In contrast, the reanalysis datasets with lower resolution showed greatly improved when satellite data are available. However, it is worth noting that at resolutions below 80 km, the influence of satellite data becomes less remarkable, and it is more likely that the results will be determined by different data assimilation schemes (Figure 7).

In order to see the change in the difference between the reanalysis and observation TCs' spatial distribution before and after the satellite era, we show the mean TC track density (TCTD) difference in the two 30-year periods in Figure 9. The TCTD is calculated by the frequency of TC tracks over the 5° latitude × 5° longitude area; one track will only be counted once in the same grid box. After 1980, consistent with a longer life cycle, all four sets of reanalysis data have a higher distribution of tracks near the Caroline Islands, in the Bay of Bengal, in central and north-eastern China to Japan, Korea and the northern North Pacific. For Figures 9D,F the multi-distribution of TC tracks located near the Caroline Islands can be explained by the TGD distribution, with both 20CRv3 and ERA5 TC having a larger generation frequency between 140°–180° N, compared to the observed tracks (Figure 5). ERA5 has the highest horizontal resolution, which corresponds to the smallest negative differences and the largest positive differences of TC tracks after 1979, and this correspondence of high resolution with less negative track deviation is also mentioned in Roberts et al. (2020).

Compared to the overestimation of trajectories in the above regional in reanalysis, it is more interesting to note the large values of observed trajectories near the Northern South China Sea, Taiwan Island and the Ryukyu Islands. The matching passages between observed and reanalyzed trajectories are distributed highly in this region, and the average distance between matched trajectories of those data does not exceed 3°N. Therefore, we believe that the underestimations of the reanalysis in this region are not a result of the inaccurate trajectories, but because of the missing TCs in the reanalysis datasets. With more TCs missing, the under-valuation of the NCAR and ERA20 shows further expansion from the original area and is more pronounced in the pre-1980 period (Figures 9A,C,E,G). In the case of 20CRv3 and ERA5 TCs in the pre-satellite era, underestimations dispersedly appear at higher latitudes. It is uncertain whether the missing TCs or the reanalysis TC's position uncertainty are blamed, as it is possible that the reanalysis trajectories diverge more from the observed positions after landfall and into higher latitudes.

4 Conclusions and discussion

4.1 Conclusions

In this work, a concise East Asia landfall TC identification scheme was used to evaluate the reanalysis TC spatially and temporally, and the NCAR, 20CRv3, ERA5, and ERA20C TC's performance before and after 1980 were carefully investigated. Overall, 20CR3 gives the most satisfactory result in this assessment, ERA5 and JRA55 also showed encouraging results. Most reanalysis TCs showed discontinuities in approximately 1980, they tended to show better simulations after that, and the newer, higher resolution reanalysis's discontinuities are lesser found than others.

By evaluating the POD, RMSE and linear trends, the reconstruction of NCAR and ERA20C improved significantly after 1980. After 1980, the downward trend of landfalling TCs is well captured by ERA5 and ERA20C, however, nearly all reanalysis data failed to display the low TC genesis years of approximately 1998 and 2014. Reanalysis TCs have longer life cycles, and their paths also cover areas near the equator to the south, the Indochina Peninsula and the Bay of Bengal to the west, and Northeast China, the Korean Peninsula and Japan to the north. The missing TCs are mostly located around the Northern South China Sea, Taiwan Island and the Ryukyu Islands, causing reanalysis TC paths appear underestimates in such areas. In the pre-satellite era, the underestimated range of TCTD became greater with the absence of more TCs.

4.2 Discussion

Apparently, the resolution has a strong relationship with the results presented by reanalysis of TCs. For the higher resolution ones, such as ERA5, fewer underestimations and larger overestimations of TC tracks occur compared to 20CRv3, which has similar TC treatments when forming the data, but owns a lower resolution. However, it's not convincing that resolution is the only impact of the disagreement between different reanalysis, especially considering the inconsistency within the same reanalysis in pre-and post-satellite time. NCAR used all available data at that time, including multiple satellite data (Kalnay et al., 1996). With no special treatment against TC, the unstable performance of NCAR shows that the inclusion of satellite

data alone can help reanalysis TC improve significantly. ERA20C is also sensitive to changes in satellite data, its inconsistency might arise from bogus TCs assimilation. The number of assimilated bogus TC increased in post-satellite time (Poli et al., 2016), but the details of bogus TC's quality change around this time and its influence still need further investigation. There are reports about ERA5 back extensions switched off quality control to avoid rejection of IBTrACS observation data, but this initiative has also led to an overestimation of TC intensity (Bell et al., 2021). Some ERA5 TCs before 1979 are found too intense with much deeper central pressure and may come with greater 10 m wind (Bell et al., 2021). In our study, due to the relative vorticity-based tracking method, the overestimated intensity did not affect the tracking result excessively. The relatively high credit of JRA55 and ERA5 TCs has been proposed in former studies (Murakami, 2014; Hodges et al., 2017; Zarzycki et al., 2021). This study shows that 20CRv3 TCs are also worth further study. For future investigations, it is necessary to demonstrate the relationship between intensity uncertainty and the overestimation of low TC genesis years and find out how the identification scheme affects the pre-satellite time TCs. This study displayed the relationships of RV and MSW peak intensity time, with the observation TC's intensification and weakening period becoming shorter (Kishtawal et al., 2012; Wang et al., 2020), it's also the direction of interest to understand TC intensity evolution in reanalysis.

Data availability statement

The IBTrACS data are openly available from: https://www.ncei.noaa.gov/data/international-best-track-archive-for-climate-stewardship-ibtracs/v04r00/access/netcdf/. The reanalysis data are available from the following website: https://psl.noaa.gov/data/gridded/data.ncep.reanalysis.html (NCAR), https://psl.noaa.gov/data/gridded/data.20thC_ReanV3.html (20CRv3), http://rda.ucar.edu/datasets/ds628.0/ (JRA55), https://www.ecmwf.int/en/forecasts/datasets/browse-reanalysis-datasets (ERAI, ERA5, ERA20C).

Author contributions

RL: Methodology, formal analysis, writing–original draft, writing–review and editing. LC: Conceptualization, methodology, writing–review and editing. GR: Funding acquisition, supervision, writing–review.

Funding

This work is supported by the National Key R&D Program of China (2018YFA0605603).

Acknowledgments

The authors are grateful to Kevin Hodges for his invaluable help.

Conflict of interest

The authors declare that the research was conducted in the absence of any commercial or financial relationships that could be construed as a potential conflict of interest.

Publisher's note

References

Ahn, Y. I., and Lee, D. K. (2002). Impact of bogus tropical cyclones on summertime circulation in regional climate simulation. *J. Geophys. Res.* 107 (D16), ACL 8-1–ACL 8-16. doi:10.1029/2001JD000416

Bell, B., Hersbach, H., Simmons, A., Berrisford, P., Dahlgren, P., Horányi, A., et al. (2021). The ERA5 global reanalysis: Preliminary extension to 1950. *Q. J. R. Meteorol. Soc.* 147 (741), 4186–4227. doi:10.1002/qj.4174

Bell, R., Strachan, J., Vidale, P. L., Hodges, K., and Roberts, M. (2013). Response of tropical cyclones to idealized climate change experiments in a global high-resolution coupled general circulation model. *J. Clim.* 26 (20), 7966–7980. doi:10.1175/JCLI-D-12-00749.1

Bengtsson, L., Botzet, M., and Esch, M. (1996). Will greenhouse gas-induced warming over the next 50 years lead to higher frequency and greater intensity of hurricanes? *Tellus A Dyn. Meteorology Oceanogr.* 48 (1), 57–73. doi:10.3402/tellusa.v48i1.11632

Bengtsson, L., Hodges, K. I., Esch, M., Keenlyside, N., Kornblueh, L., Luo, J. J., et al. (2007b). How may tropical cyclones change in a warmer climate? *Tellus A Dyn. Meteorology Oceanogr.* 59 (4), 539–561. doi:10.1111/j.1600-0870.2007.00251.x

Bengtsson, L., Hodges, K. I., and Esch, M. (2007a). Tropical cyclones in a T159 resolution global climate model: comparison with observations and re-analyses. *Tellus A Dyn. Meteorology Oceanogr.* 59 (4), 396–416. doi:10.1111/j.1600-0870.2007.00236.x

Camargo, S. J., Robertson, A. W., Gaffney, S. J., Smyth, P., and Ghil, M. (2007). Cluster Analysis of typhoon tracks. Part I: general properties. *J. Clim.* 20 (14), 3635–3653. doi:10.1175/JCLI4188.1

Camargo, S. J., and Zebiak, S. E. (2002). Improving the detection and tracking of tropical cyclones in atmospheric general circulation models. *Weather Forecast.* 17 (6), 1152–1162. doi:10.1175/1520-0434(2002)017<1152:itdato>2.0.co;2

Chan, J. C. L., and Gray, W. M. (1982). Tropical cyclone movement and surrounding flow relationships. *Mon. Weather Rev.* 110 (10), 1354–1374. doi:10.1175/1520-0493(1982)110<1354:tcmasf>2.0.co;2

Chan, J. C. L., and Xu, M. (2008). Inter-annual and inter-decadal variations of landfalling tropical cyclones in east Asia. Part I: time series analysis. *Int. J. Climatol.* 29 (9), 1285–1293. doi:10.1002/joc.1782

Chen, T., Wang, S., Yen, M., and Clark, A. J. (2009). Impact of the intraseasonal variability of the Western north pacific large-scale circulation on tropical cyclone tracks. *Weather Forecast.* 24 (3), 646–666. doi:10.1175/2008WAF2222186.1

Compo, G. P., Whitaker, J. S., Sardeshmukh, P. D., Matsui, N., Allan, R. J., Yin, X., et al. (2011). The twentieth century reanalysis project. *Q. J. R. Meteorol. Soc.* 137 (654), 1–28. doi:10.1002/qj.776

Dee, D. P., Uppala, S. M., Simmons, A. J., Berrisford, P., Poli, P., Kobayashi, S., et al. (2011). The ERA-interim reanalysis: configuration and performance of the data assimilation system. *Q. J. R. Meteorol. Soc.* 137 (656), 553–597. doi:10.1002/qj.828

Harr, P. A., and Elsberry, R. L. (1995). Large-scale circulation variability over the tropical Western north pacific. Part I: Spatial patterns and tropical cyclone characteristics. *Mon. Weather Rev.* 123 (5), 1225–1246. doi:10.1175/1520-0493(1995)123<1225:lscvot>2.0.co;2

Hersbach, H., Bell, B., Berrisford, P., Hirahara, S., Horányi, A., Muñoz-Sabater, J., et al. (2020). The ERA5 global reanalysis. *Q. J. R. Meteorol. Soc.* 146 (730), 1999–2049. doi:10.1002/qj.3803

Hodges, K., Cobb, A., and Vidale, P. L. (2017). How well Are tropical cyclones represented in reanalysis datasets? *J. Clim.* 30 (14), 5243–5264. doi:10.1175/JCLI-D-16-0557.1

Hodges, K. L. (1994). A general method for tracking analysis and its application to meteorological data. *Mon. Weather Rev.* 122 (11), 2573–2586. doi:10.1175/1520-0493(1994)122<2573:agmfta>2.0.co;2

Horn, M., Walsh, K., Zhao, M., Camargo, S. J., Scoccimarro, E., Murakami, H., et al. (2014). Tracking scheme dependence of simulated tropical cyclone response to idealized climate simulations. *J. Clim.* 27 (24), 9197–9213. doi:10.1175/JCLI-D-14-00200.1

Kalnay, E., Kanamitsu, M., Kistler, R., Collins, W., Deaven, D., Gandin, L., et al. (1996). The NCEP/NCAR 40-year reanalysis project. *Bull. Am. Meteorol. Soc.* 77 (3), 437–471. doi:10.1175/1520-0477(1996)077<0437:tnyrp>2.0.co;2

Kishtawal, C. M., Jaiswa, N., Singh, R., and Niyogi, D. (2012). Tropical cyclone intensification trends during satellite era (1986–2010). *Geophys. Res. Lett.* 39 (10). doi:10.1029/2012GL051700

Knapp, K. R., Kruk, M. C., Levinson, D. H., Diamond, H. J., and Neumann, C. J. (2010). The international best track archive for climate stewardship (IBTrACS). *Bull. Am. Meteorol. Soc.* 91 (3), 363–376. doi:10.1175/2009BAMS2755.1

Kobayashi, S., Ota, Y., Harada, Y., Ebita, A., Moriya, M., Onoda, H., et al. (2015). The JRA-55 reanalysis: General specifications and basic characteristics. *J. Meteorological Soc. Jpn.* 93 (1), 5–48. doi:10.2151/jmsj.2015-001

Liu, K. S., Chan, J. C. L., and Kubota, H. (2021). Meridional oscillation of tropical cyclone activity in the Western North Pacific during the past 110 years. *Clim. Change* 164, 23. doi:10.1007/s10584-021-02983-8

Malakar, P., Kesarkar, A. P., Bhate, J. N., Singh, V., and Deshamukhya, A. (2020). Comparison of reanalysis data sets to comprehend the evolution of tropical cyclones over north Indian ocean. *Earth Space Sci.* 7 (2), e2019EA000978. doi:10.1029/2019EA000978

Murakami, H., and Sugi, M. (2010). Effect of model resolution on tropical cyclone climate projections. *SOLA* 6, 73–76. doi:10.2151/sola.2010-019

Murakami, H. (2014). Tropical cyclones in reanalysis data sets. *Geophys. Res. Lett.* 41 (6), 2133–2141. doi:10.1002/2014GL059519

Poli, P., Hersbach, H., Dee, D. P., Berrisford, P., Simmons, A. J., Vitart, F., et al. (2016). ERA-20C: an atmospheric reanalysis of the twentieth century. *J. Clim.* 29 (11), 4083–4097. doi:10.1175/JCLI-D-15-0556.1

Pu, X., Chen, Q., Zhong, Q., Ding, R., and Liu, T. (2019). Influence of the north pacific victoria mode on western north pacific tropical cyclone Genesis. *Clim. Dyn.* 52, 245–256. doi:10.1007/s00382-018-4129-z

Roberts, M. J., Camp, J., Seddon, J., Vidale, P. L., Hodges, K., Vanniere, B., et al. (2020). Impact of model resolution on tropical cyclone simulation using the HighResMIP–PRIMAVERA multimodel ensemble. *J. Clim.* 33 (7), 2557–2583. doi:10.1175/JCLI-D-19-0639.1

Schenkel, B. A., and Hart, R. E. (2012). An examination of tropical cyclone position, intensity, and intensity life cycle within atmospheric reanalysis datasets. *J. Clim.* 25 (10), 3453–3475. doi:10.1175/2011JCLI4208.1

Scoccimarro, E., Gualdi, S., and Navarra, A. (2012). Tropical cyclone effects on Arctic Sea ice variability. *Geophys. Res. Lett.* 39. doi:10.1029/2012GL052987

Shan, K., and Yu, X. (2021). Variability of tropical cyclone landfalls in China. *J. Clim.* 34 (23), 9235–9247. doi:10.1175/JCLI-D-21-0031.1

Slivinski, L. C., Compo, G. P., Whitaker, J. S., Sardeshmukh, P. D., Giese, B. S., McColl, C., et al. (2019). Towards a more reliable historical reanalysis: improvements for version 3 of the Twentieth Century Reanalysis system. *Q. J. R. Meteorol. Soc.* 145 (724), 2876–2908. doi:10.1002/qj.3598

Strachan, J., Vidale, P. L., Hodges, K., Roberts, M., and Demory, M. (2013). Investigating global tropical cyclone activity with a hierarchy of AGCMs: the role of model resolution. *J. Clim.* 26 (1), 133–152. doi:10.1175/JCLI-D-12-00012.1

Tory, K. J., Chand, S. S., Dare, R. A., and McBride, J. L. (2013). The development and assessment of a model-grid-and basin-independent tropical cyclone detection scheme. *J. Clim.* 26 (15), 5493–5507. doi:10.1175/JCLI-D-12-00510.1

Walsh, K. (2015). Fine resolution simulations of the effect of climate change on tropical cyclones in the South Pacific. *Clim. Dyn.* 45, 2619–2631. doi:10.1007/s00382-015-2497-1

Wang, S., Rashid, T., Throp, H., and Toumi, R. (2020). A shortening of the life cycle of major tropical cyclones. *Geophys. Res. Lett.* 47 (14), e2020GL088589. doi:10.1029/2020GL088589

Whitaker, J. S., Compo, G. P., and Thépaut, J. (2009). A comparison of variational and ensemble-based data assimilation systems for reanalysis of sparse observations. *Mon. Weather Rev.* 137 (6), 1991–1999. doi:10.1175/2008MWR2781.1

Ying, M., Zhang, W., Yu, H., Lu, X., Feng, J., Fan, Y., et al. (2014). An overview of the China meteorological administration tropical cyclone database. *J. Atmos. Ocean. Technol.* 31 (2), 287–301. doi:10.1175/JTECH-D-12-00119.1

Yu, Y. B., Chen, L. S., and Yang, C. X. (2008). The features and mechanism analysis on rapid intensity change of super typhoon saomai(2006) over the offshore of China. *Chin. J. Atmos. Sci.* 32, 405–416. Available at: https://kns.cnki.net/kcms/detail/detail.aspx?

Zarzycki, C. M., Ullrich, P. A., and Reed, K. A. (2021). Metrics for evaluating tropical cyclones in climate data. *J. Appl. Meteorol. Climatol.* 60 (5), 643–660. doi:10.1175/JAMC-D-20-0149.1

Zhang, Q., Gu, X., Li, J., Shi, P., and Singh, V. P. (2018). The impact of tropical cyclones on extreme precipitation over coastal and inland areas of China and its association to ENSO. *J. Clim.* 31 (5), 1865–1880. doi:10.1175/JCLI-D-17-0474.1

Zhao, M., Held, I. M., Lin, S., and Vecchi, G. A. (2009). Simulations of global hurricane climatology, interannual variability, and response to global warming using a 50-km resolution GCM. *J. Clim.* 22 (24), 6653–6678. doi:10.1175/2009JCLI3049.1

Zhou, Y. S., and Wu, T. Y. (2019). Composite analysis of precipitation intensity and distribution characteristics of Western track landfall typhoons over China under strong and weak monsoon conditions. *Atmos. Res.* 225, 131–143. doi:10.1016/j.atmosres.2019.03.037

frontiers | Frontiers in Earth Science

TYPE Original Research
PUBLISHED 17 January 2023
DOI 10.3389/feart.2022.1033474

OPEN ACCESS

EDITED BY
Sheng Chen,
Northwest Institute of Eco-Environment and Resources (CAS), China

REVIEWED BY
Wei-Bo Chen,
National Science and Technology Center for Disaster Reduction (NCDR), Taiwan
Feifei Shen,
Nanjing University of Information Science and Technology, China
Chao Liu,
Nanjing University of Information Science and Technology, China

*CORRESPONDENCE
Qifeng Lu,
luqf@cma.cn

SPECIALTY SECTION
This article was submitted to Interdisciplinary Climate Studies, a section of the journal *Frontiers in Earth Science*

RECEIVED 31 August 2022
ACCEPTED 28 December 2022
PUBLISHED 17 January 2023

CITATION
Xiao X, Lu Q, Lv X and Shen W (2023), Assimilation of FY-4A GIIRS radiance observations in the forecast of Typhoon Bavi.
Front. Earth Sci. 10:1033474.
doi: 10.3389/feart.2022.1033474

Assimilation of FY-4A GIIRS radiance observations in the forecast of Typhoon Bavi

Xianjun Xiao[1,2], Qifeng Lu[1,2]*, Xinyan Lv[3] and Wenqi Shen[4]

[1]Earth System Modeling and Prediction Centre (CEMC), Beijing, China, [2]State Key Laboratory of Severe Weather, Beijing, China, [3]National Meteorological Center, Beijing, China, [4]CMA GDOU Joint Laboratory for Marine Meteorology and South China Sea Institute of Marine Meteorology, Guangdong Ocean University, Zhanjiang, Guangdong, China

We assimilated radiance observations from the Geostationary Interferometric Infrared Sounder (GIIRS) onboard the FengYun-4A geostationary satellite to evaluate their impact on the forecast of Typhoon Bavi using WRFDA. The temperature channels with high information content, representing 90% of the information content of all temperature channels, were selected for assimilation. All radiance observations above the cloud-top were assimilated by comparing the channel height to the cloud-top height coming from the product of the Advanced Geosynchronous Radiation Imager (AGRI). The assimilation of the GIIRS observations decreased the root-mean-square error of the temperature by 2% and improved the precipitation forecast. The rain band in southeast China was reproduced well, thus showing that infrared hyperspectral radiance observations have added value in improving the circulation around typhoons and, therefore, provide better forecasts. The increased relative humidity in the upper layer and stronger typhoon outflow were found to related to the intensify of typhoon in the analysis compared with the control experiment.

KEYWORDS

GIIRS, Typhoon Bavi, hyperspectral radiance, typhoons, 3DVAR

1 Introduction

Tropical cyclones are organized convective weather systems that occur over tropical and subtropical oceans. They usually consist of a non-frontal vortex with high temperatures and low pressures in the center of the cyclone. These major weather systems bring gales, rainstorms, and storm surges, often causing great losses to property and human lives in coastal areas. The forecast of tropical cyclones has, therefore, always been a focus of numerical weather prediction (NWP). Tropical cyclones occur over the ocean and generally weaken and dissipate rapidly after making landfall; thus, observational data over the sea are important in their forecast. Satellite remote sensing is an important way to monitor and study the tropical cyclone due to the lack of conventional observational data over the oceans.

Infrared hyperspectral instruments onboard satellites commonly have one long-wave band mainly measuring atmospheric temperature and one or two middle-wave bands measuring atmospheric moisture. Unlike other infrared (IR) instruments, hyperspectral instruments have thousands of channels that allow atmospheric observation at a higher resolution in the vertical direction. Hyperspectral payloads have developed rapidly in recent years and include the atmospheric infrared sounder (AIRS), the Cross-track Infrared Sounder (CrIs), and the infrared atmospheric sounding interferometer (IASI) on polar-orbiting satellites. The data from these hyperspectral instruments have been widely used in data assimilation (Collard, 2001; Cameron et al., 2005; Le Marshall et al., 2006; McNally et al., 2006; Joiner et al., 2007; Collard and

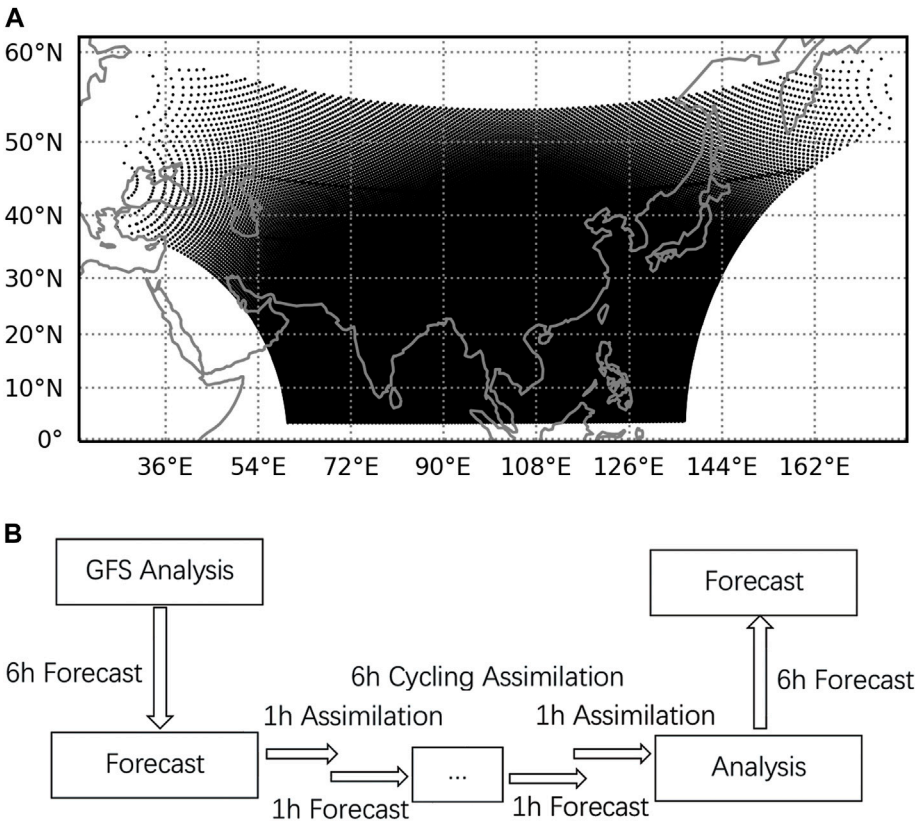

FIGURE 1
(A) Observation distribution of the GIIRS in 2 h. **(B)** Assimilation/forecast cycle. The assimilation/forecast cycles were performed every hour from August 22 to 27, 2022.

McNally, 2009; Hilton et al., 2009; Bormann et al., 2016). The hyperspectral radiance data are generally assimilated in the numerical weather prediction systems of major operational centers.

Many studies have shown that the assimilation of IR hyperspectral observations can improve the forecast of tropical cyclones. Reale et al. (2018) showed the positive effects of the AIRS on the forecast of tropical cyclones through an observational experiment, especially the method of cloud clearing, which can increase the score of the forecast after the assimilation of AIRS data. Li and Lui (2009) assimilated the temperature and humidity profiles retrieved from the AIRS, which greatly reduced the track and intensity forecast errors for Typhoon Ike. Liu and Li (2010) assimilated the temperature and humidity profiles retrieved from the AIRS and forecast the rapidly strengthening Typhoon Sinlaku, improving the vortex analysis and the track forecast. Xu et al. (2013) assessed the impact of assimilating IASI data on the analyses and forecasts of Hurricane Maria (2011) and Typhoon Megi (2010) with Weather Research and Forecasting Data Assimilation (WRFDA) and proved that IASI radiances with channels around 15-μm CO_2 band and 6.7-μm H_2O band had consistent positive impacts on the forecast skills for the track, minimum sea level pressure, and maximum wind speed.

Polar-orbiting satellites pass over a fixed location twice daily with poor temporal resolution while geostationary orbit (GEO) meteorological satellites perform a full disc scan in 1 or 2 hours, providing almost continuous measurements of the atmosphere. The observation from Polar-orbiting satellites compared with GEO meteorological satellites, lack information about the development of tropical cyclones compared with, which affects their application in numerical prediction forecasts. The FengYun-4A (FY-4A) generation of geostationary orbit meteorological satellites was launched by China in December 2016. The Geostationary Interferometric Infrared Sounder (GIIRS) onboard the FY-4A satellite was the first instrument to detect the vertical structure of the atmosphere by infrared interferometry spectroscopy in a geostationary orbit (Zhang et al., 2016; Yang et al., 2017). The satellite is fixed at 104.5° E and completes an observation of East Asia every 2 h. As a result of its extremely high spatiotemporal resolution, this satellite can observe the entire evolution of a tropical cyclone. Hyperspectral data from geostationary satellites are, therefore, expected to improve the forecast of tropical cyclones compared to polar-orbiting satellites. Yin et al. (2020) analyzed the quality of the clear-sky pixels of the GIIRS temperature channels using pixel cloud detection data from the Advanced Geostationary Radiation Imager (AGRI), showing the potential of the GIIRS in data assimilation applications. They also used the assimilation of a 30-min intensified observational dataset from the GIIRS to carry out a forecast experiment on Typhoon Maria, which proved the value of the high spatiotemporal resolution of infrared hyperspectral data in the forecast of tropical cyclones (Yin et al., 2021). Fengyun-4A GIIRS LWIR radiances have been operationally assimilated into the CMA-GFS system since 2019. Evaluations have indicated an overall neutral to positive impact

TABLE 1 Characteristics of the FY-4A GIIRS instrument.

Parameter	Specification
Spectral range	Longwave: 700–1130 cm^{-1}
	Medium wave: 1650–2250 cm^{-1}
Spectral resolution	0.625 cm^{-1}
Number of channels	Longwave: 689
	Medium wave: 961
Sensitivity	Longwave: 0.5–1.12 MW (m^2 sr cm^{-1})
	Medium wave: 0.1–0.14 MW (m^2 sr cm^{-1})
Spatial resolution	16 km (nadir)
Time resolution	<1 h (China)
	<30 min (mesoscale to small scale)
Area of detection	5000×5000 km^2 (China)
	1000×1000 km^2 (mesoscale to small scale)
Spectral calibration accuracy	10 ppm
Radiometric calibration accuracy	1.5 K

on the numerical forecasts (Han et al., 2019). Li et al. (2022a) expanded from measurements in clear sky to measurements from partially cloud-filled footprints with help from collocated imager measurements. With geostationary hyperspectral observations, more thermodynamic information in cloudy areas (also sensitive areas) is available for assimilation; thus, improvement in high-impact weather forecasts can be expected. The retrieval of moisture-tracked wind profiles from the GIIRS showed the potential of sounder sub-footprint cloud information available from the geostationary platform to provide better QC for application in weather nowcasting and forecasting (Li et al., 2022b). While the hyperspectral IR radiances provided added value for the numerical forecast, some challenges remain to be addressed. The large volume of data always poses difficulties in the timely processing, distribution, and extraction of information. Currently, the solutions are representative channel selection or PCs (Collard 2001; Antonelli et al., 2004; Collard 2007; Collard et al., 2010). A balance is needed between retaining major channel information and reducing the data volume. Different applications require different channel selections. The geostationary IR hyperspectral radiances also offer high temporal resolution information in 15 min or 30 min. Fast and slow-changing atmosphere information should be separated for better utilization of the time continuity. Thus, the retrieval method for some atmosphere parameters may differ, and the assimilation scheme may also need to change. The assimilation of IR hyperspectral radiances is limited to clear skies or above-cloud situations because of the uncertainty of the radiative transfer model (RTM) in modeling the hydrometers in clouds. The radiances of clear-sky channels (above-cloud) are assimilated in most of the NWP models as much as possible for remaining observations. The clear-sky channels can be identified by comparing the observed and simulated radiance spectra (McNally and Watts, 2003). The effectiveness of this method critically depends on the accuracy of the NWP models, and the results are easily affected by model biases.

WRFDA (Barker et al., 2012) is widely used to assimilate the radiances of remote sensing. This is the first attempt to use the three-dimensional variational (3DVAR) component (Barker et al., 2004) of WRFDA, which is technically more mature than other components, to assimilate GIIRS data. This study addresses some of the issues mentioned previously in the assimilating experiments to give some reference for subsequent studies. To avoid affecting the model bias, we modified the method described by McNally and Watts (2003) and used AGRI product assistance to identify the clear-sky channels for the GIIRS, as described as follows. A 1-h cycling assimilation scheme was designed for the GIIRS to better take advantage of the temporal continuity information. We also applied statistical analysis to determine the bias correction predictors for GIIRS. With assimilation and forecast experiments on Typhoon Bavi, we verified that IR hyperspectral radiances from geostationary satellites have added value in the assimilation/forecasts of tropical cyclones in the 2-h regional conventional observation mode.

The paper is organized as follows: Section 2 introduces the relevant data used in the data assimilation, including the assimilated observational data, the model initial field and boundary field data, and the profile set used in the channel selection. Section 3 presents the weather research and forecasting (WRF) model (Skamarock et al., 2019), WRFDA, and assimilation/forecast schemes. Section 4 introduces the preprocessing scheme of the observational data, including cloud detection, channel selection, and bias correction. Section 5 describes the experimental results for the analysis and forecast of Typhoon Bavi. Finally, Section 6 presents our discussion and conclusions.

2 Dataset and assimilation system

We used level 1 radiance data from the GIIRS onboard the FY-4A satellite for data assimilation. The GIIRS is an interferometric Fourier transform infrared hyperspectral payload that operates in an area-array detection mode with 128 detectors. It has 1600 channels with a spatial resolution of 16 km and a spectral resolution of 0.625 cm^{-1}. At present, the GIIRS can conduct regional observations every 2 h in the observation range (3°–55° N, 60°–137° E). The 2-h observations in the GIIRS are shown in Figure 1A. Table 1 gives the specific performance parameters of the GIIRS. The data assimilation forecast experiment used the regional model with initial field and boundary field data from the operational Global Forecast System of the National Centers for Environmental Prediction. The spatial resolution of the data was 0.25°, and the temporal resolution was 6 h.

The Diverse 52 profile dataset from the Numerical Weather Prediction Satellite Application Facility was augmented as the profile data in the channel selection. These data are produced by the forecast field statistics generated by the ensemble forecast system of the European Centre for Medium-Range Weather Forecasts (ECMWF). The data have 60 layers, including temperature, humidity, and ozone. This dataset is widely used in the evaluation of statistical regression and radiation transmission models.

The WRF4.2 model developed by the National Center for Atmospheric Research was used for the assimilation forecast experiment. This integrated system includes the WRF preprocessing system, the WRFDA system, the Advanced Research WRF numerical model system, and a post-processing system. The Advanced Research WRF model contains multiple physical process

TABLE 2 Channel information for cloud detection.

Channel number	Channel height (hPa)	Proportion of remaining observations (%)
32	300–50	90
13	400–500	70
51	600–700	45
71	700–800	25
38	800–850	20
594	1000	1

TABLE 3 Deviation predictors.

Predictor	Rank 1	Rank 2
Observed bright temperature	7	8
Background bright temperature	1	9
Satellite zenith angle	6	9
200–50 hPa temperature difference	2	7
850–300 hPa temperature difference	0	2
200–50 hPa thickness	5	10
850–300 hPa thickness	4	7
Total column water vapor	2	13
Temperature lapse rate convolved with weighting function	2	6
q convolved with q weighting function	5	13

packages that can simulate atmospheric motion at scales from tens of meters to thousands of kilometers. The WRFDA supports 3DVAR, 4DVAR, and mixed assimilation of 3DVAR and 4DVAR. It also integrates the assimilation interfaces of various conventional observational datasets, remote sensing data, and radar data. The WRF4.2 model is widely used in atmospheric research, including in numerical simulations, data assimilation, parameterization, and coupled models. We developed the assimilation interface of the GIIRS using the Radiative Transfer for TOVS (RTTOV) fast radiation transmission model to directly assimilate the radiation observations from the GIIRS. Through this interface, the WRFDA system can read the GIIRS level 1 data directly in the hierarchical data format, perform quality control and bias correction in the system, and carry out the assimilation analysis.

The GIIRS completes a regional scan every 2 h; therefore, we adopted an hourly cycle assimilation scheme (Figure 1B) to make full use of the high-resolution satellite data. The GIIRS data were grouped into 1-h intervals to input into the three-dimensional variational data assimilation system at every analysis point. A 6-h forecast was produced from the initial Global Forecast System data, followed by a 6-h assimilation/forecast cycle. In every 6-h assimilation/forecast cycle, the observations were assimilated using the previous 1-h model forecast as a background to produce a new estimate of the three-dimensional atmospheric fields. The new 1-h model forecast was produced from the analysis obtained from the previous assimilation. After a 6-h assimilation/forecast cycle, a 6-h forecast was carried out to analyze the tropical cyclone. This cycling assimilation process was repeated every hour to give an hourly analysis of the tropical cyclone. We respectively performed a control experiment assimilating only conventional observations and an assimilation experiment assimilating conventional observations and GIIRS radiances.

3 Cloud detection, channel selection, and bias correction

Based on the characteristics of the infrared hyperspectral data from the FY-4A satellite, we preprocessed the observational data using cloud detection, channel selection, bias correction, and quality control. In contrast with the pixel cloud detection commonly used in infrared remote sensing data, we adopted channel cloud detection, in which radiance observations with high weighting functions remained even if the pixel was covered by cloud. We used the Shannon information entropy method to select a channel subset without damaging the amount of observational information. The redundant channels were eliminated, reducing the computational burden. As differences in instrument performance lead to different sensitivities of the loads to the predictors in bias correction, we performed a predictor sensitivity analysis to obtain the appropriate predictors for bias correction of the air mass.

3.1 Cloud detection

The GIIRS has thousands of channels and provides finer-resolution information in the vertical direction. Radiance observations that are contaminated by clouds can be identified by comparing the cloud-top height and the channel height, as proposed by McNally and Watts (2003) and developed by Clarisse et al. (2010), Eresmaa (2014), Eresmaa (2017), Letertre-Danczak (2016), and Eresmaa et al. (2020). This method is currently used in operational numerical prediction by the ECMWF and the UK Met Office. This method uses numerical forecast data to compare the observed and simulated radiance spectra and identify the channels contaminated by clouds. Its performance largely depends on the quality of the numerical model. We used the AGRI cloud-top product to avoid the impact of the bias of the numerical model in the spectral comparison. The AGRI cloud-top height product is a real-time product of the National Satellite Meteorological Center of China. The identification accuracy of the cloud-top height has been verified to

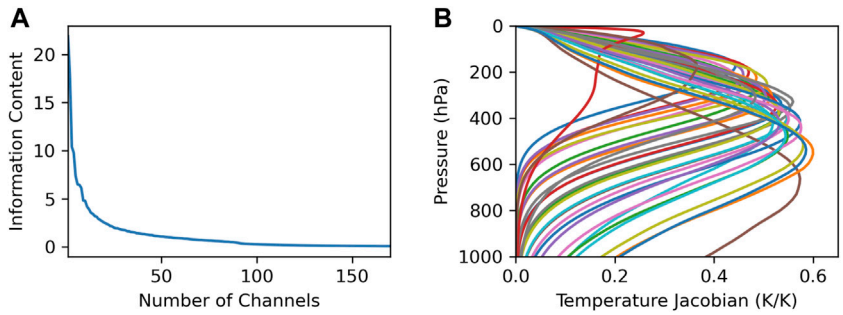

FIGURE 2
(A) Channel information content and **(B)** Jacobian matrix for the temperature in the selected channels.

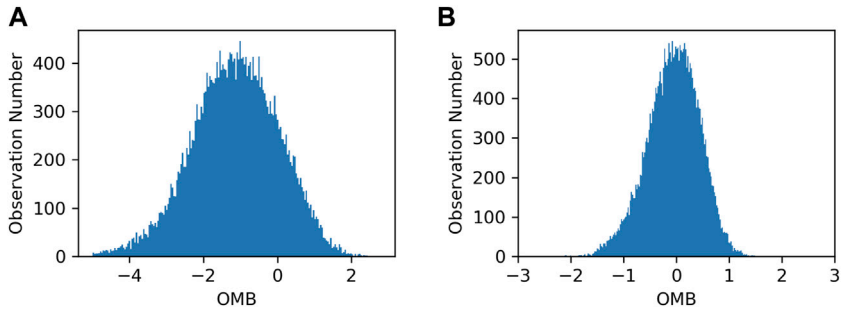

FIGURE 3
Radiance observation bias statistics **(A)** before and **(B)** after bias correction. OMB (unit: K), observation minus background.

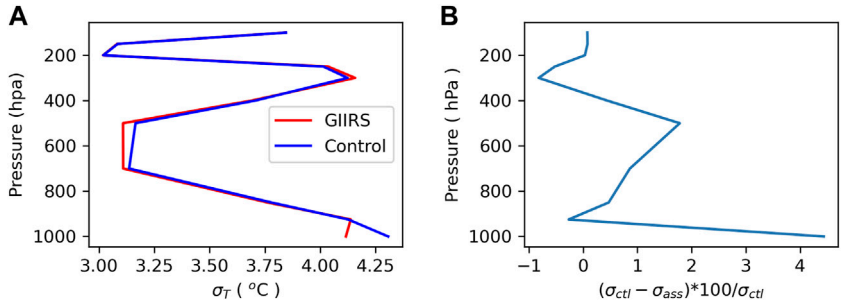

FIGURE 4
RMSE in the assimilation process from August 22 to 27 for **(A)** temperature and **(B)** percentage reduction in the RMSE for temperature. σ_T (unit: °C) is the RMSE for temperature, σ_{ctl} (unit: °C) is the RMSE for the control experiment, and σ_{ass} (unit: °C) is the RMSE for the GIIRS assimilation experiment.

be about 50 km (Wang et al., 2022), which satisfied our need for channel cloud detection. The AGRI cloud-top height product has been matched to the GIIRS pixels as the operational product distributed to the public. The peak height of the channel-weighting function is variable because of the influence of water vapor in the atmosphere. To accurately determine the channels contaminated by clouds, we calculated the real-time channel height of the assimilated GIIRS data from the temperature and humidity profiles output by the numerical model. The overcast radiance was calculated when black clouds were simulated at all levels of each profile. Black clouds are clouds that are assumed to be completely opaque to satellites above the cloud layer. The channel height is determined by the following equation:

$$|R_{clr} - R_{cld}(i)|/R_{clr} = C$$

In which the radiance for the channel is assumed to be an opaque, black cloud at level *i*. The left-hand side of the equation is calculated layer-by-layer. When the calculated value of C ≤ 0.01,

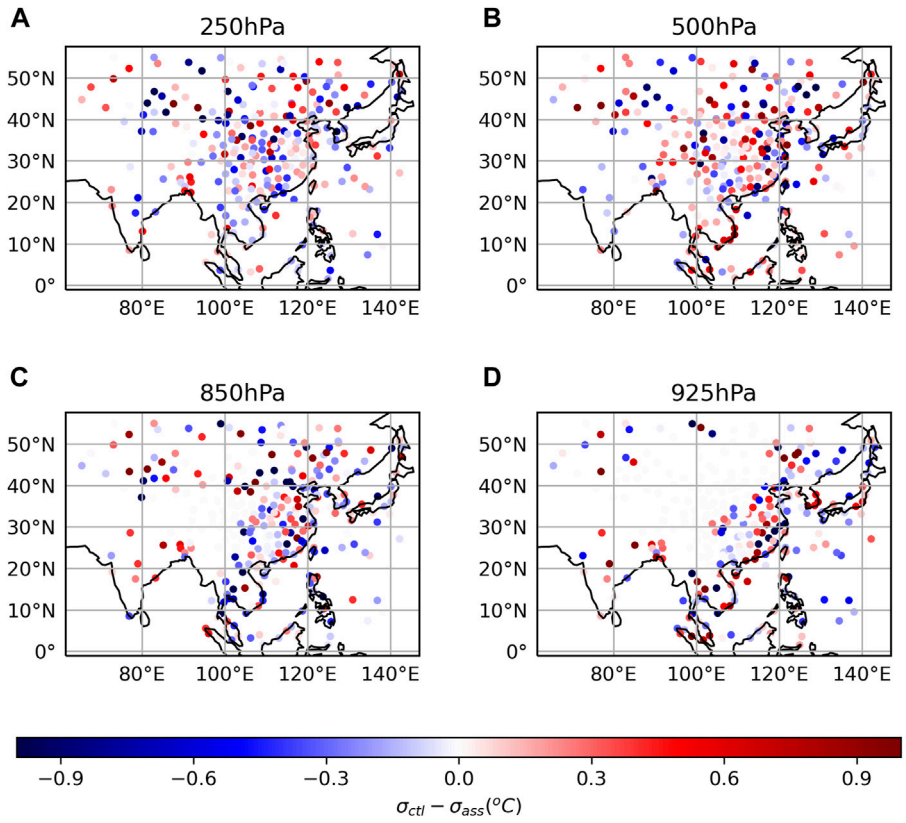

FIGURE 5
RMSE temperature difference respectively at **(A)** 250hPa **(B)** 500hPa **(C)** 850hPa **(D)** 925hPa from 22th to 27th of August between the control and assimilation experiments at the radiosonde stations. Positive values show that the assimilation is better than the control experiment.

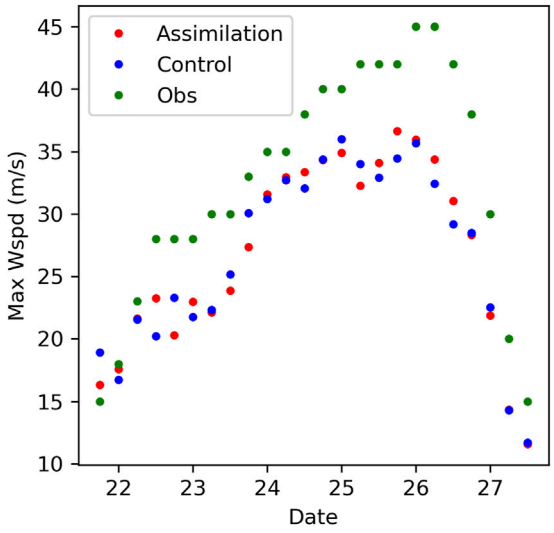

FIGURE 6
Forecast intensity of Typhoon Bavi showing statistics every 6 h from August 22 to 27.

the height of this layer is the channel height. We used RTTOV13 for radiance transfer simulation. The Fifth Generation ECMWF reanalysis (ERA5) dataset was used for the radiance simulation. The channels with heights higher than the cloud-top heights were identified as clear-sky channels and retained. Six channels with different heights were selected to check the effects of cloud detection. Table 2 shows the channel heights of these six channels and the proportions of observations remaining after cloud detection in the original data. Most observations in the level closest to the Earth's surface were contaminated by clouds, and only about 1% of the observations remained. In contrast, the reserved observations reached 90% in the upper troposphere channels, and about 50% of the observations in the mid-troposphere were retained. In general, the number of observations was higher than those with pixel cloud detection.

3.2 Channel selection

We augmented the fast radiation transfer model RTTOV13 based on the Diverse 52 profile set to calculate the sensitivity of the atmosphere variables in the full spectrum. The profile temperature, surface temperature, ozone, and humidity were perturbed separately (the profile temperature and surface temperature were perturbed by 1°C, and the ozone and humidity were perturbed by 10%). The difference between the radiation before and after perturbation was defined as the sensitivity for that quantity. The channels sensitive to surface temperature, ozone,

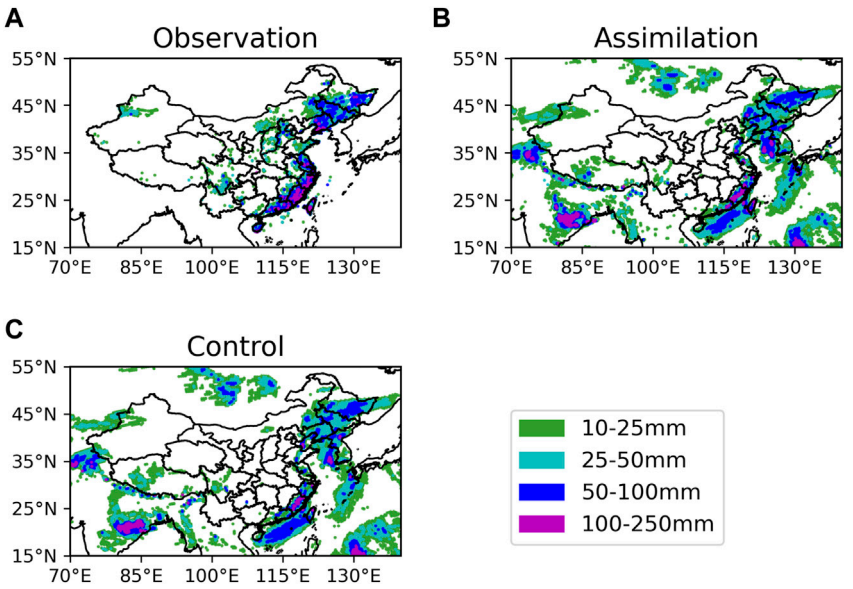

FIGURE 7
Distribution of accumulated precipitation during Typhoon Bavi from August 22 to 27. **(A)** Observations from *in situ* data. **(B)** Precipitation with GIIRS assimilation. **(C)** Precipitation control experiment without GIIRS assimilation.

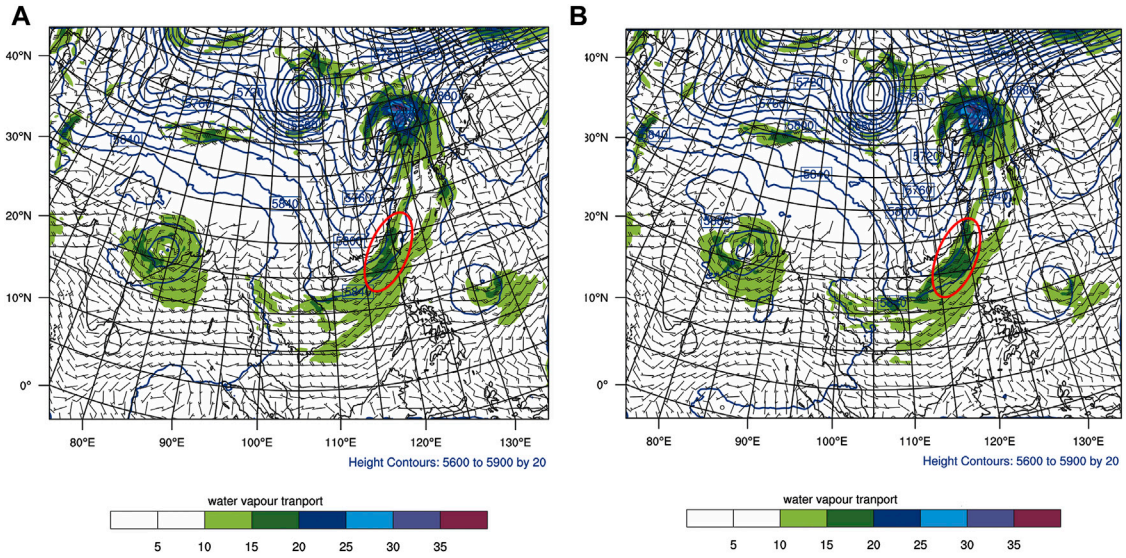

FIGURE 8
Water vapor transfer (Units: kg·(hPa)$^{-1}$m^{-1}s^{-1})) for Typhoon Bavi at 06:00 on August 26, 2020, in **(A)** the control experiment and **(B)** the assimilation experiment of the GIIRS.

and humidity were then removed from the temperature-sensitive channels so that only the temperature-sensitive channels remained. These temperature-sensitive channels of the GIIRS were mainly in two spectral bands: the carbon dioxide absorption band at 670 cm^{-1} and the water vapor absorption band at 625 cm^{-1}. After the other channels had been removed, 170 temperature-sensitive channels were used in the subsequent information entropy calculation (Collard A. 2007). The information content of each channel was calculated based on this temperature subset. The calculation formulas of the information content H were as follows:

$$H = \frac{1}{2}\ln\left|\frac{A}{B}\right|, \quad (1)$$

$$A = \left(B^{-1} + K^{T}R^{-1}K\right)^{-1}, \quad (2)$$

where K is the Jacobian for temperature. The channel information content is sorted from high to low and 30 channels with high information content are selected (Figure 2A). The rest of redundant

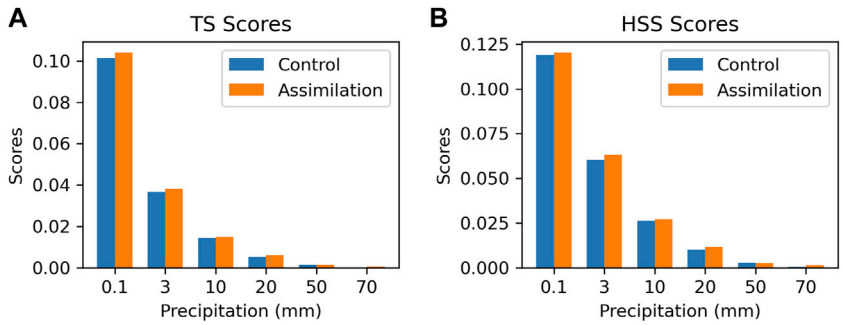

FIGURE 9
(A) TS forecast scores and **(B)** HSS forecast scores of precipitation during Typhoon Bavi from August 22 to 27.

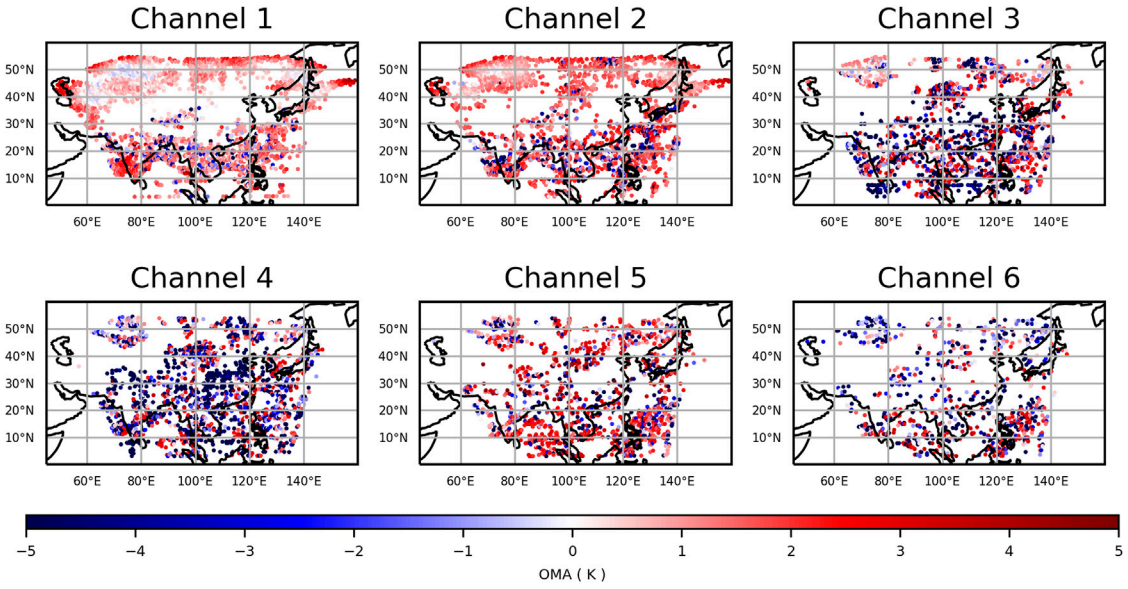

FIGURE 10
OMA (unit: °C) of brightness temperature for six channels.

channels are removed. The information content of selected channels is about 90% of the total temperature channels.

3.3 Bias correction and quality control

The radiance observed by the satellite remote sensing instrument was biased due to errors associated with the radiative transfer model and the instrument calibration. The bias was modeled in terms of atmospheric parameters referred to as bias predictors. The bias can be forecast and corrected using the bias predictors. We selected 10 predictors commonly used by other instruments and calculated the correlation coefficients between the observation minus the background of each channel and the predictors. The predictors were ranked in two levels based on the correlation coefficients. The first rank contained the channels with correlation coefficients >0.6, while the second rank contained the channels with correlation coefficients between 0.4 and 0.6. Table 3 shows the channel numbers of each predictor in the first and second ranks. Predictors with more than five channels in rank 1 or more than 10 channels in two ranks were selected. Finally, the predictors observed that brightness temperature, satellite zenith angle, 200–500 hPa air column thickness, 300–850 hPa air column thickness, total column water vapor, and the humidity convolved with the weight function had higher correlation coefficients. Therefore, these six quantities were selected to correct the bias. The bias correction formula was as follows:

$$R = \sum_{i=1}^{6}\sum_{j=1}^{6} A_i A_j T + \sum_{i=1}^{6} A_i T + B$$

where B was the bias correction factor of the constant term, A_i and A_j were the bias correction coefficients, i and j were the serial numbers of the bias correction factor, and T was the observation minus the background of the observed brightness temperature. R

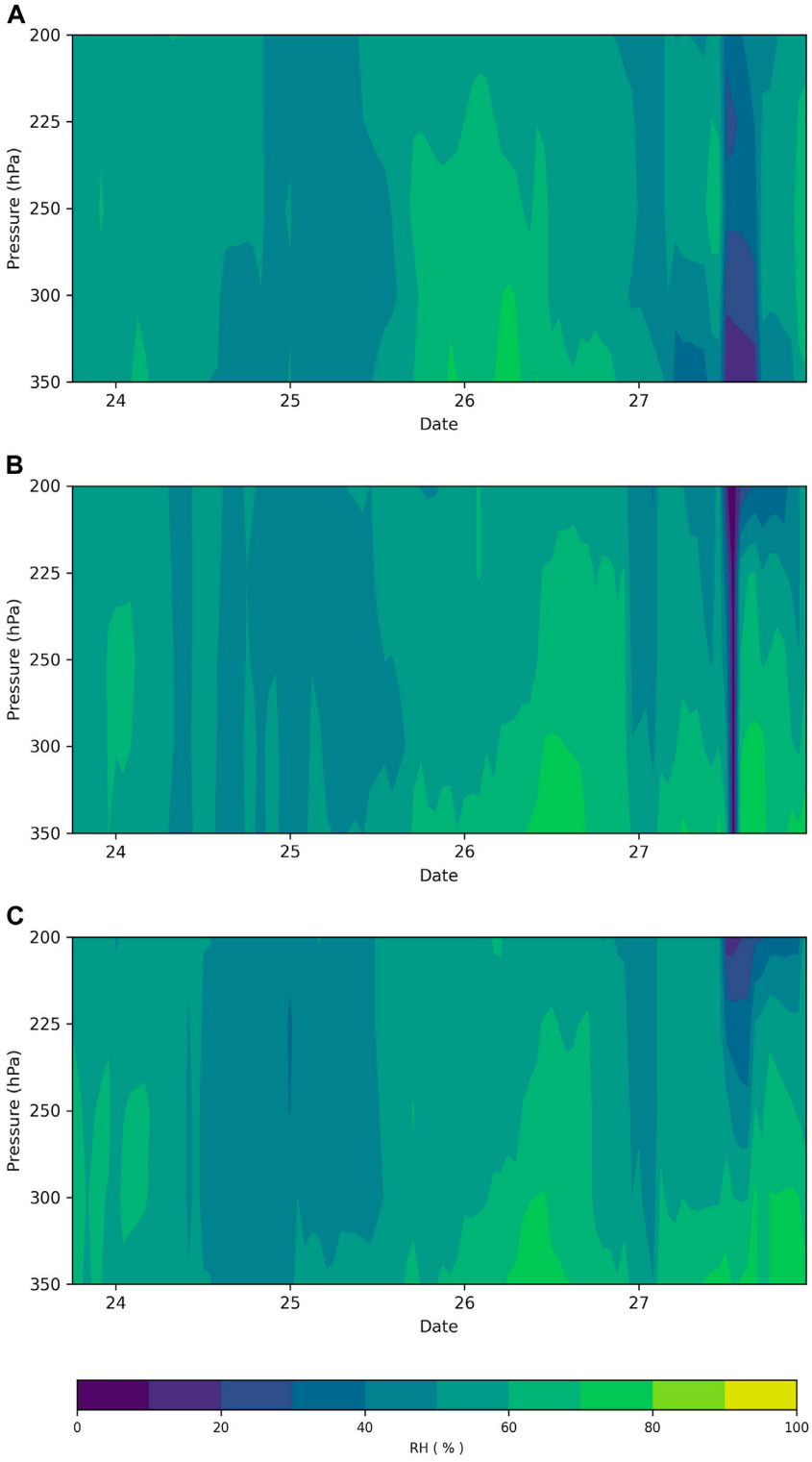

FIGURE 11
Relative humidity variation of **(A)** ERA5, **(B)** assimilation, and **(C)** CTL during Typhoon Bavi.

was the corrected observed brightness temperature. The average bias before the correction was about 2.5, which decreased to <0.1 after the correction. The observation minus the background of the brightness temperature after the correction showed a normal distribution (Figure 3).

4 Results

To evaluate the impact of the FY4-GIIRS data assimilation on the forecast of tropical cyclones, we carried out a forecasting experiment for Typhoon Bavi (August 2020) from 00:00 of August 22 to 23:00 of

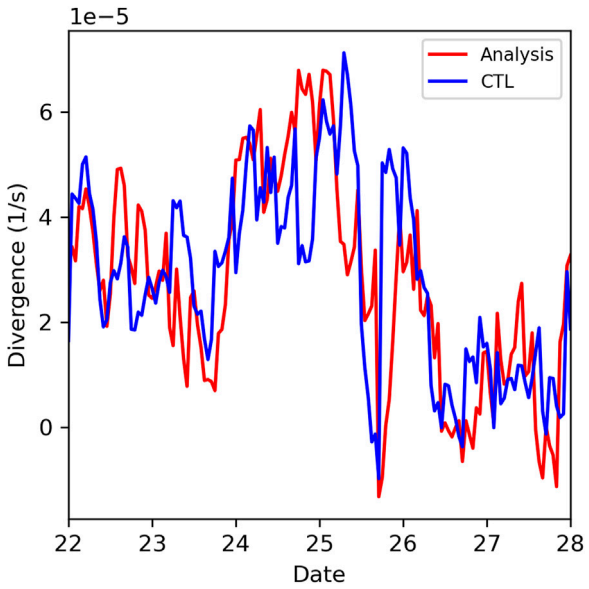

FIGURE 12
Divergence averaged around 250 km from the typhoon center.

August 28. After 6 h of cycling assimilation, 6 h forecasts were performed in this period. This assimilation/forecast cycle was performed hourly to obtain an analysis and forecast. We evaluated the forecast for Bavi against observational data to evaluate the success of the assimilation. We also analyzed the observation impact and tried to determine the reasons for the improved forecast. Typhoon Bavi was the eighth typhoon in 2020. It formed over the ocean east of Taiwan on August 22, 2020, and made landfall at 08:30 on August 27 in North Phyongan Province, North Korea. It entered northeast China at 11: 00 and then weakened rapidly. It was no longer classed as a typhoon at 20:00 on August 27. This typical northward-moving typhoon lasted for 41 h and had a maximum wind force of level 14.

4.1 Forecast evaluation

We expected that assimilation would improve the temperature field. In contrast with the reanalysis dataset, which is biased because of the numerical model, radiosonde observations are of high quality. There are >200 radiosonde stations in China, most of which are in southeast China near areas frequently affected by typhoons. We used the temperature profiles of radiosondes to validate the 6-h forecast (Figure 4). The temperature field at 800–500 hPa was improved. The root-mean-square error (RMSE) of the temperature after assimilation was about 2% less than that before assimilation, with a maximum improvement (about 4%) at 800 hPa. The peak of the GIIRS channels in the upper troposphere had little chance of being contaminated by clouds; therefore, the temperature above 800 hPa showed a greater improvement than the temperatures in the other layers. The improvement of the RMSE of the temperature in the west and north of China was greater above 500 hPa, whereas the improvement from the ground to the lower troposphere was greater in southeast China (Figure 5). In some areas, the RMSE was larger after the GIIRS assimilation than before. This error may arise from uncertainties in the emissivity of the land or regional differences in the quality of GIIRS data. Further investigations are required. The track and intensity are important indexes for forecasting tropical cyclones. The models with or without GIIRS assimilation can both predict the tropical cyclone track well, with errors <50 km. In the control experiment before assimilation, the RMSE of the prediction of the tropical cyclone intensity was 6.88 m s^{-1}, whereas that after assimilation was 6.58 m s^{-1}, a reduction of 0.3 m s^{-1} (Figure 6). Typhoon Bavi brought strong rainfall, with average rainfall in northeast China of 35 mm. Figure 7 shows the distributions of the accumulated precipitation in the observations and the assimilation and control experiments during the typhoon. The rain belt was mainly located in northeast China and the southeastern coastal areas of China (Jiangsu and Zhejiang provinces). The rainfall forecasts after assimilation were better than those in the control experiment in both areas, particularly in the southeastern coastal area. The cold, weak airflow from the north met the warm, wet airflow of the monsoon tailed with Typhoon Bavi at the sea surface; the updraft in this area resulted in strong precipitation. The assimilation of the GIIRS improved the transfer of water vapor, improving the precipitation forecast (Figure 8). Therefore, we concluded that, for this infrared instrument, the improvement in the forecast was not dependent on correcting the typhoon circulation directly, but rather on correcting the outer circulation of the typhoon. An analysis of the threat and Heidke skill scores of precipitation showed that the precipitation scores were much higher than in the control experiment (Figure 9).

4.2 Observational impact on the analysis

The present study focused on the assimilation of temperature channels in the long waveband. As shown in the weighting function of channels (Figure 2B), the information we expect to obtain from the observations will mainly come from 500 hPa to 200 hPa of the atmosphere. We expect that the most significant effects will occur in the middle and upper troposphere layers. We first examined the OMA (observation minus background) of the brightness temperature. The analysis selected six channels with a weighting function peak at approximately 200 hPa (Ch1 and Ch2), 300 hPa (Ch3 and Ch4), and 500 hPa (Ch5 and Ch6) (Figure 10). The OMA in the high-level channels of Ch1 and Ch2 had similar patterns and were positive in most areas. The OMA in the lower-level channels of Ch3–Ch6 showed no obvious bias and were larger than those in the high-level channels. The high-level channels will not deteriorate due to poor emissivity or clouds and have high quality. As expected, the OMA showed the most improvement for the upper layer temperature in the GIIRS assimilation. Therefore, the optimization of the air temperature of the upper layers provided better forecasts of temperature profiles compared to the CTL experiment shown in Figure 4.

The intensity and precipitation of Bavi also improved according to the forecast verification. Water vapor in the middle and upper layers of the troposphere is vital for typhoon intensification (Kaplan et al., 2003). With water vapor transport near the typhoon, convection develops and latent heat is released near the center of the typhoon, leading to rapid intensification. We examined the variations in relative humidity in the upper layers. From the average relative humidity around 400 km from the typhoon center, we calculated an index

representing the relative humidity variation (Figure 11). We observed a significant increase in relative humidity at 12:00 on August 25, after which Bavi strengthened and reached its maximum wind speed at 6: 00 on August 26. During this time, the relative humidity modeled in ERA5 was near-saturation, with a value >70% from 300 hPa to 200 hPa (Figure 11A). The relative humidity of the analysis near the center of the typhoon was larger than that in the CTL, which explained the larger typhoon intensity forecast compared to that in the CTL.

TC upper-level outflow can interact with the upper-level larger-scale environment and the inner core of a TC, thereby playing a mediating role between the environment and the storm core. A stronger outflow implies a stronger typhoon. The strongest TC outflow is, on average, concentrated at the troposphere upper layer and around 500 km from the TC center (W. A. Komaromi et al., 2017). The present study defined the TC outflow as the area-averaged divergence over the $8^{\circ} \times 8^{\circ}$ latitude-longitude box around the TC center, at 150 hPa. Two TC outflow peaks were observed. The first occurred at the beginning of the typhoon, and the second was observed from August 24 to 26. Compared to the CTL, the TC outflow in the analysis was much stronger at most time points (Figure 12). Particularly at the beginning of TC formation and the day before TC intensity peaked, the TC outflow in the analysis was larger than that in the CTL.

5 Discussion and conclusions

Typhoons are high-impact weather systems that can lead to disasters; therefore, they require highly accurate forecasts. Satellite remote sensing data are important in the numerical weather prediction of typhoons due to the lack of conventional observational data at sea. Infrared hyperspectral data from geostationary satellites with a high spatiotemporal resolution have great value in regional numerical weather forecasts. The GIIRS on the FY-4 satellite is the world's only hyperspectral instrument onboard a geostationary satellite. We carried out an assimilation/forecast experiment for Typhoon Bavi using the WRF model and WRFDA. To make full use of the high-resolution time data from geostationary satellites, we designed a rapidly updating assimilation scheme with hourly cycle assimilation and evaluated the GIIRS for 6-h weather forecasts of typhoons. We selected 30 channels with high information content based on Shannon information entropy for assimilation and removed the redundant channels. To make full use of the observational information, we used the cloud-top height product of the National Satellite Meteorological Center to remove channels contaminated by clouds through the channel height calculated in real-time and reserved the clear-sky channel for assimilation. We selected the six predictors with the largest correlation coefficients through hierarchical sensitivity analysis of the bias predictors. We then effectively corrected the GIIRS bias after verification.

We carried out a 6-day assimilation forecast experiment from the formation of Typhoon Bavi from August 22 until its dissipation. We evaluated the experimental results using the radiosonde and ground station precipitation data for China. The evaluation results showed that the assimilation of the temperature channel of the GIIRS improved the temperature. The RMSE of the temperature from the ground to the upper troposphere was reduced by 2% compared to the control experiment. The maximum improvement was in the mid- and upper troposphere from 800 to 500 hPa. The track prediction of the typhoon was consistent with that of the control experiment, with an RMSE of 50 km. The prediction of the intensity of the typhoon was slightly improved.

The GIIRS provides many more water vapor channels. During typhoon formation, intensification, and decay, we believe that water vapor plays a vital role. Therefore, in the future we should use more GIIRS channels in the assimilation to make full use of the data. In this study, we used the more mature 3DVAR assimilation method. The GIIRS loaded in the FY4A geostationary satellite has an even higher time resolution and 4DVAR is more appropriate. Although we showed the benefit of the GIIRS assimilation in typhoon Bavi, more typhoon cases are needed to verify our data.

The analysis of the precipitation forecast showed that infrared hyperspectral radiation was unable to penetrate the deep clouds of the typhoon, so it was difficult to directly improve the atmospheric environmental field in the center of the typhoon. However, the improvement in the mid- and high-level temperature fields around the typhoon changed the environmental circulation, enhanced the transport of water vapor in the troposphere, and significantly improved the precipitation forecast around the typhoon. Therefore, we believe that the assimilation of the temperature channel of the infrared hyperspectral data from the GIIRS can improve the 6-h forecast of typhoons, which is of great value for their analysis and prediction. Based on the real-time preprocessing and assimilation capability of the WRFDA real-time assimilation system established here, we will perform more assimilation prediction experiments to further verify the value of the GIIRS in numerical weather prediction.

Data availability statement

The original contributions presented in the study are included in the article/Supplementary materials, Further inquiries can be directed to the corresponding author.

Author contributions

XX: methodology, writing—original draft, and review and editing; QL: conceptualization, and review and editing; XL: data curation; WS: visualization.

Funding

This study was supported by the Chinese Nature Science Foundation (42130605) and Chinese Nature Science Foundation (42175016).

Conflict of interest

The authors declare that the research was conducted in the absence of any commercial or financial relationships that could be construed as a potential conflict of interest.

Publisher's note

References

Antonelli, P., Revercomb, H. E., Sromovsky, L. A., Smith, W. L., Knuteson, R. O., Tobin, D. C., et al. (2004). A principal component noise filter for high spectral resolution infrared measurements. *J. Geophys. Res.* 109, D23102–D23124. doi:10.1029/2004JD004862

Barker, D., Huang, X.-Y., Liu, Z., Auligné, T., Zhang, X., Rugg, S., et al. (2012). The weather research and forecasting model's community variational/ensemble data assimilation system: Wrfda. *Bull. Amer. Meteor. Soc.* 93, 831–843. doi:10.1175/bams-d-11-00167.1

Barker, D. M., Huang, W., Guo, Y. R., and Xiao, Q. N. (2004). A three-dimensional (3DVAR) data assimilation system for use with MM5: Implementation and initial results. *Mon. Wea. Rev.* 132, 897–914. doi:10.1175/1520-0493(2004)132<0897:ATVDAS>2.0.CO;2

Bormann, N., Bonavita, M., Dragani, R., Eresmaa, R., Matricardi, M., and McNally, A. (2016). Enhancing the impact of IASI observations through an updated observation-error covariance matrix. *Quart. J. Roy. Meteor. Soc.* 142, 1767–1780. doi:10.1002/qj.2774

Cameron, J., Collard, A., and English, S. (2005). "Operational use of AIRS observations at the Met. Office,"Proceedings of the Fourteenth International TOVS Study Conference, Beijing, China, 25–31.

Clarisse, L., Prata, F., Lacour, J.-L., Hurtmans, D., Clerbaux, C., and Coheur, P.-F. (2010). A correlation method for volcanic ash detection using hyperspectral infrared measurements. *Geophys. Res. Lett.* 37, 332. doi:10.1029/2010gl044828

Collard, A. (2007). Selection of IASI channels for use in numerical weather prediction. *Q. J. R. Meteorol. Soc.* 133, 1977–1991. doi:10.1002/qj.178

Collard, A. D. (2001). "Assimilation of IASI and AIRS data: Information content and quality control," in Proceedings of the ECMWF Seminar on Exploitation of the New Generation, New York, NY, USA.

Collard, A. D., McNally, A. P., Hilton, F. I., Healy, S. B., and Atkinson, N. C. (2010). The use of principal component analysis for the assimilation of high-resolution infrared sounder observations for numerical weather prediction. *Q. J. R. Meteorol. Soc.* 136, 2038–2050. doi:10.1002/qj.701

Collard, A., and McNally, A. P. (2009). The assimilation of infrared atmospheric sounding interferometer radiances at ECMWF. *Q. J. R. Meteorol. Soc.* 135, 1044–1058. doi:10.1002/qj.410

Eresmaa, R. (2014). Imager-assisted cloud detection for assimilation of infrared atmospheric sounding interferometer radiances. *Q. J. R. Meteorol. Soc.* 140, 2342–2352. doi:10.1002/qj.2304

Eresmaa, R., Letertre-Danczak, J., Lupu, C., Bormann, N., and McNally, A. P. (2017). The assimilation of cross-track infrared sounder radiances at ECMWF. *Q. J. R. Meteorol. Soc.* 143, 3177–3188. doi:10.1002/qj.3171

Eresmaa, R., Letertre-Danczak, J., and McNally, A. P. (2020). "Screening routines for aerosol and trace-gas-affected infrared radiances,"Proceedings of the 22nd International TOVS Study Conference, Saint-Sauveur, Canada.

Han, W., Yin, R., Di, D., Li, J., Wang, J., Shen, X., et al. (2019). "Assimilation of high temporal resolution giirs in global 4D-var,"Proceedings of the 2019 Joint Satellite Conference, Boston, USA.

Hilton, F., Atkinson, N. C., English, S. J., and Eyre, J. R. (2009). Assimilation of IASI at the Met Office and assessment of its impact through observing system experiments. *Quart. J. Roy. Meteor. Soc.* 135, 495–505. doi:10.1002/qj.379

Joiner, J., Brin, E., Treadon, R., Derber, J., Van Delst, P., Da Silva, A., et al. (2007). Effects of data selection and error specification on the assimilation of AIRS data. *Q. J. R. Meteorol. Soc.* 133, 181–196. doi:10.1002/qj.8

Kaplan, J., and DeMaria, M. (2003). Large-scale characteristics of rapidly intensifying tropical cyclones in the North Atlantic basin. *Weather Forecast.* 18 (6), 1093–1108. doi:10.1175/1520-0434(2003)018<1093:lcorit>2.0.co;2

Komaromi, W. A., and Doyle, J. D. (2017). Tropical cyclone outflow and warm core structure as revealed by HS3 dropsonde data. *Mon. Weather Rev.* 4, 1339–1359. doi:10.1175/mwr-d-16-0172.1

Letertre-Danczak, J. (2016). The use of geostationary radiance observations at ECMWF and aerosol detection for hyper-spectral infrared sounders: 1st and 2nd years report. *EUMETSAT/ECMWF Fellowsh. Programme Res. Rep.*, 40, 18.

Li, J., Geer, A. J., Okamoto, K., Otkin, J. A., Liu, Z., Han, W., et al. (2022a). Satellite all-sky infrared radiance assimilation: Recent progress and future perspectives. *Adv. Atmos. Sci.* 39, 1–13.

Li, J., and Liu, H. (2009). Improved hurricane track and intensity forecast using single field-of-view advanced IR sounding measurements. *Geophys. Res. Lett.* 36, L11813. doi:10.1029/2009gl038285

Li, J., Zhang, Y., Di, D., Ma, Z., Li, Z., Schmit, T. J., et al. (2022b). The influence of sub-footprint cloudiness on three-dimensional horizontal wind from geostationary hyperspectral infrared sounder observations. *Geophys. Res. Lett.* 49, e2022GL098460. doi:10.1029/2022gl098460

Liu, H., and Li, J. (2010). An improvement in forecasting rapid intensification of typhoon Sinlaku (2008) using clear-sky full spatial resolution advanced IR soundings. *J. Appl. Meteorol. Clim.* 49, 821–827. doi:10.1175/2009jamc2374.1

Marshall, L., and Coauthors, J. (2006). Improving global analysis and forecasting with AIRS. *Bull. Amer. Meteor. Soc.* 87 (7), 891–895. doi:10.1175/BAMS-87-7-891

McNally, A. P., and Watts, P. D. (2003). A cloud detection algorithm for high-spectral-resolution infrared sounders. *Q. J. R. Meteorol. Soc.* 129, 3411–3423. doi:10.1256/qj.02.208

McNally, A. P., Watts, P., Smith, J., Engelen, R., Kelly, G., Thepaut, J. N., et al. (2006). The assimilation of AIRS radiance data at ECMWF. *Q. J. R. Meteorol. Soc.* 132, 935–957. doi:10.1256/qj.04.171

Reale, O., McGrath-Spangler, E. L., McCarty, W., Holdaway, D., and Gelaro, R. (2018). Impact of adaptively thinned AIRS cloud-cleared radiances on tropical cyclone representation in a global data assimilation and forecast system. *Weather Forecast* 33 (4), 909–931. doi:10.1175/waf-d-17-0175.1

Skamarock, W. C., Klemp, J. B., Dudhia, J., Gill, D. O., Liu, Z., Berner, J., et al. (2019). A description of the advanced research WRF version 4. NCAR Tech.Rep. *Natl. Cent. Atmos. Res. Boulder Co Mesoscale Microscale* 4. doi:10.5065/1dfh-6p97

Wang, F., Min, M., Xu, N., Liu, C., Wang, Z., and Zhu, L. (2022). Effects of linear calibration errors at low-temperature end of thermal infrared band: Lesson from failures in cloud top property retrieval of FengYun-4A geostationary satellite. *IEEE Trans. Geosci. Remote Sens.* 2022 (60), 1–11. doi:10.1109/tgrs.2022.3140348

Xu, D., Liu, Z., Huang, X. Y., Min, J., and Wang, H. (2013). Impact of assimilating IASI radiance observations on forecasts of two tropical cyclones. *Meteorol. Atmos. Phys.* 122, 1–18. doi:10.1007/s00703-013-0276-2

Yang, J., Zhang, Z. Q., Wei, C. Y., Lu, F., and Guo, Q. (2017). Introducing the new generation of Chinese geostationary weather satellites, Fengyun-4. *Bull. Am. Meteorol. Soc.* 98, 1637–1658. doi:10.1175/bams-d-16-0065.1

Yin, R., Han, W., Gao, Z., and Di, D. (2020). The evaluation of FY4A's Geostationary Interferometric Infrared Sounder (GIIRS) longwave temperature sounding channels using the GRAPES global 4D-Var. *Q. J. R. Meteorol. Soc.* 146, 1459–1476. doi:10.1002/qj.3746

Yin, R., Han, W., Gao, Z., and Li, J. (2021). Impact of high temporal resolution FY-4A Geostationary Interferometric Infrared Sounder (GIIRS) radiance measurements on typhoon forecasts: Maria (2018) case with GRAPES Global 4D-Var assimilation system. *Geophys. Res. Lett.* 48, e2021GL093672. doi:10.1029/2021gl093672

Zhang, P., Guo, Q., and Chen, B. Y. (2016). The Chinese next-generation geostationary meteorological satellite FY-4 compared with the Japanese Himawari-8/9 satellites. *J. Adv. Meteorol. Sci. Technol.* 6, 72–75. [in Chinese].

frontiers | Frontiers in Earth Science

TYPE Original Research
PUBLISHED 28 February 2023
DOI 10.3389/feart.2023.1101809

OPEN ACCESS

EDITED BY
Chunlei Liu,
Guangdong Ocean University, China

REVIEWED BY
Lingjing Zhu,
Guangdong Ocean University, China
Chunsong Lu,
Nanjing University of Information Science and Technology, China
Wei-Bo Chen,
National Science and Technology Center for Disaster Reduction (NCDR), Taiwan

*CORRESPONDENCE
Liwen Wang,
wanglw@gd121.cn
Banglin Zhang,
zhangbl@gd121.cn

SPECIALTY SECTION
This article was submitted to Interdisciplinary Climate Studies, a section of the journal Frontiers in Earth Science

RECEIVED 18 November 2022
ACCEPTED 17 February 2023
PUBLISHED 28 February 2023

CITATION
Chen Y, Wang L, Leung JC-H, Xu D, Chen J and Zhang B (2023), Systematic diurnal bias of the CMA-MESO model in southern China: Characteristics and correction.
Front. Earth Sci. 11:1101809.
doi: 10.3389/feart.2023.1101809

Systematic diurnal bias of the CMA-MESO model in southern China: Characteristics and correction

Yuxiao Chen[1], Liwen Wang[2]*, Jeremy Cheuk-Hin Leung[2], Daosheng Xu[2], Jing Chen[3] and Banglin Zhang[1,2,4]*

[1]College of Atmospheric Sciences, Lanzhou University, Lanzhou, China, [2]Guangzhou Institute of Tropical and Marine Meteorology/Guangdong Provincial Key Laboratory of Regional Numerical Weather Prediction, China Meteorological Administration (CMA), Guangzhou, China, [3]CMA Earth System Modeling and Prediction Centre, CMA, Beijing, China, [4]Southern Marine Science and Engineering Guangdong Laboratory, Zhuhai, China

Model error is an important source of numerical weather prediction (NWP) errors. Among model errors, the systematic diurnal bias plays an important role in high-resolution numerical weather prediction models. The main purpose of this study is to explore the characteristics of the systematic diurnal bias of a high-resolution NWP model in southern China and reduce the diurnal bias to improve the forecast results, hence providing a better background field for data assimilation. Based on the China Meteorological Administration Meso-scale (CMA-MESO) high-resolution NWP model, a 15-day sequential numerical weather prediction experiment was performed in southern China, and the forecast results were analyzed. A sequential bias correction scheme (SBCS) based on analysis increments was designed to reduce the systematic diurnal bias of the CMA-MESO model, and 15-day sequential comparative experiments were carried out. The analysis results showed that the CMA-MESO model has apparent systematic diurnal biases, and the characteristics differ among variables. A large diurnal bias was mainly found in the lower model layers, and it was concentrated in areas with a complex underlying surface for the horizontal distribution, such as the Qinghai-Tibet Plateau and South China Coast. The results based on the 15-day sequential experiment showed that the sequential bias correction scheme partly reduced the systematic diurnal biases of the CMA-MESO model. The mean biases of meridional wind, zonal wind, potential temperature, and water vapor mixing ratio were reduced by 45%, 35%, 20%, and 10%, respectively, and the root mean square errors (RMSEs) were reduced by approximately 5%. This study revealed the characteristics of the systematic diurnal bias of CMA-MESO model in southern China, which may be caused by the diurnal variation in the thermal and dynamic exchange on underlying surfaces. The effectiveness of the sequential bias correction scheme was also verified, and the results had good prospects for providing more reference information for high-resolution numerical prediction models and data assimilation.

KEYWORDS

systematic diurnal bias, bias characteristics, CMA-MESO, sequential bias correction scheme, southern China

1 Introduction

Numerical weather prediction (NWP) refers to a process in which the atmospheric governing equations are numerically integrated under given initial and boundary conditions to obtain the future atmospheric state (Xue and Chen, 2008). NWP isn't only the basis of modern weather prediction but has also become an important research tool to determine the physical mechanisms and influencing factors of the occurrence and development of weather disasters. However, due to the non-linear and chaotic characteristics of the atmosphere, the initial errors and model errors of the NWP have a great impact on weather prediction (Lorenz, 1963; Bauer et al., 2015), which cause inaccurate forecast results.

Model errors can be classified as random errors and systematic bias (Dalcher and Kalnay, 1987; Murphy, 1988; Krishnamurti et al., 1999). The systematic bias mainly includes the mean and periodic bias such as associated with the annual cycle and the diurnal cycle (Bhargava et al., 2018), associated with the presence of short- or long-term bias, such as weather highs and lows, or the phase of El Niño (Danforth et al., 2007; Danforth and Kalnay, 2008a; Danforth and Kalnay, 2008b). Several studies have found that the systematic biases have some important influences on the forecast results. For example, the diurnal biases of atmospheric water vapor mixing ratio and the temperature play important roles in the energy budget and precipitation prediction for the NWP model (Dee and Todling, 2000; Dee, 2005; Svensson and Lindvall, 2015; Zhang et al., 2016; Bhargava et al., 2018; Patel et al., 2021). Dee and Todling (2000) analyzed the systematic bias in the NWP model and found that the systematic bias of the atmospheric water vapor mixing ratio plays an important role in the precipitation forecast of the model. The systematic bias of the 2-m temperature was found to show a strong diurnal cycle in the Global Forecast System (GFS) winter forecast results (Patel et al., 2021). In data assimilation, a background field that is assumed to be unbiased is needed to obtain the background error of the model and an accurate initial field. If the background field itself contains systematic bias, then the resulting initial field will also contain such bias (Dee and Arlindo, 1998; Dee, 2005; Zhang et al., 2016). This means that the systematic bias of an NWP model could also have a negative impact on its initial field through data assimilation (Bhargava et al., 2018). Therefore, it is necessary to identify the impacts of systematic bias on model forecasts and explore how it can be reduced.

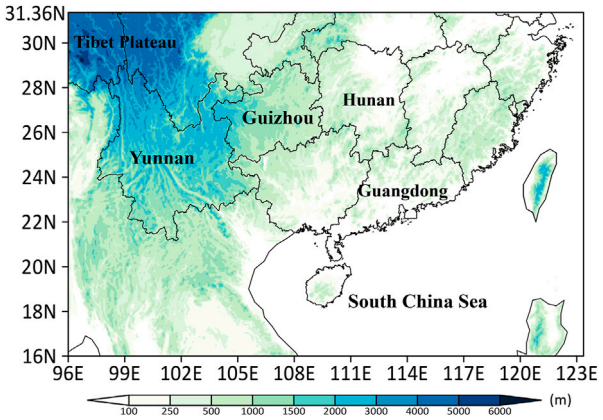

FIGURE 1
The model region and terrain height.

In recent years, due to the increasing frequency of severe convective weather events and the demand for refined forecasting with a high spatial and temporal resolution, increasing attention has been given to high-resolution NWP models. It is worth noting that the systematic bias of short-term forecasts in high-resolution models often presents systematic diurnal bias (Bannister et al., 2019; Scaff et al., 2019; Chen et al., 2021). This bias plays an essential role in high-resolution models (Bhargava et al., 2018), and its influence cannot be ignored. (Faghih et al., 2022). Furthermore, the southern China is located in a subtropical and tropical region that is affected by tropical and temperate systems with complex underlying surfaces and often experiences heavy rains, tornados and other disastrous weather (Wu et al., 2011). Under such a complex background, if a high-resolution model directly performs a short-term forecast or data assimilation without considering the systematic diurnal bias, it may cause errors in the forecast and assimilation results. To solve these problems, some prior works proposed the systematic diurnal bias correction schemes based on Newtonian relaxation (nudging) method (Dee and Todling, 2000; Dee, 2005; Danforth et al., 2007), while some introduced the incremental analysis update (IAU) method (Zhang et al., 2016; Bhargava et al., 2018). For example, Dee and Todling (2000), Dee (2005) proposed an unbiased sequential analysis algorithm and corrected water

TABLE 1 Configuration of the CMA-MESO.

Parameter term	Parameter configuration
Model version	CMA-MESO
Horizontal resolution	0.03° × 0.03°
Vertical levels	51
Initial conditions	NCEP-GFS
Lateral boundary conditions	NCEP-GFS
Model region	16°–31.36°N, 96°–123.36°E
Physical parameterization scheme	WSM6 (Hong and Lim, 2006), MRF (Hong and Pan, 1996), Monin–Obukhov (Beljaars, 1994), RRTM (Mlawer et al. 1997), Dudhia (Dudhia, 1989), Noah (Wang and Chen, 2013)

TABLE 2 Configuration of the analysis bias experiment.

Experiment configuration	Parameter configuration
Forecast start time	0000, 0600, 1200, and 1800 UTC each day
Forecast lead time	6 h
Forecast dates	June 1 to 15, 2022

vapor. And on top of Dee's research, Zhang et al. (2016) proposed a correction algorithm to correct the diurnal bias of temperature, water vapor and wind. From the above studies, it can be found that the methods like IAU or Newtonian relaxation, which use analysis increments as constant forcings to gradually add them into the process of model integration (Bloom et al., 1996; Takacs et al., 2018), are effective means to correct the systematic bias.

However, most of the early studies focused on the correction of systematic bias in medium-term and long-term forecasts with low-resolution global models. Limited works were found for high-resolution short-term forecast in southern China. Therefore, this study aims at examining the characteristics of the systematic diurnal bias of the high-resolution model in southern China and correcting these biases. A 15-day sequential experiment was conducted based on the CMA-MESO model with a 3 km resolution in southern China, and the bias characteristics of the forecast results were analyzed. According to the analysis results a sequential bias correction scheme (SBCS) was designed based on the IAU approach, and 15-day sequential comparative experiments were carried out to test the SBCS performance. The results of this study are expected to be useful for reducing the systematic diurnal bias of the model, improving forecast results, and providing a better background field for data assimilation.

This paper is organized as follows. Section 2 introduces the model, analysis methods and experimental configuration. Section 3 analyzes the results, and Section 4 presents the conclusions.

TABLE 3 Configuration of the analysis bias experiment.

Experiment configuration	Parameter configuration	
Historical bias (number of days of data)	7 days before forecast	
Forecast start time	0000, 0600, 1200, 1800 UTC each day	
Forecast lead time	6 h	
Forecast dates	June 8 to 23, 2022	
Experiment name	CTL	BC
Bias correction scheme	None	SBCS

2 Model, methods, and experimental configuration

2.1 Model configuration

A regional mesoscale model called the CMA-MESO that was developed by the China Meteorological Administration (CMA) Earth System Modeling and Prediction Centre (Chen et al., 2008) is used in this study. Table 1 shows the configurations of this model. The main features of the CMA-MESO include a fully compressible dynamic core with non-hydrostatic approximation, a semi-implicit and semi-Lagrangian scheme for time integration, and height-based terrain-following coordinates. The forecast region covers southern China and the South China Sea (16°–31.36°N, 96°–123.36°E) (shown in Figure 1), and the horizontal resolution of the model is 0.03° × 0.03° (3 km) with 51 vertical levels. The lateral boundary conditions and initial conditions of CMA-MESO are provided (directly downscaled) from the GFS developed by the National Center for Environmental Prediction (NCEP) and National Oceanic and Atmospheric Administration (NOAA).

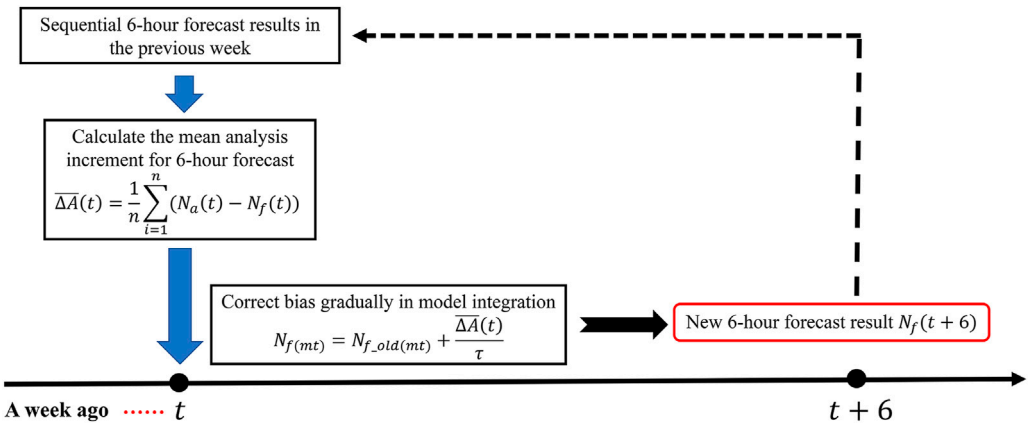

FIGURE 2
The flowchart of the SBCS.

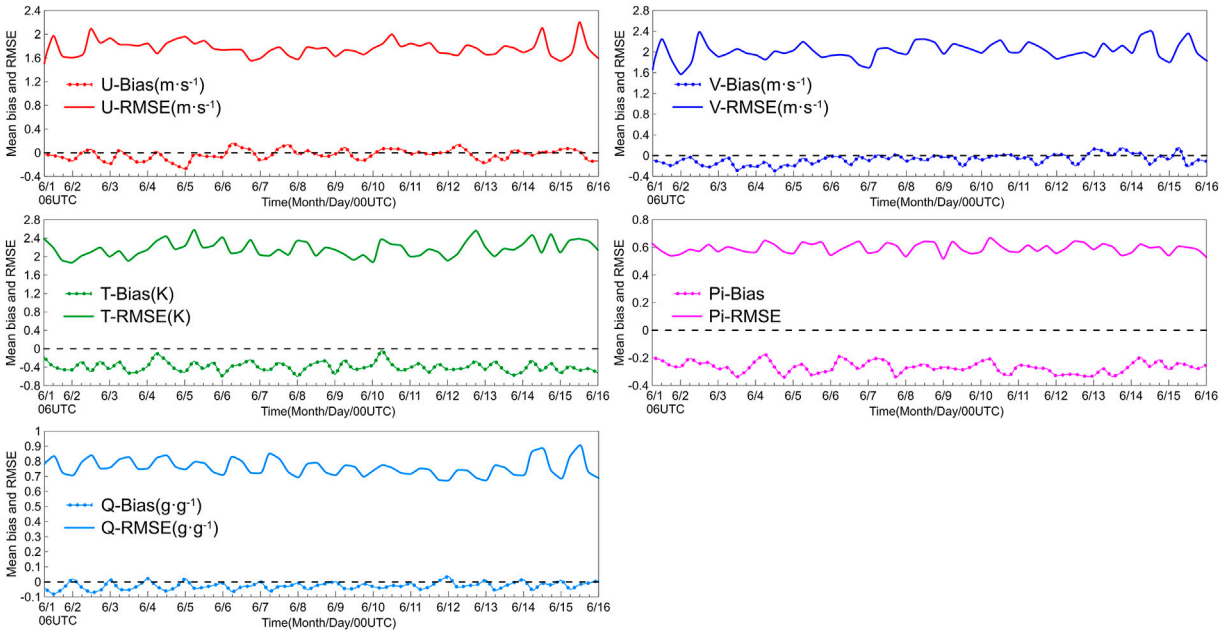

FIGURE 3
Evolution of the mean bias (dotted line) and RMSE (line) over time for U, V, T, Pi, and Q (Initialized at 0000, 0600, 1200, and 1800 UTC every day, with a forecast of 6 h, from 1 to 15 June 2022) (Pi and Q are multiplied by 1,000).

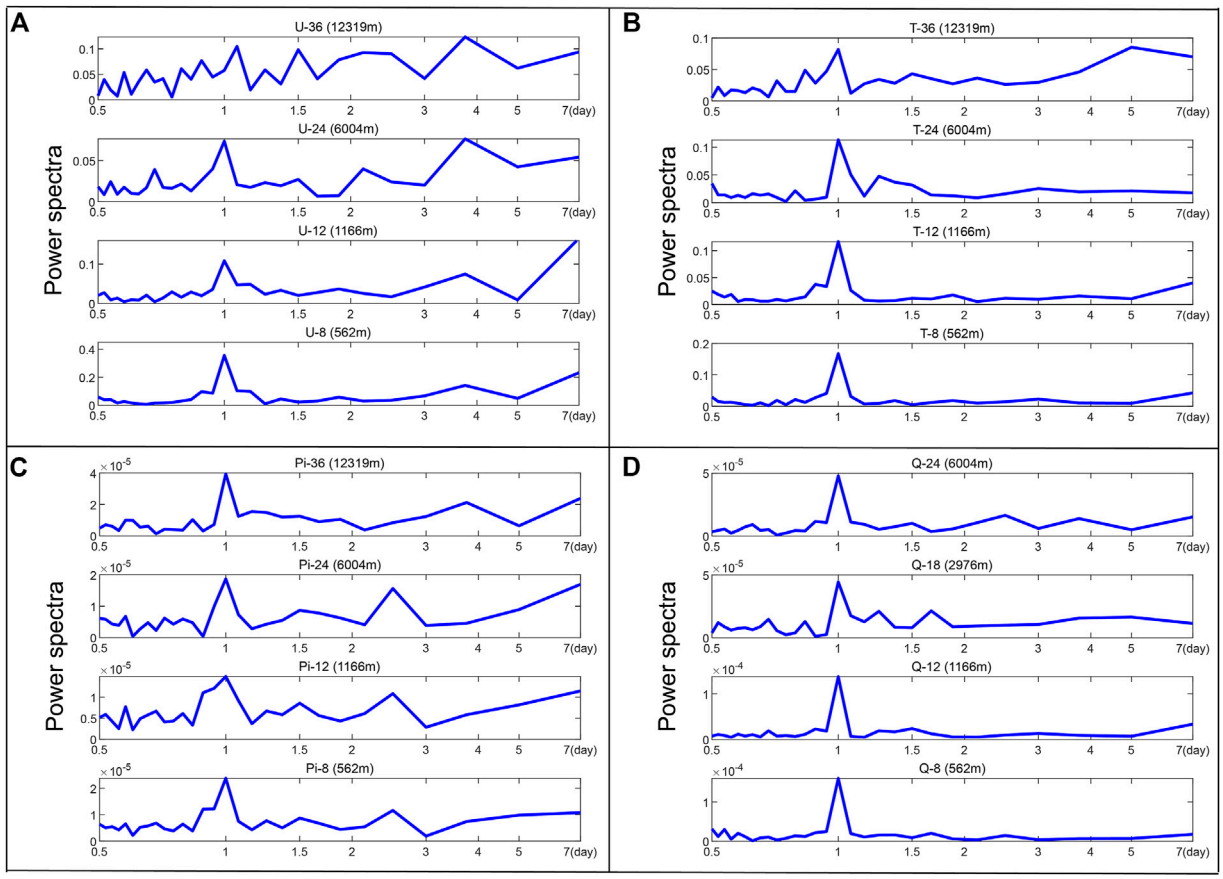

FIGURE 4
The power spectra of **(A)** U, **(B)** T, **(C)** Pi, and **(D)** Q in the forecast mean bias time series from June 1 to 15, 2022.

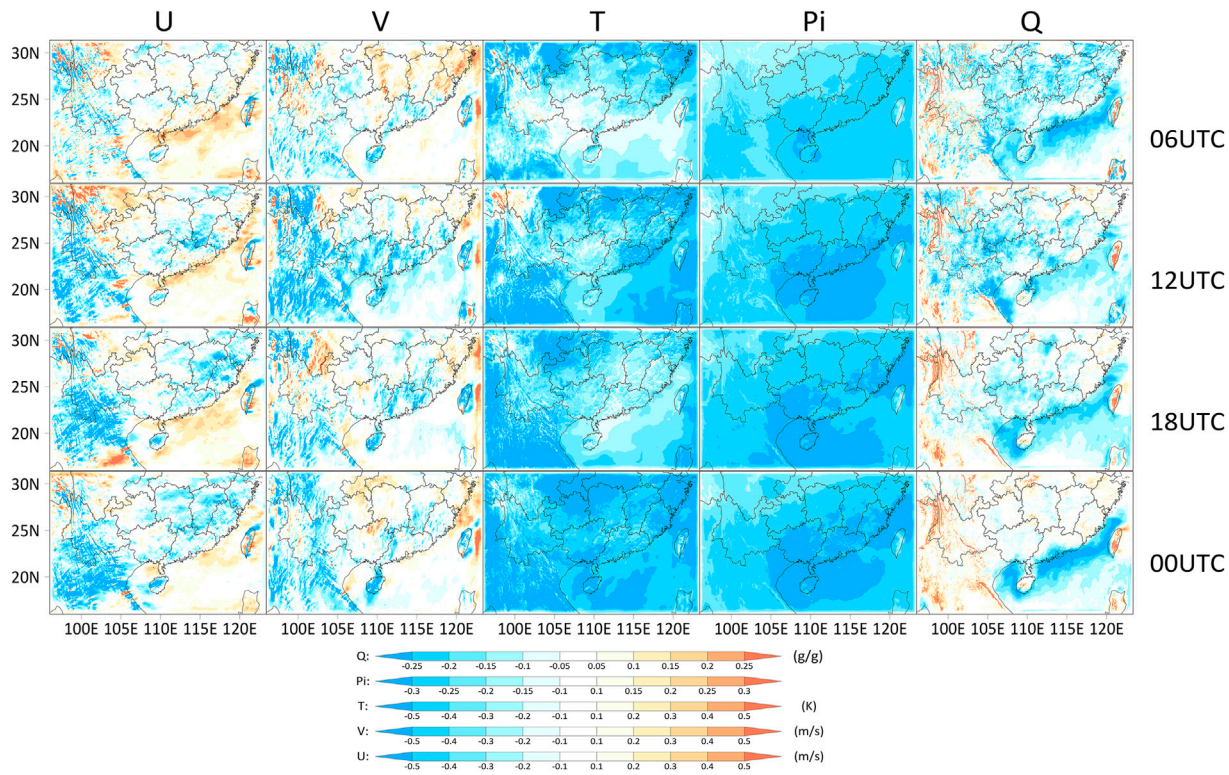

FIGURE 5
The spatial distribution of the vertical mean bias at different times (cool colors represent a negative bias and warm colors represent a positive bias) (Pi and Q are multiplied by 1,000).

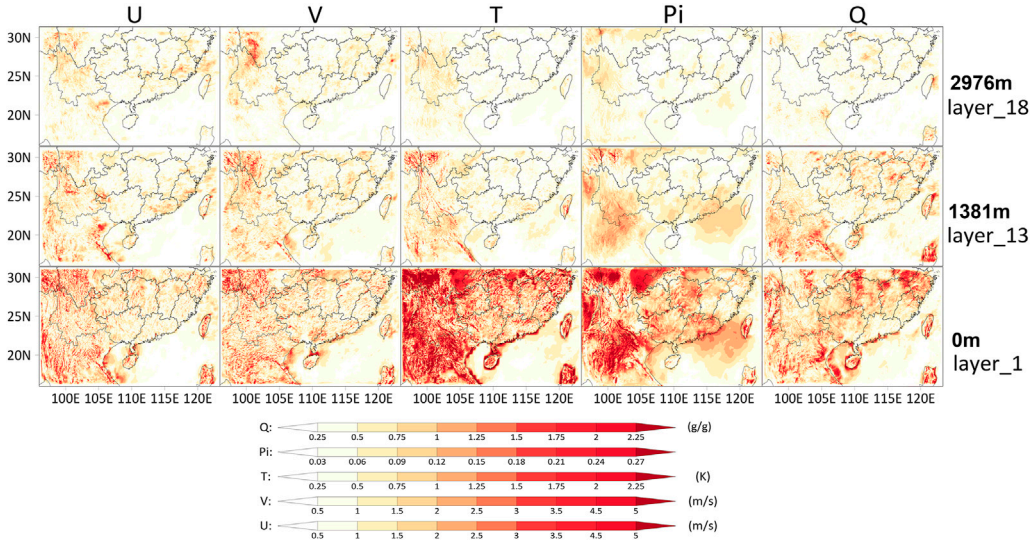

FIGURE 6
The spatial distribution of the DBA at 1, 13, and 18 model layers (Pi and Q are multiplied by 1,000).

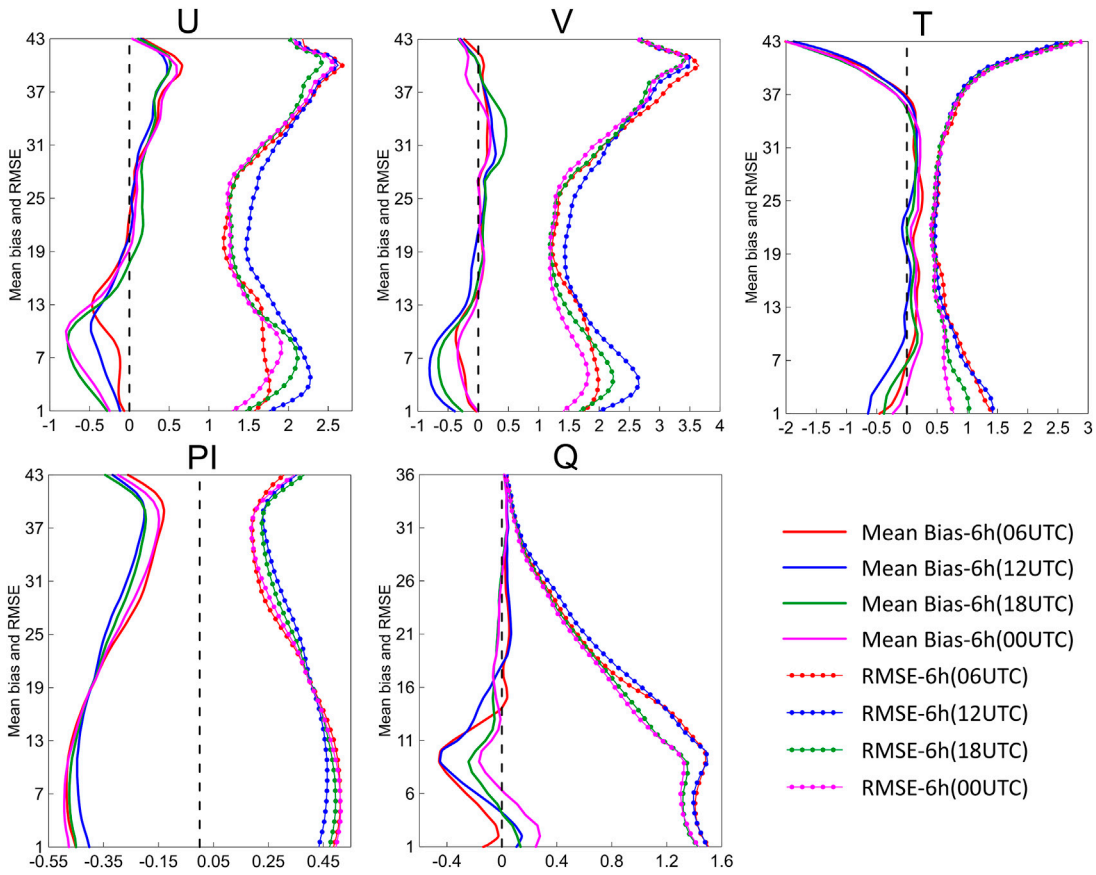

FIGURE 7
The vertical profiles of the horizontal mean bias and RMSE from June 1 to 15, 2022 (Pi and Q are multiplied by 1,000).

2.2 Bias analysis method and experimental configuration

In this study, the NCEP-GFS analysis field (hereafter referred to as the analysis data) is applied to evaluate the forecasts. The variables including the meridional wind (U), zonal wind (V), potential temperature (T), dimensionless pressure (Pi), and water vapor mixing ratio (Q) are derived from standard initialization process using the NCEP-GFS analysis data. It should be noted that all variables in this study are analyzed and corrected at the model layer.

Three evaluation metrics are applied in the following analysis, including the bias, the root-mean-square error (RMSE) and the diurnal bias amplitude (DBA):

$$Bias = A_t - F_t \tag{1}$$

$$RMSE = \sqrt{\frac{1}{n}\sum_{i=1}^{n}(A_t - F_t)^2} \tag{2}$$

$$DBA = |Bias_{tmax} - Bias_{tmin}| \tag{3}$$

In the above equations, A_t represents the analysis at time t; F_t represents the forecast at time t; $Bias_{tmax}$ represents the maximum bias at different forecast times in a day; and $Bias_{tmin}$ represents the minimum bias at different forecast times in a day.

To analyze the characteristics of the bias in the CMA-MESO, 15-day sequential experiments are conducted (as shown in Table 2). The forecasts start at 0000, 0600, 1200, and 1800 UTC each day from June 1 to 15, 2022. The forecast lead time is 6 h.

2.3 Sequential bias correction scheme and experimental configuration

In this study, following Danforth et al. (2007), Danforth and Kalnay (2008a) and Bhargava et al. (2018), a sequential bias correction scheme (SBCS) based on the analysis increment was designed to correct the model diurnal bias. The 6-h analysis increment is obtained by subtracting the 6-h forecast result from the analysis data. This analysis increment can represent the systematic diurnal bias to a certain extent.

The detailed procedure for the SBCS is as follows:

Definitions: the model forecast value of a grid is defined as $N_f(t)$, which is calculated by $N_f(t) = M[t]$, where t and $M[t]$ are the time and the process of the model forecast at the time, respectively. The analysis value of a grid is defined as $N_a(t)$, which is calculated by $N_a(t) = A[t]$, where $A[t]$ is the analysis value at time t. In this study, N specifically refers to the variables to be corrected, namely, meridional

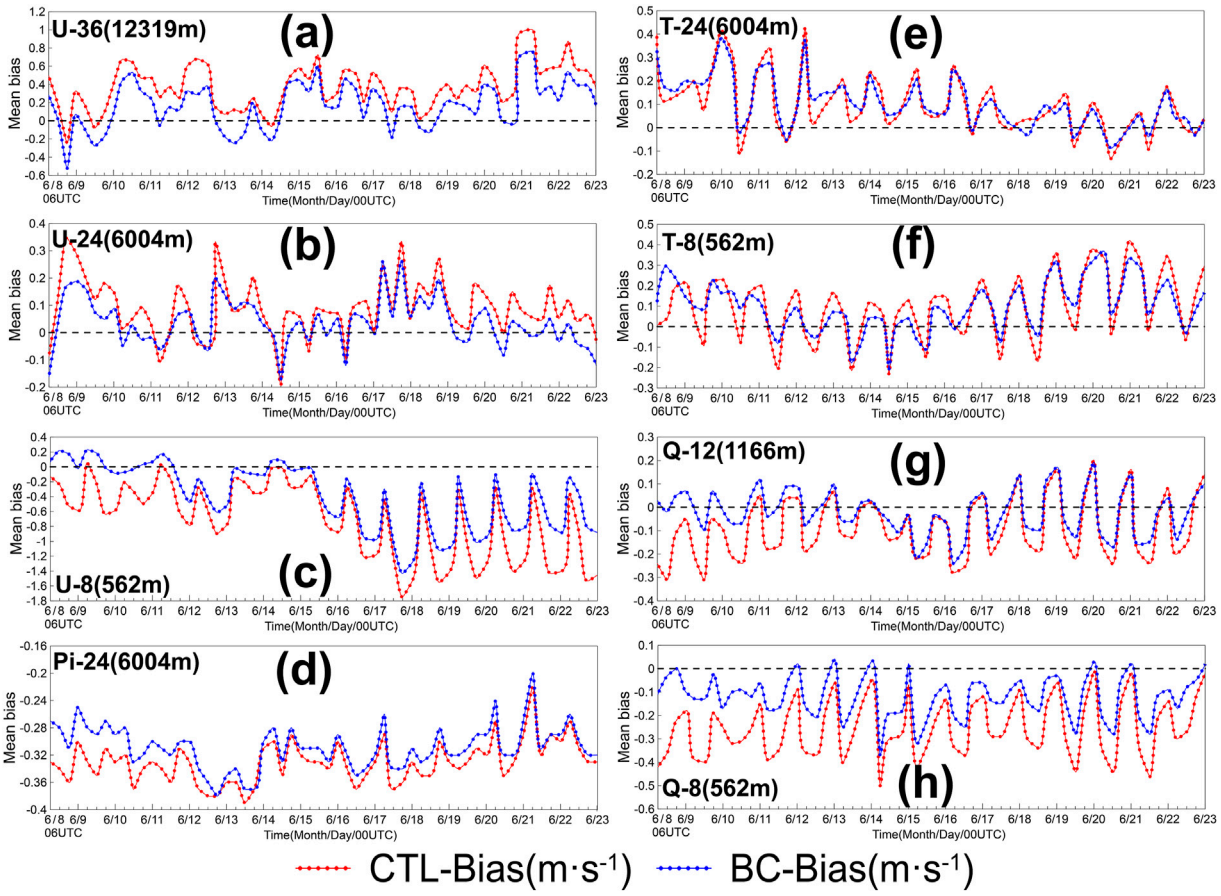

FIGURE 8
Evolution of the mean bias (dotted line) over time for the U, T, Pi, and Q values at different model layers. **(A)** U in 36-layer, **(B)** U in 24-layer, **(C)** U in 8-layer, **(D)** Pi in 24-layer, **(E)** T in 24-layer, **(F)** T in 8-layer, **(G)** Q in 12-layer, and **(H)** Q in 8-layer (initialized at 0000, 0600, 1200, and 1800 UTC every day, with a forecast of 6 h, from 8 to 23 June 2022) (Pi and Q are multiplied by 1,000).

wind (U), zonal wind (V), potential temperature (T), dimensionless pressure (Pi), and water vapor mixing ratio (Q).

(1) Derive the analysis increment $\Delta A(t)$ at time t by subtracting the forecast value $N_f(t)$ from the analysis value $N_a(t)$ (as in Eq. 4.
(2) Calculate the average analysis increment $\overline{\Delta A}(t)$ by taking the mean value of the 6-h analysis increment $\Delta A(t)$ at different time t in the previous week Eq. 5. n represents the sample number of $\Delta A(t)$ that is used to obtain the statistical average, and in this study, $n = 7$.
(3) In the process of model integration, the corrected value $N_{f(mt)}$ of the variable $N_{f\_old(mt)}$ is calculated by Eq. 6, which is corrected stepwise at each step of integration. τ and mt are the number of steps and each moment in the model integration, respectively.

$$\Delta A(t) = N_a(t) - N_f(t) \tag{4}$$

$$\overline{\Delta A}(t) = \frac{1}{n}\sum_{i=1}^{n}\Delta A(t) \tag{5}$$

$$N_{f(mt)} = N_{f\_old(mt)} + \frac{\overline{\Delta A}(t)}{\tau} \tag{6}$$

Figure 2 gives the flowchart of the SBCS. As an example, to correct the systematic diurnal bias of the forecast at 0000 UTC on June 8, the average analysis increment $\overline{\Delta A}(t)$ is first derived from the forecast results of the previous week from 0000 UTC on June 1 to 0000 UTC on June 7. Then, the diurnal bias at 0000 UTC June 8 is corrected by subtracting $\overline{\Delta A}(t)$.

In accordance with the above scheme, two groups of experiments were carried out from June 8 to 23, 2022. The CTL experiment was a control experiment without any bias correction scheme, and the BC experiment was a correction experiment using the SBCS (as shown in Table 3).

3 Results

3.1 Diurnal bias characteristics

To analyze the characteristics of the bias in the CMA-MESO, 15-day sequential experiments are conducted. The systematic model bias can be detected by comparing forecasts against observations and calculating the regional averages of the mean biases in a relatively long time period (Dee and Todling, 2000). Figure 3 shows the evolution of the mean bias (dotted line) and RMSE (line) over time for the five variables. Because the Pi and Q values are too small, they are multiplied by 1,000 in this figure (the same treatment is hereafter noted in the

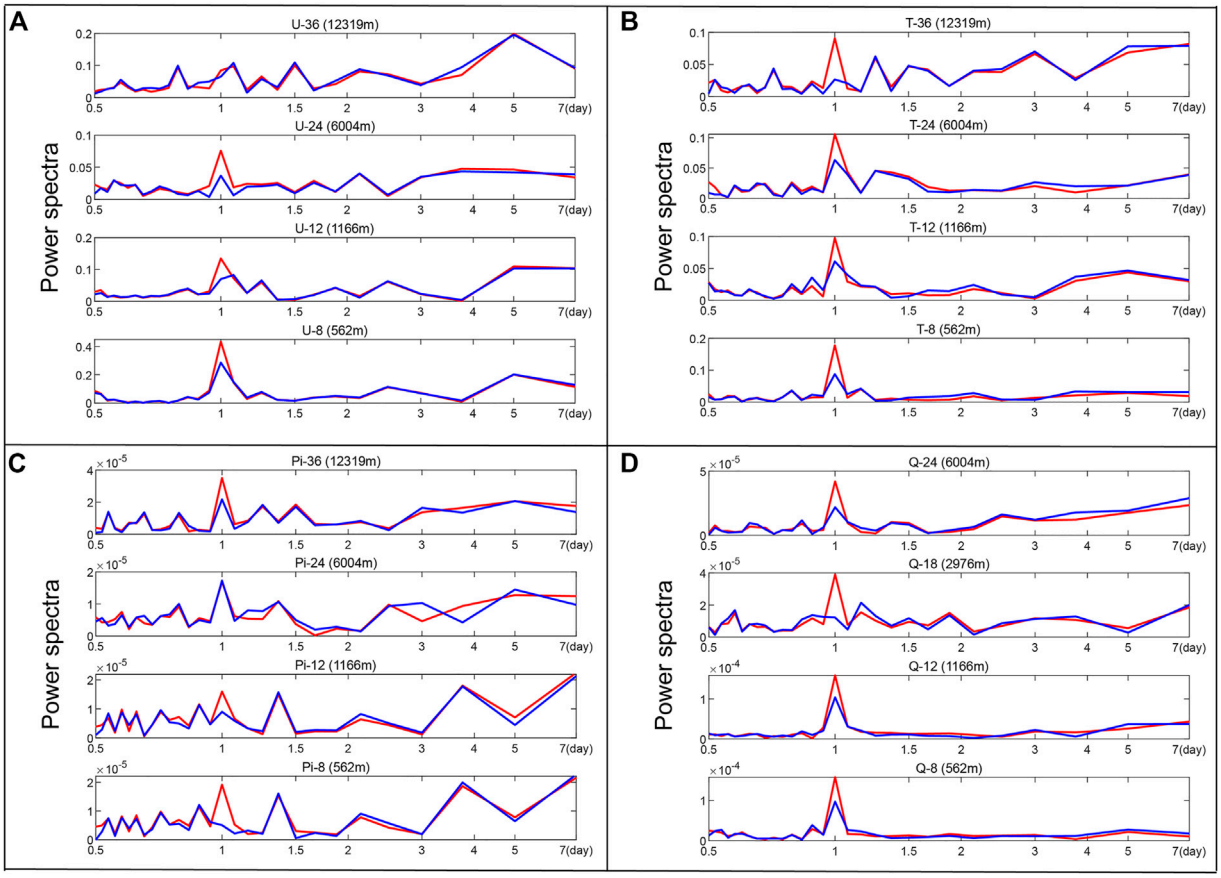

FIGURE 9
The power spectra of **(A)** U, **(B)** T, **(C)** Pi and **(D)** Q in the forecast mean bias time series for the BC (blue line) and CTL (red line) experiments at different model layers from June 8 to 23, 2022.

figure title). Figure 3 shows that the mean bias of the model variables has diurnal characteristics. This diurnal characteristic of the mean bias presents some periodic diurnal changes with some irregular fluctuations in U, V, and Pi. However, it shows a continuous periodic diurnal cycle in T and Q, which presents obvious diurnal fluctuations. For example, the forecast mean bias of Q at 0000 UTC every day is always the lowest; then, it increases gradually at 0600 UTC, reaches the maximum mean bias at 1200 UTC, and finally decreases at 1800 UTC. This fluctuation obviously shows the diurnal characteristics. Other evolutions of mean bias, such as for U, also show diurnal characteristics, although noise exists. On the other hand, the RMSE also shows similar diurnal characteristics as the mean bias, which means that periodic diurnal bias exists in the CMA-MESO.

The power spectra of bias time series are another metric used to examine periodic characteristic (Zhang et al., 2016). Therefore, the 15-day forecast bias is used for Fourier spectrum analysis. Figure 4 shows the power spectra of (a) U, (b) T, (c) Pi and (d) Q in the forecast bias times series at different model layers from June 1 to 15, 2022 (the power spectra of V is similar to those of U, so they aren't shown). The peaks are mostly concentrated in the spectrum within a 1-day period. This means that the most important periodic variation is the diurnal cycle for the mean bias of all variables. Among the four variables, the periodic variation in T and Q is dominated by the diurnal cycle, but the periodic variation in U and Pi is slightly more complicated. There are still serval secondary peaks, such as the 2-day and 4-day peaks, in the power spectra of U and Pi, which indicates periodic variation on a synoptic scale. On the other hand, the periodic variations in the low and middle model layers are still dominated by the diurnal cycle, and this characteristic is not obvious in the high model layer. This means that the mean bias of the diurnal cycle is mainly in the low and middle model layers.

Figure 5 shows the spatial distribution of the vertical mean bias at different times (for example, the result at 0,600 UTC is the forecast result that started at 0000 UTC and forecasted 6-h). First, there are different spatial distributions of the vertical mean bias at different times, which means that the spatial distributions of the vertical mean bias have diurnal characteristics. For example, for U, the negative bias region is mainly on the Qinghai-Tibet Plateau and Yunnan-Guizhou Plateau, and the positive bias region is mainly on the South China Coast at 0600 UTC. At 1200 UTC, the negative bias region is mainly on the Qinghai-Tibet Plateau, Yunnan-Guizhou Plateau and in Guangdong Province, the maximum becomes larger, and the Qinghai-Tibet Plateau also shows some positive bias. At 1800 UTC, the area of negative bias increases, and there are only a small number of positive biases in Southeast Asia and the South China Sea. At 0000 UTC, the whole area is dominated by negative bias. Second, the

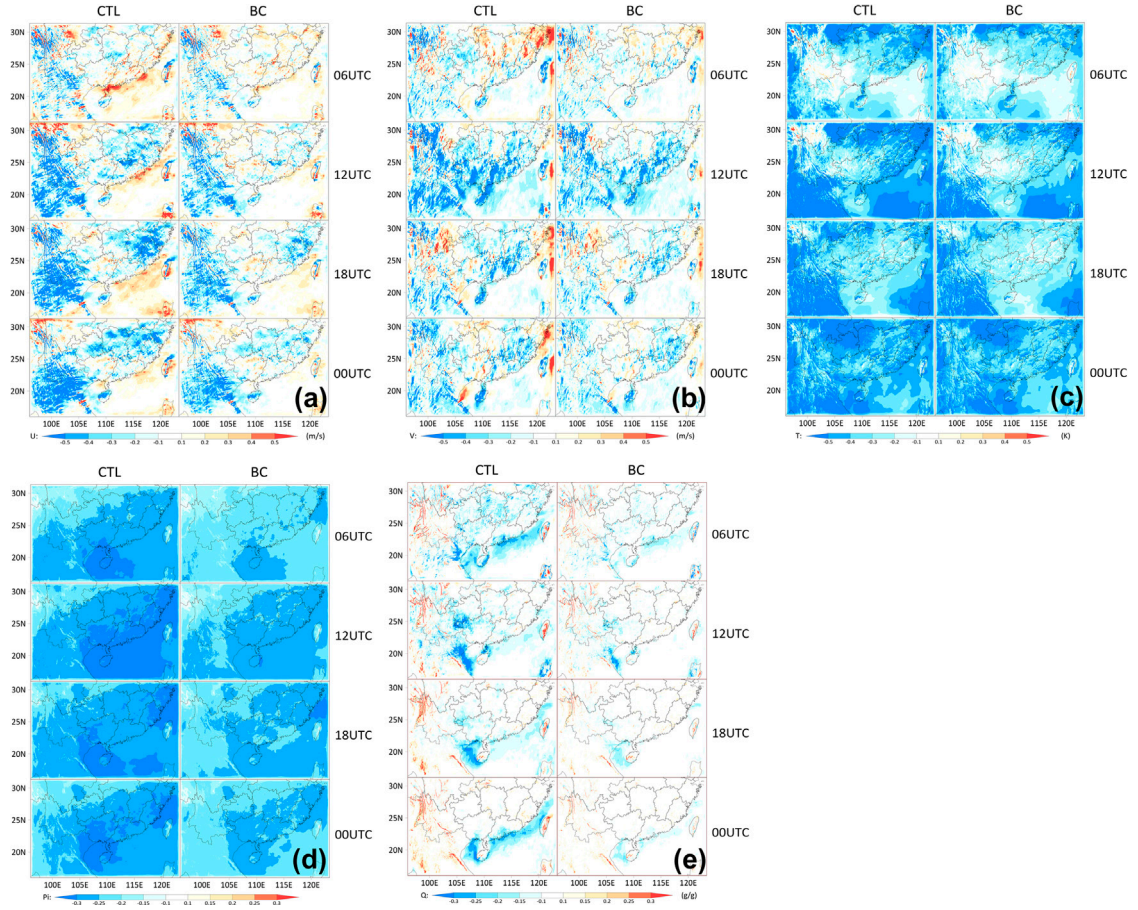

FIGURE 10
The spatial distribution of the vertical mean bias at different times for the BC and CTL experiments. **(A)** U, **(B)** V, **(C)** T, **(D)** Pi and **(E)** Q. (Pi and Q are multiplied by 1000).

spatial distribution of the vertical mean bias has some characteristics related to the underlying surface. For U and V, the large bias region is mainly on the Qinghai-Tibet Plateau and Yunnan-Guizhou Plateau, which have high altitudes, many mountains and a complex topography. For Pi and Q, the large bias region is mainly in the South China Coast and South China Sea, which have the ocean and coasts.

To explore the impact of the underlying surface on the diurnal bias variation for the low model layers, an indicator called DBA is defined. The DBA is calculated by Eq. 3, and it can show the region with a large diurnal variation in the bias. Figure 6 shows the spatial distribution of DBA at layers 1, 13 and 18. From Figure 6, it can be seen that the region of large DBA is mainly concentrated on the Qinghai-Tibet Plateau, Yunnan-Guizhou Plateau, in Taiwan, and Southeast Asia; these areas are characterized by high altitudes, multiple mountains, and complex underlying surfaces. Especially for T, the temperature is easily affected by the radiation of the underlying surface. Therefore, the DBA value of T is large in 1-layer, and it shows an obvious relation between the underlying surface, as shown in Figure 6. However, in the 13-layer and 18-layer, the impact of the underlying surface gradually decreases with increasing altitude. This means that the diurnal bias may be directly affected by the diurnal variation in the thermal and dynamic exchange on underlying surfaces, and this influence will gradually decrease with increasing altitude.

Figure 7 is the vertical profile of the horizontal forecast mean bias and RMSE from June 1 to 15, 2022. First, the mean bias has an overall trend of large values in the lower and high model layers and small values in the middle model layers. Second, the vertical profile of the four start times presents a different distribution, especially for the lower layer. For example, the vertical profiles of U and V show clear diurnal characteristics. It can also be found that the amplitude of the diurnal bias is large in the lower layer but small in the middle and high layers. On the other hand, the vertical profile of the RMSE also presents a similar feature to that of mean bias. The results of the vertical profile verify the previous results. The lower layer is easily affected by changes in the underlying surface, and the systematic diurnal bias is mainly present in the lower model layer.

According to the above results, it can be found that the forecast mean bias and RMSE of CMA-MESO have some diurnal features. These diurnal biases are concentrated on plateaus and mountains and in oceans and lakes for the horizontal distribution and in the low model layer for the vertical distribution. This phenomenon may be mainly caused by the direct impact of the diurnal variation on the underlying surface.

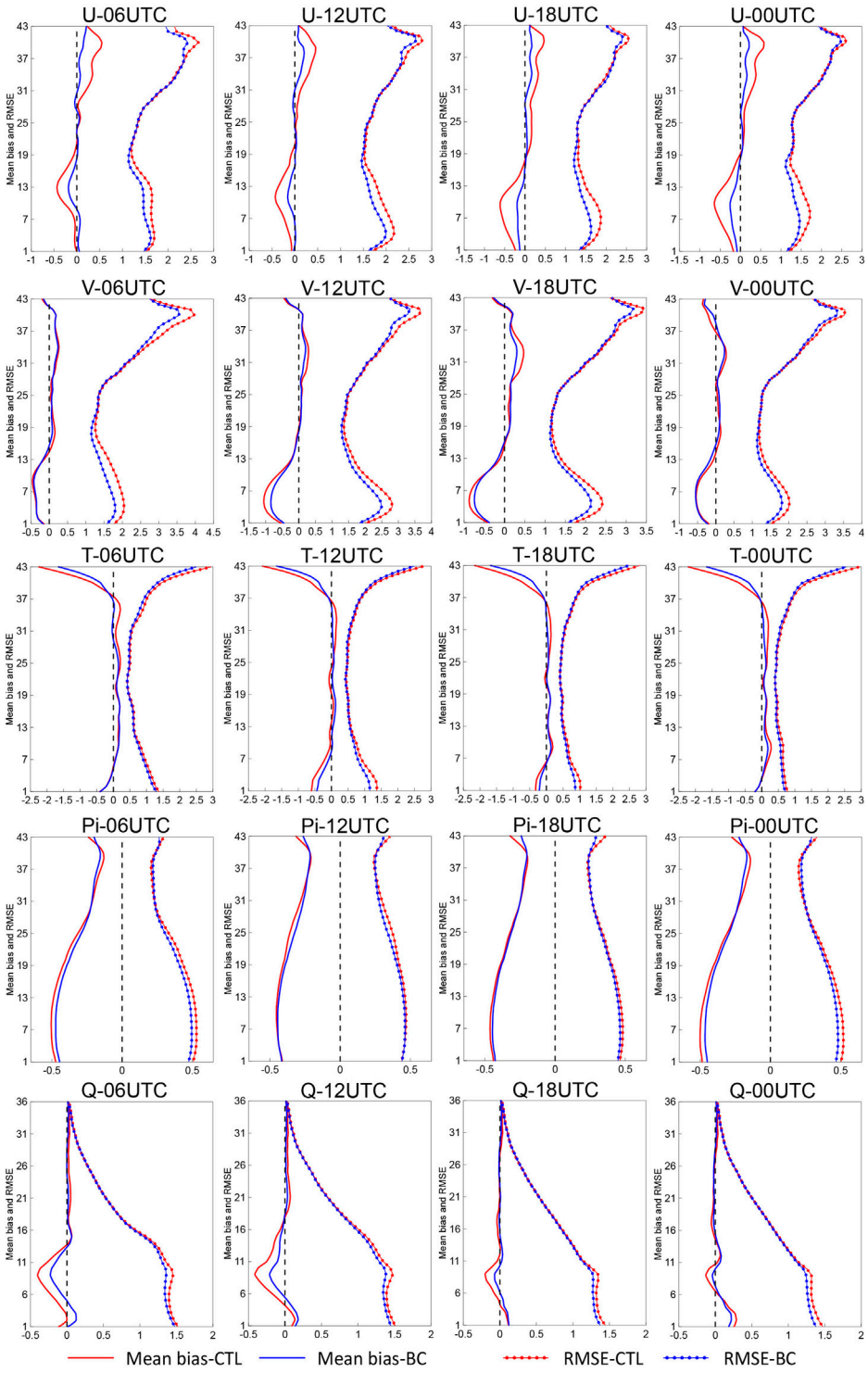

FIGURE 11
The vertical profiles of the horizontal mean bias and RMSE for the BC and CTL experiments (initialized at 0000, 0600, 1200, and 1800 UTC every day, with a forecast of 6 h, from 8 to 23 June 2022). (Pi and Q are multiplied by 1,000).

3.2 Diurnal bias correction

From the above analysis, it can be seen that there are systematic diurnal biases in the CMA-MESO forecast results in southern China. To correct these biases in the model and improve the forecast results, the SBCS is designed, and two comparative experiments are carried out. One is the BC experiment using the SBCS, and the other is the CTL experiment without any bias correction scheme. According to

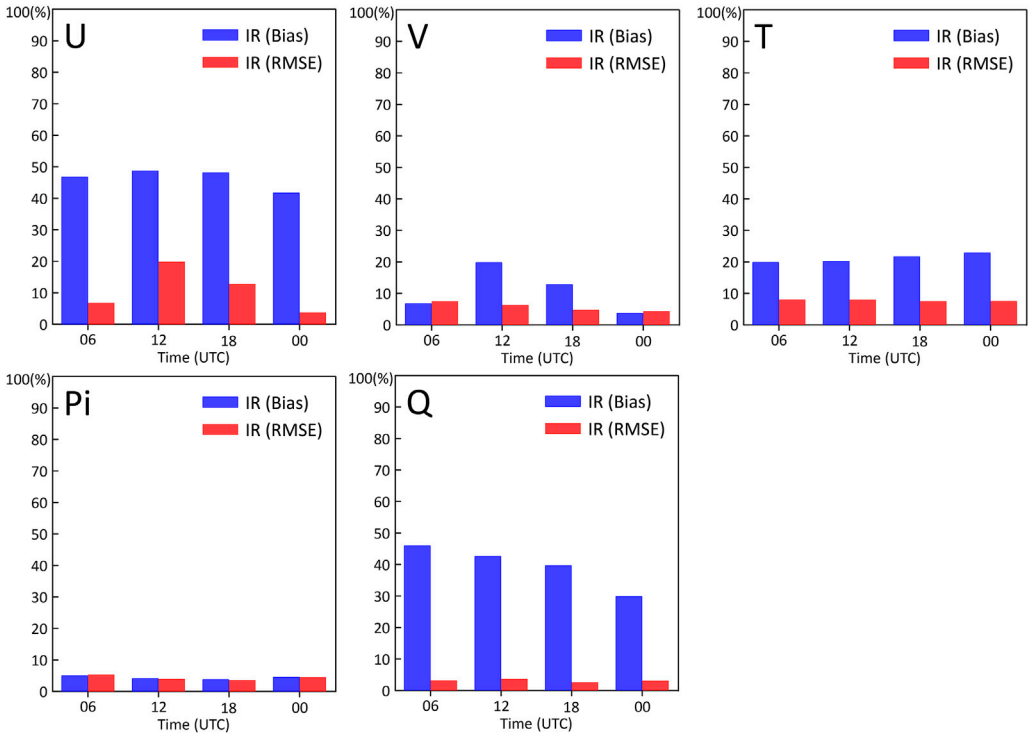

FIGURE 12
The improvement rate for the BC and CTL experiments at different times (blue bars indicate the improvement rate of the bias, and red bars indicate the improvement rate of the RMSE).

the results, Figure 8 shows the evolution of the mean bias (dotted line) over time for some variables with important weather information at different model layers. In addition, in Figure 8, the 36-layer, 24-layer, 12-layer and 8-layer are selected to represent high layer, middle layer, middle-lower layer and lower layer in the model, respectively. The mean bias of U generally decreases in the high layer, middle layer and lower layer after using the SBCS (as shown in Figures 8A–C). Moreover, it is worth noting that the amplitude of the diurnal bias also decreases, especially in the lower layer (as shown in Figure 8C), which means that the systematic diurnal bias is reduced. For the Pi in the middle layer, which is often used to represent synoptic situations, the mean bias of the BC experiment is lower than that of the CTL experiment (as shown in Figure 8D). For T in the middle layer, the mean biases of the two experiments are similar (as shown in Figure 8E). However, in the lower layer, the mean bias of the BC experiment is lower than that of the CTL experiment, and the amplitude of the diurnal bias also decreases (as shown in Figure 8F). For Q in the middle-lower layer and lower layer, the mean biases of the BC experiment are lower than those of the CTL experiment, and the amplitude of the diurnal bias also decreases (as shown in Figures 8G, H). In general, the mean biases and the amplitude of the diurnal bias are partly reduced after correction with the SBCS scheme.

Figure 9 shows the power spectra of (a) U, (b) T, (c) Pi and (d) Q in the forecast bias times series for the BC (blue line) and CTL (red line) experiments at different model layers from June 8 to 23, 2022 (the power spectra of V is similar to U, so they aren't shown). The peak of the CTL experiment is still mostly concentrated in the spectrum within a 1-day period. However, the peak of the BC experiment within a 1-day period decreases at most layers. For some of these variables, such as the T at the high layer, the peak over a 1-day period even disappears. In addition, although the peak is decreased, diurnal fluctuation still exists for most of the variables. This means that the SBCS scheme can only partly reduce the systematic diurnal bias but cannot completely eliminate the influence of such bias on the model forecast results.

To determine if there is any change in the spatial distribution of the model bias after using the SBCS, Figure 10 shows the spatial distribution of the vertical mean bias at different times for the BC and CTL experiments. Figure 10A shows that the area and value of the U mean bias in the BC experiment are smaller than those in the CTL experiment in areas such as the Qinghai-Tibet Plateau, Yunnan-Guizhou Plateau and southeast region. Figures 10B–D also show similar the results as Figure 10A, the mean biases of the BC experiment are reduced, and the forecast results are improved. In addition, the improved regions are different. In detail, for the V, the improved region is concentrated in the South China Coast and on Qinghai-Tibet Plateau; for the T, the improved region is concentrated in the north and southeast; for the Pi, the improved region is concentrated in the South China Coast and South China Sea areas; and for the Q, the improved region is concentrated in the South China Coast and on Yunnan-Guizhou Plateau. In general, the improved region is closely related to the underlying surface, such as plateau, mountain, coast and ocean.

As mentioned earlier, the diurnal bias is closely related to the underlying surface, and Figure 10 also shows an improvement in the BC experiment in regions with a complex underlying surface. What are the characteristics of the mean bias and RMSE at different vertical layers after using the SBCS? Figure 11 shows the vertical profiles of the horizontal mean bias (line) and RMSE (dotted line) for the BC (blue) and CTL (red) experiments. The mean bias of the BC experiment is generally smaller than that of the CTL experiment, which means that the forecast result of the BC is improved and the diurnal bias of the model is partly corrected. For U, V, T, and Q, the model bias of the BC experiment is obviously reduced in the high and lower layers, and there is little change in the middle layer. On the other hand, for the forecast results at different times, the correction effect at 1200 UTC and 1800 UTC is better than that at 0000 UTC and 0600 UTC. However, for Pi, this improvement is not apparent. The mean bias of the BC experiment decreases at 0000 UTC and 0600 UTC in the lower layers, and there is little change at other times in the high and middle layers. In general, it can be seen that the results of the BC experiment show lower mean bias and RMSE, especially for the lower model layers, which shows apparent improvement.

The improvement rate (IR, which is calculated by equation $IR = \frac{(|X_{CTL}|-|X_{BC}|)}{|X_{CTL}|} \times 100\%$, where X represents the mean bias or RMSE) at different times is introduced to better show the improvement of the forecast results using the SCBS (as shown in Figure 12). Here, X represents the mean bias or RMSE of all grids respectively. A positive IR represents a positive improvement, and a negative IR represents a worse performance. From the Figure 12, it is found that both the bias and RMSE show positive improvement in all variables at all times. Specifically, the IR (bias) of U at all times nearly exceeds 40%; the IR (bias) of T at all times nearly exceeds 20%; and the IR (bias) of Q at all times nearly exceeds 30%. The improvement of V and Pi is relatively small; the IR (bias) of V is only approximately 10%, and that of Pi is only approximately 5%. On the other hand, the IR (RMSE) is generally lower than the IR (bias), and those of U, V, T, Pi, and Q are approximately 10%, 7%, 8%, 5%, and 4%, respectively.

According to the above results, it is found that the mean bias and RMSE of the BC experiment using the SBCS are generally lower than those of the CTL experiment. Furthermore, the SBCS reduced the systematic diurnal bias and improved the forecast results in the CMA-MESO.

4 Summary and discussion

In this study, the bias characteristics of the 15-day sequential experiment results in southern China are analyzed based on the CMA-MESO high-resolution NWP model. According to the analysis results, the sequential bias correction scheme called the SBCS was designed to reduce systematic diurnal bias with using analysis increments in the CMA-MESO. Two sequential, 15-day comparative experiments are carried out, one using the SBCS and the other being a control treatment without any bias correction scheme.

The detailed procedures related to the SBCS within CMA-MESO are addressed in this paper. Specifically, the historical 6-h continuous forecast results of the week before the forecast time are used to obtain the analysis increments of each grid point through statistical averaging. Then, through model integration, the variable is corrected stepwise at each step of integration.

The preliminary results of the bias analysis show that the CMA-MESO has a systematic diurnal bias in southern China. The bias of each variable has different characteristics at different times of the day. Specifically, for the horizontal distribution, the systematic diurnal bias is mainly concentrated on the Qinghai-Tibet Plateau, Yunnan-Guizhou Plateau, South China Coast and in the South China Sea. These areas have complex underlying surfaces, such as plateaus, mountains, lakes, coasts and oceans. For the vertical distribution, the systematic diurnal bias is concentrated in the lower model layer, which is susceptible to the underlying surface. This phenomenon may be caused by the influence of the diurnal variation in the thermal and dynamic exchange on underlying surfaces. On the other hand, the preliminary results of bias correction show that the SBCS partly reduces systematic diurnal biases, and reduces the mean bias of the CMA-MESO 6-h forecast by 5%–50% and the RMSE by 4%–10%. This means that the SBCS reduces the systematic diurnal bias and improves the forecast results of the CMA-MESO in southern China.

This study shows the characteristics of systematic diurnal bias in southern China with the CMA-MESO high-resolution model and the positive correction effect of the SBCS. However, with in-depth research, there are still some problems and challenges that need to be overcome. First, in this study, the purpose of the SBCS is to improve both the model forecast results and the background field in data assimilation. However, we have not conducted an assimilation experiment using the corrected forecast results with the SBCS. This will be our next major research direction. Second, for the improvement of the forecast results with the SBCS, we have only carried out a 6-h forecast at present, without carrying out a longer-term (such as 24-h or 36-h) forecast experiment. More sensitive experiments are needed. In the future, we will further explore these problems.

Data availability statement

The raw data supporting the conclusions of this article will be made available by the authors, without undue reservation.

Author contributions

YC: Conceptualization, methodology, design and experiment, investigation, formal analysis, writing draft. LW: Methodology, funding acquisition, supervision, writing—review and editing. JL: Methodology, writing—review and editing. DX: Writing—review and editing. JC: Resources. BZ:

Conceptualization, funding acquisition, supervision, writing—review and editing.

Funding

This work was supported by National Key R&D Program of China (Grant No. 2021YFC3000902), the National Natural Science Foundation of China (Grant No. U2142213), and the Guangdong Basic and Applied Basic Research Foundation (Grant No. 2020A1515110040).

Support for model computing resources was provided by the CMA Earth System Modeling and Prediction Centre. And the initial and boundary conditions for this work were provided by the CMA Earth System Modeling and Prediction Centre.

Conflict of interest

The authors declare that the research was conducted in the absence of any commercial or financial relationships that could be construed as a potential conflict of interest.

Publisher's note

References

Bannister, D., Orr, A., Jain, S. K., Holman, I. P., Momblanch, A., Phillips, T., et al. (2019). Bias correction of high-resolution regional climate model precipitation output gives the best estimates of precipitation in Himalayan catchments. *J. Geophys. Res.-Atmos.* 124, 14220–14239. doi:10.1029/2019JD030804

Bauer, P., Thorpe, A., and Brunet, G. (2015). The quiet revolution of numerical weather prediction. *Nature* 525, 47–55. doi:10.1038/nature14956

Beljaars, A. C. M. (1994). The parametrization of surface fluxes in large-scale models under free convection. *Quart. J. Roy. Meteor. Soc.* 121, 255–270. doi:10.1002/qj.49712152203

Bhargava, K., Kalnay, E., Carton, J. A., and Yang, F. (2018). Estimation of systematic errors in the GFS using analysis increments. *J. Geophys. Res. Atmos.* 123, 1626–1637. doi:10.1002/2017jd027423

Bloom, S. C., Takacs, L. L., Sliva, A. M. D., and Ledvina, D. (1996). Data assimilation using incremental analysis updates. *Mon. Wea. Rev.* 124, 1256–1271. doi:10.1175/1520-0493(1996)124<1256:dauiau>2.0.co;2

Chen, D. H., Xue, J. S., Yang, X. S., Zhang, H., Shen, X., Hu, J., et al. (2008). New generation of multiscale NWP system (GRAPES): General scientific design. *Chin. Sci. Bull.* 53, 3433–3445. doi:10.1007/s11434-008-0494-z

Chen, Y. D., Fang, K. M., Chen, M., and Wang, H. L. (2021). Diurnally varying background error covariances estimated in RMAPS-ST and their impacts on operational implementations. *Atmos. Res.* 257, 105624. doi:10.1016/j.atmosres.2021.105624

Dalcher, A., and Kalnay, E. (1987). Error growth and predictability in operational ECMWF forecasts. *Tellus A* 39A (5), 474–491. doi:10.3402/tellusa.v39i5.11774

Danforth, C. M., and Kalnay, E. (2008b). Impact of online empirical model correction on nonlinear error growth. *Geophys. Res. Lett.* 35, L24805. doi:10.1029/2008gl036239

Danforth, C. M., Kalnay, E., and Miyoshi, T. (2007). Estimating and correcting global weather model error. *Mon. Weather Rev.* 135, 281–299. doi:10.1175/mwr3289.1

Danforth, C. M., and Kalnay, E. (2008a). Using singular value decomposition to parameterize state-dependent model errors. *J. Atmos. Sci.* 65, 1467–1478. doi:10.1175/2007jas2419.1

Dee, D. P., and Arlindo, M. D. S. (1998). Data assimilation in the presence of forecast bias. *Quart. J. Roy. Meteor. Soc.* 124, 269–295. doi:10.1002/qj.49712454512

Dee, D. P. (2005). Bias and data assimilation. *Quart. J. Roy. Meteor. Soc.* 131, 3323–3343. doi:10.1256/qj.05.137

Dee, D. P., and Todling, R. (2000). Data assimilation in the presence of forecast bias: The GEOS moisture analysis. *Mon. Wea. Rev.* 128, 3268–3282. doi:10.1175/1520-0493(2000)128<3268:daitpo>2.0.co;2

Dudhia, J. (1989). Numerical study of convection observed during the Winter Monsoon Experiment using a mesoscale two-dimensional model. *J. Atmos. Sci* 46, 3077–3107. doi:10.1175/1520-0469(1989)046,3077:NSOCOD.2.0.CO;2

Faghih, M., Brissette, F., and Sabeti, P. (2022). Impact of correcting sub-daily climate model biases for hydrological studies. *Hydrology Earth Syst. Sci.* 26, 1545–1563. doi:10.5194/hess-26-1545-2022

Hong, S.-Y., and Pan, H.-L. (1996). Nonlocal boundary layer vertical diffusion in a medium-range forecast model. *Mon. Weather. Rev.* 124, 2322–2339. doi:10.1175/1520-0493(1996)124,2322:NBLVDI.2.0.CO;2

Hong, S.-Y., and Lim, J.-O. J. (2006). The WRF single-moment 6-class microphysics scheme (WSM6). *J. Korean Meteor. Soc.* 42 (2), 129–151.

Krishnamurti, T. N., Kishtawal, C. M., Timothy, T., Bachiochi, D. R., Zhang, Z., Williford, C. E., et al. (1999). Improved weather and seasonal climate forecasts from multimodel super ensemble. *Science* 285 (5433), 1548–1550. doi:10.1126/science.285.5433.1548

Lorenz, E. N. (1963). Deterministic nonperiodic flow. *J. Atmos. Sci.* 20 (2), 130–141. doi:10.1175/1520-0469(1963)020<0130:dnf>2.0.co;2

Mlawer, E. J., Taubman, S. J., Brown, P. D., Iacono, M. J., and Clough, S. A. (1997). Radiative transfer for inhomogeneous atmospheres: RRTM, a validated correlated-k model for the longwave. *J. Geophys. Res.* 102, 16663–16682. doi:10.1029/97JD00237

Murphy, A. H. (1988). Skill scores based on the mean square error and their relationships to the correlation coefficient. *Mon. Weather Rev.* 116 (12), 2417–2424. doi:10.1175/1520-0493(1988)116<2417:ssbotm>2.0.co;2

Patel, R. N., Yuter, S. E., Miller, M. A., Rhodes, S. R., Bain, L., and Peele, T. W. (2021). The diurnal cycle of winter season temperature errors in the operational Global Forecast System (GFS). *Geophys. Res. Lett.* 48, e2021GL095101. doi:10.1029/2021gl095101

Scaff, L., Prein, A. F., Li, Y., Liu, C., Rasmussen, R., and Ikeda, K. (2019). Simulating the convective precipitation diurnal cycle in North America's current and future climate. *Clim. Dynam.* 55, 369–382. doi:10.1007/s00382-019-04754-9

Svensson, G., and Lindvall, J. (2015). Evaluation of near-surface variables and the vertical structure of the boundary layer in CMIP5 models. *J. Clim.* 28, 5233–5253. doi:10.1175/jcli-d-14-00596.1

Takacs, L. L., Suárez, M. J., and Todling, R. (2018). The stability of incremental analysis update. *Mon. Weather Rev.* 146 (10), 3259–3275. doi:10.1175/mwr-d-18-0117.1

Wang, L. L., and Chen, D. H. (2013). Improvement and experiment of hydrological process on GRAPES NOAH-LSM land surface model. *China. J. Atmos. Sci.* 37 (6), 1179–1186. doi:10.3878/j.issn.1006-9895.2013.1210

Wu, H. Y., Du, Y. D., and Qin, P. (2011). Climate characteristics and variation of rainstorm in South China. *Meteorol. Mon.* 37 (10), 1262–1269. doi:10.7519/j.issn.1000-0526.2011.10.009 (in Chinese).

Xue, J. S., and Chen, D. H. (2008). *Scientific design and application of GRAPES numerical prediction system*. Beijing: Science Press, 383pp. (in Chinese).

Zhang, B., Tallapragada, V., Weng, F., Sippel, J., Zaizhong, M. A., and Group, I. (2016). Estimation and correction of model bias in the nasa/gmao geos5 data assimilation system: Sequential implementation. *Adv. Atmos. Sci.* 33, 659–672. doi:10.1007/s00376-015-5155-y

frontiers | Frontiers in Earth Science

TYPE Original Research
PUBLISHED 28 February 2023
DOI 10.3389/feart.2022.1052517

OPEN ACCESS

EDITED BY
Sheng Chen,
Northwest Institute of Eco-Environment and Resources (CAS), China

REVIEWED BY
Chunsong Lu,
Nanjing University of Information Science and Technology, China
Yuanjian Yang,
Nanjing University of Information Science and Technology, China

*CORRESPONDENCE
Feng Xu,
gdouxufeng@126.com
Banglin Zhang,
zhangbl@gd121.cn

SPECIALTY SECTION
This article was submitted to Interdisciplinary Climate Studies, a section of the journal *Frontiers in Earth Science*

RECEIVED 24 September 2022
ACCEPTED 05 December 2022
PUBLISHED 28 February 2023

CITATION
Zhang S, Xu F, Xue Y, Xu D, Leung JC-H, Han L, Yang J, Zheng M, Li Y, Huang F and Zhang B (2023), Heat balance characteristics in the South China Sea and surrounding areas simulated using the TRAMS model—a case study of a summer heavy rain and a winter cold spell.
Front. Earth Sci. 10:1052517.
doi: 10.3389/feart.2022.1052517

Heat balance characteristics in the South China Sea and surrounding areas simulated using the TRAMS model—a case study of a summer heavy rain and a winter cold spell

Shaojing Zhang[1,2,3], Feng Xu[1,2]*, Yufeng Xue[1,2], Daosheng Xu[3], Jeremy Cheuk-Hin Leung[3], Liguo Han[1,2], Jinyi Yang[1,2], Meiying Zheng[1,2], Yongchi Li[1,2], Fei Huang[4] and Banglin Zhang[3]*

[1]College of Ocean and Meteorology, Guangdong Ocean University, Zhanjiang, China, [2]South China Sea Institute of Marine Meteorology, Guangdong Ocean University, Zhanjiang, China, [3]Guangzhou Institute of Tropical and Marine Meteorology/Guangdong Provincial Key Laboratory of Regional Numerical Weather Prediction, CMA, Guangzhou, China, [4]Zhuhai Meteorological Bureau, Zhuhai, Guangdong, China

Introduction: This study is first to apply d iagnostic analysis of the forecast tendencies to evaluate the simulation of equilibrium features in the South China Sea and its surrounding areas using The Tropical Regional Atmosphere (TRAMS) model, and further identify the sources of simulation biases of the model.

Methods: On the basis of the quasi equilibrium between dynamic and physical processes, the deviation of net forecast tendencies, which reflects the overall equilibrium of the model, serves as a good indicator of the model simulations bias. The sources of the forecast error can be further inferred by decomposing the net forecast tendencies into the dynamic and each physical process.

Results: Focusing on moisture and temperature tendencies, the results show that the TRAMS model generally captures the thermal equilibrium characteristics and the contributions of each physical process, which are markedly different between summer and winter and are affected by the Northwest Pacific Subtropical High (WPSH) and deep trough of East Asia respectively. Furthermore, the underestimation of vapour consumption by cloud microphysical parameterisation and the overestimation of sea surface heat flux by boundary layer parameterisation near the surface contribute the most to systematic model bias. The temperature bias from 900 to 300 hPa during winter mainly originates from the responses of radiation, cumulus convection, and cloud microphysical parameterisations because water vapour absorbs long wave radiation, heating the atmosphere, and clouds reduce short wave radi ation absorption, cooling it.

Discussion: The presented analyses provide a reference for further optimisation and improvement of the model.

KEYWORDS

model diagnosis, forecast tendencies, thermal equilibrium, systematic bias, physical parameterization

1 Introduction

The dynamical core and physical parameterisation schemes are two important components of the numerical model. The dynamical core involves the numerical calculation of advection, convection, and diffusion on a discrete grid, whereas the physical parameterisation schemes control the sub-grid process related to energy source sinks (Droegemeier et al., 1991; Chen et al., 2008; Skamarock et al., 2008). Commonly used physical parameterisation schemes include cumulus convection, cloud microphysical, atmospheric boundary layer, radiation, and land surface process parameterisations. During integration, the model dynamical core is first called; each physical process parameterisation scheme is then called sequentially. After calculating the tendencies of the dynamic and physical processes, they are multiplied by the time step and added to the state of the atmospheric field at the previous time step to obtain the forecast field of the next timestep. Forecast tendencies refer to the changing rate of variables, such as temperature and moisture, with time. Thus, forecast tendencies can be regarded as the response of each component to the current atmospheric state.

The dynamic and physical processes usually maintain a quasi-equilibrium state in the actual atmosphere. For example, during the cumulus convection process, the instability energy created by large-scale processes (advection, radiation, and near-surface turbulence) is almost completely consumed by small- and medium-scale convective processes at the same rate, which contributes to the basis of the mass-flux-based convective parameterisation scheme (Yanai et al., 1973; Arakawa and Schubert, 1974). In the context of forecast tendency, the sum of tendencies (i.e., the net tendency) from the dynamical core and different physical parameterisation schemes can be seen as an indicator of the equilibrium in the model atmosphere. For example, the boundary layer process transports vapour from the near surface, and cumulus convection and cloud microphysical parameterisation consume the vapour through the formation of clouds. Their joint effects approximately result in a thermal quasi-equilibrium of moisture in the lower troposphere.

Owing to the shortcomings in the design of the individual module schemes, the model forecast tendency bias may affect the general equilibrium features in numerical simulations. Early studies (Rodwell and Palmer, 2007; Martin et al., 2010; Zhang et al., 2011; Kay et al., 2011; Williams et al., 2013; Klocke and Rodwell, 2014; Crawford et al., 2020; Wong et al.,.2020) demonstrated a clear correspondence between the model's net forecast tendencies and forecast biases and that diagnostic analyses of the tendencies of each process can reveal their contributions to the simulation results (Klinker and Sardeshmukh, 1992; Phillips et al., 2004; Rodwell et al., 2010; Ma et al., 2016; Chen et al., 2021).

Therefore, to improve the accuracy of numerical weather models, diagnostic analyses of the tendencies from dynamic processes and each physical process (such as radiation, cumulus convection, and cloud microphysical processes) are important to optimise the dynamical core and physical parameterisation schemes (Tron and Davis, 2012). Cavallo et al. (2016) applied this method to diagnose the region model first and found that erroneously strong low-level heating originates from the boundary layer parameterisation impacting the upward sensible heat fluxes.

The Tropical Regional Atmosphere Model (TRAMS), developed and operated by the Guangzhou Institute of Tropical Marine Meteorology of the China Meteorological Administration, focuses on numerical weather prediction in the South China Sea and surrounding areas. Previous studies have indicated that the simulation of TRAMS usually has errors due to the weak typhoon intensity, inaccurate summer rainstorm location, and slow cold front movement (Chen et al., 2016; Xu et al., 2019; Li et al., 2021; Lin et al., 2022). However, the sources of its systematic forecast bias remain unclear because of the lack of a diagnostic method for the dynamic core and physical parameterisation schemes. At present, the tendency analysis method provides an effective means of searching for sources of error. The weather systems and causes of model error are different in winter and summer. The analysis of typical atmospheric circulation during the seasons is expected to provide a reference for further optimisation and improvement of the simulation in the South China Sea and surrounding areas.

The paper is organised as follows: Section 2 introduces the model, cases, and diagnostic method used in the experiment; Section 3 analyses the forecast tendency characteristics of each physical process; the relationships among them are discussed in Section 4; and Section 5 provides the conclusions and discussion.

2 Description of model, case, and method

2.1 Model and data

The data used in this study included operational analysis and forecast data (grid 0.09° × 0.09°) from the European Centre for Medium-Range Weather Forecasts (ECMWF) and fifth-generation ECMWF atmospheric reanalysis of the global climate reanalysis data (ERA5) (gridded 0.25° × 0.25°). The TRAMS model domain covers an area of 81.6°E–160°E and 0.8°N–50.8°N (Figure 1), with a horizontal resolution of 9 km and terrain following the vertical coordinates of 65 layers up to 31 km. The initial and lateral boundary fields are obtained from the global analysis data of the ECMWF (gridded at 0.09° × 0.09°), and the lateral boundary condition is updated every 6 h. The integration time step of the model is 90 s. The physics schemes included the WRF single-moment 6-class (WSM6) microphysical scheme (Hong et al., 2004), the improved New Simplified

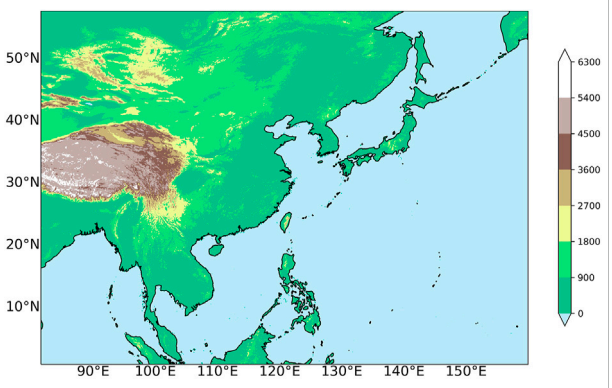

FIGURE 1
Model domain (the filled colours in the figure indicate terrain height).

Arakawa-Schubert (NSAS) cumulus parameterisation scheme (Han and Pan, 2011; Xu et al., 2015), the New Medium-Range Forecast (NMRF) planetary boundary layer scheme (Hong and Pan, 1996; Zhang et al., 2022), the RRTMG long-wave and short-wave radiation schemes (Laconao et al., 2008), and the slab land-surface model (Dudhia et al., 1996).

2.2 Description of the case study

This study focused on two typical weather types in South China: 1) heavy summer rain and 2) cold winter spells. The cases were heavy rain from 1200 UTC 21 to 1200 UTC 24 May 2020 and cold spells from 0000 UTC 27 to 0000 UTC 30 December 2020. The mean circulation of heavy rain from ERA5 showed that South China was at the bottom of the deep trough of East Asia and behind the eastward short-wave trough (Figure 2A), which is a typical circulation for the rainstorms in South China (Xu et al., 2016). The mean circulation of winter cold spells is characterised by a low-pressure trough and cold tongue overlap in most of the country, with dense isothermal lines in South China (Figure 2B), which is also a typical circulation of cold spells. Therefore, we selected these two typical weather types to evaluate the simulation of thermal equilibrium characteristics in the South China Sea and surrounding areas using TRAMS.

2.3 Method

According to the method proposed by Klinker and Sardeshmukh (1992), during data assimilation, analysis at the previous time i-1 and the state of the atmosphere of this forecast at the lead time (ΔX_i) are used to initialise the "first-guess" forecast (FC_i):

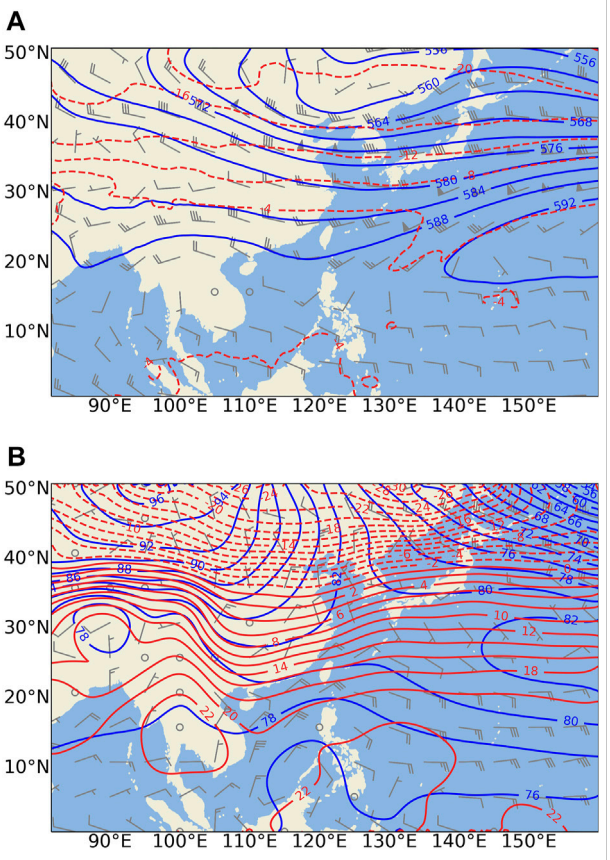

FIGURE 2
Mean circulation from ERA5 reanalysis data. **(A)** 500 hPa of summer heavy rain; **(B)** 925 hPa of winter cold spell. Potential height (blue line, dgpm, temperature (red line, °C); wind (vector, m/s).

$$FC_i \equiv AN_{i-1} + \Delta X_i. \quad (1)$$

The analysis increment (INC_i) is derived by "optimally combining" information from various observations and then adding it to the first-guess forecast. The updated analysis at time i (AN_i) is calculated as follows:

$$AN_i = FC_i + INC_i. \quad (2)$$

Although the new observations have errors and cannot completely describe the atmospheric state, if the new analysis is closer to the truth than the first-guess forecast, these increments can be informative in identifying the model errors. The forecast error (FE_i) during mode integration can be derived from Eqs 1, 2 as

$$FE_i \equiv FC_i - AN_i (= -INC_i) = AN_{i-1} + \Delta X_i - AN_i. \quad (3)$$

Hence, the forecast error is considered negative for the increment. If the observation and first-guess forecast are exactly correct, then the increment is zero. Assuming that the

observation errors are random and that the sample is sufficient, the mean observation error is zero. Thus, the non-zero analysis increment is due to errors in the model's representation of the atmosphere's dynamic or physical processes.

By averaging Eq. 3 over n consecutive analysis cycles and with $\bar{Y} = \frac{\sum_{i=1}^{n} Y_i}{n}$,

$$\overline{FE} = -\overline{INC} = \overline{\Delta X} - \frac{AN_n - AN_0}{n}. \tag{4}$$

The term $\frac{AN_n - AN_0}{n}$ is the evolution of the flow over the time span of n analysis cycles. Depending on the length of n, this can include the daily or annual of the atmosphere. However, we assume that this term is negligible relative to the forecast error.

Considering the first-guess forecast as an average tendency over the time window ($\bar{\dot{X}} = \frac{\overline{\Delta X}}{\Delta t}$) and decomposing it into the contribution from each process represented in the model (Cavallo et al., 2016),

$$\overline{FE} = -\overline{INC} \approx \bar{\dot{X}}\Delta t = \left(\bar{\dot{X}}_{Dyn} + \bar{\dot{X}}_{Rad} + \bar{\dot{X}}_{Gwd} + \bar{\dot{X}}_{Vdif} + \bar{\dot{X}}_{Conv} + \bar{\dot{X}}_{Cloud} + \ldots + \bar{\dot{X}}_{res}\right)\Delta t, \tag{5}$$

where the right-hand brackets of the equation indicate the dynamics, radiation, gravity spell drag, vertical diffusion, convection, cloud, and other residential tendencies. The last term in the mean is usually ignored. Eq. 5 implies the theoretical correspondence of the model tendency and error, and the systematic forecast bias of the model can be regarded as the deviation of the net tendency with respect to the equilibrium state (net tendency equal to 0); while the dynamical core and physics schemes of the model should be in a quasi-equilibrium state in the ideal case, the deviation of the forecast tendency with respect to 0 (net tendency) can be used to assess the overall equilibrium features of the model. By decomposing the net forecast tendencies into the dynamical and each physical tendency, their contributions to simulations under different weather conditions can be further estimated.

3 Comparative analysis of moisture and temperature tendencies

Because of the weak baroclinicity of the tropical weather system in the South China Sea and its surrounding area, the convective instability energy mainly comes from the latent heat released by the condensation of warm and humid airflow in the lower troposphere. Therefore, we mainly discuss the thermal equilibrium characteristics of the TRAMS model from the perspective of temperature and water vapour. The moisture ($\bar{q}$) and temperature ($\bar{T}$) tendencies of the dynamical and each physical parameterisation scheme during model integration can be written as

$$\frac{\partial \bar{T}}{\partial t} = \underbrace{-\bar{u}\frac{\partial \bar{T}}{\partial x} - \bar{v}\frac{\partial \bar{T}}{\partial y} - \bar{w}\frac{\partial \bar{T}}{\partial z}}_{Dyn} + Bl + Conv + Cloud + Rad, \tag{6}$$

$$\frac{\partial \bar{q}}{\partial t} = \underbrace{-\bar{u}\frac{\partial \bar{T}}{\partial x} - \bar{v}\frac{\partial \bar{T}}{\partial y} - \bar{w}\frac{\partial \bar{T}}{\partial z}}_{Dyn} + Bl + Conv + Cloud, \tag{7}$$

where $(\bar{u}, \bar{v}, \bar{w})$ are the three-dimensional wind field and Bl, Conv, Cloud, and Rad are the source-sink terms of the boundary layer, cumulus convection, cloud microphysical, and radiation parameterisations, respectively. The first three terms on the right-hand side of Eqs 6, 7 represent the advection process in the grid scale, which corresponds to the tendency of the dynamical core. According to the aforementioned two equations, the thermodynamic balance characteristics and contributions of each component in various weather systems can be determined.

3.1 Analysis of moisture and temperature tendencies from dynamic and total physics

First, the tendencies of each integration step are summed to get 72-h accumulated tendencies. Second, the regional average of the accumulated tendencies is calculated. Finally, we add the averaged tendencies of the dynamic (Dyn) and the physical (Phy) processes to obtain the net forecast tendencies (Net) (Figure 3).

The deviations in moisture tendencies are mainly concentrated below 200 hPa (troposphere) in both summer and winter (Figures 3A,B). Regardless of the season, because of water vapour transport from the near-surface by the vertical movement of the grid-scale (the third term on the right side of Eq. 7), the dynamic tendencies of moisture exhibit negative values near the surface, while showing a vertically extended positive value in the middle and upper troposphere, with a maximum at 950 hPa in summer (-4×10^{-3} g/kg) and winter (-7×10^{-3} g/kg). The physical and dynamic tendencies are roughly the opposite. The positive physical tendencies in the lower layers are attributed to the upward diffusion of evaporated water vapour from the near-surface and the evaporation of raindrops, whereas the negative physical tendencies in the middle and upper layers are mainly attributed to the water vapour condensation of the cumulus convection and cloud microphysical parameterisation. However, a net moisture tendency imbalance remains, with relatively obvious positive values from 925 to 700 hPa in both summer and winter, which suggests that the TRAMS overestimates moisture at 925–700 hPa in the South China Sea and its surrounding areas, with the same maximum value at 900 hPa (1×10^{-3} g/kg).

The temperature tendencies differed between summer and winter (Figures 3C,D), with deviations mainly below 250 hPa in

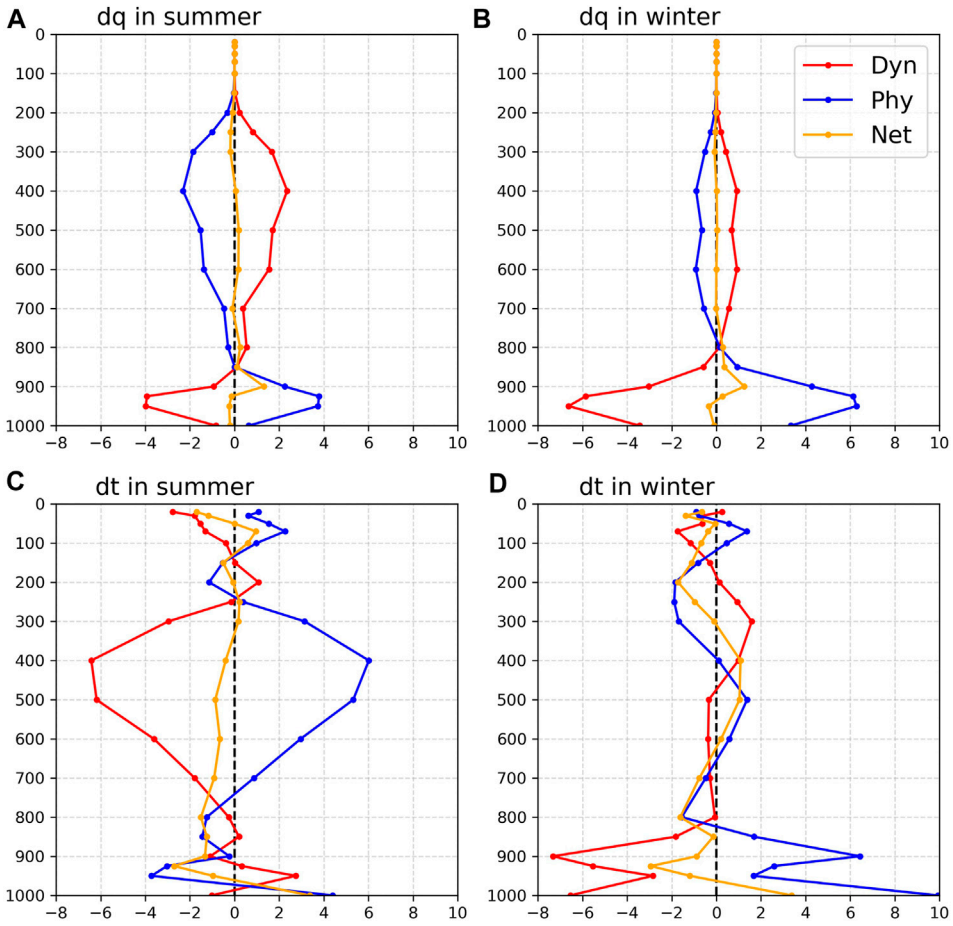

FIGURE 3
Regional average vapour and temperature tendencies. **(A)** Summer vapour tendency. **(B)** Winter vapour tendency. **(C)** Summer temperature tendency (°C). **(D)** Winter temperature tendency; dynamic process tendency (red line), physical process tendency (blue line), and net tendency (yellow).

summer and below 800 hPa in winter. During summer, the convection is relatively strong and deep; thus, the physical tendency is mainly positive in the middle and upper troposphere, with a maximum at 400 hPa (6°C) for strong latent heat release. Meanwhile, the dynamic process transports heat from the South China Sea and its surrounding regions to the middle and high latitudes through Hadley circulation and then reach temperature equilibrium. In the lower troposphere, the positive dynamic tendency originates from the warm and humid airflow brought by the southerly wind, while the negative physical tendency is mainly caused by the evaporation of raindrops, which absorb the heat from the atmosphere. In winter, the convection is relatively weak and shallow, resulting in a smaller positive physical tendency in the middle troposphere at 400–100 hPa. However, the negative tendency of the dynamic process near the surface, with a maximum at 900 hPa (6.5°C), mainly originates from the cold advection, and the greater temperature differences between the sea surface and atmosphere cause the physical process to deeply heat the lower atmosphere. The dynamic and physical tendencies are inverse between summer and winter, as discussed later.

Under the joint effect of dynamic and physical processes, the net temperature tendencies showed a negative bias in the forecast temperature in the lower troposphere, with a maximum value (-3°C) at 925 hPa in the simulation of the South China Sea and its surrounding areas during summer. The differences in temperature tendencies between summer and winter are centered at 600–300 hPa, whereas positive tendencies are observed in winter. In addition, the temperature deviation above the tropopause mainly originates from the mode dynamical core, which may be related to the low top height of the model.

The comparison between summer and winter showed that the moisture and temperature tendency deviations were mainly concentrated in the middle troposphere during the summer and in the lower troposphere during the winter. The similarity in the

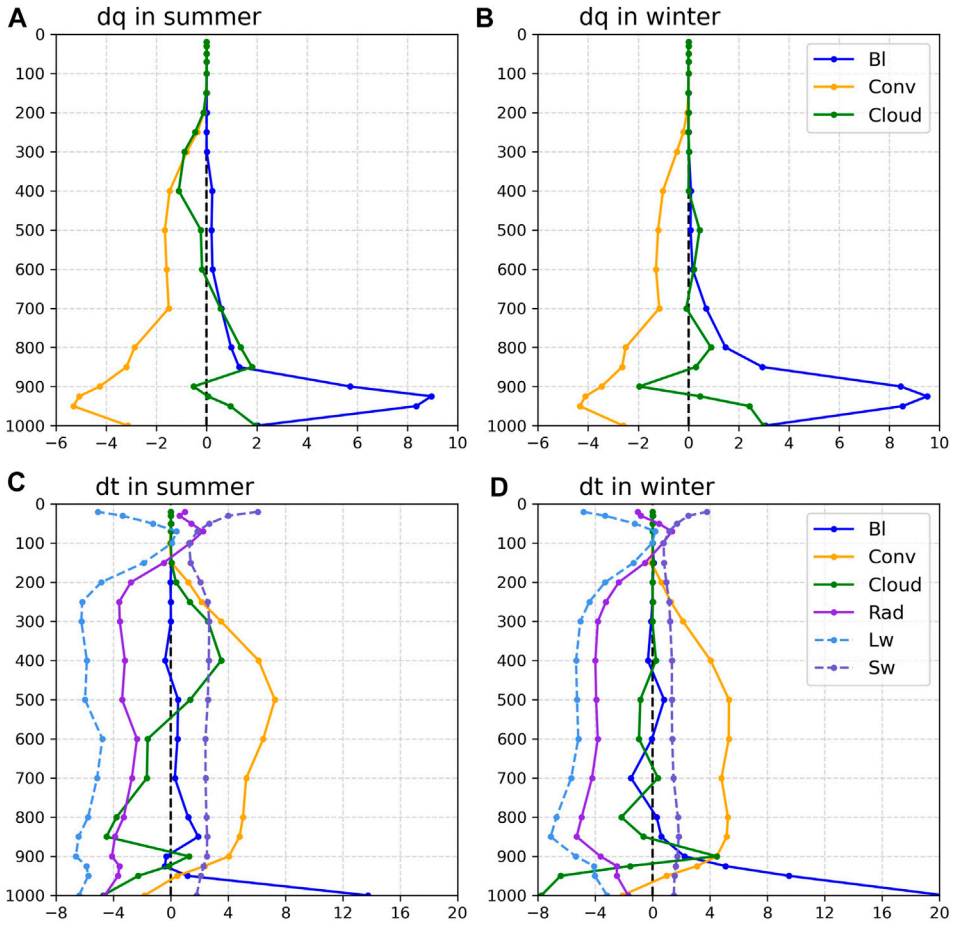

FIGURE 4
Regional average vapour and temperature tendencies from each physical scheme. **(A)** Summer vapour tendency (10^{-3} g/kg). **(B)** Winter vapour tendency (10^{-3} g/kg). **(C)** Summer temperature tendency (°C). **(D)** Winter temperature tendency (°C).

simulation errors of moisture and temperature between summer and winter at the lower troposphere may be the result of systematic bias in the model due to shallow or weak convection. Thus, the consumption of water vapour is low and the release of latent heat is insufficient, resulting in a cold and wet lower layer. However, the differences in the simulation errors, especially those in the middle troposphere during winter, may originate from the bias in the response of the physical parameterisation schemes, which will be discussed in the next section.

3.2 Analysis of moisture and temperature tendencies for individual physical processes

The regional average moisture tendencies from the boundary layer (BL), cumulus convection (Conv), and cloud microphysical (Cloud) processes are shown in Figures 4A,B. The variation trends in moisture tendencies for each physical process were similar in the summer and winter. The vapour in the lower troposphere mainly comes from water evaporation from the ground and sea surface. Therefore, the moisture regional average tendencies of the boundary layer process were mainly positive, with the same maximum at 925 hPa in both summer and winter (9×10^{-3} g/kg). The high temperature and humidity in the lower troposphere enhance low-level instability and favour convection that transports vapour upward further. Hence, the regional average moisture tendencies of the cumulus convection process were mainly negative throughout the troposphere, reaching the same minimum at 950 hPa (5×10^{-3} g/kg) in both summer and winter.

Generally, the stronger the deep convection, the higher the cloud. Hence, the moisture tendency in the cloud microphysical process is mainly negative for vapour condensation in the upper troposphere and positive for

water evaporation in the middle and lower troposphere during summer. This occurs mainly in the lower troposphere during winter due to weak convection.

The regional average temperature tendencies of the boundary layer (BL), cumulus convection (Conv), cloud microphysical (Cloud), radiation (Rad), long-wave radiation (Lw) process, and short-spell radiation (Sw) processes are shown in Figures 4C,D. The heat from the ground and sea surface has a moderating effect on the temperature near the surface; therefore, the boundary layer process mainly contributed positively to the temperature at the low level, reaching a maximum at 1000 hPa in both summer (14°C) and winter (20°C). However, a negative tendency was also observed at 800–600 hPa in winter, which may be related to the turbulent entrainment process near the tops of stratocumulus clouds. During the cumulus convection process, the lifted vapour condenses and releases latent heat, which heats the atmosphere. Therefore, the temperature tendencies are mainly positive, with a maximum at 500 hPa in summer (7°C) and winter (5°C).

Vapour condensation releases heat and increases the temperature, and water evaporation absorbs heat and decreases the temperature. In the cloud microphysical process, the temperature is influenced by the phase change of the vapour. Hence, the temperature and moisture tendencies of the cloud microphysical process are approximately inverse. The troposphere is mostly cooled by long-wave radiation and heated by short-wave radiation. The long-wave radiation temperature tendencies are 2–3 times higher than those of short-wave radiation; therefore, the radiation process mainly cools the atmosphere. Above the boundary layer, the tendencies of the radiation and convection processes are almost in equilibrium.

In conclusion, the contributions of each physical process to the thermal equilibrium simulated by the TRAMS are generally reasonable in the South China Sea and surrounding areas. The regional average moisture and temperature tendencies of each physical process reveal that the boundary layer parameterisation always has positive contributions to moisture and temperature in the lower troposphere by transporting water vapour and heat from the near-surface to the lower troposphere. The cumulus convection parameterisation has negative contributions to moisture and temperature in the lower troposphere to further transport water vapour and heat, whereas it has a negative contribution to moisture and a positive contribution to temperature for water vapour condensation and latent heat release. The cloud microphysical parameterisation has positive contributions to moisture and negative contributions to temperature for water evaporation and heat absorption and opposite contributions to the middle and upper troposphere for water vapour condensation and latent heat release. However, the contribution altitude of cloud microphysical parameterisation differs between winter and summer owing to the convection.

In addition, the negative temperature tendencies in summer and bias of temperature tendencies from 900 to 300 hPa in winter mainly come from the radiation parameterisation, which may be affected by the cumulus convection and cloud microphysical parameterisation (cf. Figures 3,4) because water vapour absorbs long-wave radiation to heat the atmosphere and clouds reduce short-wave radiation absorption to cool the atmosphere. Additionally, the inverse temperature tendencies of the dynamic and physical tendencies originate from the height of the cloud microphysics latent heat release and heating influence of the boundary layer (cf. Figures 3C,D,4C,D,5E,F).

3.3 Further analysis of moisture and temperature tendencies from BL, Conv, and Cloud

Next, we analysed the latitudinal average and horizontal patterns with an apparent deviation of the boundary layer, cumulus convection, and cloud microphysical processes, which have a major effect on moisture and temperature predictions.

The moisture and temperature tendencies of the boundary layer process were mainly observed in the lower troposphere in both cases, especially over the ocean and coastal areas (Figure 5), which are mainly influenced by turbulent diffusion. During the summer, vapour and heat are mainly observed over Kuroshio and the downwelling area controlled by the WPSH (Figure 5C). In addition, a positive temperature tendency was observed at the bottom of the troposphere (Figure 5E). During the winter, the atmosphere energy mainly comes from the ocean; thus, the boundary layer process has a wider and higher influence on moisture and temperature compared to that in the summer, especially in the mid-latitudes, where the temperature differences between the sea surface and atmosphere are large. In addition, the warm and moist air was lifted by the topography of the Tibetan Plateau to condense and release latent heat near the height of 500 hPa at 80°E–120°E (Figures 5E,F). A comparison of net temperature tendencies revealed that the positive tendencies near the surface may be attributed to the overestimation of the sea surface heat flux by the boundary layer parameterisation (cf. Figures 3C,D,5E,F), which is consistent with the conclusion reported by Cavallo et al. (2016).

The moisture and temperature tendencies of the cumulus convection process are displayed in Figure 6. By transporting vapour and heat from the surface, the boundary layer process potentially enhance instability in the lower troposphere and favour the development of convection, which further transports vapour upward and heats the atmosphere with latent heat. Thus, the value of the tendencies is higher in summer owing to the more vigorous and deeper convection.

10.3389/feart.2022.1052517

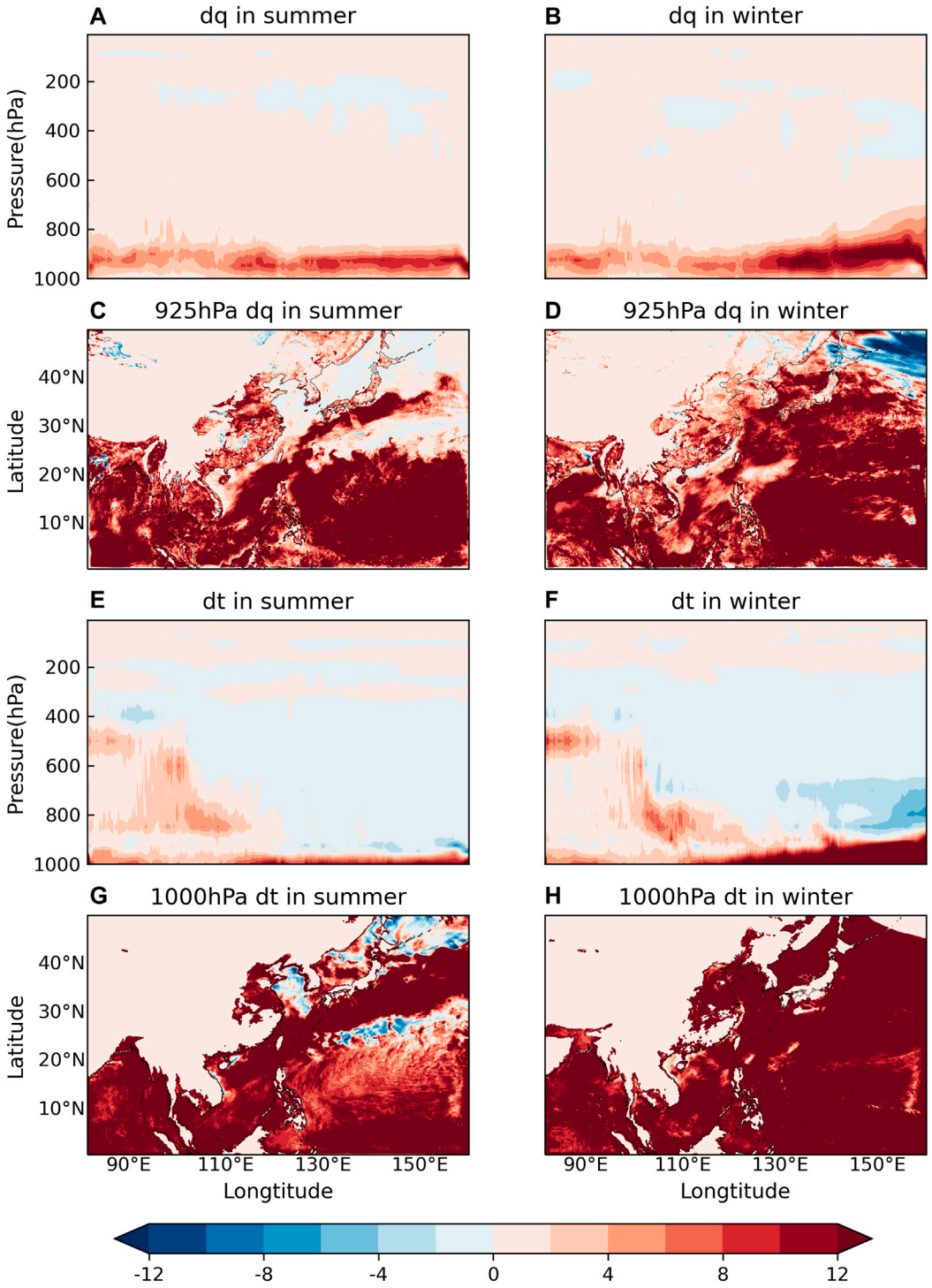

FIGURE 5
Vapour and temperature tendencies of the boundary layer process. **(A–D)** Vapour tendency (10−3 g/kg). **(E–H)** Temperature tendency (°C). **(A,E)** Latitudinal average cross-section in the summer. **(B,F)** Latitudinal average cross-section in the winter. **(C)** 925 hPa in the summer. **(D)** 925 hPa in the winter. **(G)** 1000 hPa in the summer. **(H)** 1000 hPa in the winter.

10.3389/feart.2022.1052517

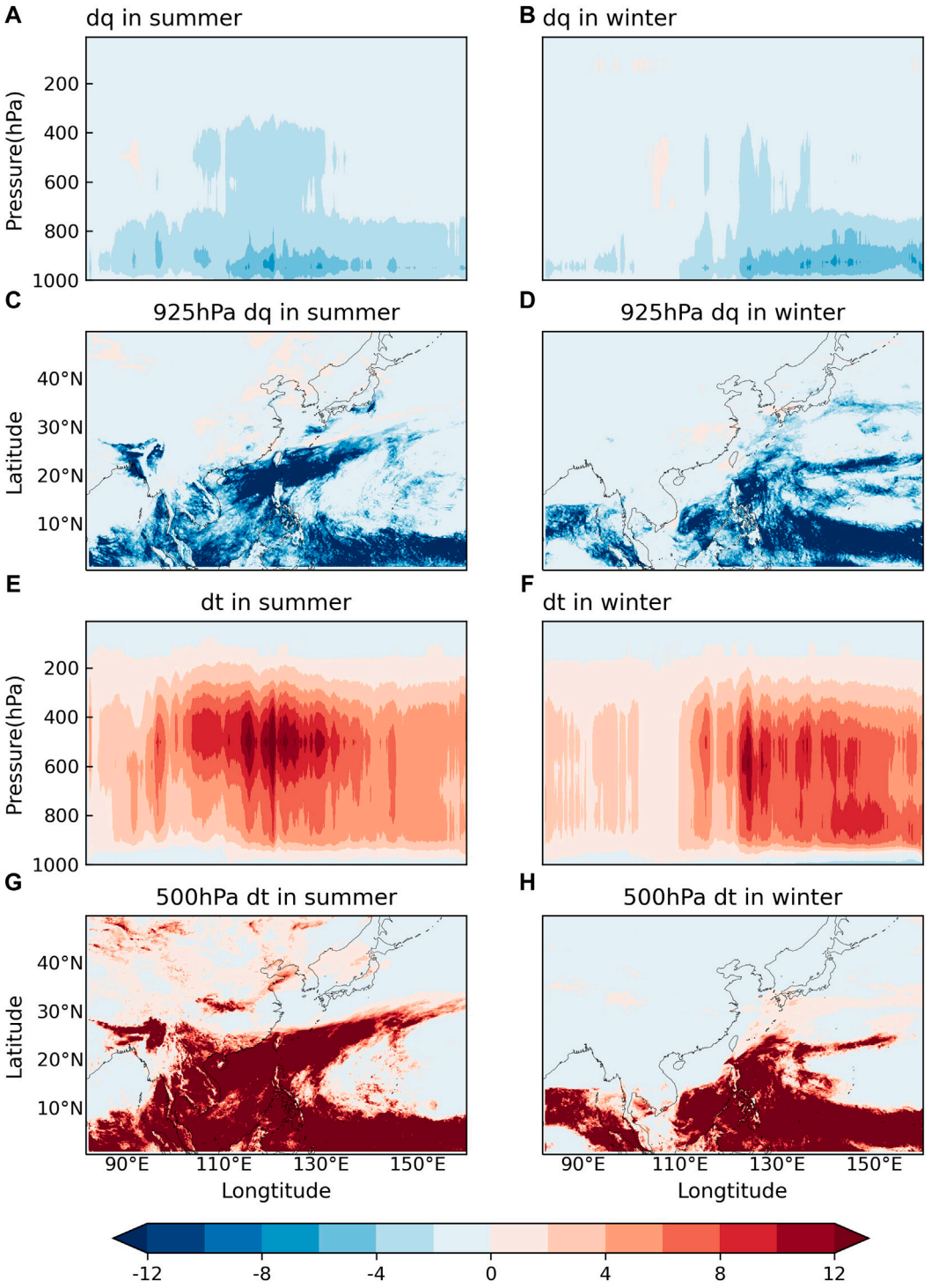

FIGURE 6
Vapour and temperature tendencies of the cumulus convection process. **(A–D)** Vapour tendency (10−3 g/kg). **(E–H)** Temperature tendency (°C). **(A,E)** Latitudinal average cross-section in the summer. **(B,F)** Latitudinal average cross-section in the winter. **(C)** 925 hPa in the summer. **(D)** 925 hPa in the winter. **(G)** 500 hPa in the summer. **(H)** 500 hPa in the winter.

10.3389/feart.2022.1052517

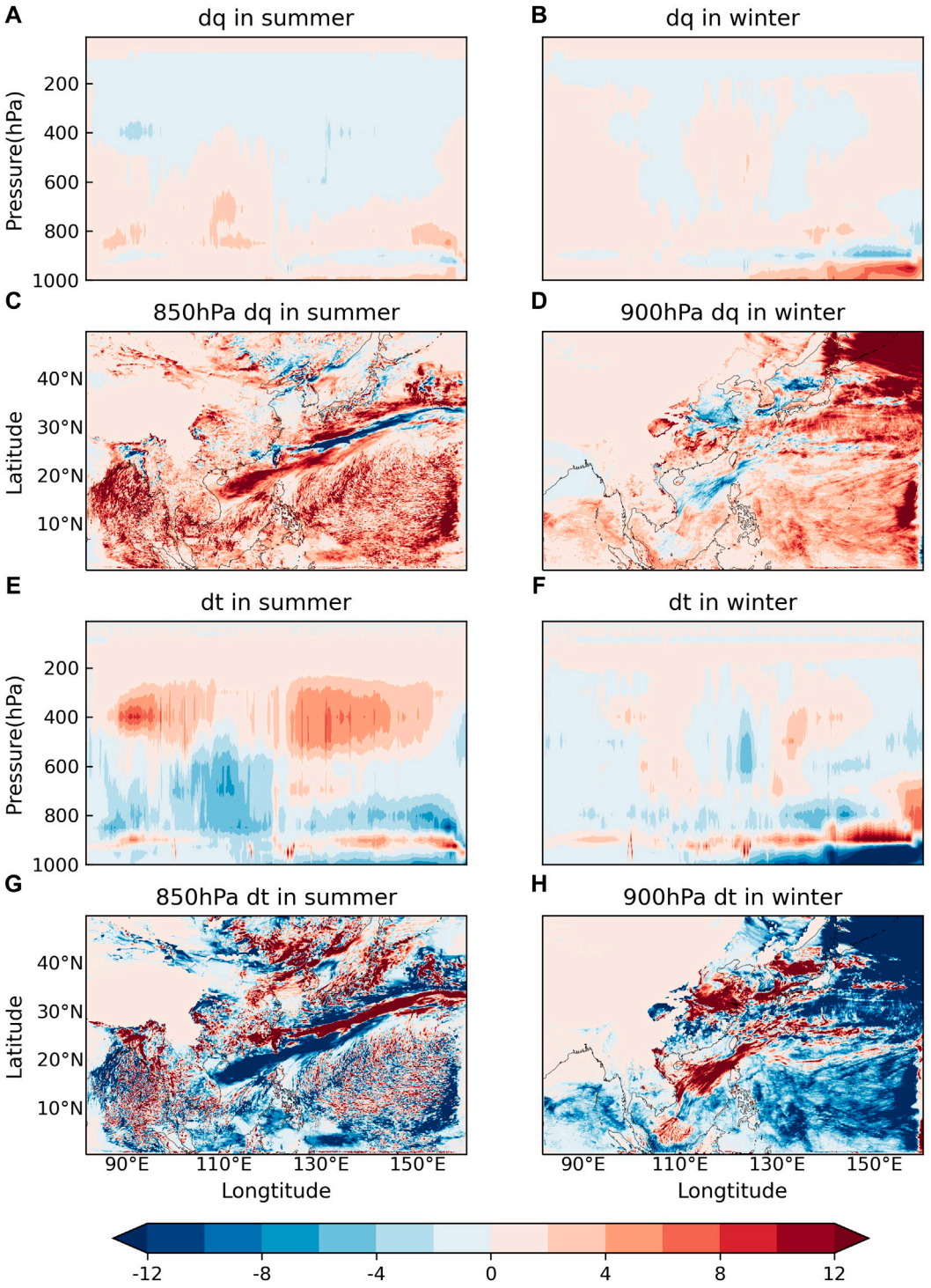

FIGURE 7
Vapour and temperature tendencies of the cloud microphysical process. **(A–D)** Vapour tendency (10−3 g/kg). **(E–H)** Temperature tendency (°C). **(A,E)** Latitudinal average cross-section in the summer. **(B,F)** Latitudinal average cross-section in the winter. **(C)** 850 hPa in the summer. **(D)** 900 hPa in the winter. **(G)** 850 hPa in the summer. **(H)** 900 hPa in the winter.

TABLE 1 Correlation coefficients of the vapour tendencies for each process in the summer.

Process	Physics	Boundary layer	Cumulus convection	Qv in cloud	Qc in cloud
Boundary layer	0.901*				
Cumulus convection	−0.695*	−0.882*			
Qv in cloud	0.342	0.195	−0.422		
Qc in cloud	0.554*	0.646*	−0.852*	0.617*	
Qi in cloud	0.523*	0.316	−0.291	0.491	0.396

Note: Qv in the cloud indicates the tendency of water vapour caused by cloud microphysical processes. Thus, Qc (liquid water) and Qi (ice) are in the cloud.

TABLE 2 Correlation coefficients of the vapour tendencies for each process in the winter.

Process	Physics	Boundary layer	Cumulus convection	Qv in cloud	Qc in cloud
Boundary layer	0.959*				
Cumulus convection	−0.844*	−0.908*			
Qv in cloud	0.347	0.157	−0.352		
Qc in cloud	0.825*	0.877*	−0.953*	0.322	
Qi in cloud	−0.092	0.010	−0.003	−0.401	0.140

TABLE 3 Correlation coefficients of the temperature tendencies for each process in the summer.

Process	Physics	Boundary layer	Cumulus convection	Cloud
Boundary layer	0.253			
Cumulus convection	0.258	−0.325		
Cloud	0.356	−0.598*	0.152	
Radiation	0.059	−0.325	−0.502	0.180

TABLE 4 Correlation coefficients of the temperature tendencies for each process in the winter.

Process	Physics	Boundary layer	Cumulus convection	Cloud
Boundary layer	0.795*			
Cumulus convection	−0.125	−0.388		
Cloud	−0.359	−0.806*	0.320	
Radiation	0.036	0.059	−0.817*	−0.014

Note: * indicates that the 95% confidence check was passed.

Furthermore, a southwest–northeast zone with relatively obvious temperature tendencies is observed in South China during the summer (Figure 6G), corresponding to the rainfall zone. While related to the deviation of temperature tendencies, once the deep convection is triggered, the consumption of vapour and formation of clouds reduces the absorption of both long-wave and short-wave radiation and cools the atmosphere.

In the cloud microphysical process, the moisture tendencies are mainly negative (Figures 7A,B), and the temperature tendencies are usually positive (Figures 7E,F) when vapour condenses into drops and ice in the cloud

after lifting to the condensation height by convection. The clouds are usually higher and more widespread in summer but be lower and concentrated over the ocean in winter. Moisture and temperature tendencies are mainly affected by the WPSH in summer and the deep trough of East Asia in winter (cf. Figures 2, 7C,D,G,H). The warm and moist airflow brought by the southwesterly wind meets the cold and dry airflow moving southward at the northern branch of the WPSH, which is conducive to the convergence of vapour and the formation of clouds and rain. The deep trough of East Asia is also favorable for the upward movement and condensation of vapour. The moisture tendencies of the cloud microphysical process are mainly observed above the ocean in winter but expand to land in summer because of the westward extension of the WPSH. A comparison of net moisture tendencies showed that the positive tendencies in the lower troposphere may occur due to the underestimation of vapour consumption by the cloud microphysical parameterisation (cf. Figures 3A,B,5E,F).

The boundary layer process transports vapour and energy to the lower troposphere *via* turbulent diffusion and is conducive to the development of convection. After lifting to the condensation height by convection, vapour condenses and is partly converted into raindrops and ice in the cloud in the cumulus convection and cloud microphysical processes, which heats the atmosphere through latent heat. Therefore, the WPSH and deep trough of East Asia, which favour the upward and convergence of airflow, primarily affect the moisture and temperature in the simulation of the South China Sea and its surrounding areas.

The results show that the underestimation of the vapour consumption by cloud microphysical parameterisation and the overestimation of the sea surface heat flux by boundary layer parameterisation yield relatively high moisture and temperature in the lower troposphere. The temperature forecast bias from 900 to 300 hPa is mainly caused by the responses of radiation, cumulus convection, and cloud microphysical parameterisations.

4 Correlation of moisture and temperature regional average tendencies from dynamic and physics

To further analyse the interactions of the dynamic and each physical process, we calculated the correlation coefficients of the regional average moisture and temperature tendencies from the dynamic and each physical process (each fold in Figure 4).

The boundary layer and cumulus convection processes showed major contributions to the moisture tendencies in both summer and winter and were always anti-correlated, with correlation coefficients as high as 0.882 in summer and 0.908 in winter (Tables 1,2). In addition, the obvious positive correlation between vapour (Qv) and water (Qc) in the cloud microphysical process during summer (correlation coefficient 0.617) suggested the important role of the warm cloud process in the cloud microphysical process.

None of the physical processes is significantly correlated with the total physical process in summer, and only the boundary layer process showed significant effects on temperature prediction in winter (Tables 3,4). The correlation coefficients of the boundary layer and the total physical processes in winter were larger than those in summer because the ground and ocean are the main sources of heat. In addition, the inverse relationship between the radiation process and cumulus convection process in winter also supported the idea that vapour consumption and cloud formation reduce the absorption of both long-wave and short-wave radiation and cool the atmosphere. Furthermore, their correlation coefficient was not low in the summer, although the difference was not statistically significant.

The boundary layer and cumulus convection processes contribute markedly to moisture and temperature prediction. Their interactions are important for the simulation of the thermal equilibrium. The importance of the boundary layer process can be inferred from its significant correlations with both temperature and moisture. In addition, the inverse relationship between the radiation and cumulus convection processes also supports the idea that the reduction of vapour by deep convection is favourable for radiation cooling.

5 Conclusion and discussion

Focusing on two typical weather types in the South China Sea and its surrounding areas, this study evaluated the thermal equilibrium simulated by the TRAMS in terms of forecast tendencies. By examining the contributions of the dynamic and each physical process, we identified the sources of simulation biases and provide a reference for further optimisation and improvement of the model. The conclusions are as follows.

1) The equilibrium characteristics of the model simulation are generally reasonable, showing that the dynamic and physical processes have opposite trends and largely balance each other. Consistent with the actual situation, moisture and temperature departures are mainly concentrated in the middle troposphere during the summer and in the lower troposphere during the winter.
2) The contributions of each physical process to the thermal equilibrium are generally reasonable; however, the differences between summer and winter are marked. The results showed that the underestimation of vapour consumption by cloud microphysical parameterisation and the overestimation of sea surface heat flux by the boundary layer parameterisation near the surface dominate the systematic bias of the model. The temperature bias from 900 hPa to 300 hPa during the winter mainly originates from the responses of radiation, cumulus convection, and cloud microphysical parameterisations. Water vapour absorbs long-wave radiation to heat the atmosphere, whereas clouds reduce short-wave radiation absorption to cool the atmosphere.

3) The WPSH and deep trough of East Asia, which are conducive to uplift and convergence, primarily affected the difference in each physical parameterisation response between summer and winter in the simulation of the South China Sea and its surrounding areas.

This study mainly focused on the evaluation of thermal equilibrium in the troposphere. However, relatively distinct deviations occur near the surface and above the stratosphere, the causes of which remain unclear. Furthermore, this study only analysed the thermal equilibrium of the dynamic and physical processes and the interaction of each physical process. Several other equilibria require further evaluation in this model. Studies are needed to compare the tendencies of the TRAMS to the standard tendency data provided by the Year of Tropical Convection (YOTC) project (Moncrieff et al., 2012) to analyse the deviation of each process and further evaluate its impact on the forecast.

Data availability statement

This study analyzed publicly available datasets. These data can be found at https://cds.climate.copernicus.eu/cdsapp#!/home.

Author contributions

SZ was responsible for the study conception, manuscript writing, and figure development. FX, BZ and YX provided guidance and funding support. DX and JC-HL were responsible for discussion and manuscript revision. LH, JY, MZ, YL, and FH were contributed to the conception and design of the work.

Funding

This study was supported by the Special Project for Research and Development in Key area of Guangdong Province (Grant 2020B0101130021) and the National Key Research and Development Program of China (Grant 2018YFC1506902).

Acknowledgments

We thank the Guangzhou Institute of Tropical Marine Meteorology of the China Meteorological Administration for providing the facilities to conduct the numerical analysis.

Conflict of interest

The authors declare that the research was conducted in the absence of any commercial or financial relationships that could be construed as a potential conflict of interest.

Publisher's note

References

Arakawa, A., and Schubert, W. H. (1974). Interaction of a cumulus cloud ensemble with the large-scale environment, Part I. *J. Atmos. Sci.* 31 (3), 674–701. doi:10.1175/1520-0469(1974)031<0674:ioacce>2.0.co;2

Cavallo, S. M., Berner, J., and Snyder, C. (2016). Diagnosing model errors from time-averaged tendencies in the weather research and forecasting (WRF) model. *Mon. Weather Rev.* 144 (2), 759–779. doi:10.1175/mwr-d-15-0120.1

Chen, D.-H., Xue, J.-S., Yang, X.-S., Zhang, H.-L., Shen, X.-S., Hu, J.-L., et al. (2008). New generation of multi-scale NWP system (GRAPES): General scientific design. *Sci. Bull. (Beijing).* 53 (22), 3433–3445. doi:10.1007/s11434-008-0494-z

Chen, X.-J., Liu, Q.-J., and Ma, Z.-S. (2021). A diagnostic study of cloud scheme for the GRAPES global forecast model. *Acta Meteorol. Sin. (in Chin.)* 79 (01), 65–78. doi:10.11676/qxxb2020.066

Chen, Z.-T., Dai, G.-F., Luo, Q.-H., Zhong, S.-X., Zhang, Y.-X., Xu, D.-S., et al. (2016). Study on the coupling of model dynamics and physical processes and its influence on the forecast of typhoons. *J. Trop. Meteorology* 32 (01), 1–8. doi:10.16032/j.issn.1004-4965.2016.01.001

Crawford, W., Frolov, S., McLay, J., Reynolds, C. A., Barton, N., Ruston, B., et al. (2020). Using analysis corrections to address model error in atmospheric forecasts. *Mon. Weather Rev.* 148 (9), 3729–3745. doi:10.1175/mwr-d-20-0008.1

Droegemeier, K. K., Xue, M., Reid, P. V., Straka, J., Bradley, J., III, and Lindsay, R. (1991). *The advanced regional prediction system (ARPS) version 2. 0: Theoretical and numerical formulation*. Oklahoma: Center for Analysis and Prediction of Storms Rep. CAPS91-001, 55.

Dudhia, J. (1996). *The Sixth PSU/NCAR mesoscale model users' workshop*. Boulder, CO, USA: National Center for Atmospheric Research, 49–50. A multi-layer soil temperature model for MM5.

Han, J., and Pan, H.-L. (2011). Revision of convection and vertical diffusion schemes in the NCEP global forecast system. *Weather Forecast.* 26 (4), 520–533. doi:10.1175/WAF-D-10-05038.1

Hong, S.-Y., Dudhuia, J., and Chen, S.-H. (2004). A revised approach to ice microphysical processes for the bulk parameterization of clouds and precipitation. *Mon. Weather Rev.* 132 (1), 103–120. doi:10.1175/1520-0493(2004)132<0103:aratim>2.0.co;2

Hong, S.-Y., and Pan, H.-L. (1996). Nonlocal boundary layer vertical diffusion in a medium-range forecast model. *Mon. Weather Rev.* 124 (10), 2322–2339. doi:10.1175/1520-0493(1996)124<2322:nblvdi>2.0.co;2

Iacono, M. J., Delamere, J. S., Mlawer, E. J., Shephard, M. W., Clough, S. A., and Collins, W. D. (2008). Radiative forcing by long-lived greenhouse gases: Calculations with the AER radiative transfer models. *J. Geophys. Res.* 113 (D13), D13103. doi:10.1029/2008JD009944

Kay, J. E., Raeder, K., Gettelman, A., and Anderson, J. (2011). The boundary layer response to recent arctic sea ice loss and implications for high-latitude climate feedbacks. *J. Clim.* 24 (2), 428–447. doi:10.1175/2010jcli3651.1

Klinker, E., and Sardeshmukh, P. D. (1992). The diagnosis of mechanical dissipation in the atmosphere from large-scale balance requirements. *J. Atmos. Sci.* 49 (7), 608–627. doi:10.1175/1520-0469(1992)049<0608:tdomdi>2.0.co;2

Klocke, D., and Rodwell, M. J. (2014). A comparison of two numerical weather prediction methods for diagnosing fast-physics errors in climate models. *Q. J. R. Meteorol. Soc.* 140 (679), 517–524. doi:10.1002/qj.2172

Li, H.-R., Xu, D.-S., and Zhang, B.-L. (2021). Implementation of the incremental analysis update initialization scheme in the tropical regional atmospheric modeling system under the replay configuration. *J. Meteorol. Res.* 35 (1), 198–208. doi:10.1007/s13351-021-0078-2

Lin, X.-X., Feng, Y.-R., Xu, D.-R., Jian, Y.-R., Huang, F., and Huang, J.-C. (2022). Improving the nowcasting of strong convection by assimilating both wind and reflectivity observations of phased array radar: A case study. *J. Meteorol. Res.* 36 (1), 61–78. doi:10.1007/s13351-022-1034-5

Ma, Z.-S., Liu, Q.-J., and Qin, Y.-Y. (2016). Validation and evaluation of cloud and precipitation forecast performance by different moist physical processes schemes in GRPAES_GFS model. *Plateau Meteorol. (in Chin.)* 35 (04), 989–1003. doi:10.7522/j.issn.1000-0534.2015.00063

Martin, G. M., Milton, S. F., Senior, C. A., Brooks, M. E., Ineson, S., Reichler, T., et al. (2010). Analysis and reduction of systematic errors through a seamless approach to modeling weather and climate. *J. Clim.* 23 (22), 5933–5957. doi:10.1175/2010jcli3541.1

Moncrieff, M. W., Waliser, D. E., Miller, M. J., Shapiro, M. A., Asrar, G. R., and Caughey, J. (2012). Multiscale convective organization and the YOTC virtual global field campaign. *Bull. Am. Meteorol. Soc.* 93 (8), 1171–1187. doi:10.1175/BAMS-D-11-00233.1

Phillips, T. J., Potter, G. L., Williamson, D. L., Cederwall, R. T., Boyle, J. S., Fiorino, M., et al. (2004). Evaluating parameterizations in general circulation models: Climate simulation meets weather prediction. *Bull. Am. Meteorol. Soc.* 85, 1903–1916.

Rodwell, M. J., Jung, T., Bechtold, P., Berrisford, P., Bormann, N., Cardinali, C., et al. (2010). *Developments in diagnostics research*. Reading, England: ECMWF Technical Memorandum, 637.

Rodwell, M. J., and Palmer, T. N. (2007). Using numerical weather prediction to assess climate models. *Q. J. R. Meteorol. Soc.* 133 (622), 129–146. doi:10.1002/qj.23

Skamarock, W. C., Klemp, J. B., Dudhia, J., Gill, D. O., Barker, D. M., Wang, W., et al. (2008). *A description of the advanced research WRF version 2*. University Corporation for Atmospheric Research, Boulder, Colorado, United States,

Torn, R. D., and Davis, C. A. (2012). The influence of shallow convection on tropical cyclone track forecasts. *Mon. Weather Rev.* 140 (7), 2188–2197. doi:10.1175/mwr-d-11-00246.1

Williams, K. D., Bodas-Salcedo, A., Déqué, M., Fermepin, S., Medeiros, B., Watanabe, M., et al. (2013). The transpose-AMIP II experiment and its application to the understanding of southern ocean cloud biases in climate models. *J. Clim.* 26 (10), 3258–3274. doi:10.1175/jcli-d-12-00429.1

Wong, M., Romine, G., and Snyder, C. (2020). Model improvement via systematic investigation of physics tendencies. *Mon. Weather Rev.* 148 (2), 671–688. doi:10.1175/mwr-d-19-0255.1

Xu, D.-S., Zhang, B.-L., Zeng, Q.-C., Feng, Y.-R., Zhang, Y.-X., and Dai, G.-F. (2019). A typhoon initialization scheme based on incremental analysis updates technology. *Acta Meteorol. Sin.* 77 (6), 1053–1061. doi:10.11676/qxxb2019.060

Xu, D.-S., Zhang, Y.-X., Wang, G., Meng, W.-G., and Chen, Z.-T. (2015). Improvement of meso-SAS cumulus parameterization scheme and its application in a model of 9 km resolution. *J. Trop. Meteorology (in Chinese)* 31 (5), 608–618. doi:10.16032/j.issn.1004-4965.2015.05.004

Xu, M., Zhao, Y.-C., Wang, X.-F., and Wang, X.-K. (2016). Statistical characteristics and circulation pattern of sustained torrential rainduring the pre-flood season in South China for recent 53 years. *Torrential Rain and Disasters* 35, 109–118. doi:10.3969/j.issn.1004—9045.2016.02.003

Yanai, M., Esbensen, S., and Chu, J.-H. (1973). Determination of bulk properties of tropical cloud clusters from large-scale heat and moisture budgets. *J. Atmos. Sci.* 30 (4), 611–627. doi:10.1175/1520-0469(1973)030<0611:dobpot>2.0.co;2

Zhang, H., Lin, Z.-H., and Zeng, Q.-C. (2011). The mutual response between dynamical core and physical parameterizations in atmospheric general circulation models. *Climatic and Environmental Research (in Chinese)* 16 (01), 15–30. doi:10.3878/j.issn.1006-9585.2011.01.02

Zhang, Y.-X., Chen, Z.-T., Meng, W.-G., and Xu, D.-S. (2022). Applicability of temperature discrete equation to NMRF boundary layer scheme in GRAPES model. *jtm.* 28 (1), 12–28. doi:10.46267/j.1006-8775.2022.002

frontiers | Frontiers in Earth Science

TYPE Original Research
PUBLISHED 16 March 2023
DOI 10.3389/feart.2023.1102887

OPEN ACCESS

EDITED BY
Xing Yuan,
Nanjing University of Information Science and Technology, China

REVIEWED BY
Chunsong Lu,
Nanjing University of Information Science and Technology, China
Shengping He,
University of Bergen, Norway

*CORRESPONDENCE
Feng Xu,
gdouxufeng@126.com

SPECIALTY SECTION
This article was submitted to Interdisciplinary Climate Studies, a section of the journal Frontiers in Earth Science

RECEIVED 19 November 2022
ACCEPTED 24 February 2023
PUBLISHED 16 March 2023

CITATION
Zheng M, Xu F, Liu S, Li Y, Zhang S and Yang J (2023), Decadal variation of the relationship between the previous autumn IOD and the South China Sea summer monsoon.
Front. Earth Sci. 11:1102887.
doi: 10.3389/feart.2023.1102887

Decadal variation of the relationship between the previous autumn IOD and the South China Sea summer monsoon

Meiying Zheng[1,2], Feng Xu[1,2]*, Shengyuan Liu[1,2], Yongchi Li[1,2], Shaojing Zhang[1,2] and Jinyi Yang[1,2]

[1]College of Ocean and Meteorology, Guangdong Ocean University, Zhanjiang, China, [2]South China Sea Institute of Marine Meteorology, Guangdong Ocean University, Zhanjiang, China

Using reanalysis data from the ECMWF and Hadley Centre of the UK Meteorological Office, the present study analyzes the relationship between Indian Ocean Dipole (IOD) in the previous autumn (September–November) and South China Sea Summer (June–August) Monsoon (SCSSM) from 1951 to 2021. It is found that the relationship between the two indices was significantly enhanced from the late 1970s to the beginning of the 21st century, with a significant resonance cycle of 2–4a. The previous autumn IOD forced the Gill pattern in the upper troposphere by changing the Sea Surface Temperature Anomaly (SSTA) of the following summer in the Tropical Indian Ocean (TIO), resulting in the anticyclonic circulation anomaly in the Philippine Sea. It eventually alters the southwest monsoon near the South China Sea and the Philippine Sea. However, for a decade or more, as the Pacific Decadal Oscillation (PDO) phase turns from warm to cold and the relationship between El Niño–Southern Oscillation (ENSO) and IOD weakens, the impact of the previous autumn IOD on Indian Ocean SSTA in the summer of the following year weakens, resulting in a decrease in the correlation between the previous autumn IOD and SCSSM. The impact of the previous autumn's Indian Ocean SSTA on the following year's SCSSM is more considered in terms of the eastern Bay of Bengal and the Somali Sea basin. In addition, during the warm phase of PDO, the IOD of the previous autumn can cause abnormal summer precipitation in South China by strengthening or weakening the Western Pacific Subtropical High (WPSH) of the following summer, but there is no significant effect in the cold phase of PDO.

KEYWORDS

South China Sea summer monsoon (SCSSM), Indian Ocean dipole (IOD), El Niño–Southern oscillation (ENSO), pacific decadal oscillation (PDO), Western Pacific subtropical high (WPSH), tropical Indian Ocean (TIO)

1 Introduction

Since Saji et al. (1999) first proposed Indian Ocean Dipole (IOD), its climate effects have attracted more and more attention from researchers (Xiao et al., 2009; Jiang et al., 2021). The Sea Surface Temperature Anomaly (SSTA) at the east and west poles of IOD will not only cause abnormally land temperature and precipitation in countries west and east of the Indian Ocean but also affect climatic factors in many parts of Asia through teleconnection pattern (Saji and Yamagata, 2003). For example, in 1994, the positive IOD event caused climate anomalies in East Asia through Rossby waves (Guan and

Yamagata, 2003). Extreme positive IOD in 2019 led to extreme warm anomalies in East Asia in the boreal winter and extreme plum rains in East Asia in the early boreal summer of 2020 (Doi et al., 2020; Takaya et al., 2020; Zhou et al., 2021).

IOD and the Asian monsoon interact with each. The Asian monsoon circulation provides a favorable state for the development of IOD (Xiang et al., 2011). IOD can directly affect the Asian summer monsoon by affecting the lower tropospheric wind, and can also indirectly affect the Asian summer monsoon by affecting the Tibetan high in the upper troposphere and the Northwest Pacific subtropical high (Li and Mu, 2001).

The South China Sea is located in the center of the Asian-Australian monsoon zone. The South China Sea summer monsoon (SCSSM) is the link between the four monsoon subsystems of subtropical East Asia (EA) monsoon, tropical Indian monsoon, Northwest Pacific (WNP) monsoon, and Australian monsoon (Wang et al., 2009). The onset of the SCSSM marks the transition of atmospheric circulation in Asia from a winter to a summer one and the onset of a massive summer monsoon on the EA and WNP at the same time (Tao and Chen 1987; Lau and Yang, 1997). El Niño–Southern Oscillation (ENSO) is critical to SCSSM as the strongest interannual variation signal in a sea-air coupling system. In the warm phase of ENSO, the onset of SCSSM in this year and the next year was late, while in the cold phase, the onset of SCSSM was earlier (Tao and Zhang, 1998; Chen et al., 2018). In recent years, Ding et al. (2016) found that the decadal shift in the onset date of SCSSM is affected by the decadal difference between the eastern Pacific (EP) type and the central Pacific (CP) type ENSO. Although the interannual variability of Sea Surface Temperature (SST) in the tropical Indian Ocean (TIO) is much smaller than in the Pacific Ocean, its impact on the SCSSM is also crucial. IOD and SCSSM are closely related, and their physical connection has been extensively studied. Yan et al. (2005) used the IAP AGCM-II, an atmospheric circulation model, to show that in the absence of the influence of SSTA in the equatorial eastern Pacific Ocean during the simple positive IOD phase, the southwest summer monsoon in East Asia broke out late, and there was a clear westerly wind response from the eastern Bay of Bengal to the

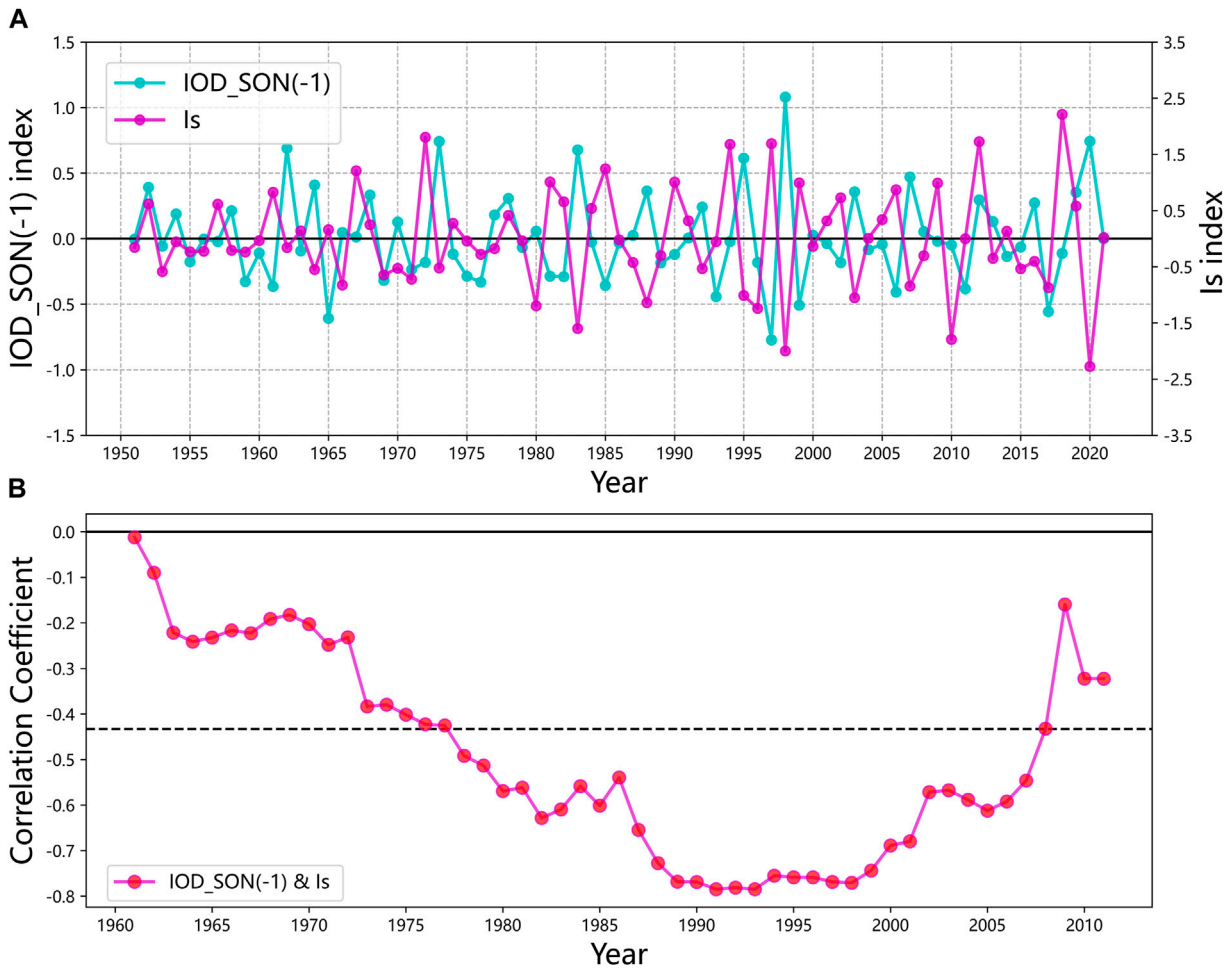

FIGURE 1
(A) Time series of Is and the previous autumn IOD index from 1951 to 2021. **(B)** The 21a sliding correlation coefficient of the SCSSM index with the previous autumn IOD index (the year in the figure represents the center of the sliding window. The dashed black line indicates the statistical significance level of 0.05 reliability).

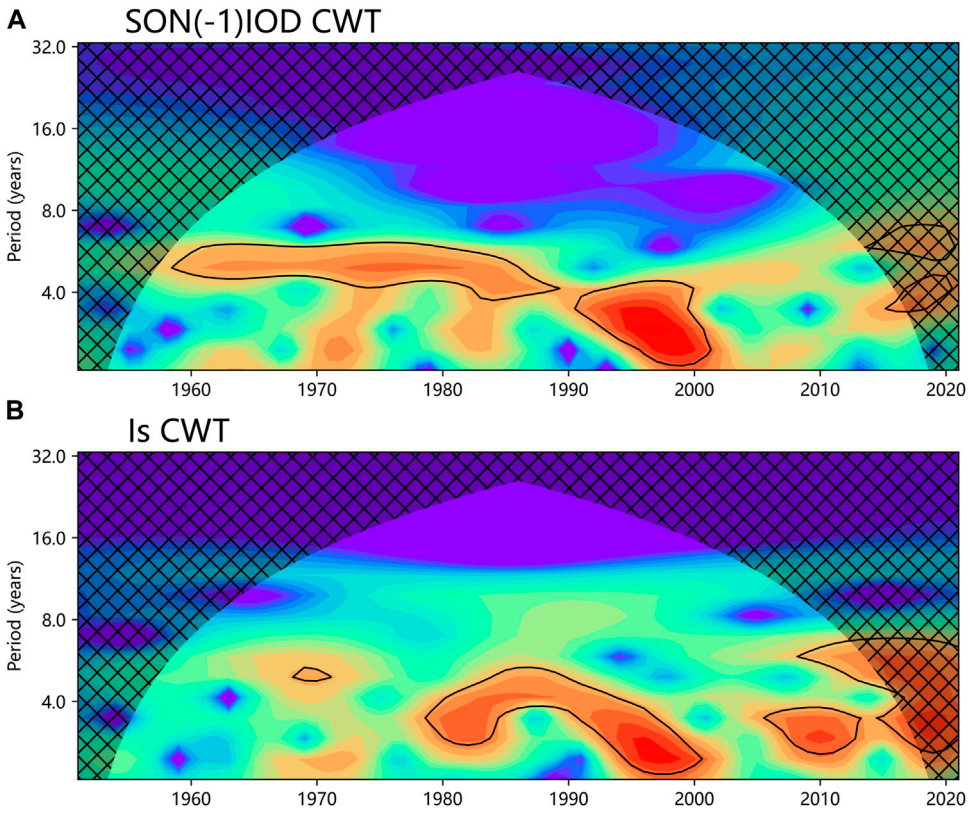

FIGURE 2
Wavelet power spectrum analysis of **(A)**the previous autumn IOD index **(B)** the SCSSM index; The range surrounded by a thick solid line is tested by the standard spectrum of red noise at a significance level of 0.05; the inverted U-shape is an influence cone curve (COI), and the power spectrum outside this curve is not considered due to boundary effects.

South China Sea, which strengthened the Indian summer monsoon and the SCSSM. From the perspective of SCSSM onset pentad, Yuan et al. (2008a) pointed out that the SCSSM onset was late in the next year of the negative IOD year, and there was no obvious abnormality in the positive IOD year. In addition, if the extreme positive IOD event reaches a strong intensity before the onset of the SCSSM of the same year, positive IOD can weaken the Indian Ocean summer monsoon circulation and the upper South China Sea monsoon flow, and develop an abnormal anticyclone in the TIO, thereby hindering the advance of the southwest monsoon in the Indian Ocean to the South China Sea, making the SCSSM onset late in the year (Yuan and Li, 2009). However, under normal circumstances, IOD begins to develop in summer and matures in autumn, so the strength of the Asian summer monsoon may determine the phase and intensity of IOD in that year. The IOD in the early stage may affect the intensity of the SCSSM. As pointed out by Li et al. (2007) study, the intensity of the SCSSM is weakened (enhanced) when positive (negative) IOD mode exists in the TIO in the previous autumn. When the intensity of the SCSSM increases (decreases), a positive (negative) IOD mode appears in the TIO in the autumn of that year.

Several articles have revealed the relationship between IOD and SCSSM and the mechanism of its influence, but in the context of global warming, the mean climate of the TIO will undergo considerable changes. These changes are likely to affect the IOD, e.g., stronger SST warming in the western part of the TIO than in the eastern part, leading to a shift of the convective zone to the west, favoring the westward development of the equatorial easterly wind anomaly, and stimulating non-linear processes that contribute significantly to strong positive IOD events, leading to an increase in the probability of strong positive IOD events (Cai et al., 2013; Cai et al., 2020). Along with the change of climate variability in the Indian Ocean, how will the relationship between the previous autumn IOD and SCSSM change? In this paper, the decadal changes of the influence of the previous autumn IOD on SST and atmospheric circulation in the following summer will be used to explain the reasons for the change in their relationship and their climatic effects.

2 Data and methods

The reanalysis data used in this paper include: 1) monthly mean reanalysis dataset ERA5 from the European Centre for Medium-Range Weather Forecasts (ECMWF) (Hersbach et al., 2020), with a horizontal resolution of 0.25° × 0.25°; 2) monthly mean sea surface temperature dataset HadISST from the Hadley Centre of the UK Meteorological Office (Rayner et al., 2003), horizontal

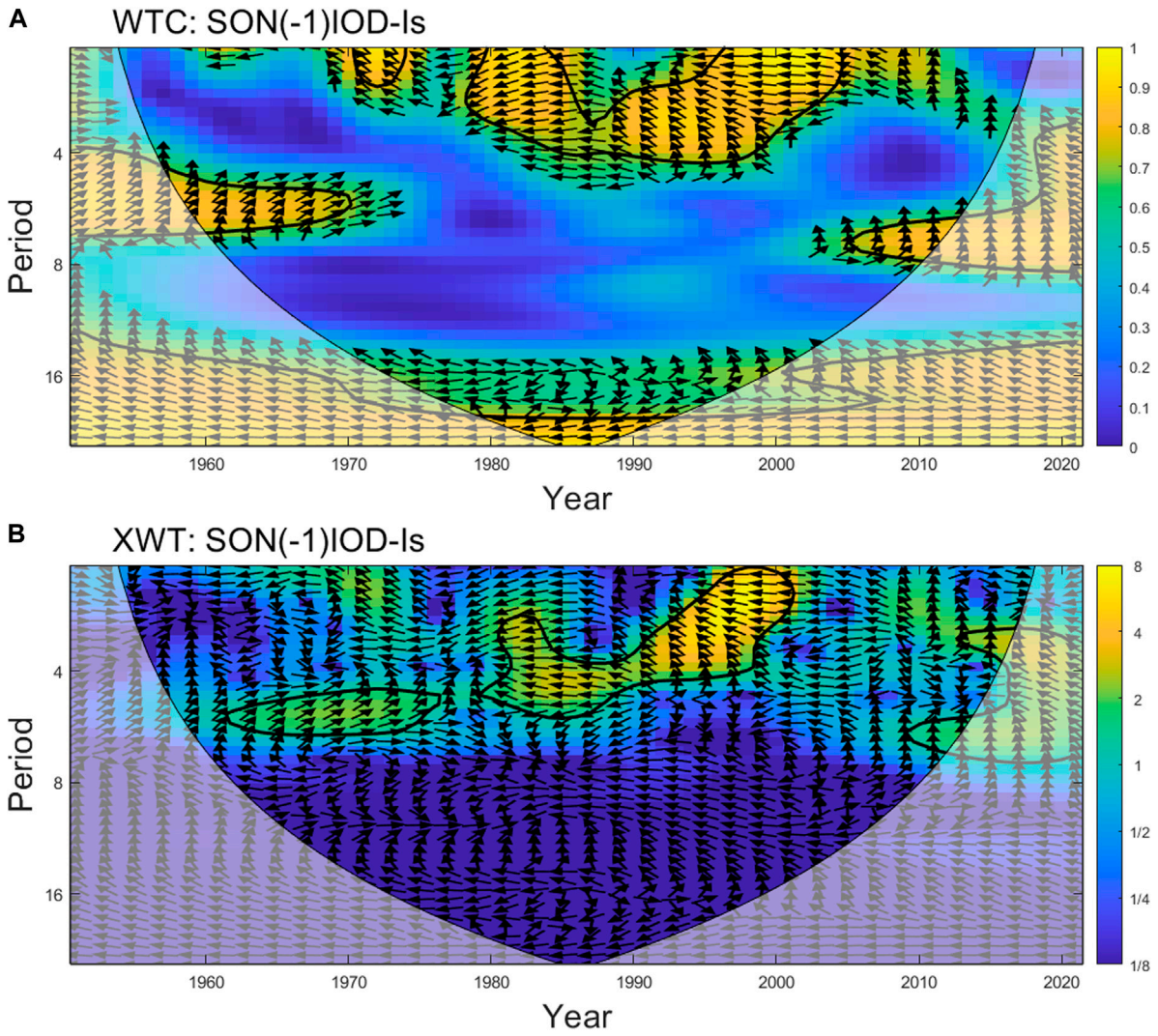

FIGURE 3
(A) Wavelet coherence spectrum **(B)** cross-wavelet spectrum of the previous autumn IOD and SCSSM index; In the figure, the arrow indicates the relative bit difference, the right arrow indicates that the two change bits are consistent, and the left arrow indicates that the change bits are opposite (The others are the same as Figure 2).

resolution 1.0° × 1.0°. The length of the data used above is 1950–2021, a total of 72 years. The seasons mentioned in the text are relative to the northern hemisphere.

This paper adopts the SCSSM intensity index defined by Wu et al. (2002). It is defined as the normalized southwest wind component of 850 hPa in the South China Sea (5°N–20°N, 105°E–120°E) area in the summer (June—August), with the following formula:

$$I_s = \frac{V_{sw} - \overline{V_{sw}}}{\sigma_{sw}}$$

Specifically, $V_{sw} = \frac{(u+v)}{\sqrt{2}}$ is a projection of the summer mean 850 hPa winds at the direction of southwest over the region; $\overline{V_{sw}}$ is the multi-year mean over the season; σ_{sw} is the standard deviation of V_{sw}.

The IOD index is expressed by the difference of the mean SSTA between the tropical West Indian Ocean (10° S-10°N, 50° –70°E) and the tropical Southeast Indian Ocean (10°S-0°, 90°–110°E) in autumn (September-November) as defined by Saji et al. (1999).

The anomalies of all variables in this paper are defined as the deviation from the multi-year average after removing the long-term linear trend. 9a Butterworth high-pass filtering is applied to each dataset to focus on the interannual variability of the SCSSM and previous autumn IOD. The research methods in this paper mainly include wavelet analysis, singular value decomposition (SVD), regression analysis, correlation analysis, and composite analysis. The level of statistical significance in statistical analysis is determined based on the two-tailed p-value of the Student's t-test.

3 Decadal variation of the correlation between previous autumn IOD and SCSSM

The interannual variation of the time series of the SCSSM index and the previous autumn IOD index is obvious (Figure 1A). To

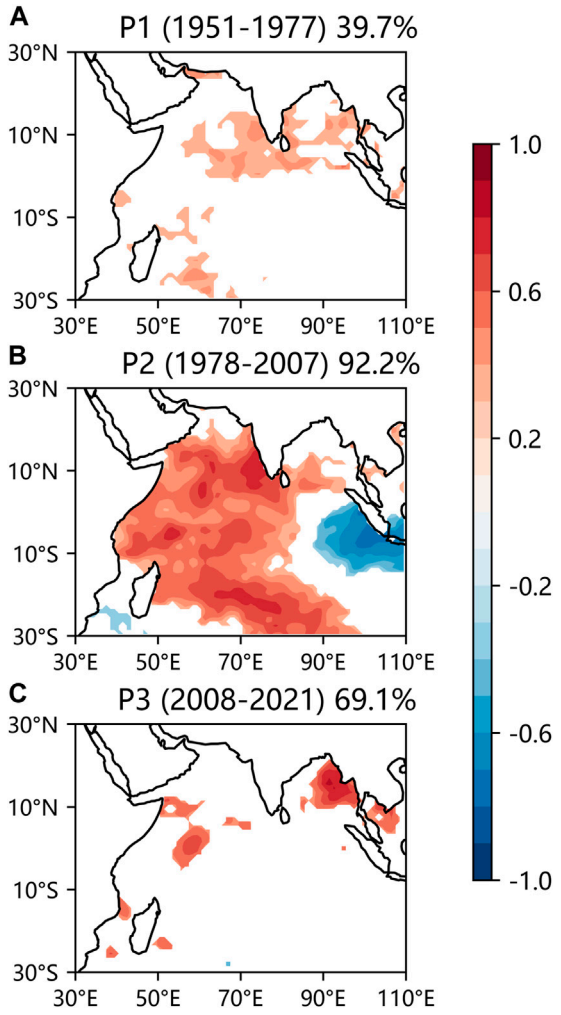

FIGURE 4
The correlation coefficient of the previous autumn Indian Ocean SSTA with the right-field time series of SVD-PC1 during. **(A)** P1, **(B)** P2, and **(C)** P3. The left field used for SVD is: SSTA in the TIO (30°S–30°N, 30°E–110°E) in the previous autumn; The right field is: the 850 hPa wind field anomalies in the summer of the South China Sea (5°N–20°N, 105°E–120°E), only showing the area that passed the 90% significance test (Figures 6–10 is also the same).

examine the decadal variation of the relationship between the previous autumn IOD and SCSSM, the 21a sliding correlation between SCSSM and the previous autumn IOD index was calculated in this paper for the period 1951–2021. As can be seen from (Figure 1B), the correlation was low (did not pass the 0.05 reliability test) until the 1970s, and after the late 1970s, the correlation value between the two indexes increased to greater than 0.43, showing a significant negative correlation. With the decadal change of the two indices, their 21a sliding correlation coefficients first increased and then decreased. In the early 1990s, the correlation was the strongest. After the late 2000s, the correlation coefficient between the two indices decreased and was not statistically significant. Therefore, according to whether the 21a sliding correlation between the two indexes can pass the 0.05 confidence test, this paper divides the period from 1951 to 2021 into three periods: P1 (1951–1977), P2 (1978–2007) and P3 (2008–2021) to discuss the causes of decadal changes in the correlation between the two indices.

4 Possible mechanism analysis

4.1 Periodic analysis

The change in the correlation is determined by the main periodic characteristics of the two-time series and the corresponding bit-phase differences. As can be seen from Figure 2A, the IOD index exhibits mainly a 4-7a cycle from the 1960s to the 1980s, and the cycle was significantly shortened to a 2-5a cycle in the 1990s, with no significant cycle after the 21st century. The SCSSM index had a short quasi-6a cycle from the late 1960s to the early 1970s (Figure 2B), and it mainly exhibited a 2-7a cycle from the late 1970s to the early 2000s, and a 2-4a cycle existed from the late 2000s to the mid-2010s. During the P2, the two indices are closer to each other in the main cycle, and from the wavelet coherence spectrum analysis of the two indices looking at (Figure 3A), in the late 1970s to the early 21st century, there existed a significant resonance cycle of 2-4a opposite bits between the previous autumn IOD and SCSSM. In contrast, during the P1 and P3, there is no significant resonance cycle for the two indices.

Previous studies have shown that when the Pacific Decadal Oscillation (PDO) is in a warm phase, stronger El Niño events are induced by SSTA in the North Pacific, and the Walker circulation and anticyclonic circulation associated with El Niño events are also strengthened, thus making the ENSO-SCSSM relationship stronger, while in the cold phase of the PDO, stronger La Nina events often cannot be induced (Fan and Fan, 2017). The asymmetric response of the PDO to El Niño and La Niña events leads to a strengthening of the ENSO-SCSSM relationship during the warm PDO phase (P2). The SCSSM with a strengthened relationship with ENSO exhibits a 2-7a cycle similar to ENSO. The period of SCSSM is close to the period of 4-7a and 2-5a of IOD during P2, and they show a resonance period of 2-4a. On the cross-wavelet spectrum (Figure 3B), the period range and time scale of the occurrence of energy extremes also correspond well to the wavelet coherent spectrum.

4.2 SST and atmospheric circulation analysis

To examine the decadal variation of the synergistic relationship between the previous autumn Indian Ocean SSTA and the summer South China Sea 850 hPa wind, the singular value decomposition (SVD) is performed for the summer 850 hPa wind in the South China Sea (5°N–20°N, 105°E–120°E) and the previous autumn Indian Ocean SSTA (30°S–30°N, 30°E–110°E) during the three periods of 1951–1977, 1978–2007 and 2008–2021, respectively. The previous autumn SSTA in the southeastern Arabian Sea and southwestern Bay of Bengal (eastern Bay of Bengal and the Somali Sea basin) in the

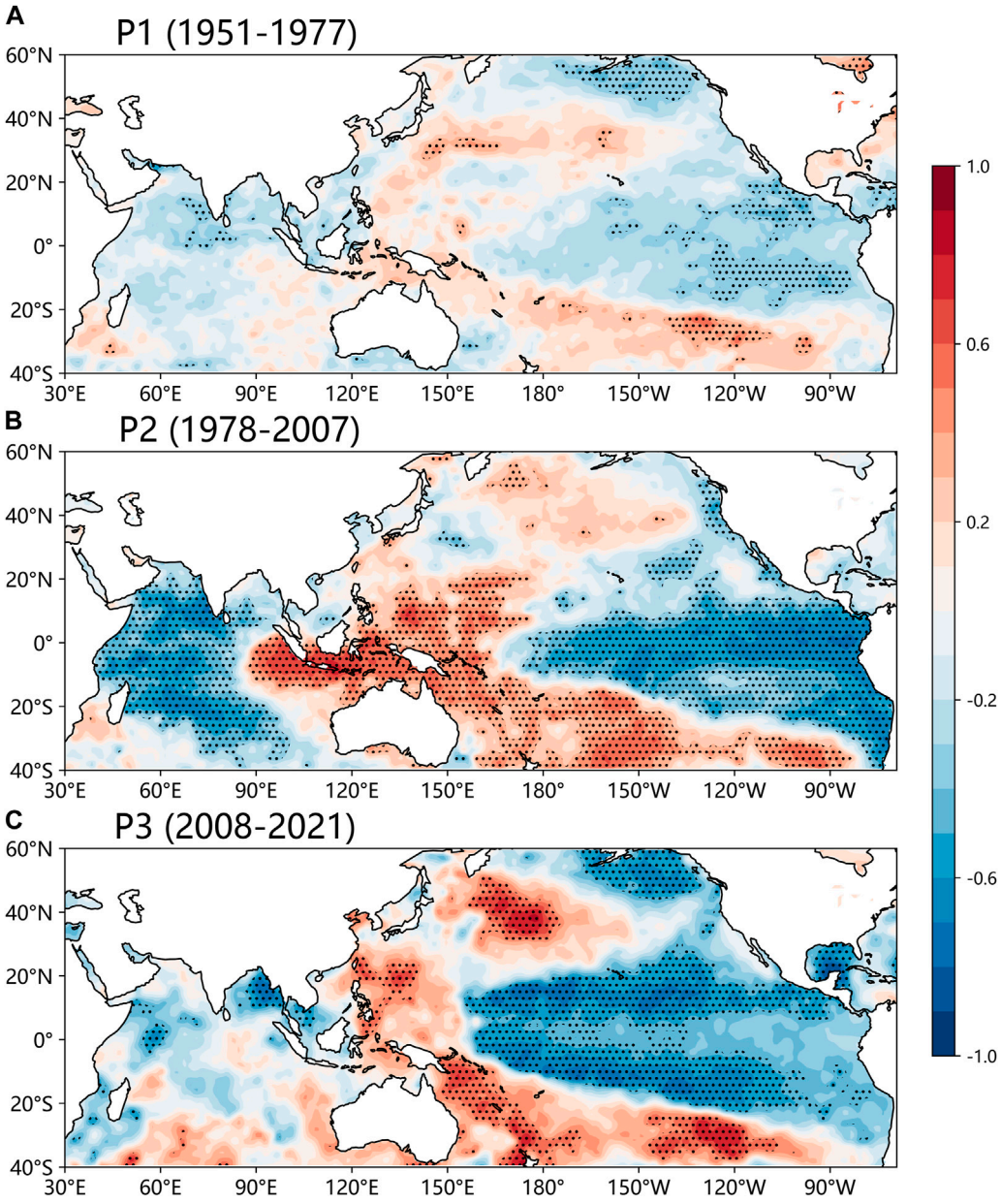

FIGURE 5
Spatial distribution of the correlation coefficients between SCSSM index and SSTA in the previous autumn during **(A)** P1, **(B)** P2, and **(C)** P3. The dotted area indicates that it can pass the 90% significance test.

Indian Ocean have a significant impact on SCSSM during P1 (P3), with a variance contribution of 39.7% (69.1%) (Figures 4A, C). The difference is that the IOD mode in the previous autumn plays a key role for SCSSM during P2 (Figure 4B). The variance contribution rate was as high as 92.2%, which also explained why the correlation between the previous autumn IOD and the SCSSM during P2 was significantly enhanced.

There was no significant correlation signal between SCSSM and the TIO(Pacific Ocean) SSTA in the previous autumn during P1 (Figure 5A). During P2 the SCSSM is positively (negatively) correlated with the East (West) Indian Ocean SSTA and negatively (positive) with the East (West) Pacific SSTA. SCSSM was influenced by both IOD and ENSO in the previous autumn (Figure 5B). During P3, the relationship between SCSSM and the Indian Ocean SSTA was not obvious, but the relationship between SCSSM and the Pacific Ocean SSTA was similar to that in P2. It is noteworthy that the largest negative correlation occurs in the central tropical Pacific rather than the eastern tropical Pacific (Figure 5C). The frequency of CP-type El Niño events has been increasing in recent decades (Yu et al., 2012). It reminds us that the influence of CP-type El Niño on SCSSM predominates in two types of El Niño events during P3.

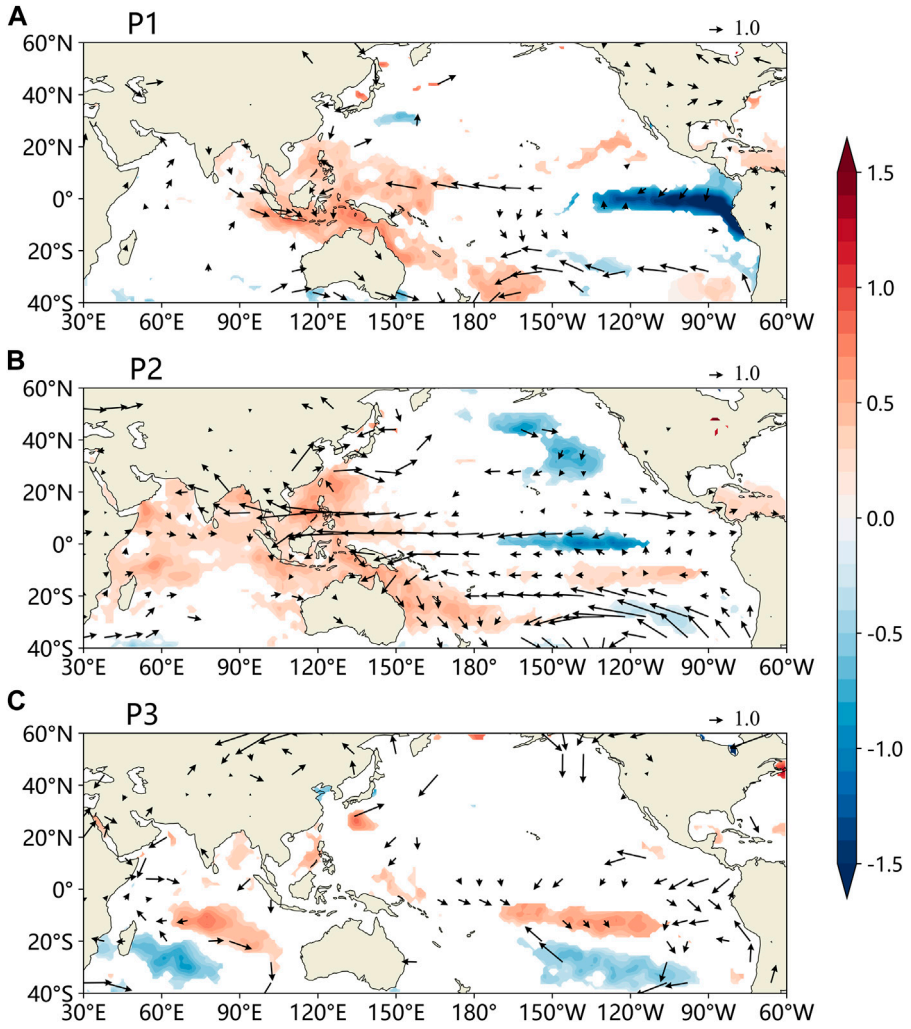

FIGURE 6
Regression coefficient of the previous autumn IOD index projected to the SSTA (shadows; Unit: ˚C) and 850 hPa wind anomalies (vector; Unit: m/s) in the summer during **(A)** P1, **(B)** P2 and **(C)** P3.

The positive IOD in the previous autumn during P2 is associated with a significant warm SSTA in the TIO in the following summer. The TIO SST warming will excite an easterly wind anomaly at the low level in the western Pacific and the South China Sea through a remote Gill-type response (Figure 6B) (Gill, 1980). In addition, a warmer TIO SSTA will induce an anomalous reversed Walker circulation over the tropical Indo–Pacific Ocean, which leads to descending motion and hence suppressed convection in the western Pacific. Subsequently, the strengthened Philippine anticyclone pushed westward, obstructing the extension of the Indian Ocean westerly winds to the South China Sea area, and not conducive to the development of the SCSSM (Figure 7B) (Yuan et al., 2008b). A southwesterly wind anomaly at the upper level originates in the maritime continent and crosses the South China Sea and the western Pacific, which favors the maintenance of easterly winds at the low level (Figure 8B). The northeast-southwest trending sea level pressure meridional gradient also contributes to the anticyclonic circulation anomaly at a low level, which further strengthens the low-level easterly wind anomaly (Figure 8B) (Chakravorty et al., 2013). In contrast, during P1 and P3 the effect of the previous autumn IOD on SST and atmospheric circulation in the following summer is not as significant as in P2 (Figures 6A, C–8A, C). The significant difference between P2 and P1 (P3) in the previous autumn IOD was the effect on the SSTA in the TIO. The impact of the previous autumn IOD on TIO SSTA during P2 can continue in the following summer. However, during P1 and P3, the correlation between them has descended rapidly in spring, and has been not significant in summer (Figure 9). TIO SSTA warming has a great impact on the Asian monsoon circulation. Positive precipitation anomalies occur in much of the Indian Ocean basin when TIO SSTA warms (Figure 10B), forcing Gill patterns in the upper troposphere and weakening of the southwest monsoon near the South China Sea and the Philippine Sea. Abnormal anticyclonic circulation was formed over the subtropical

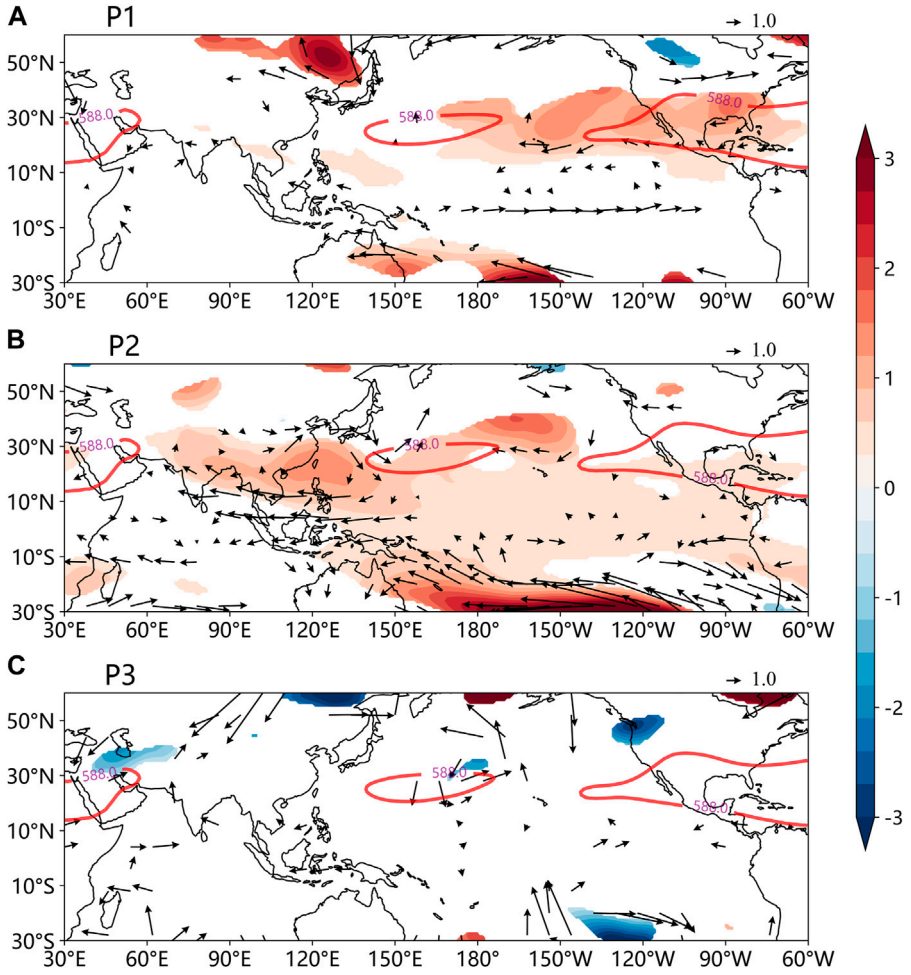

FIGURE 7
Regression coefficient of the previous autumn IOD index projected to the 500 hPa potential height anomalies (shadow; Unit: 10gpm) and 500 hPa wind anomalies (vector; Unit: m/s) in the summer during **(A)** P1, **(B)** P2 and **(C)** P3. (The red contours show the 588gpm contours of the multi-year average).

northwest Pacific Ocean in coordination with the negative precipitation anomaly in the Northwest Pacific Ocean, and finally weakened the South China Sea summer monsoon (Yang et al., 2007; Xie et al., 2009; Xie et al., 2010).

There are two reasons for the decadal shift in the relationship between the previous autumn IOD and SCSSM. On the one hand, it has been shown that the Indian Ocean does not have an independent decadal mode. PDO is one of the sources of its decadal variability (Krishnamurthy and Krishnamurthy, 2016; Xie et al., 2021), which changed from a cold to a warm phase in the late 70s of the 20th century, and to a cold phase in the early 21st century (Mantua and Hare, 2002; Grassi et al., 2012). To examine the difference in the atmospheric circulation of the summer of the following year of IOD under different phases of the PDO, the IOD index of 71a (1950–2020) greater than (less than) 0.6 standard deviations was selected as positive (negative) IOD years (Table 1). To maintain the coordination of positive and negative IOD event ratios, the event samples from the cold phase of PDO are combined and discussed. Under the cold phase of PDO, there are no significant wind anomalies in the western Pacific and South China Sea (Figures 11A, B). In the summer following the positive (negative) IOD of the warm phase of the PDO, the western Pacific and South China Sea regions showed significant easterly (westerly) wind anomalies(Figures 11C, D), weakening (strengthening) the SCSSM. Under different PDO phases, the summer zonal wind anomalies of 850 hPa following positive (negative) IOD events differed significantly in the Western Pacific and South China Sea regions (Figures 11E, F). The warm phase of PDO strengthened the relationship between the previous autumn IOD and the SCSSM.

On the other hand, the decadal variation of the relationship between SCSSM and IOD in the autumn of the previous year is influenced by the relationship between IOD and ENSO. Although the Indian Ocean Dipole Model (IODM) and Indian Ocean Basin Model (IOBM) have different spatial distributions and life histories, they are not independent of each other, there is a process of transformation from IODM to IOBM (Du, 2006). The process of the transition from IODM to IOBM is influenced by the decadal transition of the relationship between IOD and ENSO. In the period of high correlation between IOD and ENSO, the transition is significant,

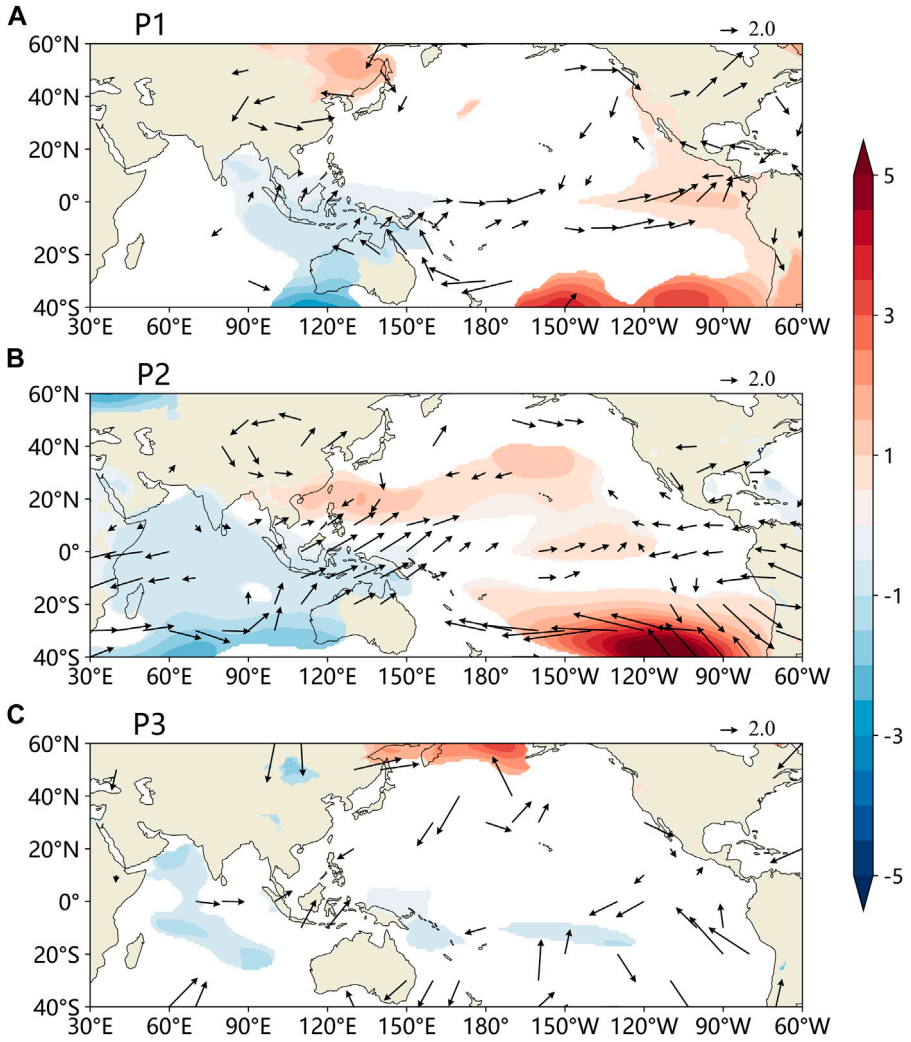

FIGURE 8
Regression coefficient of the previous autumn IOD index projected to the sea level pressure anomalies (shadows; Unit: hPa) and 200 hPa wind anomalies (vector; Unit: m/s) in the summer during **(A)** P1, **(B)** P2 and **(C)** P3.

TABLE 1 The positive and negative IOD years of the previous year for P1(1951–1977), P2 (1978–2007), and P3 (2008–2021).

	Positive IOD	Negative IOD
P1 (1951–1977) (PDO cold phase)	1961 1963 1967 1972	1950 1952 1954 1955 1956 1957 1958 1959 1960 1964 1968 1970 1971 1973 1974 1975
P2 (1978–2007) (PDO warm phase)	1982 1987 1994 1997 2002 2006	1980 1981 1984 1992 1996 1998
P3 (2008–2021) (PDO cold phase)	2007 2011 2012 2015 2017 2018 2019	

while in the period of low correlation, there is almost no transition phenomenon (Guo and Wu, 2022). During P2, the Walker circulation on the Maritime Continent was enhanced and the rising motion increased, which further increased the SST connection between the eastern Indian Ocean and the Western Pacific Ocean, resulting in the enhanced IOD-ENSO relationship, the correlation coefficient between the previous autumn IOD index and the previous winter Nino3.4 index was 0.78, which could pass the 99% significance test (Yuan and Li, 2008). Therefore, during P2, the transition process from autumn IODM to spring-summer IOBM is also more significant, strengthening the relationship between the previous autumn IOD and SCSSM. However, during P1(P3) the correlation coefficient between the previous autumn IOD index and the previous winter Nino 3.4 index was 0.49 (0.51), which could pass the 99% (90%) significance test. The conversion

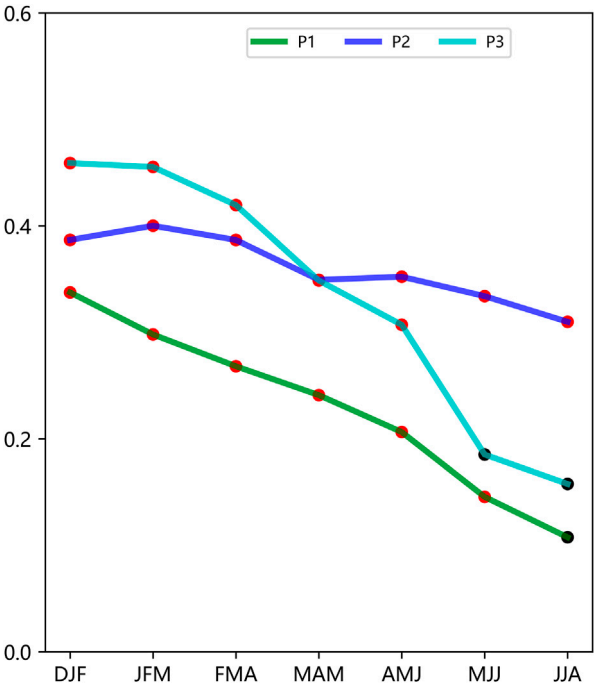

FIGURE 9
Regression coefficient of the previous autumn IOD index projected to the regional mean SSTA in the TIO (10°S–20°N, 30°–110°E) from the previous winter to the following summer. A red dot indicates a pass of the 90% significance test, and a black dot indicates a failure.

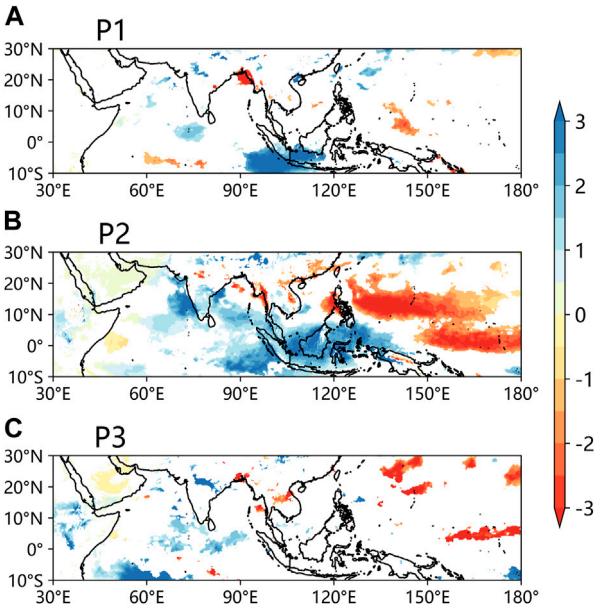

FIGURE 10
Regression coefficient of the previous autumn IOD index projected to the precipitation anomalies (shadows; Unit: mm) in the summer during **(A)** P1, **(B)** P2, and **(C)** P3.

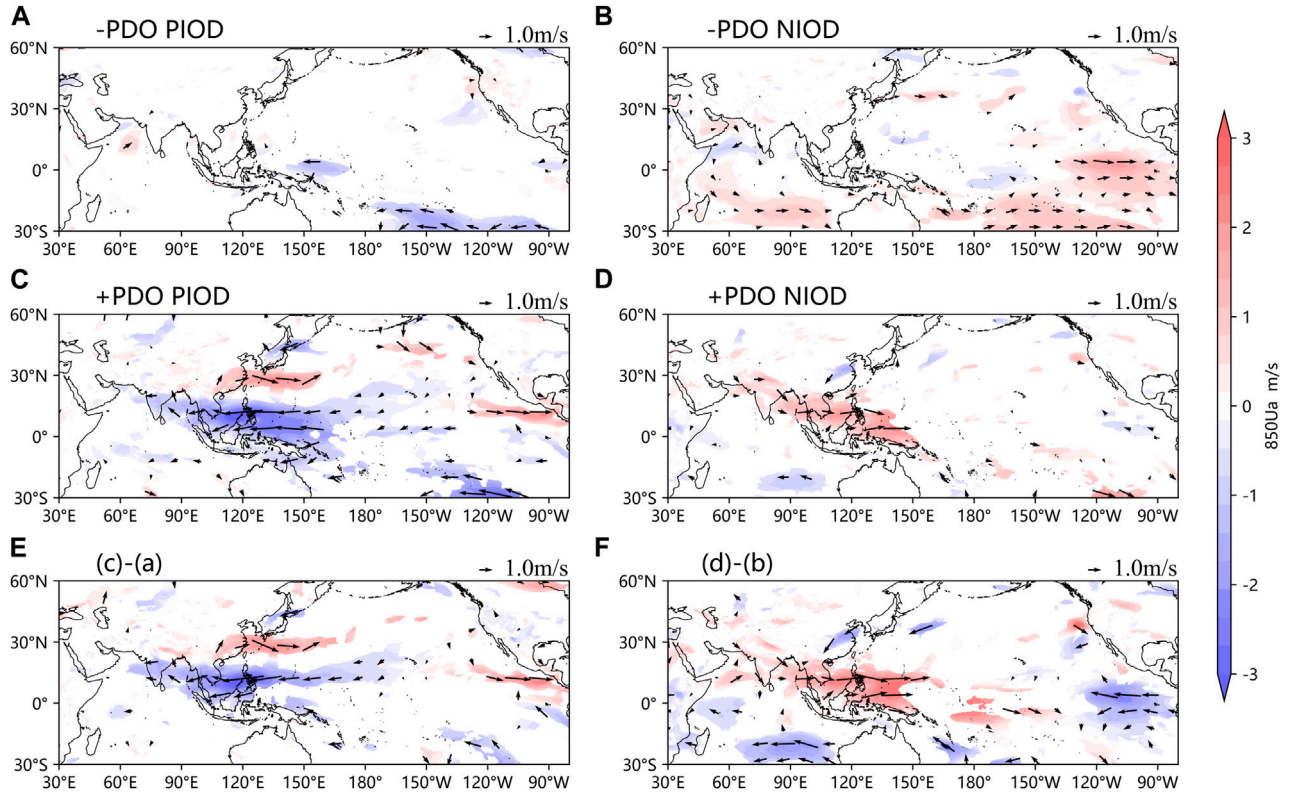

FIGURE 11
(A,B) Under the PDO cold phase, **(C,D)** PDO warm phase **(A,C)** positive IOD, **(B,D)** negative IOD 850 hPa wind anomaly in the following summer (vector; Unit: m/s); PDO cold and warm phase **(E)** positive IOD **(F)** negative IOD 850 hPa wind anomaly difference in the following summer (vector; Unit: m/s); Colour shade indicates latitudinal wind anomalies.

from IODM to IOBM was not significant, and the correlation between IOD and SCSSM decreased.

5 Conclusion and discussion

In the past 71 years, with the phase conversion of PDO and the change of the relationship between IOD and ENSO, the relationship between the previous autumn IOD and SCSSM has changed decadal. It strengthened in the late 1970s and weakened in the late 2000s. The decadal changes in their relationship may be related to the decadal changes in their cycles and the effects of the previous autumn IOD on TIO SSTA and atmospheric circulation in the following summer. From the late 1970s to the beginning of the 21st century, under the coordination of the warm PDO phase and El Niño, the main period of the two indices was similar. There existed a significant resonance cycle of 2-4a opposite bits between the previous autumn IOD and SCSSM. The previous autumn IOD forced the Gill pattern in the upper troposphere by altering the SSTA of TIO of the following summer, resulting an anomaly anticyclonic circulation in the Philippine Sea and eventually altering the southwest monsoon near the surface of the South China Sea and the Philippine Sea. In addition, the previous autumn IOD also induced a northeast-southwest trend sea level pressure meridional gradient over the tropical Indian Ocean and the northwest Pacific Ocean in the following summer, thus promoting low-level anticyclonic circulation anomalies and further strengthening the low-level easterly wind anomaly. In such a circulation configuration, the correlation between the previous autumn IOD and SCSSM is strengthened during P2. However, for a decade or more, with the phase conversion of PDO and the change of the relationship between IOD and ENSO, the influence of the previous autumn IOD on the TIO SSTA of the next summer has weakened, and the atmospheric circulation anomalies affected by TIO SST are not as significant as in the P2, resulting in a decrease in the correlation between the previous autumn IOD and SCSSM. The impact of the previous autumn's Indian Ocean SSTA on the SCSSM is more considered in terms of the eastern Bay of Bengal and the Somali Sea basin.

It is worth mentioning that the previous autumn IOD had a significant impact on the precipitation in South China in summer of the following year during P2. It can be explained by the two-stage thermal adaptation theory proposed by Wu et al. (2000). According to the first level of thermal adaptation: sensible heat heating adaptation, the SSTA of the central equatorial Indian Ocean (Figure 6B) increases the evaporation of water vapor and the sea-air temperature difference, resulting in an abnormal increase in sensible heat heating, and a cyclonic circulation appears in the near strata whose eastern region developing abnormal southerly winds carried large amounts of water vapor to the north. Finally, a positive precipitation anomaly was produced in the eastern Bay

of Bengal (Figure 10B). According to the secondary thermal adaptation: latent heat heating adaptation, abnormal precipitation in the eastern Bay of Bengal extends northeast with deep convective latent heat heating. At this time, in the lower and middle troposphere, due to the increase of heating with height, southerly winds develop. Eventually, the 500 hPa Western Pacific Subtropical High (WPSH) strengthened to the east of the heating zone, namely, the South China Sea and the Western Pacific region (Figure 7B). Previous studies have suggested that the longitudinal position of the 500 hPa WPSH has an important impact on summer precipitation in China, when the high ridge extends westward (retreats eastward), South China will have less (more) rainfall (Yang and Sun, 2003). The westward push of the WPSH during P2 controlled South China, and the easterly wind in the south of it abnormally blocked the water vapor transported from the Bay of Bengal to South China, combined with the diverging flow in the mid- and low-level troposphere (Yuan et al., 2008a). As a result, South China has less rainfall (Figure 10B). Therefore, in the warm phase of PDO, IOD in the previous autumn can cause summer precipitation anomalies in South China by strengthening or weakening the 500 hPa WPSH in the following summer, but in the cold phase of PDO, there is no significant effect.

Li et al. (2007) showed that in the warm phase of PDO, the effect of the previous autumn IOD on SCSSM was achieved by affecting anomalous trans-equatorial airflow west of Sumatra. The results of this study further show that in the warm phase of PDO, the influence of the previous autumn IOD on SCSSM can also be realized by influencing the abnormal zonal winds in the western Pacific and South China Seas caused by TIO SSTA. From previous studies, it can be seen that IOD events interact with ENSO, and ENSO and IOD interact mainly through the Walker circulation anomaly coupled between the TIO and the tropical Pacific Ocean and the associated ocean fluctuation processes (Zhang and Tan, 2003; Luo et al., 2010; Wang, 2019; Yue et al., 2021). ENSO affects SCSSM through Walker circulation and WPSH anomalies (Zhou and Chan, 2007; Hu et al., 2020). Although we reveal the possible mechanism by which the previous autumn IOD affects SCSSM and its decadal variation, our results are not independent effects of IOD on SCSSM. In the next step, the removal of ENSO signals can be considered to study the influence mechanism of pure IOD on SCSSM and its decadal changes. In addition, the results of this study are based on a statistical analysis of reanalysis data, and the results can be further verified by climate models in future studies.

Data availability statement

Publicly available datasets were analyzed in this study. This data can be found here: https://cds.climate.copernicus.eu/cdsapp#!/search?type=dataset https://www.metoffice.gov.uk/hadobs/index.html.

Author contributions

MZ was responsible for the study conception, manuscript writing,and figure development. FX provided guidance and funding support. SL were responsible for discussion and manuscript revision. YL, JY, and SZ were contributed to the conception and design of the work.

Funding

This study was supported by the Special Project for Research and Development in Key area of Guangdong Province (Grant 2020B0101130021) and the National Key Research and Development Program of China (Grant 2018YFC1506902).

Acknowledgments

The authors would like to thank the funding agencies and the team of ECMWF/ Hadley Centre of the UK Meteorological Office for making this study possible. We would also like to thank the editors and the reviewers for their valuable suggestions.

Conflict of interest

The authors declare that the research was conducted in the absence of any commercial or financial relationships that could be construed as a potential conflict of interest.

Publisher's note

References

Cai, W., Yang, K., Wu, L., Huang, G., Santoso, A., Ng, B., et al. (2020). Opposite response of strong and moderate positive Indian Ocean Dipole to global warming. *Nat. Clim. Change* 11, 27–32. doi:10.1038/s41558-020-00943-1

Cai, W., Zheng, X.-T., Weller, E., Collins, M., Cowan, T., Lengaigne, M., et al. (2013). Projected response of the Indian Ocean Dipole to greenhouse warming. *Nat. Geosci.* 6, 999–1007. doi:10.1038/ngeo2009

Chakravorty, S., Chowdary, J. S., and Gnanaseelan, C. (2013). Spring asymmetric mode in the tropical Indian ocean: Role of El Niño and IOD. *Clim. Dyn.* 40, 1467–1481. doi:10.1007/s00382-012-1340-1

Chen, W., Ding, S., Feng, J., Chen, S., Xue, X., and Zhou, Q. (2018). Progress in the study of impacts of different types of ENSO on the East Asian monsoon and their mechanisms. *Chin. J. Atmos. Sci.* 42 (3), 640–655. (in Chinese). doi:10.3878/j.issn.1006-9895.1801.17248

Ding, S., Wen, Z., and Chen, W. (2016). Interdecadal change in the relationship between the South China Sea summer monsoon onset and two types of Pacific sea surface temperature anomaly. *Chin. J. Atmos. Sci.* 40 (2), 243–256. (in Chinese). doi:10.3878/j.issn.1006-9895.1507.15102

Doi, T., Behera, S. K., and Yamagata, T. (2020). Wintertime impacts of the 2019 super IOD on East Asia. *Geophys. Res. Lett.* 47, e2020GL089456. doi:10.1029/2020GL089456

Du, Z., Tan, Y., Zhang, R., He, J., and Liu, H. (2006). Two modes of Sea Surface temperature anomalies in the tropical Indian ocean: Monopole, dipole and their interactions. *Chin. J. of Atmos. Sci.* 30 (1), 11–24. (in Chinese).

Fan, Y., and Fan, K. (2017). Pacific decadal oscillation and the decadal change in the intensity of the interannual variability of the South China Sea summer monsoon. *Atmos. Ocean. Sci. Lett.* 10, 162–167. doi:10.1080/16742834.2016.1256189

Gill, A. E. (1980). Some simple solutions for heat-induced tropical circulation. *Q. J. R. Meteorological Soc.* 106 (449), 447–462. doi:10.1002/qj.49710644905

Grassi, B., Redaelli, G., Canziani, P. O., and Visconti, G. (2012). Effects of the PDO phase on the tropical belt width. *J. Clim.* 25, 3282–3290. doi:10.1175/JCLI-D-11-00244.1

Guan, Z., and Yamagata, T. (2003). The unusual summer of 1994 in East Asia: IOD teleconnections. *Geophys. Res. Lett.* 30. doi:10.1029/2002GL016831

Guo, P., and Wu, Q. (2022). Interdecadal variation of transition from Indian Ocean Dipole to Indian Ocean Basin mode and its causes. *Trans. Atmos. Sci.* 45, 562–572. (in Chinese). doi:10.13878/j.cnki.dqkxxb.20200113009

Hersbach, H., Bell, B., Berrisford, P., Hirahara, S., Horányi, A., Muñoz-Sabater, J., et al. (2020). The ERA5 global reanalysis. *Q. J. R. Meteorological Soc.* 146, 1999–2049. doi:10.1002/qj.3803

Hu, P., Chen, W., Chen, S., Liu, Y., and Huang, R. (2020). Extremely early summer monsoon onset in the South China Sea in 2019 following an El Niño event. *Mon. Weather Rev.* 148, 1877–1890. doi:10.1175/MWR-D-19-0317.1

Jiang, J., Liu, Y., and Li, J. (2021). Indian Ocean Dipole:a review and perspective. *Adv. Earth Sci.* 36, 579–591. (in Chinese). doi:10.11867/j.issn.1001-8166.2021.066

Krishnamurthy, L., and Krishnamurthy, V. (2016). Decadal and interannual variability of the Indian Ocean SST. *Clim. Dyn.* 46, 57–70. doi:10.1007/s00382-015-2568-3

Lau, K. M., and Yang, S. (1997). Climatology and interannual variability of the southeast Asian summer monsoon. *Adv. Atmos. Sci.* 14, 141–162. doi:10.1007/s00376-997-0016-y

Li, C., and Mu, M. (2001). The dipole in the equatorial Indian Ocean and its impacts on climate. *Chin. J. of Atmos. Sci.* 25, 433–443. (in Chinese).

Li, D., Zhang, G., Zhu, Y., Tan, Y., and Wang, X. (2007). Relationships between autumn Indian Ocean Dipole Mode and the strength of SCS summer monsoon. *J. Trop. Meteorology* 13 (1), 29–32.

Luo, J.-J., Zhang, R., Behera, S. K., Masumoto, Y., Jin, F.-F., Lukas, R., et al. (2010). Interaction between El Niño and extreme Indian Ocean Dipole. *J. Clim.* 23, 726–742. doi:10.1175/2009JCLI3104.1

Mantua, N. J., and Hare, S. R. (2002). The pacific decadal oscillation. *J. Oceanogr.* 58, 35–44. doi:10.1023/A:1015820616384

Rayner, N. A., Parker, D. E., Horton, E. B., Folland, C. K., Alexander, L. V., Rowell, D. P., et al. (2003). Global analyses of sea surface temperature, sea ice, and night marine air temperature since the late nineteenth century. *J. Geophys. Res. Atmos.* 108, 4407. doi:10.1029/2002JD002670

Saji, N. H., Goswami, B. N., Vinayachandran, P. N., and Yamagata, T. (1999). A dipole mode in the tropical Indian Ocean. *Nature* 401, 360–363. doi:10.1038/43854

Saji, N. H., and Yamagata, T. (2003). Possible impacts of Indian Ocean Dipole mode events on global climate. *Clim. Res.* 25, 151–169. doi:10.3354/cr025151

Takaya, Y., Ishikawa, I., Kobayashi, C., Endo, H., and Ose, T. (2020). Enhanced meiyu-baiu rainfall in early summer 2020: Aftermath of the 2019 super IOD event. *Geophys. Res. Lett.* 47, e2020GL090671. doi:10.1029/2020GL090671

Tao, S., and Chen, L. (1987). A review of recent research on the East Asian summer monsoon in China. *Monsoon Meteorol.*, 60–92.

Tao, S., and Zhang, Q. (1998). Response of the asian winter and summer monsoon to ENSO events. *Sci. Atmos. Sin.* 22 (4), 300–407. (in Chinese).

Wang, B., Huang, F., Wu, Z., Yang, J., Fu, X., and Kikuchi, K. (2009). Multi-scale climate variability of the South China sea monsoon: A review. *Dyn. Atmos. Oceans* 47, 15–37. doi:10.1016/j.dynatmoce.2008.09.004

Wang, C. (2019). Three-ocean interactions and climate variability: A review and perspective. *Clim. Dyn.* 53, 5119–5136. doi:10.1007/s00382-019-04930-x

Wu, G., Liu, P., Liu, Y., and Li, W. (2000). Impacts of the sea surface temperature anomaly in the Indian ocean on the subtropical anticyclone over the Western Pacific—Two stage thermal adaptation in the atmosphere. *Acta Meteorol. Sin.* 58 (5), 513–522. (in Chinese).

Wu, S., and Liang, J. (2002). Intensity index of South China Sea monsoon and its variation characteristics. *J.of Trop. Meteorology* 9.

Xiang, B., Yu, W., Li, T., and Wang, B. (2011). The critical role of the boreal summer mean state in the development of the IOD. *Geophys. Res. Lett.* 38. doi:10.1029/2010GL045851

Xiao, Y., Zhang, Z., and He, J. (2009). Progresses in the studies on Indian ocean dipoles. *J. Trop. Meteorology* 25 (5), 621–627. (in Chinese).

Xie, S.-P., Du, Y., Huang, G., Zheng, X.-T., Tokinaga, H., Hu, K., et al. (2010). Decadal shift in El Niño influences on indo–western pacific and east asian climate in the 1970s. *J. Clim.* 23, 3352–3368. doi:10.1175/2010JCLI3429.1

Xie, S.-P., Hu, K., Hafner, J., Tokinaga, H., Du, Y., Huang, G., et al. (2009). Indian ocean capacitor effect on indo–western pacific climate during the summer following El Niño. *J. Clim.* 22, 730–747. doi:10.1175/2008JCLI2544.1

Xie, T., Li, J., Chen, K., Zhang, Y., and Sun, C. (2021). Origin of Indian ocean multidecadal climate variability: Role of the North atlantic oscillation. *Clim. Dyn.* 56, 3277–3294. doi:10.1007/s00382-021-05643-w

Yan, X.-Y., and Zhang, M. (2005). Numerical simulation of the influence of Indian Ocean Dipole on climate variations over east Asian monsoon region during equatorial east Pacific Ocean SSTA. *J. Trop. Meteorology* 11 (1), 60–66.

Yang, H., and Sun, S. (2003). Longitudinal displacement of the subtropical high in the Western Pacific in summer and its influence. *Adv. Atmos. Sci.* 20, 921–933. doi:10.1007/BF02915515

Yang, J., Liu, Q., Xie, S.-P., Liu, Z., and Wu, L. (2007). Impact of the Indian Ocean SST basin mode on the Asian summer monsoon. *Geophys. Res. Lett.* 34, L02708. doi:10.1029/2006GL028571

Yu, J.-Y., Lu, M.-M., and Kim, S. T. (2012). A change in the relationship between tropical central Pacific SST variability and the extratropical atmosphere around 1990. *Environ. Res. Lett.* 7, 034025. doi:10.1088/1748-9326/7/3/034025

Yuan, Y., and Li, C. (2008). Decadal variability of the IOD-ENSO relationship. *Chin. Sci. Bull.* 53, 1745–1752. doi:10.1007/s11434-008-0196-6

Yuan, Y., and Li, C. (2009). Possible impacts of the tropical Indian Ocean SST anomaly modes on the South China Sea summer monsoon onset. *Chin. J. Atmos. Sci.* 33 (2), 325–336. (in Chinese).

Yuan, Y., Yang, H., Zhou, W., and Li, C. (2008a). Influences of the Indian Ocean Dipole on the Asian summer monsoon in the following year. *Int. J. Climatol.* 28, 1849–1859. doi:10.1002/joc.1678

Yuan, Y., Zhou, W., Chan, J. C. L., and Li, C. (2008b). Impacts of the basin-wide Indian Ocean SSTA on the South China Sea summer monsoon onset. *Int. J. Climatol.* 28, 1579–1587. doi:10.1002/joc.1671

Yue, Z., Zhou, W., and Li, T. (2021). Impact of the Indian Ocean Dipole on evolution of the subsequent ENSO: Relative roles of dynamic and thermodynamic processes. *J. Clim.* 34, 3591–3607. doi:10.1175/JCLI-D-20-0487.1

Zhang, R., and Tan, Y. (2003). "El Nino and interannual variation of the sea surface temperature in the tropical Indian Ocean," in *Atmospheric and oceanic processes, Dynamics, and climate change (SPIE)* (Munich, Germany: European Geosciences Union), 11–17. doi:10.1117/12.466694

Zhou, W., and Chan, J. C. L. (2007). ENSO and the South China Sea summer monsoon onset. *Int. J. Climatol.* 27, 157–167. doi:10.1002/joc.1380

Zhou, Z.-Q., Xie, S.-P., and Zhang, R. (2021). Historic Yangtze flooding of 2020 tied to extreme Indian Ocean conditions. *Proc. Natl. Acad. Sci.* 118, e2022255118. doi:10.1073/pnas.2022255118

frontiers | Frontiers in Earth Science

TYPE Methods
PUBLISHED 24 April 2023
DOI 10.3389/feart.2023.1099344

OPEN ACCESS

EDITED BY
Jianjun Xu,
Guangdong Ocean University, China

REVIEWED BY
Husi Letu,
Aerospace Information Research Institute (CAS), China
Chao Wang,
Nanjing University of Information Science and Technology, China

*CORRESPONDENCE
Wu Qishu,
172475076@qq.com

SPECIALTY SECTION
This article was submitted to Interdisciplinary Climate Studies, a section of the journal Frontiers in Earth Science

RECEIVED 15 November 2022
ACCEPTED 31 March 2023
PUBLISHED 24 April 2023

CITATION
Mei H, Qishu W, Huijun L, Siyu Y and Guofei W (2023), Correction method by introducing cloud cover forecast factor in model temperature forecast.
Front. Earth Sci. 11:1099344.
doi: 10.3389/feart.2023.1099344

Correction method by introducing cloud cover forecast factor in model temperature forecast

Han Mei[1,2], Wu Qishu[1,2]*, Liu Huijun[1,2], Yin Siyu[1,2] and Wei Guofei[1,2]

[1]Fujian Meteorological Observatory, Fuzhou, China, [2]Fujian Provincial Key Laboratory of Disaster Weather, Fuzhou, China

Objective temperature forecast products can achieve better forecast quality by using one-dimensional regression correction directly based on the present model temperature forecast product, and the forecast accuracy can be further improved by adding appropriate auxiliary factors. In this paper, ECMWF forecast products and ground observation data from Fujian are used to revise the surface temperature at 2 m by introducing a cloud cover forecast factor based on the model temperature forecast correction method. Analysis shows that the forecast deviation of daily maximum and minimum temperature after the revision of a single-factor forecast is obviously correlated with cloud cover. A variety of prediction schemes are designed, and the final scheme is determined through comparative testing. The following conclusions are drawn: all schemes based on cloud cover grouping can improve forecast performance, and the total cloud cover scheme is generally better than the low cloud cover scheme. There is a good positive correlation between the forecast deviation of maximum temperature and the mean total cloud cover; that is, the more cloud cover, the bigger the deviation. The minimum temperature is negatively correlated with cloud cover when the cloud cover is less than 40% and positively correlated for the rest. The absolute forecast deviations of the maximum and minimum temperatures are larger when the total cloud cover is less. Whether for T_{max} or T_{min} forecast, the binary regression scheme after grouping consistently showed the best performance, with the lowest MAE. The final scheme was used to forecast the maximum and minimum temperature in 2021, and most verification indicators showed improvement in most forecast periods. The forecast accuracy for the 36-h daily maximum and minimum temperature is 81.312% and 91.480%, respectively, which is 2.4%–2.6% higher than the single-factor regression scheme. The forecast skill scores (FSS) reach 0.065 and 0.086, indicating that the method can effectively improve forecast quality in a stable manner and can be used for practical forecasting.

KEYWORDS

the maximum temperature, the minimum temperature, cloud cover, MOS method, forecast accuracy, mean absolute deviation

1 Introduction

In recent years, with the advancement of numerical forecast and the continuous improvement of statistical methods such as model output statistics (MOS), perfect prognosis (PP), artificial neural networks (ANN), Kalman filter (KF), and the support vector machine (SVM) (Huang and Xie, 1993; Zhang and Sha, 2001; Wang et al., 2004; Chen et al., 2005; Wu et al., 2007; Qian et al., 2010; Chen et al., 2011; Li et al., 2011), the accuracy of temperature forecasts has been greatly improved, but it is still unable to meet people's growing demand for accurate and refined temperature forecasts. Therefore, methods of improving the accuracy of forecasts is an urgent issue. Temperature is sensitive to local weather and geographical characteristics. The MOS is the most commonly method used in daily temperature forecasting. It can introduce many forecast factors that are difficult to introduce by other methods, match local weather and climate characteristics, and make appropriate corrections to the systematic deviations of numerical models (Liu et al., 2004).

The MOS forecast method usually requires a certain length of historical data samples to achieve better forecast results. The samples should preferably have the same climate background characteristics, and the consistency factors of the samples should be as large as possible. Che et al. (2011) used the K-mean clustering method to make seasonal divisions in North China for temperature forecasts; the forecast error is generally smaller than the traditional seasonal division. Zhi et al. (2010, 2014) compared the different training periods of super-ensemble temperature forecasts and found that a sliding training period is better than a fixed training period. Wu et al. (2016) further optimized the division method of the training period. They used the quasi-symmetric sliding training period method to revise the model temperature forecast by selecting the sample data 1 month before and after the forecast date and also considered the model consistency and the sample's climate characteristics, which significantly improved the forecast quality. However, methods that highlight the training period do not consider the influencing factor of temperature. Many scholars in China have introduced multiple factors. Liu et al. (2004) selected multiple factors for MOS forecasts, and the forecast verification results showed that the short-term temperature forecast was improved in most cases. Zhang et al. (2011) used the MOS method to select 11 factors on the basis of T213 to forecast the daily maximum and minimum temperatures of 124 stations in Yunnan Province, and the forecast results were improved, especially in summer. Zhu and Mu (2013) established a MOS forecast equation based on the WRF model, using temperature, wind, sea level pressure, relative humidity, and precipitation at Urumqi Airport as forecast factors. The accuracy of the hourly temperature forecast was significantly improved compared with the forecast results directly output by the model. The introduction of multiple factors to establish equations can improve temperature prediction, but the factors should be selected to optimize the role of the main factors.

The local variation of temperature depends on temperature advection, pressure change, atmospheric stability, and diabatic processes (Zhu et al., 2000). Liang and Huang (2006) pointed out that in the absence of large-scale system transit, the diabatic processes are the main factors that affect the temperature change in the near-surface layer, while the diabatic processes are affected by many factors, such as the sky condition, the topography, underlying surface, and vegetation type. Therefore, it is necessary to fully consider the role of cloud cover in temperature forecast. Qin et al. (2007) analyzed the relationship between cloud cover and temperature in Nanning City and found that total cloud cover has a significant negative correlation with mean temperature and maximum temperature, while low cloud cover has a significant negative correlation with maximum temperature and a significant positive correlation with minimum temperature. Zheng et al. (2013) adopted the optimized cloud scheme in GRAPES, and the surface temperature simulated by the model was closer to the observed value. Luo et al. (2014) classified the sky conditions and established the classic MOS forecast model. They selected the numerical forecast product factors corresponding to the general occurrence time of maximum and minimum temperature, which positively and significantly improved the quality of local temperature forecast. Forecasters also make adjustments to temperature forecasts by evaluating the cloud cover in practice, but the specific adjustment extent varies from person to person and cannot be uniformly regulated.

Currently, most MOS temperature forecast methods directly perform one-dimensional regression correction on the model temperature forecast product, which can achieve good correction effects. The forecast quality is not worse than that of multi-factor modeling correction and has been widely used in many meteorological departments. Different amounts of cloud cover will cause differences in the deviation between the model temperature forecast and the actual observation. Therefore, it is meaningful to introduce cloud cover forecast as an auxiliary factor to further optimize the MOS temperature forecast, but few people have studied and applied it in practice. The Fujian Provincial Meteorological Observatory divided temperature samples according to different total cloud cover, established independent models for each subset, and achieved good correction effects. It ranked first in the comprehensive skill of temperature in the 2021 National Meteorological System Intelligent Forecast Technology Method Exchange Competition. In this paper, the optimal scheme of daily maximum and daily minimum temperature forecasts based on cloud cover is selected by further studying the cloud cover groupings and comparing several schemes.

2 Data and pre-processing

2.1 Data

In this paper, the maximum and minimum temperature at 2 m, total cloud cover, and low cloud cover of ECMWF from 2018 to 2021 issued by the China Meteorological Administration were adopted. The ECMWF data are obtained twice a day at 08: 00 and 20:00 (Beijing time, same below), and the forecast time period is 0–240 h, the horizontal resolution is 0.125° × 0.125°, and the time resolution is 3 h for 0–72 h and 6 h for 78–240 h. To ensure calculation efficiency and reliability of the observation data, the testing stations are 70 national meteorological stations in Fujian Province.

2.2 Data pre-processing

The inverse distance weighting interpolation method is used to interpolate the ECMWF fine grid point surface elements to the station, and the Cressman objective interpolation method is used as a reference for the weighting coefficients. This is carried out for station-based modeling and forecast. The interpolation method is as follows:

$$P_k = \frac{\sum_{i=1}^{m}\sum_{j=1}^{n} W_{kij} P_{ij}}{\sum_{i=1}^{m}\sum_{j=1}^{n} W_{kij}} \quad (1)$$

In Formula 1, P_k is the forecast value of the element at the kth station obtained by interpolation, P_{ij} is the forecast value of the element at the grid point (i, j), W_{kij} is the weight factor, and m and n are the numbers of grid points in the latitudinal and longitudinal directions, respectively. The weighting factor used in this paper can be expressed as follows:

$$W_{kij} = \begin{cases} \frac{R^2 - d_{kij}^2}{R^2 + d_{kij}^2}, & d_{kij} < R \\ 0, & d_{kij} \geq R \end{cases} \quad (2)$$

In Formula 2, R is the effective influence radius and d_{kij} is the distance from grid point (i, j) to station k. In operational work, for the convenience of calculation, the difference between longitude and latitude is used to represent the distance, and the effective influence radius is taken as 1°.

The daily maximum temperature (T_{max}) and the daily minimum temperature (T_{min}) are calculated as the maximum and minimum temperatures over a 24-h period, respectively. Cloud cover (total cloud cover or low cloud cover) is calculated as the 12-h mean cloud cover, and the mean cloud cover at a given point is the mean of all available cloud cover forecasts at that point within a given forecast time period. Because the latest ECMWF data are usually obtained later than the forecast start time, the forecast in this paper is the correction of the model lag of 12 h; that is, the first day of operational forecast corresponds to the 12–36-h period of the model forecast and so on for the other forecast periods.

3 Methods

3.1 Correction method

The one-dimensional linear regression equations for T_{max} and T_{min} at a certain forecast period for each station are established using the least square method:

$$S_i = a + bF_i. \quad (3)$$

In Formula 3, S_i is regression correction temperature at the ith forecast period, F_i is the temperature forecast value of the model at this period, a is a constant, and b is the regression coefficient. Taking cloud cover as the division basis, the forecast value and observation value are used to establish a and b for each subset after division and are updated twice a day, and the obtained regression equation is used to correct T_{max} and T_{min} of the corresponding subset.

During the day, direct solar radiation can reach the earth's surface and warm it. If there is cloud cover, the cloud layer will reflect some of the solar radiation, reducing the energy input to the surface and hindering warming. At night, the heat released from the surface dissipates upwards, causing the surface temperature to decrease. If there is cloud cover, the cloud layer can reflect the heat from the surface, thereby weakening heat dissipation and hindering cooling. Therefore, the effect of cloud cover on surface temperature is opposite during the day and night, and the reverse is true under clear skies. Because cloud cover at night and during the day has opposite effects on temperature, daytime cloud cover is used as the auxiliary factor for the correction of T_{max}, and nighttime cloud cover is used as the auxiliary factor for correction of T_{min}.

3.2 Training period

The quasi-symmetric mixed sliding training period method can significantly improve the quality of a temperature forecast by the MOS method and has great application value in operational work (Wu et al., 2016). This paper continues to use this method, and the total samples during the training period mixed samples from 35 days before the forecast date and samples from 35 days after the forecast day of the previous year and used sliding sampling with the forecast date.

3.3 Inspection method

To evaluate the operational performance of the MOS forecast, the mean absolute error of temperature forecast (*MAE*, Zhou et al., 2006), the temperature forecast accuracy (*FA*), and the temperature forecast skill scores (FSS) were used in this paper:

$$FA = \frac{N_r}{N_f} \times 100\%. \quad (4)$$

In Formula 4, *FA* is the percentage of the absolute deviation between the temperature forecast whose observed value does not exceed 2°C, N_r is the number of stations (times) where the value of the difference between the forecast temperature and the observed value does not exceed 2°C, and N_f is the total number of stations (times) that have been forecasted.

$$FSS = \frac{MAE_0 - MAE_N}{MAE_0} \quad (5)$$

In Formula 5, MAE_O is the *MAE* of the temperature forecast of the initial scheme and MAE_N is the *MAE* of the temperature forecast for the improved scheme. When $MAE_O = 0$, $FSS = 1.01$.

4 Scheme comparison and improvement

4.1 Initial scheme design

Based on the observed temperature data from 2019 to 2020 and temperature, total cloud cover, and low cloud cover forecast data from

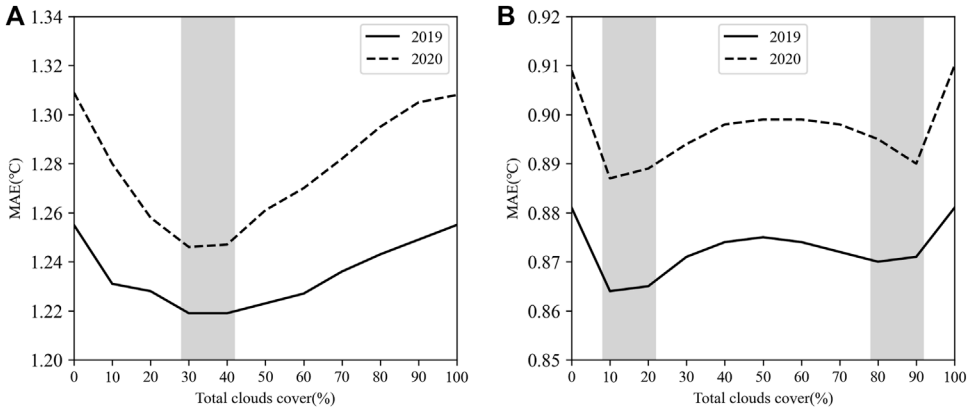

FIGURE 1
Comparison of the *MAE* of different total cloud cover threshold forecasts on the first day. **(A)** T_{max}; **(B)** T_{min}.

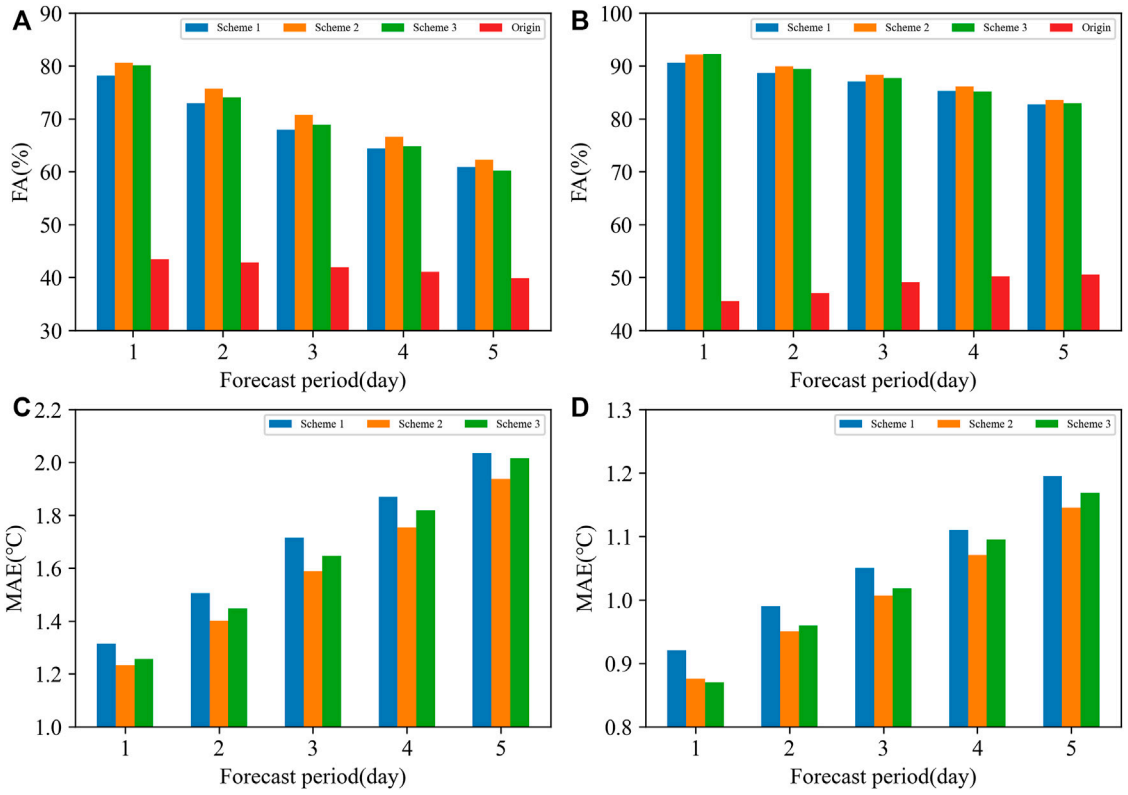

FIGURE 2
Comparison of the forecast results of the three schemes from 2019 to 2020. **(A)** *FA* of T_{max} (unit: %), **(B)** *FA* of T_{min} (unit: %), **(C)** *MAE* of T_{max} (unit: °C), and **(D)** *MAE* of T_{min} (unit: °C).

ECMWF, three schemes are designed and compared to discuss the feasibility and the improvement direction of introducing cloud cover.

Scheme 1: No grouping, using the quasi-symmetric mixed sliding training period method (one-dimensional regression) to model and revise all temperature forecast samples (Wu et al., 2016).

Scheme 2: Grouping by total cloud cover, the temperature forecast samples with total cloud cover less than the specified threshold value are grouped for separate modeling correction, and the remaining samples are grouped as another group. The exhaustive method is used for the cloud cover threshold, starting from 0% total cloud cover as the threshold, increasing to 100% at 5% intervals; 21 cloud cover values were selected as grouping thresholds for correction.

Scheme 3: Grouping by low cloud cover, the temperature forecast samples with cloud cover less than the specified

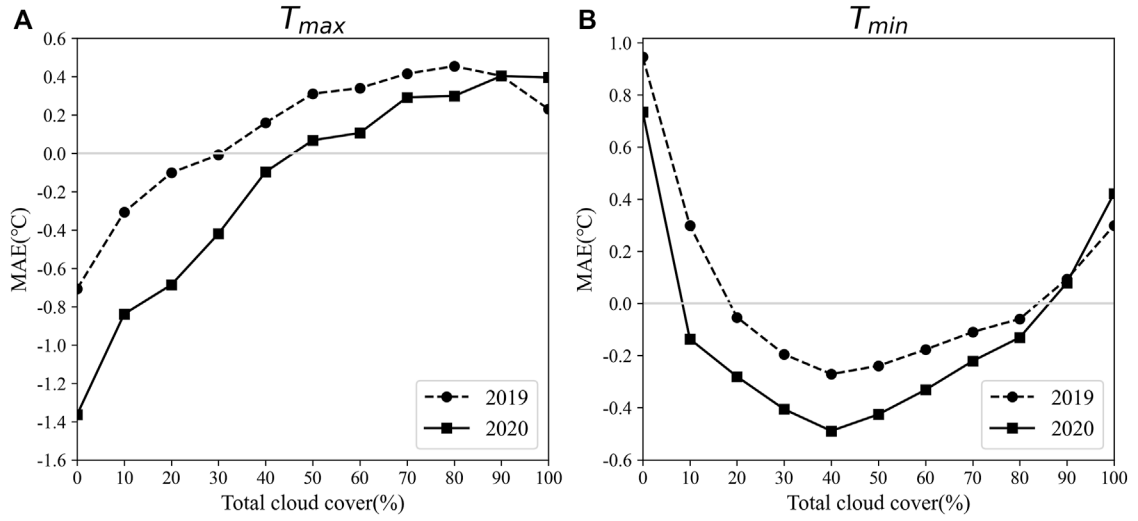

FIGURE 3
Relationship between the mean deviations of 12–36 h forecasts of temperature and the total cloud cover in 2019 and 2020. **(A)**: T_{max} and **(B)**: T_{min}.

threshold are grouped for separate modeling correction, and the remaining samples are grouped as another group. Groupings of the cloud thresholds are the same as in Scheme 2.

According to the forecast results of Scheme 2 (Figure 1A), the absolute forecast deviation of T_{max} for the first day is less than that of no grouping (the threshold of 0% cloud cover can be approximated to no grouping). When about 30%–40% cloud cover is used as the grouping threshold, the forecast result is better, the *MAE* is small, and the *MAE* of the optimal threshold can be reduced by about 0.05°C. For the T_{min} forecast (Figure 1B), the *MAE* of grouping is also less than that of no grouping. The improvement is obvious when grouping by the less and more cloud cover threshold intervals, and grouping by the less cloud cover threshold is slightly better than grouping by the more cloud cover threshold. Because the potential for improvement of the T_{min} forecast is smaller than that of the T_{max} forecast, there is not much difference between the different thresholds. The performance of Scheme 3 is similar to that of Scheme 2 and will not be presented separately.

The optimal threshold scheme of T_{max} and T_{min} among the 21 grouping methods of Scheme 2 and Scheme 3 was selected to compare with Scheme 1 and the original uncorrected results. The results are shown in Figure 2. Seen from *FA*, the forecast results of T_{max} and T_{min} in all three revised schemes were significantly improved compared with the original uncorrected ones, and the improvement rate in the first 5 days was 100% or above. For T_{max}, the scheme grouping by total cloud cover performed better than the other two schemes in all forecast periods in terms of *FA* and *MAE* (Figures 2A, C). The *FA* of the scheme grouping by low cloud cover improved compared with no grouping in the first 4 days, but it was not better on the fifth day, while the *MAE* improved in all time periods. For T_{min}, the performance of Scheme 2 was also the best compared with the other schemes in all forecast periods (Figures 2B, D), followed by Scheme 3, and both schemes were better than Scheme 1 in terms of *FA* and *MAE*. In general, the introduction of cloud cover improved the forecast performance, and the introduction of total cloud cover was better than low cloud cover.

4.2 Relationship between cloud cover and temperature correction forecast deviation

In general, the least squares method is used to directly model and correct based on the modeled temperature forecast products. The ideal result of the mean deviation of the objective temperature forecast is unbiased; however, there is a significant correlation between forecast deviation of temperature and cloud cover. Figure 3 shows the relationship between the mean forecast deviation of T_{max} and T_{min} based on Scheme 1 and the total cloud cover with a 12–36 h forecast period in 2019 and 2020 for 70 national meteorological stations. The relationship between low cloud cover and temperature forecast is similar to the total cloud cover, which is not given in the paper. It can be seen that for T_{max} (Figure 3A), the 2-year mean forecast deviation of temperature has a good positive linear correlation with cloud cover; the correlation coefficient is 0.85 in 2019 and 0.95 in 2020. The forecast value is often less than the actual when the cloud cover is below 30%–40% and has a large linear slope. The forecast tends to be greater than the actual when the cloud cover is above 40% and has a smaller slope. For T_{min} (Figure 3B), a negative correlation exists below the threshold of 40% cloud cover, with a steep linear slope; the correlation coefficients were −0.96 in 2019 and −0.89 in 2020. Conversely, a positive correlation with a smaller linear slope was found above the threshold of 40% cloud cover; the correlation coefficients were 0.95 in 2019 and 0.96 in 2020. The common point of T_{max} and T_{min} is that the absolute deviation will be larger when the cloud cover is low. Although the influence of cloud cover has been considered in the ECMWF temperature forecast, there is still a strong mean correlation between the mean forecast deviation and cloud cover. Meanwhile, schemes of grouping by cloud cover demonstrate an improvement in forecast accuracy. Therefore, the multiple regression scheme introduces a cloud cover factor based on cloud cover grouping that can be used in professional work. In the following, schemes will be designed and compared to select the best.

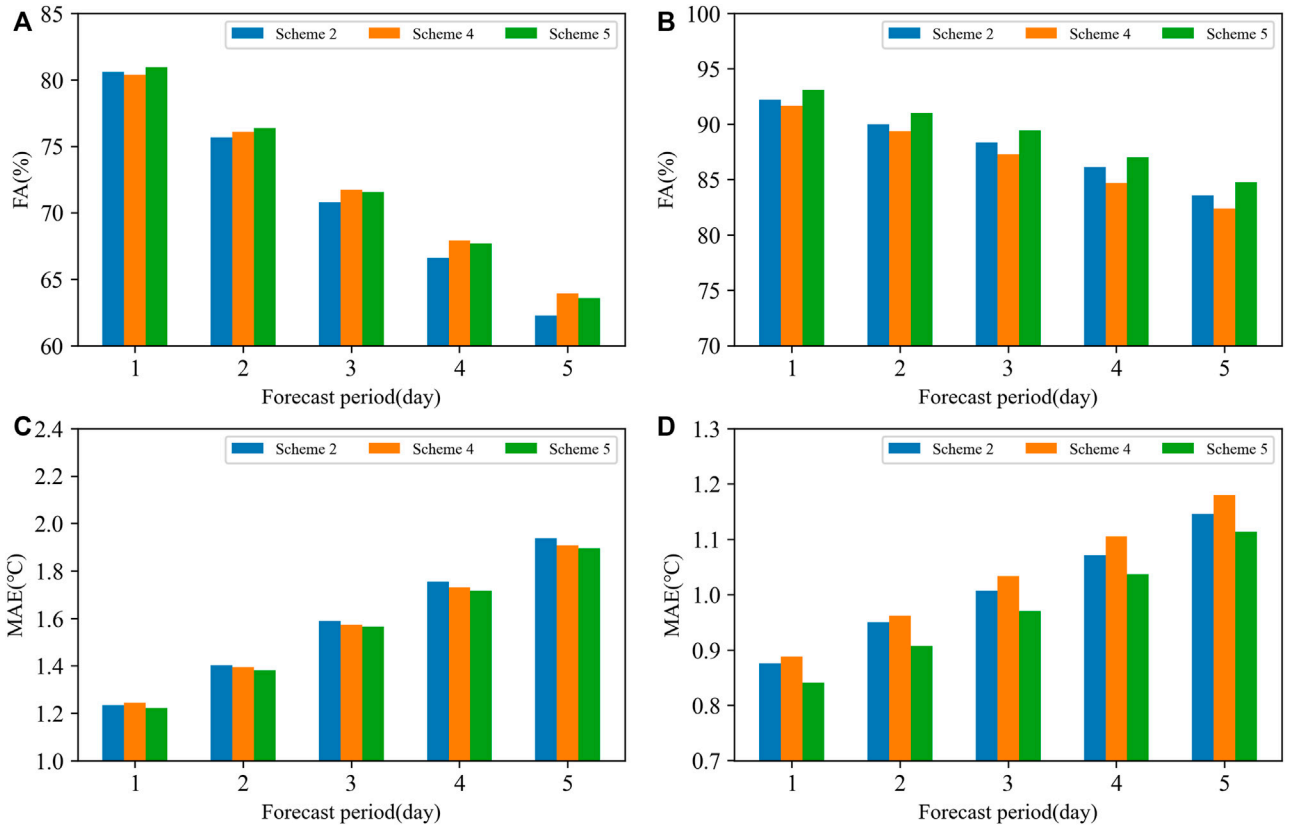

FIGURE 4
Comparison of the forecast results of the three schemes from 2019 to 2020. **(A)** *FA* of T_{max} (unit: %), **(B)** *FA* of T_{min} (unit: %), **(C)** *MAE* of T_{max} (unit: °C), and **(D)** *MAE* of T_{min} (unit: °C).

4.3 Improving scheme design

Based on the aforementioned discussion, improvement plans were designed to maximize forecast performance by considering the roles of total cloud cover, grouping methods, and binary regression methods in the forecast.

Scheme 4: Binary regression, using the quasi-symmetric mixed sliding training period method (Wu et al., 2016), taking temperature and total cloud cover forecast as two forecast factors to establish the forecast equation.

Scheme 5: After grouping by total cloud cover, correction is performed using Scheme 4. From Figure 1A, it can be seen that the optimal threshold for the high-temperature grouping is at 30%–40% cloud cover, and Figure 3 shows that the 40% cloud cover is a special turning point in both T_{max} and T_{min} forecasts. In practical applications, less cloud cover is conducive to the increase of daytime T_{max} and the decrease of nighttime T_{min}. Therefore, the 40% cloud cover is used as the grouping threshold. After grouping, the cloud cover is introduced for binary regression to establish the forecast equation.

Using the aforementioned two plans, a verification experiment was conducted for T_{max} and T_{min} from 2019 to 2020, and the results were compared with Scheme 2 whose grouping threshold is set at 40% cloud cover (Figure 4). In terms of forecast verification results, for T_{max} (Figures 4A, C), the *FA* in Scheme 5 is generally larger than that in Scheme 2. With increased forecast time, the improvement is more obvious, but it is slightly less than that of Scheme 4 on the third to fifth days, while Scheme 4 is slightly worse than Scheme 2 on the 1st day. In terms of *MAE*, Scheme 5 has a slight decrease, which is better than the other two schemes. For T_{min} (Figures 4B, D), the overall improvement of Scheme 5 is more significant than that of T_{max}, and all forecast indicators at all forecast periods are improved compared with other schemes. Scheme 3 is better than Scheme 4. In general, Scheme 5 is superior to other schemes. For T_{max}, there is a linear relationship between the mean forecast deviation and cloud cover, with different slopes between low cloud cover and high cloud cover. Each of the three schemes has advantages, but the performance of the binary regression scheme after grouping performs more stably in terms of *MAE*. For T_{min}, the mean forecast deviation has an opposite relationship between less and more cloud cover. Therefore, the binary regression scheme after grouping can better improve the forecast quality.

4.4 Availability and stability of improvement schemes

Scheme 5 was used for temperature forecast in 2021 to test the usability and stability of the method, and the verification results are shown in Table 1. According to the results of the T_{max} forecast, all

TABLE 1 Test results of T_{max} and T_{min} forecasts at 1–7 d by Scheme 1 and Scheme 5 in 2021.

Statistics		Scheme	1 d	2 d	3 d	4 d	5 d	6 d	7 d
T_{max}	FA (%)	1	78.706	74.178	69.951	67.544	64.179	60.138	55.477
		5	81.312	76.127	72.159	69.034	66.317	62.065	56.718
		Improvement	2.606	1.949	2.208	1.490	2.138	1.927	1.241
	MAE (°C)	1	1.300	1.460	1.610	1.710	1.830	2.000	2.210
		5	1.215	1.380	1.532	1.657	1.775	1.958	2.204
		FSS	0.065	0.055	0.048	0.031	0.030	0.021	0.003
T_{min}	FA (%)	1	89.124	87.771	86.064	83.868	81.034	77.621	74.858
		5	91.480	89.657	87.676	85.228	82.697	78.661	76.374
		Improvement	2.356	1.886	1.612	1.360	1.663	1.040	1.516
	MAE (°C)	1	0.970	1.030	1.090	1.150	1.240	1.350	1.440
		5	0.887	0.950	1.023	1.099	1.171	1.296	1.378
		FSS	0.086	0.078	0.061	0.044	0.056	0.040	0.043

verification indicators in Scheme 5 show significant improvements compared to Scheme 1, with an overall increase in *FA* of 1.2–2.6%. The highest increase is 2.6% on the 1st day; after the improvement, the mean accuracy rate reached 81%. The accuracy continued to increase by about 2% in the fifth to sixth days. *MAE* decreased by 0.04–0.08°C on all forecast periods, except for slightly less on the 7th day. The first 3 days decreased by about 0.08°C, and the FSS can reach 0.05–0.06. In terms of the T_{min} forecast, all indicators of all forecast periods also showed improvement, with an increase of 1.0%–2.4% in FA, and the highest increase was 2.36% on the first day. *MAE* decreased by approximately 0.05°C–0.08°C. The FSS in the first 3 days reached 0.06 to 0.08, and the *FA* on the first day reached 91.48%.

In recent years, the application of the quasi-symmetric sliding training period MOS forecast method has greatly improved T_{max} and T_{min} forecast results in Fujian Province. The method ranks among the top in national forecast quality inspections; especially, the *FA* of T_{min} is basically more than 90%. Under the condition that the forecast accuracy of the original model has not been improved, there is some room for improvement of the forecast results, but the forecast accuracy of Scheme 5 increased by about 2% compared with Scheme 2 in T_{max} and T_{min} forecast in 2021. These findings show that this method can further improve the forecast quality, and it has a certain stability. At present, it has achieved good results in the operational application of actual temperature forecasts in Fujian. Although Scheme 5 showed some improvement in T_{max} forecasts compared to Scheme 4, the difference was not significant, and the best plan should be selected based on local conditions and corresponding evaluations in practical applications.

5 Conclusion

This paper designs a MOS forecast method that uses total cloud cover as a predictor for the 2 m temperature forecast. Different schemes are designed and optimized using multiple verification indicators. The results show that:

1. All grouping schemes based on cloud cover show improvement in forecast performance, and the introduction of total cloud cover shows advantages over low cloud cover.
2. There is a good positive correlation between the annual mean forecast deviation of the T_{max} and the mean total cloud cover. For T_{min}, there is a negative correlation below 40% cloud cover and a positive correlation above it. Both T_{max} and T_{min} forecasts have larger absolute deviations when total cloud cover is less than 40%.
3. Whether for T_{max} or T_{min} forecast, the binary regression scheme after grouping consistently showed the best performance, with the lowest MAE.
4. Based on the optimization of the scheme in the last 2 years, the improved scheme is used to forecast the T_{max} and T_{min} in 2021. The verification indicators show certain improvements in most forecast periods, with *FA* for T_{max} and T_{min} being 81.312% and 91.480%, respectively, which is an improvement of 2.4%–2.6% relative to single-factor regression plans. The FSS of 0.065 for T_{max} and 0.086 for T_{min} indicate that this method effectively improves forecast quality and stability, making it suitable for practical forecasting. The introduction of total cloud cover to the MOS forecast can significantly improve the forecast quality, but the correction effect may be poor when the model's cloud cover forecast has large biases from observations. Further research is needed to determine the reliability of cloud cover forecasts from multiple models and ensemble prediction products.

Data availability statement

The raw data supporting the conclusion of this article will be made available by the authors, without undue reservation.

Author contributions

HM: methodology and writing. WQ: data curation and software. LH: visualization. YS: editing and translation. WG: validation.

Funding

This work was supported by the Natural Science and Technology Program of Fujian Province (2021J01457), the National Key R&D Program (2018YFC1506905), and the Innovation Project of the China Meteorological Administration (CXFZ2021Z009). The Chinese Meteorological Administration's retrospective summary project (FPZJ2023-061).

Conflict of interest

The authors declare that the research was conducted in the absence of any commercial or financial relationships that could be construed as a potential conflict of interest.

Publisher's note

All claims expressed in this article are solely those of the authors and do not necessarily represent those of their affiliated organizations, or those of the publisher, the editors, and the reviewers. Any product that may be evaluated in this article, or claim that may be made by its manufacturer, is not guaranteed or endorsed by the publisher.

References

Che, Q., Zhao, S., and Fan, G. (2011). Seasonal partition problem of MOS forecast for extreme temperature in North China[J]. *J. Of Appl. Meteorological Sci.* 22 (4), 429–436. doi:10.11898/1001-7313.20110405

Chen, F., Jiao, M., and Chen, J. (2011). A new scheme calibration of ensemble forecast products based on bayesian processor of output and its study results for temperature prediction [J]. *Meteorol. Mon.* 37 (1), 14–20. doi:10.7519/j.issn.1000-0526.2011.1.002

Chen, Y., Chen, X., Ma, J., and Wen, L. P. (2005). Nano neodymium oxide induces massive vacuolization and autophagic cell death in non-small cell lung cancer NCI-H460 cells. *J. Arid Meteorology* 23 (4), 52–60. doi:10.1016/j.bbrc.2005.09.018

Huang, J., and Xie, Z. (1993). The application of kalman filter technique to weather forecast[J]. *Meteorol. Mon.* 21 (2), 3–7. doi:10.7519/j.issn.1000-0526.1994.9.009

Li, Q., Hu, B., and Wang, X. (2011). Analysis of hail disasters in the central region of gansu Province[J]. *J. Arid Meteorology* 29 (2), 231–235. doi:10.3969/j.issn.1006-7639.2011.02.017

Liang, L., and Huang, G. (2006). Research on forecast method of maximum and minimum temperature at single station[J]. *J. Of Guangxi Meteorology* 27 (3), 4–6.

Liu, H., Zhao, S., and Lu, Z. (2004). Objective element forecast at nmc—MOS system [J]. *Xin Jiang Meteorol.* 27 (3), 4–7.

Luo, J., Zhou, J., and Yan, Y. (2014). Local temperature MOS forecast method based on numerical forecast products and superior guidance[J]. *Meteorological Sci. Technol.* 42 (003), 443–450. doi:10.3969/j.issn.1671-6345.2014.03.015

Qian, L., Lan, X., and Yang, Y. (2010). The application of optimal subset neural network to temperature objective forecast in wuwei[J]. *Meteorol. Mon.* 36 (5), 102–107. doi:10.7519/j.issn.1000-0526.2010.5.015

Qin, W., Huang, D., and Liao, X. (2007). Analysis of the variation characteristics of cloudiness in nanning and relationship with temperature and precipitation[J]. *J. Of Meteorlogical Res. Appl.* 28 (4), 14–19.

Wang, X., Yang, X., and Shi, D. (2004). Application of numerical forecast products to summer high temperature prediction[J]. *Meteorological Sci. Technol.* 32 (S1), 47–49. doi:10.3969/j.issn.1671-6345.2004.z1.012

Wu, J., Pei, H., and Shi, Y. (2007). The forecast of surface air temperature using BP-MOS method based on the numerical forecast results [J]. *Sci. Meteorol. Sin.* 27 (4), 430–435. doi:10.3969/j.issn.1009-0827.2007.04.012

Wu, Q., Han, M., and Guo, H. (2016). The optimal training period scheme of MOS temperature forecast[J]. *J. Appl. Meteorological Sci.* 27 (4), 426–434. doi:10.11898/1001-7313.20160405

Zhang, W., and Sha, W. C. (2001). An interpolation and similarity method of the study on temperature prediction[J]. *Sci. Meteorol. Sin.* 21 (2), 241–245. doi:10.3969/j.issn.1009-0827.2001.02.017

Zhang, X., Cao, J., and Yang, S. (2011). Multi-model compositive MOS method application of fine temperature forecast[J]. *J. Yunnan Univ.* 33 (1), 67–70.

Zheng, X., Xu, G., and Rongqing, W. (2013). Introducting and influence testing of the new cloud fractiong scheme in the GRAPES[J]. *Meteorol. Mon.* 39 (1), 57–66. doi:10.7519/j.issn.1000-0526.2013.01.007

Zhi, X., Li, G., and Peng, T. (2014). On the probabilistic forecast of 2 meter temperature of a single station based on bayesian theory[J]. *Trans. Atmos. Sci.* 37 (6), 740–748. doi:10.13878/j.cnki.dqkxxb.20130613006

Zhi, X., Wu, Q., Bai, Y., and Qi, H. (2010). The multimodel superensemble prediction of the surface temperature using the IPCC AR4 scenario runs. *J. Meteorological Sci.* (5), 708–714.

Zhou, B., Zhao, C., and Zhao, S. (2006). Multi-model ensemble forecast technology with analysis and verification of the results[J]. *J. Appl. Meteorological Sci.* 17, 104–109. doi:10.3969/j.issn.1001-7313.2006.z1.015

Zhu, G., and Mu, H. (2013). Application of model outout Statistics into objective element forecast at Airport[J]. *Desert Oasis Meteorology* 7 (3), 13–16. doi:10.3969/j.issn.1002-0799.2013.03.004

Zhu, Q., Lin, J., and Shaowen, S. (2000). *Principle of synoptic meteorology[M]*. Beijing: Meteorological Press, 26–27.

frontiers | Frontiers in Earth Science

TYPE Original Research
PUBLISHED 23 May 2023
DOI 10.3389/feart.2023.1106291

OPEN ACCESS

EDITED BY
Sheng Chen,
Chinese Academy of Sciences (CAS), China

REVIEWED BY
Chunsong Lu,
Nanjing University of Information Science and Technology, China
Li Tao,
Nanjing University of Information Science and Technology, China

*CORRESPONDENCE
Zheng Ling,
lingz@gdou.edu.cn

RECEIVED 23 November 2022
ACCEPTED 10 May 2023
PUBLISHED 23 May 2023

CITATION
Wu P, Ling Z and He H (2023), The effects of intraseasonal oscillations on landfalling tropical cyclones in the Philippines during the boreal summer.
Front. Earth Sci. 11:1106291.
doi: 10.3389/feart.2023.1106291

The effects of intraseasonal oscillations on landfalling tropical cyclones in the Philippines during the boreal summer

Peicong Wu[1], Zheng Ling[1,2,3]* and Hailun He[3]

[1]Key Laboratory of Climate, Resources and Environment in Continental Shelf Sea and Deep Sea of Department of Education of Guangdong Province, College of Ocean and Meteorology, Guangdong Ocean University, Zhanjiang, China, [2]Southern Marine Science and Engineering Guangdong Laboratory (Zhuhai), Zhuhai, China, [3]State Key Laboratory of Satellite Ocean Environment Dynamics, Second Institute of Oceanography, Ministry of Natural Resources, Hangzhou, China

As a kind of weather phenomenon with destructive wind and heavy rainfall, tropical cyclones (TCs), especially the landing TCs, can cause severer economic damage and losses of life. Philippines is one of the countries mostly affected by Tropical cyclones (TCs). Based on the best-track TC data and global atmospheric and oceanic reanalysis data, the present paper investigates the isolated and combined effects of two intraseasonal oscillations, the Madden-Julian oscillation (MJO) and the quasi-biweekly oscillation (QBWO), on landfall of TCs in the Philippines during boreal summer (May-September) in 1979-2019. The results show that both the MJO and the QBWO can significantly affect the frequency, landfall intensity, location, and translation speed of TCs that make landfall in the Philippines. During the convective (non-convective) phases of the MJO and the QBWO, more (less) frequent and stronger (weaker) TCs make landfall in the Philippines. This is due to the increased (decreased) frequency of TCs formation in the NWP and environmental factors in the region east of the Philippines that are favorable (unfavorable) for the development of TCs. With the northward propagation of the convective signals of the MJO and QBWO, the Western Pacific Subtropical High (WPSH) shifts eastward, and the steering flow is unfavorable for westward movement of NWP TCs. This, in turn, causes a northward shift in the landfall locations and a decrease in the translation speed of TCs. These results are helpful for the prediction of the TCs affecting the Philippines.

KEYWORDS

Philippines, tropical cyclones, Madden-Julian oscillation, quasi-biweekly oscillation, western Pacific subtropical high

1 Introduction

The Philippines is located in the western boundary of the northwestern Pacific (NWP), the most active region of tropical cyclone (TC) activity in the world. This makes the Philippines the country mostly affected by TCs. Every year on average, 18 TCs affect the Philippines and 3.6–6 TCs make landfall in the Philippines (Takagi and Esteban, 2016; Corporal-Lodangco and Leslie, 2017). These landfalling TCs bring very strong winds, heavy rains and storm surges, which cause loss of life and considerable economic damage in the Philippines (Warren, 2016).

The TCs affecting the Philippines have been widely studied (Lyon and Camargo, 2009; Corporal-Lodangco et al., 2016; Corporal-Lodangco and Leslie, 2016; Warren, 2016). Kubota

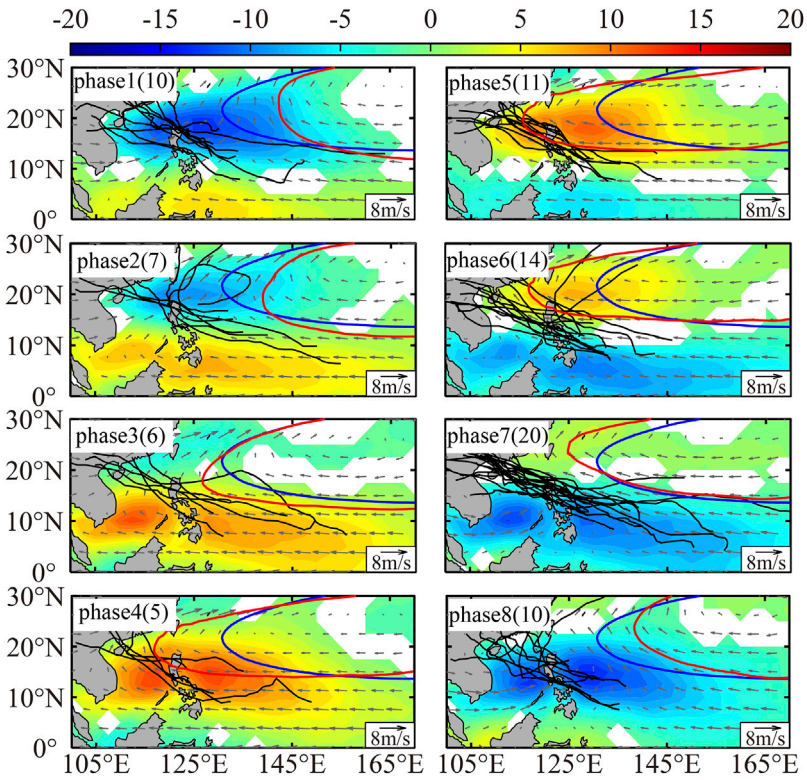

FIGURE 1
The composite OLR anomalies (color, W m^{-2}), tracks of TCs (black lines), location of western Pacific subtropical high and 300–850 hPa mass weighted steering flow (vector, m s^{-1}) in each phase of the MJO. Blue curves denote the location of the climatological 5,870 geopotential height at 500 hPa, and the red curves denote the location of the 5,870 geopotential height at 500 hPa in each phase of the MJO. Numbers in brackets are number of the landfalling TCs in each phase of the MJO. The phase that the TC belongs to is determined by the landfalling day.

and Chan (2009) found that the TC Landfall Frequency in the Philippines (TLFP) has a significant interdecadal variation. Prior to 1939, this variability had a period of about 32 years, but after 1945 the period has decreased to about 10–22 years. Kubota and Chan found that the decadal variation of the TLFP was related to the different phases of ENSO and the Pacific decadal oscillation (PDO). During the negative phase of the PDO, more (fewer) TCs made landfall in the Philippines in El Niño (La Niña) years. However, during the positive phase of PDO, the difference in TLFP frequency between El Niño and La Niña years is not obvious. Corporal-Lodangco and Leslie (2017) showed that the annual variation of TLFP was affected by El Niño/Southern Oscillation (ENSO). They found that the TLFP decreases in El Niño years, while it increases (decreases) from April to June and October to December (from January to March and July to September) in La Niña years. Cinco et al. (2016) analyzed the TCs affecting the Philippines during 1951–2013 and found that there was a slight decreasing trend in the number of landfalling TCs in the Philippines, which has become more pronounced over the last two decades.

Landfall intensity is an important factor for the disaster prevention. Previous studies have shown that the intensity of TC landing in the Philippines was affected by several factors. Takagi and Esteban (2016) conducted a case analysis of two Super Typhoons (STY) that made landfall in the Philippines: *STY Haiyan* and *STY Zeb*. They found that the abnormally high sea surface temperature (SST) around the Philippines was the main reason for the extreme development of these two TCs into STYs. Choi et al. (2015) analyzed changes in TC intensity over the past 62 years (1951–2012) by calculating the annual average minimum central pressure of TCs that affected the Philippines between July to September. Their results showed that the middle atmospheric humidity, lower atmospheric temperature and SST are all important factors driving the generation and intensification of TCs.

The NWP is affected by two intraseasonal oscillations, the Madden-Julian oscillation (MJO), with a period of about 30–60 days (Madden and Julian, 1971), and the quasi-biweekly oscillation (QBWO), with a period of about 10–20 days (Krishnamurti and Bhalme, 1976). Previous studies have shown that these intraseasonal oscillations can significantly affect the genesis, motion and intensity of TCs over the NWP (Kim et al., 2008; Mao and Wu, 2010; Huang et al., 2011; Li and Zhou, 2013a; Yoshida et al., 2014; Zhao et al., 2015a; Zhao et al., 2015b; Kikuchi, 2021; Nakano et al., 2021). Li and Zhou (2013b) further found that both the MJO and the QBWO significantly affect the TC landfall frequency in China, the Philippines, Korea and Japan. In addition, other factors, such as landfall location, landfall intensity and translation speed are important for the degree of damage caused by the landfalling TCs. In the present study, a comprehensive

TABLE 1 Number of Philippines landfalling TCs, duration and daily landfall Rate (DLR) in each phase of the MJO and the QBWO. The number of TCs in each phase is determined by the day when each TC made landfall in the Philippines. The entries followed by one and two asterisks (*) are statistically significant at the 90% and 95% confidence level, respectively. The phase that the TC belongs to is determined by the landfalling day.

		1	2	3	4	5	6	7	8	Total
MJO	Number	10	7	6	5	11	14	20	10	83
	Days	742	743	849	798	777	714	892	758	6,273
	DLR	1.34%	0.94%	0.71%	0.63%*	1.42%	1.96%	2.24%**	1.32%	1.32%
QBWO	Number	9	16	25	15	9	4	2	3	83
	Days	780	697	758	802	751	785	831	869	6,273
	DLR	1.15%	2.30%**	3.30%**	1.87%	1.20%	0.51%	0.24%**	0.35%**	1.32%

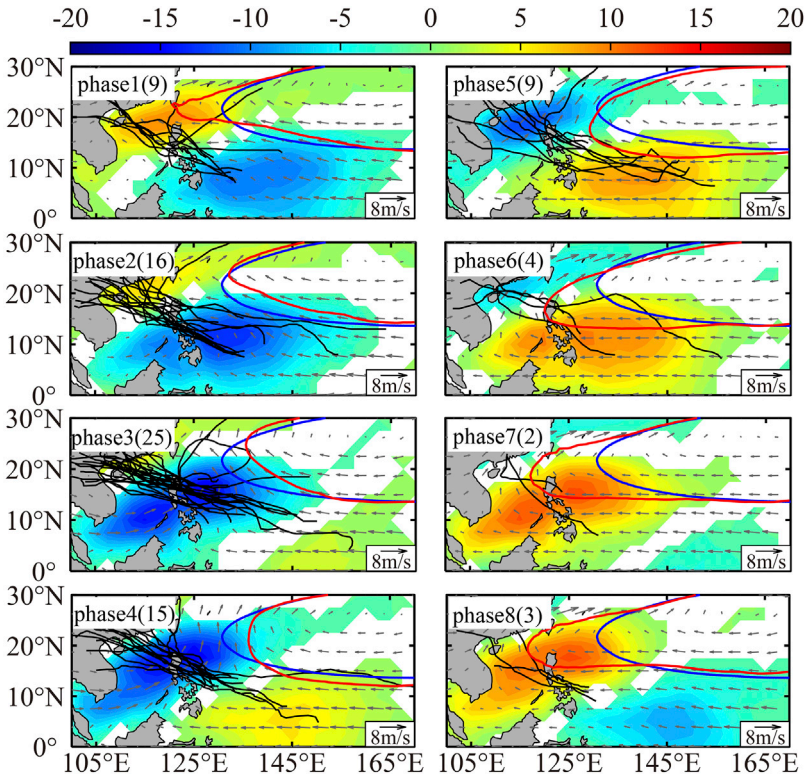

FIGURE 2
The same as Figure 1, but for the QBWO.

analysis of the impact of the MJO and the QBWO on the characteristics of landfalling TCs in the Philippines is conducted.

2 Data and methodology

2.1 Data

The best track data of TCs was obtained from the Japan Meteorological Agency. This data records at 6-h intervals the track of tropical cyclones with maximum intensity levels reaching tropical storm and above. It includes location, minimum central pressure, maximum sustained wind speed and other meteorological variables.

The atmospheric datasets were obtained from the European Centre for Medium Range Weather Forecasts (ECMWF). The dataset version used in the present study is the fifth generation ECMWF analysis data (ERA5, Hersbach et al., 2023). The variables used in the present study are divergence at 200 hPa, geopotential height at 500 hPa, relative humidity from 500 to 700 hPa, winds from 200 to 850 hPa. The temporal and spatial resolutions of the ERA5 dataset are 6h and 0.25° × 0.25°, respectively.

Daily outgoing longwave radiation (OLR) is obtained from U.S. National Oceanic and Atmospheric Administration (NOAA)

TABLE 2 The number, genesis location of TCs and ratio between the landfalling TCs and total number of NWP TCs during each phase of the MJO and the QBWO in the NWP. The phase that the TC belongs to is determined by the TC genesis day. Entries followed by one and two asterisks are statistically significant at the 90% and 95% confidence level, respectively.

Phase		1	2	3	4	5	6	7	8	All
MJO	Number	95	62	68	49	49	65	113	109	610
	(deviation)	(+18.7)	(−14.3)	(−8.3)	(−27.3)	(−27.3)	(−11.3)	(+36.7)	(+32.7)	
	Ratio	7.4%	8.1%	7.4%	10.2%	28.6%	30.8%	13.3%	11%	13.6%
	Lon.	143.7	146.1	147.5*	147.7*	143.5	143.4	142.2	139.5**	143.6
	Lat.	17.1**	16.1	16.1	17.8**	16.2	12.8**	13.6**	15.2	15.4
QBWO	Number	85	98	101	71	58	59	54	54	610
	(deviation)	(+8.7)	(+21.7)	(+24.7)	(−5.3)	(−18.3)	(−17.3)	(−22.3)	(−22.3)	
	Ratio	15.3%	17.3%	15.8%	7%	10.3%	11.9%	5.6%	29.6%	13.6%
	Lon.	143.4	138.9**	140.4**	143.5	147.1*	142.8	151.9**	146*	143.6
	Lat.	13.4**	14.7*	16.5**	17.2**	17.8**	17.8**	15.8	12.1**	15.4

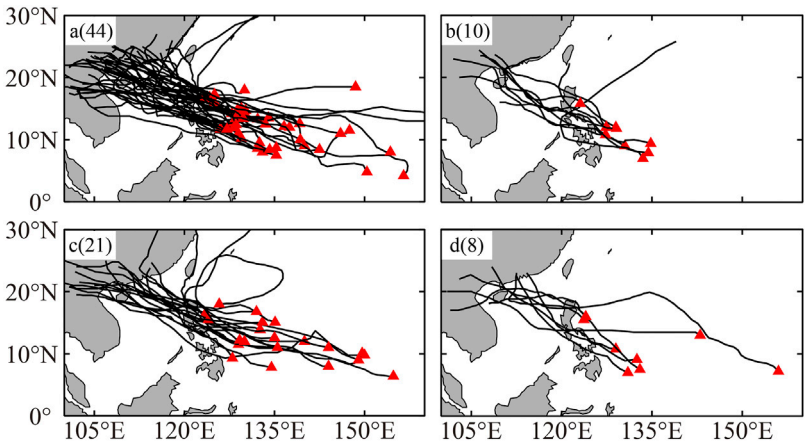

FIGURE 3
Tracks (black lines) and number (numbers in brackets) of Philippines landfalling TCs as a function of the phases of the MJO and the QBWO. Red triangles represent the location of tropical cyclogenesis. **(A)** Convective phases of both the MJO and the QBWO; **(B)** convective phases of the MJO and non-convective phases of the QBWO; **(C)** convective phases of the QBWO and non-convective phases of the MJO; **(D)** non-convective phases of both the MJO and the QBWO. The phase that the TC belongs to is determined by the landfalling day.

(Liebmann and Smith, 1996), with a spatial resolution is 2.5° × 2.5°. All the above datasets cover the time period May to September of each year from 1979 to 2019.

2.2 Determination of phase of the MJO and QBWO

To get the phase of MJO and QBWO, we firstly used a Gaussian filter to get the 10–20 days and 30–60 days filtered OLR. Then an empirical orthogonal function (EOF) analysis is applied to the 10–20 days and 30–60 days filtered OLR to get the dominant modes of the MJO and the QBWO, as done in previous studies (Kim et al., 2008; Huang et al., 2011; Li and Zhou, 2013a). Using the first two principal components, the MJO and QBWO modes are divided into 8 phases, as was done by Jia and Yang (2013). In order to emphasize the propagation characteristics of MJO and QBWO around the Philippines, a region of 0°–30°N, 100°–170°E is chosen in the present study for performing the EOF analysis, instead of adopting a meridional range of 15°S–15°N as in Wheeler and Hendon (2004).

3 Results

As shown in Figure 1, convective signals (i.e., negative OLR anomalies) of the MJO appear to the south of the Philippines in phase 5 and then propagate northeastward during phases 6, 7, 8 and 1, which affects most regions of South China Sea and the

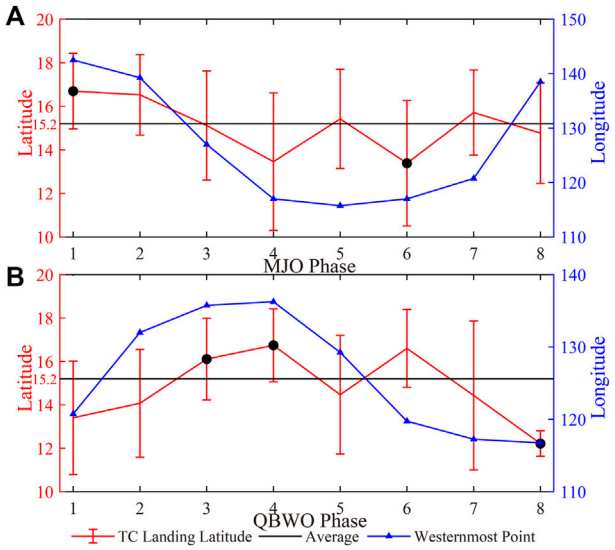

FIGURE 4
The mean latitude and its standard deviation (red lines) of landfalling TCs in each phase of the MJO **(A)** and the QBWO **(B)**. The blue line indicates the westward extension of the pole of the WPSH. The black dots indicate results that are statistically significant at the 95% level. The phase that the TC belongs to is determined by the landfalling day.

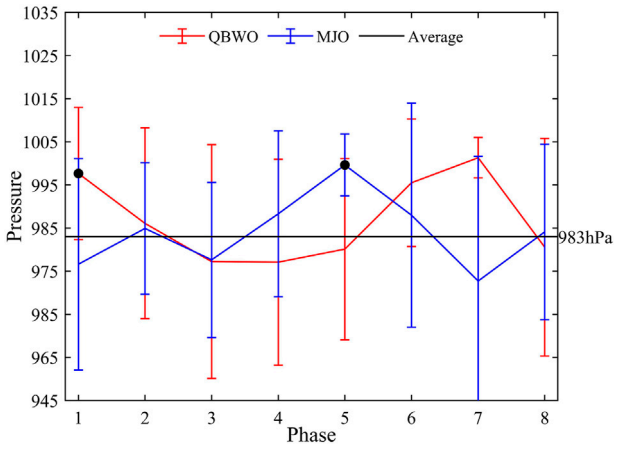

FIGURE 5
The mean minimum central pressure and its standard deviation of the Philippine landfalling TCs during different phases of the MJO (blue line) and the QBWO (red line). The black dots indicate pressures that exceed the 95% confidence level based on a Student's t-test. The phase that the TC belongs to is determined by the landfalling day.

Philippines. In phase 2, convective and non-convective signals (i.e., positive OLR anomalies) dominate the northern and southern Philippines, respectively. In phases 3-5, non-convective signals of the MJO cover most of Philippines. With respect to the QBWO, the convective signals appear to the southeast of the Philippines during phase 1 and then propagate northwestward. These convective signals affect most of the Philippines and the South China Sea during phases 2–4, and then affect the northern Philippines and the southern coast of China during phase 5. The non-convective signals of the QBWO appear over the southeastern Philippines in phase 5, dominate the Philippines during phases 6–8, affect the northern Philippines during phase 1 and no longer affect the Philippines during phase 2. Based on the above characteristics of the MJO and QBWO, the phases of the MJO and QBWO are divided to two groups: convective and non-convective. Convective phases include phases 1, 6–8 of the MJO and phases 2–5 of the QBWO when convective signals are close to the Philippines, while non-convective phases include the phases 2–5 of the MJO and phases 1, 6–8 of the QBWO when non-convective signals are close to the Philippines.

Knowledge of the frequency, landfall intensity, location and translation speed of the TCs are important for the disaster prevention. The impact of the MJO and the QBWO on these factors and the mechanisms behind the behavior are systematically discussed below.

3.1 Frequency

Among the 610 TCs that formed in the NWP (excluding the TCs that formed in the South China Sea), 83 made landfall in the Philippines (excluding Batanus Island and other small islands to the north of Luzon Island) during summer (May-September) between 1979–2019. As shown in Table 1, the number of Philippines landfalling TCs shows significant variation in the different phases of the MJO and the QBWO. With respect to the MJO, up to 20 TCs made landfall in the Philippines during phase 7, while only 5 TCs made landfall in the Philippines during phase 4. More (less) TCs made landfall in Philippines during the convective (non-convective) phase of the MJO. There were 54 TCs that made landfall in the Philippines during the convective phases (phases 1, 6–8), while only 29 TCs made landfall in the Philippines during the MJO's non-convective phases (phases 2–5). With respect to the QBWO, the number of TCs that made landfall in the Philippines reaches its maximum during phases 3 (25 TCs) and its minimum during phase 7 (2 TCs). There were 65 TCs that made landfall in the Philippines during the QBWO's convective phases (phases 2–5), while only 18 TCs made landfall in the Philippines in its non-convective phases (phases 1, 6–8). The ratio between the number of landfalling TCs during the QBWO's convective phases and its non-convective phases (about 3.61) is nearly twice of that of the MJO (about 1.86), indicating that the modulation of the number of TCs that made landfall in the Philippines is much stronger in the QBWO. As shown in Table 1, the number of days in each phase of the MJO and the QBWO are different. To better evaluate the impact of the MJO and the QBWO on the frequency of the Philippines landfalling TCs, the daily landfall rate (DLR, the number of landfalling TCs divided by the duration of each phase) is used hereafter in this study. In generally, the variation of the DLR is similar to the number of landfalling TCs, which is larger (smaller) during convective (non-convective) phases of the MJO and the QBWO. The DLR shows that the landfall activity is significantly enhanced (suppressed) in phase 7 (4) of the MJO and phases 2–3 (7–8) of the QBWO.

Previous studies have shown that the Western Pacific Subtropical High (WPSH) has a great influence on the motion

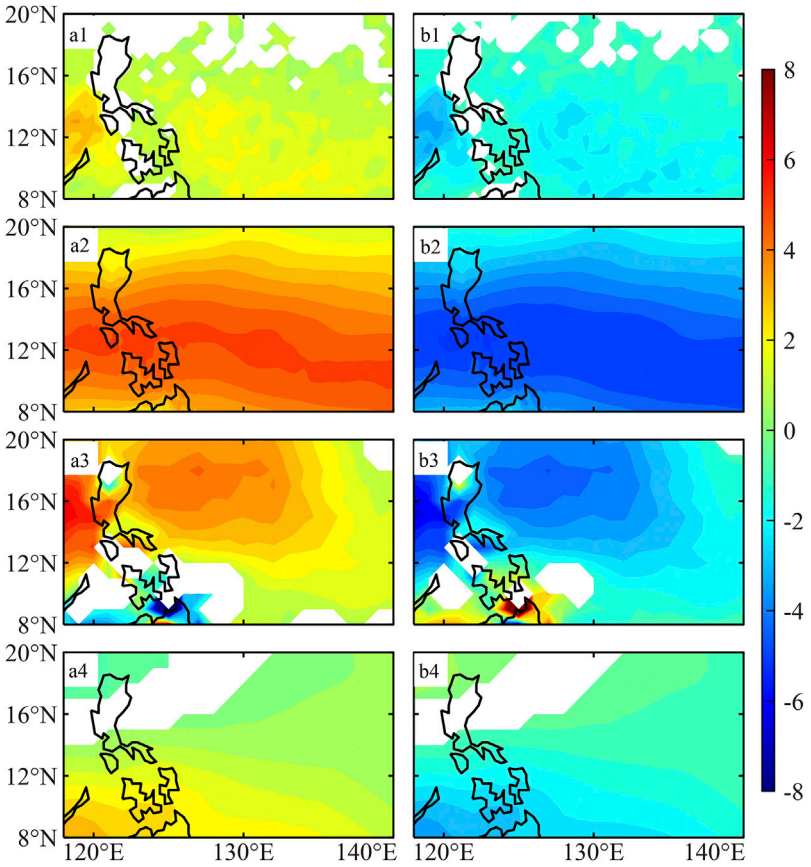

FIGURE 6
Composite anomalies of the **(A1,B1)** divergence at 200 hPa ($10^{-6}s^{-1}$), **(A2,B2)** relative humidity at 500–700 hPa (%), **(A3,B3)** relative vorticity at 850 hPa ($10^{-6}s^{-1}$), **(A4,B4)** vertical wind shear at 200-850 hPa (m s^{-1}) during **(A)** convective and **(B)** non-convective phases of the MJO. Only values exceeding 95% confidence level are plotted.

of TCs that form in the NWP(Chen, 2009; Li and Zhou, 2013b; Wang and Wang, 2013; Choi et al., 2015; Ling et al., 2015). When the WPSH shifts westward (eastward), the steering flow favors the westward propagation (recurving northward) of NWP TCs. As shown in Figures 1, 2, with the northward propagation of convective (non-convective) signals of the MJO and the QBWO, the WPSH shifts eastward (westward). Although the WPSH shifts more eastward during MJO phases 1,2,8 and QBWO phases 2, 3, 4, more TCs make landfall in the Philippines (Table 1) during these phases. This is because more NWP TCs formed during these or previous phases when the convective signals of the MJO and the QBWO were located over the NWP (Table 2). As shown in Table 2, a total of 266 TCs formed during phases1, 2, 8 of the MJO, and 270 TCs formed during phases 2, 3, 4 of the QBWO. The ratio between the number of Philippine landfalling TCs and the total number of NWP TCs in each phase shows that a lower (higher) proportion of NWP TCs made landfall in the Philippines when the position of the WPSH was more eastward (westward), except during phases 2 and 3 of the QBWO. The reason for this was that the genesis locations of NWP TCs were closer to the Philippines during these phases. As shown in Table 2, the mean longitude of the western Pacific tropical cyclones was 138.9°E and 140.4°E during phases 2 and 3 of the QBWO, respectively, which were significantly westward of the mean genesis longitude of the NWP TCs at 143.6°E.

Figure 3 shows the combined effects of the MJO and the QBWO on the number of TCs that made landfall in the Philippines. Among the 83 landfalling TCs, 44 TCs made landfall in the Philippines during the active phases of both the MJO and the QBWO (Figure 3A), while only 8 TCs made landfall in the Philippines during the inactive phases of both the MJO and the QBWO (Figure 3D). As shown in Figures 3B, C, the number of Philippine landfalling TCs was 21 (10) during the convective (non-convective) phases of the QBWO and the convective (non-convective) phases of the MJO. These results reveal that both the MJO and the QBWO have great impact on the frequency of TCs making landfall in the Philippines. The number of TCs during the convective MJO and non-convective QBWO phases is nearly equal to the number of TCs during both non-convective phases of the MJO and QBWO, which indicates that the frequency of Philippine landfalling TCs is significantly suppressed during the inactive phases of the QBWO. This confirms that the modulation of the frequency of Philippine landfalling TCs by the QBWO is stronger than that by the MJO.

10.3389/feart.2023.1106291

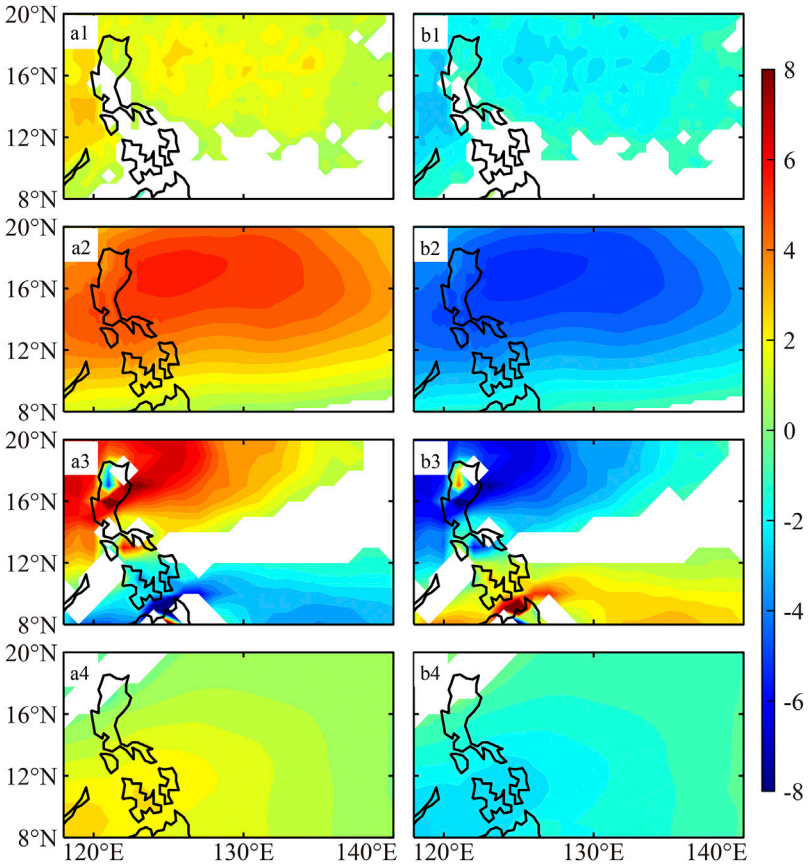

FIGURE 7
Composite anomalies of the **(A1,B1)** divergence at 200 hPa (10−6s−1), **(A2,B2)** relative humidity at 500–700 hPa (%), **(A3,B3)** relative vorticity at 850 hPa (10−6s-1), **(A4,B4)** vertical wind shear at 200-850hPa (m s−1) during **(A)** convective and **(B)** non-convective phases of the QBWO. Only values exceeding 95% confidence level are plotted.

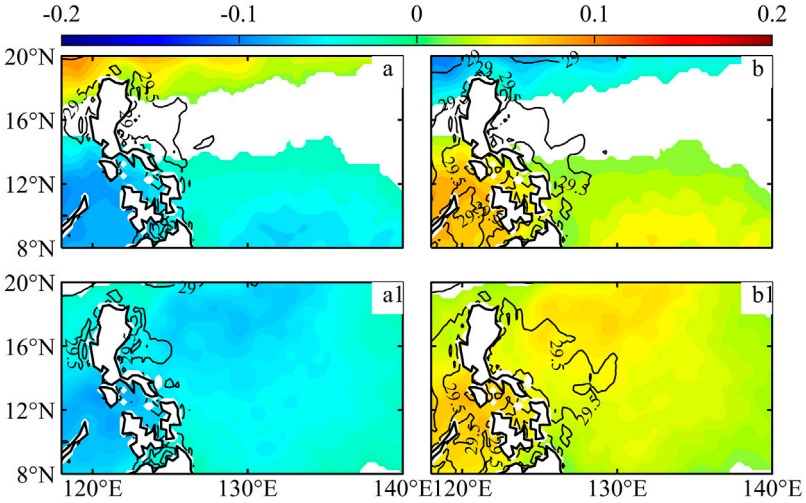

FIGURE 8
Composite anomalies of the SST (color, °C) and SST (black lines, °C) during **(A,A1)** convective and **(B,B1)** non-convective phases of the MJO (first line) and QBWO(second line). Only values exceeding 95% confidence level are plotted.

TABLE 3 The time between the genesis and landfall of TCs in each phase of the MJO and the QBWO. Entries followed by one or two asterisks are statistically significant at the 90% and 95% confidence, respectively.

	Phase	1	2	3	4	5	6	7	8	Mean
MJO	Days	3.5	4.1*	3.8	2.2	1.6**	1.7**	3.6	1.6**	2.7
QBWO	Days	1.3**	2.3	2.9	3.2	4.3*	3.3	1**	1.3*	2.7

3.2 Landfall location

Considering the geography of the Philippines, the latitude of TC landfall is used to represent the landfall location of a TC. As shown in Figure 4, the range of average landfall latitude was 13.4°N-17.0°N during different MJO phases and 12.2°N-16.7°N during different QBWO phases. For the MJO, the landfall latitude gradually moves southward during phases 1–4 and then shifts northward during MJO phases 1, 6, 7, 8. For the QBWO, the landfall latitude shifts northward during phases 1–4 and southward during phases 6–8. The variation in landfall latitude is consistent with the movement of the WPSH. Figure 4 shows the longitude of the westward extending pole of the WPSH. It is obvious that when the WPSH shifts westward (eastward), the landfall latitude shifts southward (northward). With the northward propagation of convective signals during phases 1–4 of the QBWO and phases 1, 6–8 of the MJO (Figures 1, 2), the WPSH gradually shifts eastward, leading to a northward shift of the landfall latitude. In phases 2–5 of the MJO and phases 5–8 of the QBWO, the WPSH extends westward when the non-convective signals dominate the region around the Philippines (Figures 1, 2), resulting in a southward shift of the landfall latitude. In addition, the north-south shift of the landfall location may also be affected by the location of cyclogenesis. As shown in Table 1, the latitude of TC genesis gradually shifts northward following the northward propagation of the convective signals of the MJO and the QBWO, which can also lead to a northward shift of the landfall location.

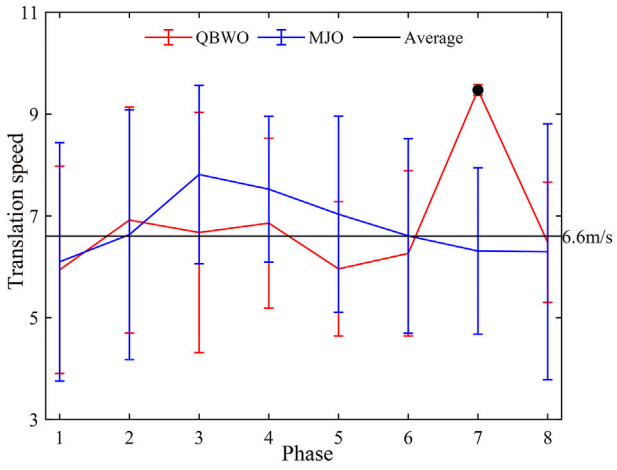

FIGURE 9
The mean translation speed (ms^{-1}) and its standard deviation of the TCs that made landfall in the Philippines during each phase of the MJO (blue line) and the QBWO (red line). The black dot indicates results that are statistically significant at the 95% confidence level. The phase that the TC belongs to is determined by the landfalling day.

3.3 Landfall intensity

The TC dataset from the Japanese Meteorological Agency only provides the maximum wind speeds exceeding 35 knots, therefore the minimum central pressure was chosen to represent TC intensity. As shown in Figure 5, the landfall intensity is stronger (weaker) in phases 1, 3, 7 (2, 4, 5, 6, 8) of the MJO and phases 3, 4, 5, 8 (1, 2, 6, 7) of the QBWO. Generally, the landfall intensity was stronger (weaker) during the convective (nonconvective) phases, which is clearly seen during the different QBWO phases. The development of a TC is affected by several factors, and the anomalies of these factors during the convective and non-convective phases are examined in Figures 6, 7. During the convective (non-convective) phases of the MJO and the QBWO, the anomalous relative vorticity at 850 hPa, divergence at 200 hPa and relative humidity at 500 hpa were positive (negative), which is favorable (unfavorable) for the development of TCs. The vertical wind shear between 200 and 850 hPa was positive (negative), which is unfavorable (favorable) for the development of TCs. However, the magnitude of the anomalous vertical wind shear is small (less than 1 m/s) in most of the region east of Philippines.

Besides the atmospheric conditions, the ocean thermal condition is also crucial to TC development. Figure 8 shows the SST anomaly (SSTa) in the convective and non-convective phases of MJO and QBWO. As shown in Figures 8A, B, the SSTa is negative (positive) in the southern (southern) region of the NWP in the convective (non-convective) phases of MJO. The magnitude of SSTa in the region east of Philippines are the smallest. To QBWO, the SSTa is negative (positive) in the convective (non-convective) phases (Figures 8A1, B1), which is unfavorable (favorable) for the development of the TCs. However, the magnitude of the SSTa in the convective and non-convective phases of MJO and QBWO is small (less than 0.2°C) in most regions. And the SST is above 29°C, which is favorable for TC development. Though the anomalies of the vertical wind shear and SSTa are unfavorable (favorable) for TC development, the magnitude of the anomalies is small. Consequently, the landfall intensity is stronger (weaker) during convective (non-convective) phases as a result of the combined effects of the above atmospheric and oceanic factors.

As mentioned above, the landfall intensity is not as clearly stronger (weaker) during the convective (non-convective) phases of the MJO as they are for the QBWO. There are two possible reasons for this difference. One is the propagation direction of the intraseasonal signals. The propagation direction of the QBWO signals is consistent with the motions of TCs, while that of the MJO is contrary to the motions of the TCs. This would significantly affect the interaction time between the TCs and the favorable conditions introduced by the intraseasonal signals. Another reason is the duration of storm

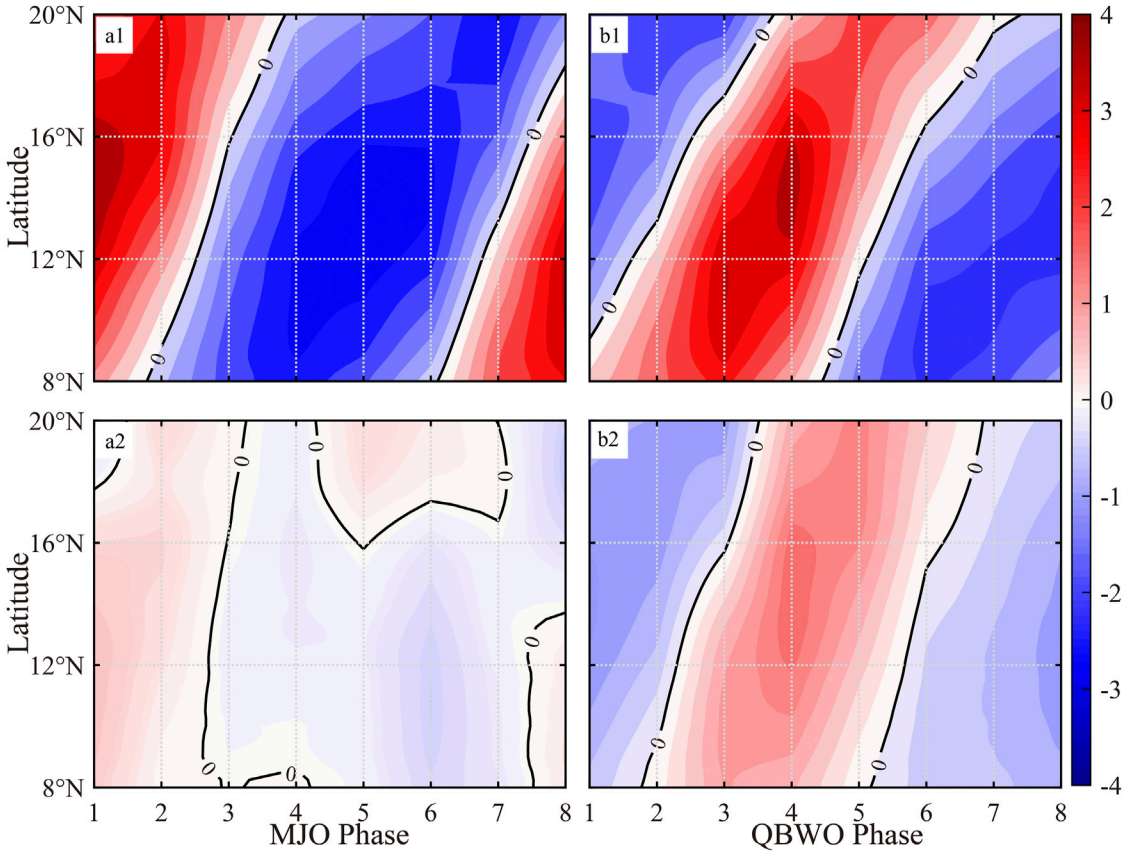

FIGURE 10
Composite anomalies of **(A1,B1)** zonal and **(A2,B2)** meridional winds (ms^{-1}) during different phases of the MJO (left column) and the QBWO (right column) in the region to the east of the Philippines (8°N-20°N, 122°E-125°E).

development (time between genesis and landfall). As shown in Table 3, the time between genesis and landfall of TCs landing in the Philippines during MJO phases 2, 3 are 4.1 days and 3.8 days, respectively, while those during phases 6 and 8 are only 1.6 and 1.7 days. Shorter time between the genesis and the landfall means that the TCs have a very short time to develop, resulting in relatively weak landfall intensities during phases 6, 8 of the MJO. This also provides an explanation for why the landfall intensity during some less favorable non-convective phases is slightly stronger than that during more favorable convective phases. For the QBWO, the time between the genesis and landfall are longer (shorter) during convective (non-convective) phases, so the fact that landfall intensity is stronger (weaker) in convective (non-convective) phases is more readily apparent.

3.4 Translation speed at time of landfall

Translation speed at the landfall time can significantly affect the impact duration and the integrated precipitation over the Philippines. As shown in Figure 9, the mean translation speed for TCs making landfall in the Philippines is about 6.6 m/s. The translation speed during the different MJO phases shows a regular variation, with increases during phases 1, 2, 3 of the MJO, and a gradual decrease from phase 3 to phase 8. For the QBWO, the translation speed is faster (slower) than the mean value during phases 2, 3, 4, 7 (1, 5, 6, 8). While the translation speed reaches a large maximum (9.5 m/s) during phase 7 of QBWO, it should be noted that there were only two TCs that made landfall in the Philippines during this phase (Table 1). During the convective phases of both the MJO and the QBWO (phases 2–5 of the QBWO and phases 6, 7, 8, 1 of the MJO), the translation speed tends to be slower.

Translation speed is significantly affected by the steering flow. Figure 10 shows the anomalous steering flow at different latitudes in the region to the east of the Philippines (122°E–125°E) during different phases of the MJO and the QBWO. The steering flow is defined as the mass-weighted mean flow between 300 and 850 hPa (Holland, 1983). For the MJO, anomalous westerlies (easterlies) dominate the region to the east of the Philippines during convective (non-convective) phases. Anomalous southerlies (northerlies) appear during phases 1 and 2 (phases 3-8) of the MJO, but their amplitude is much weaker than the zonal winds. For the QBWO, anomalous westerlies and southerlies (easterlies and northerlies) dominate the region to the east of Philippines during the convective (non-convective) phases, with the meridional winds lagging the zonal winds by one phase. Since TCs landfalling in the Philippines take westward or northwestward trajectories, anomalous easterlies and southerlies (westerlies and northerlies) favors the acceleration (deceleration) of these TCs. With the northward propagation of the convective signals of the MJO and the QBWO, anomalous westerlies

TABLE 4 The total number of SCS TCs and the number that made landfall in the Philippines during each phase of the MJO and the QBWO. The phase that the TC belongs to is determined by the landfalling day.

Phase		1	2	3	4	5	6	7	8	Total
MJO	Landfall genesis	2	0	0	0	0	0	1	4	7
		19	11	2	1	2	11	19	17	82
QBWO	Landfall genesis	0	0	4	2	1	0	0	0	7
		8	11	19	25	7	4	1	8	82

spread from the south to the north, leading to a deceleration of the translation speed (Figure 8), although anomalous southerlies favor the acceleration of TCs. During non-convective phases, anomalous easterlies also spread from the south to the north, but the translation speed does not show a clear acceleration tendency. This may be the result of the fewer number of TCs that made landfall in the Philippines during these phases.

4 Conclusion and discussion

In the present study, the effects of the MJO and the QBWO on TCs that made landfall in the Philippines were investigated. The results show that more (less) TCs landfall in the Philippines during the convective (non-convective) phases of the MJO and the QBWO. This resulted from the fact that more (less) TCs were generated, and the locations of tropical cyclogenesis were closer to (farther away from) the Philippines, although the WPSH shifted eastward (westward). Compared to the MJO, the effect of the QBWO on the number of TCs that made landfall in Philippine is more significant. The ratio of the number of Philippine landfalling TCs between the convective and non-convective phases of the QBWO is about twice of that of the MJO. During the convective (non-convective) phases of the MJO and the QBWO, the WPSH moves eastward (westward), resulting in a northward (southward) shift in landfall locations in the Philippines. Generally, the landfall intensity is stronger (weaker) during the convective phase (non-convective phase), resulting from an environment that is favorable (unfavorable) for the development of TCs. This behavior is more pronounced during the different phases of the QBWO. There are two reasons for this: one is that the propagation direction of the QBWO is consistent with that of the TCs, while the propagation direction of the MJO is counter to that of the TCs. Another reason is the time between the genesis and landfall of TCs is longer (shorter) during the convective (non-convective phases) of QBWO giving the TCs more (less) time to intensify, while the time between the genesis and landfall during some convective phases of the MJO is much shorter than that in some non-convective phases of the MJO. The translation speed of the landfalling TCs in the Philippines is also modulated by the MJO and the QBWO. During the convective phases, abnormal westerlies dominate the region to the east of Philippines and spread from the south to the north, which is conducive to the deceleration (acceleration) of the landfalling TCs. While there is not a clear acceleration tendency during non-convective phases, even though abnormal easterlies prevail in the region to the east of Philippines, this may be an artifact from the scarcity of TCs make landfall in the Philippines during these phases.

In addition to the TCs from the NWP, some TCs that formed in the South China Sea (SCS) also made landfall in the Philippines. As shown in Table 4, there were only 7 SCS TCs that made landfall in the Philippines in boreal summer between 1979 and 2019. All 7 landfall events occurred during phases 1, 7, 8 of the MJO and phases 3, 4, 5 of the QBWO. This is because the eastward motion of TCs originating in the SCS is controlled by intraseasonal oscillations (Yang et al., 2015; Ling et al., 2016; Ling et al., 2020). In the convective phases, the WPSH shifts eastward, and the steering flow is favorable for the eastward movement of the SCS TCs. Although the number of TCs from the SCS that made landfall in the Philippines is much less than those from the NWP, the genesis location of the SCS TCs is closer to the Philippines, which leads to a rapid landfall after tropical cyclogenesis.

Data availability statement

Publicly available datasets were analyzed in this study. This data can be found here: http://www.jma.go.jp/jma/jma-eng/jma-center/rsmc-hp-pub-eg/besttrack.html. https://cds.climate.copernicus.eu/cdsapp#!/dataset/. http://www.esrl.noaa.gov/psd/.

Author contributions

Conceptualization: ZL, HH and PW. Methodology: ZL, HH and PW. Software: PW and ZL. Formal analysis: PW. Writing- Original draft: PW and ZL. Writing- Reviewing and Editing: ZL and PW. Visualization: PW and ZL. All authors listed have made a substantial, direct, and intellectual contribution to the work and approved it for publication.

Funding

This study was supported by Guangdong Provincial College Innovation Team Project (2019KCXTF021), First-class Discipline Plan of Guangdong Province (080503032101, 231420003) and Oceanic Interdisciplinary Program of Shanghai Jiao Tong University (SL2020MS030).

Acknowledgments

The Japan Meteorological Agency best track TC dataset was downloaded from http://www.jma.go.jp/jma/jma-eng/jma-center/rsmc-hp-pub-eg/besttrack.html. The ERA-5 data were downloaded from https://cds.climate.copernicus.eu/cdsapp#!/dataset/. The OLR data were downloaded from http://www.esrl.noaa.gov/psd/.

Conflict of interest

The authors declare that the research was conducted in the absence of any commercial or financial relationships that could be construed as a potential conflict of interest.

Publisher's note

References

Chen, G. (2009). Interdecadal variation of tropical cyclone activity in association with summer monsoon, sea surface temperature over the Western North Pacific. *Chin. Sci. Bull.* 54 (8), 1417–1421. doi:10.1007/s11434-008-0564-2

Choi, K.-S., Kim, B.-J., Kang, S.-D., and Kim, H.-D. (2015). Interannual variation of the Philippines affecting tropical cyclone intensity and its possible causes. *Theor. Appl. Climatol.* 122 (1-2), 295–301. doi:10.1007/s00704-014-1281-1

Cinco, T. A. d. G., Ortiz, R. G., Delfino, A. M. D., Lasco, R. J. P., Hilario, R. D., Juanillo, F. D., et al. (2016). Observed trends and impacts of tropical cyclones in the Philippines. *J Int. J. Climatol. A J. R. Meteorological Soc.* 36, 4638–4650. doi:10.1002/joc.4659

Corporal-Lodangco, I., and Leslie, L. (2016). Cluster analysis of philippine tropical cyclone climatology: Applications to forecasting. *J. Climatol. Weather Forecast.* 4. doi:10.4172/2332-2594.1000152

Corporal-Lodangco, I. L., and Leslie, L. M. (2017). Climatology of philippine tropical cyclone activity: 1945-2011. *Int. J. Climatol.* 37 (9), 3525–3539. doi:10.1002/joc.4931

Corporal-Lodangco, I. L., Leslie, L. M., and Lamb, P. J. (2016). Impacts of ENSO on philippine tropical cyclone activity. *J. Clim.* 29 (5), 1877–1897. doi:10.1175/jcli-d-14-00723.1

Hersbach, H., Bell, B., and Berrisford, P. (2023). ERA5 hourly data on pressure levels from 1940 to present. *Copernicus Climate Change Service (C3S) Climate Data Store (CDS).* doi:10.24381/cds.bd0915c6

Holland, G. J. (1983). Tropical cyclone motion: Environmental interaction plus a beta effect. *J. Appl. Meteorol* 15, 1252–1264. doi:10.1175/1520-0469(1983)040<0328:TCMEIP>2.0.CO;2

Huang, P., Chou, C., and Huang, R. (2011). Seasonal modulation of tropical intraseasonal oscillations on tropical cyclone geneses in the western north pacific. *J. Clim.* 24 (24), 6339–6352. doi:10.1175/2011jcli4200.1

Jia, X., and Yang, S. (2013). Impact of the quasi-biweekly oscillation over the Western North Pacific on East Asian subtropical monsoon during early summer. *J. Geophys. Research-Atmospheres* 118 (10), 4421–4434. doi:10.1002/jgrd.50422

Kikuchi, K. (2021). The boreal summer intraseasonal oscillation (BSISO): A review. *J. Meteorological Soc. Jpn.* 99 (4), 933–972. doi:10.2151/jmsj.2021-045

Kim, J.-H., Ho, C.-H., Kim, H.-S., Sui, C.-H., and Park, S. K. (2008). Systematic variation of summertime tropical cyclone activity in the Western north Pacific in relation to the madden-julian oscillation. *J. Clim.* 21 (6), 1171–1191. doi:10.1175/2007jcli1493.1

Krishnamurti, T. N., and Bhalme, H. N. J. J. o. t. A. S. (1976). Oscillations of a monsoon system. Part I. Observational aspects. *Obs. Asp.* 33 (10), 1937–1954. doi:10.1175/1520-0469(1976)033<1937:ooamsp>2.0.co;2

Kubota, H., and Chan, J. C. L. (2009). Interdecadal variability of tropical cyclone landfall in the Philippines from 1902 to 2005. *Geophysical Research Letters.* 36. doi:10.1029/2009gl038108

Li, R. C. Y., and Zhou, W. (2013a). Modulation of western north pacific tropical cyclone activity by the ISO. Part I: Genesis and intensity. *J. Clim.* 26 (9), 2904–2918. doi:10.1175/jcli-d-12-00210.1

Li, R. C. Y., and Zhou, W. (2013b). Modulation of western north pacific tropical cyclone activity by the ISO. Part II: Tracks and landfalls. *J. Clim.* 26 (9), 2919–2930. doi:10.1175/jcli-d-12-00211.1

Liebmann, B., and Smith, C. A. J. B. A. M. S. (1996). Description of a complete (interpolated). *Outgoing Longwave Radiat. Dataset* 77, 1275–1277.

Ling, Z., Wang, G., and Wang, C. (2015). Out-of-phase relationship between tropical cyclones generated locally in the South China Sea and non-locally from the Northwest Pacific Ocean. *Clim. Dyn.* 45 (3-4), 1129–1136. doi:10.1007/s00382-014-2362-7

Ling, Z., Wang, Y., Wang, G., and He, H. (2020). Impact of intraseasonal oscillations on the activity of tropical cyclones in summer over the South China sea: Nonlocal tropical cyclones. *Front. Earth Sci.* 8. doi:10.3389/feart.2020.609776

Ling, Z., Wang, Y., and Wang, G. (2016). Impact of intraseasonal oscillations on the activity of tropical cyclones in summer over the South China sea. Part I: Local tropical cyclones. *J. Clim.* 29 (2), 855–868. doi:10.1175/jcli-d-15-0617.1

Lyon, B., and Camargo, S. J. (2009). The seasonally-varying influence of ENSO on rainfall and tropical cyclone activity in the Philippines. *Clim. Dyn.* 32 (1), 125–141. doi:10.1007/s00382-008-0380-z

Madden, R. A., and Julian, P. R. J. J. o. A. S. (1971). Detection of a 40-50 Day oscillation in the zonal wind in the tropical pacific. *J. Atmos. Sci.* 28, 702–708. doi:10.1175/1520-0469(1971)028<0702:doadoi>2.0.co;2

Mao, J., and Wu, G. (2010). Intraseasonal modulation of tropical cyclogenesis in the Western north pacific: A case study. *Theor. Appl. Climatol.* 100 (3-4), 397–411. doi:10.1007/s00704-009-0195-9

Nakano, M., Vitart, F., and Kikuchi, K. (2021). Impact of the boreal summer intraseasonal oscillation on typhoon tracks in the Western North Pacific and the prediction skill of the ECMWF model. *Geophys. Res. Lett.* 48 (9), e2020GL091505. doi:10.1029/2020GL091505

Takagi, H., and Esteban, M. (2016). Statistics of tropical cyclone landfalls in the Philippines: Unusual characteristics of 2013 typhoon haiyan. *Nat. Hazards* 80 (1), 211–222. doi:10.1007/s11069-015-1965-6

Wang, C., and Wang, X. (2013). Classifying El Nino modoki I and II by different impacts on rainfall in southern China and typhoon tracks. *J. Clim.* 26 (4), 1322–1338. doi:10.1175/jcli-d-12-00107.1

Warren, J. F. (2016). "Philippine Typhoons since the seventeenth century," in *Natural hazards and peoples in the Indian ocean world: Bordering on danger*. Editors G. Bankoff and J. Christensen (New York: Palgrave Macmillan US), 105–141.

Wheeler, M. C., and Hendon, H. H. J. M. W. R. (2004). An all-season real-time multivariate MJO index: Development of an index for monitoring and prediction. *Mon. Weather Rev.* 132 (8), 1917–1932. doi:10.1175/1520-0493(2004)132<1917:aarmmi>2.0.co;2

Yang, L., Du, Y., Wang, D., Wang, C., and Wang, X. (2015). Impact of intraseasonal oscillation on the tropical cyclone track in the South China Sea. *Clim. Dyn.* 44 (5-6), 1505–1519. doi:10.1007/s00382-014-2180-y

Yoshida, R., Kajikawa, Y., and Ishikawa, H. (2014). Impact of boreal summer intraseasonal oscillation on environment of tropical cyclone genesis over the western north pacific. *Sola* 10, 15–18. doi:10.2151/sola.2014-004

Zhao, H., Jiang, X., and Wu, L. (2015a). Modulation of northwest pacific tropical cyclone genesis by the intraseasonal variability. *J. Meteorological Soc. Jpn.* 93 (1), 81–97. doi:10.2151/jmsj.2015-006

Zhao, H., Yoshida, R., and Raga, G. B. (2015b). Impact of the madden-julian oscillation on western north pacific tropical cyclogenesis associated with large-scale patterns. *J. Appl. Meteorology Climatol.* 54 (7), 1413–1429. doi:10.1175/jamc-d-14-0254.1

frontiers | Frontiers in Earth Science

TYPE Original Research
PUBLISHED 19 June 2023
DOI 10.3389/feart.2023.1102957

OPEN ACCESS

EDITED BY
Lynn Donelson Wright,
William & Mary's Virginia Institute of Marine Science, United States

REVIEWED BY
Nobuhito Mori,
Kyoto University, Japan
Shaoqing Zhang,
Ocean University of China, China

*CORRESPONDENCE
Tao Xian,
xiant@sustech.edu.cn
Lian-Ping Wang,
wanglp@sustech.edu.cn

RECEIVED 19 November 2022
ACCEPTED 09 June 2023
PUBLISHED 19 June 2023

CITATION
Thankaswamy A, Xian T and Wang L-P (2023), Typhoons and their upper ocean response over South China Sea using COAWST model.
Front. Earth Sci. 11:1102957.
doi: 10.3389/feart.2023.1102957

Typhoons and their upper ocean response over South China Sea using COAWST model

Anandh Thankaswamy[1], Tao Xian[2]* and Lian-Ping Wang[1,2,3]*

[1]Southern Marine Science and Engineering Guangdong Laboratory, Guangzhou, China, [2]Guangdong Provincial Key Laboratory of Turbulence Research and Applications, Center for Complex Flows and Soft Matter Research and Department of Mechanics and Aerospace Engineering, Southern University of Science and Technology, Shenzhen, Guangdong, China, [3]Guangdong-Hong Kong-Macao Joint Laboratory for Data-Driven Fluid Mechanics and Engineering Applications, Southern University of Science and Technology, Shenzhen, China

The formation and intensification of typhoons is a complex process where energy and mass exchanges happen between the ocean and the atmosphere. In most typhoon numerical studies, a static ocean and a dynamic atmosphere are used to reduce the complexity of modeling. Using the COAWST model, we studied the air-sea interactions of Typhoon Mujigae in 2015, Typhoon Merbok in 2017, and Typhoon Hato in 2017 over the South China Sea. With different translation speeds, track shapes, and intensities between these cyclones, they act as an excellent case study to analyze the air-sea coupling in the models. The inclusion of coupling between the ocean and atmosphere is found to improve the typhoon track simulation significantly. The bias in the cyclone tracks is reduced by 10%–40% in the coupled model. The upper ocean response to the typhoon was also analyzed using the coupled model output. The coupled simulations show that the major energy extraction occurs to the right of the track, which is consistent with satellite observation and latent heat release analysis. The coupling process shows the air-sea interactions and exchanges in the upper ocean along with the energy released during the passage of typhoons. The heat budget analysis shows that the cooling of the upper ocean is mainly attributed to the advection associated with the typhoon forcing. This study shows that it is necessary to include ocean feedback while analyzing a typhoon, and the application of coupled models can improve our understanding as well as the forecasting capability of typhoons.

KEYWORDS

typhoons, coupled modelling, South China Sea, air-sea interactions, latent heat

1 Introduction

The South China Sea (SCS) is extremely vulnerable to tropical cyclones. Typhoons that pass over SCS have their origins in the northern tropical Pacific Ocean and SCS itself. In the past 70 years of records, typhoons have seen to form throughout the year over the SCS but high intense storms form in the late summer and fall seasons (Zhang et al., 2019; Le Mau et al., 2021). Due to global warming, typhoons over the SCS are expected to decrease in number but the frequency of strong typhoons is expected to increase (Emanuel, 2013; Tsuboki et al., 2015; Tsou et al., 2016; Yao et al., 2021). About 10 typhoons pass over the northwest Pacific making landfall over southern China, Vietnam, and the Philippines every year (Wang et al., 2007; Ma et al., 2021). Generally, tropical cyclones form near the lower latitudes, where the sea surface temperature (SST) is above 26°C (Fisher, 1958). As the waters of SCS remain more than this temperature throughout the year, the sea is always exposed to the formation of tropical cyclones (Herbeck

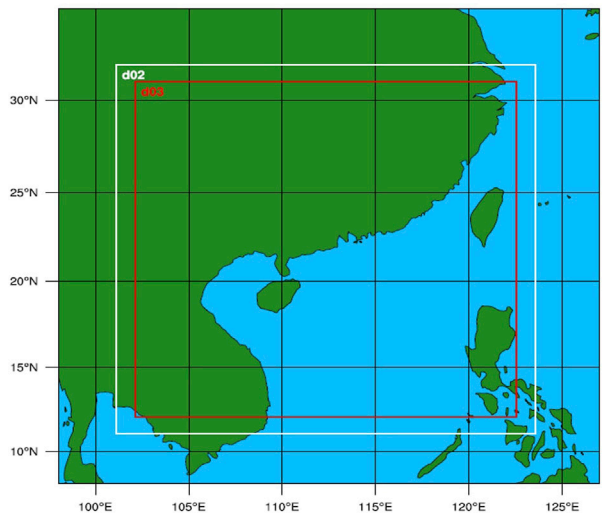

FIGURE 1
WRF domain configuration, showing the two-way nested and the inner most domains.

et al., 2011). The strong evaporation over this region results in the formation of stratification layers in the upper ocean (Price, 1981), which impact the energy exchanges and thereby the transfer of heat to the atmosphere (Brister and Emanual, 1998).

Typhoons are one of the most destructive events in nature, which may cause heavy loss of human lives and the economy through strong wind, torrential rain, and storm surges (Adriano et al., 2014; Gettelman et al., 2018). Because of the long coastline and dense population, China is one of the severely affected countries by typhoons (Xiao and Xiao, 2010; Meng et al., 2021; Wang et al., 2021). Analyzing and understanding the development and track of typhoons is a priority so that we can be vigilant when typhoons occur in the future. Improvement of typhoon track forecasting (with a precision of <100 km) has been achieved by increasing the grid resolution, assimilating high-quality observation datasets (Davis et al., 2008), and improving the initial conditions (Done et al., 2004; Wang and Wu, 2004; Gopalakrishnan et al., 2012). However, the development of typhoon intensity forecasting has been rather slow, which is partly attributed to the complex interactions between the upper ocean and atmosphere for typhoon intensification. The upper ocean supplies heat energy and moisture content to the typhoons for their intensification (Emanuel, 1999, 2003). Emanual. (1986) proposed the theory for typhoon intensity estimation based on the surface heat exchange. Modelling and observational studies have showed that the typhoon intensification is accompanied by increases in the sea-to-air latent heat flux (e.g., Bell et al., 2008; Lin et al., 2014; Jaimes et al., 2015; Gao et al., 2017). Numerical models employ various parameterizations to understand the physical processes involved in the sub-grid scale events (Kueh, 2012; Islam et al., 2015; Di et al., 2019; Shen et al., 2019). In most of the numerical analyses of typhoons, the bottom boundary condition (i.e., the status of the upper ocean) is kept static and disconnected from the numerical analysis in the models. This static ocean condition can result in misrepresenting the oceanic thermodynamical forcings acting on a typhoon. The above drawbacks can be overcome by coupling an atmosphere model with a dynamic ocean model.

Coupling atmosphere models with ocean models to improve the numerical simulation of tropical cyclones has been attempted by many scholars. Inaccurate representation of ocean layers can undermine the heat exchange occurring between ocean and atmosphere which can be lessened in a coupled model. Ocean mixed layers are found to influence the intensification of tropical cyclones (Wada et al., 2013) which should be properly included in the numerical modelling. Further, the subsurface oceanic conditions also affect the sea surface temperature (SST) variation under a typhoon condition (Shay et al., 2010; Wada et al., 2014), which can only be analyzed by a coupled ocean-atmosphere model. Using a coupled ocean-atmosphere model improves the understanding of the interactions between oceanic eddies and typhoons (Ma et al., 2013; Anandh et al., 2020). These eddies can also contribute to the intensifications or dissipations of the typhoons depending on their dynamic features.

Using a coupled ocean-atmosphere model, we analyze the impact of sea-air interaction for the accuracy of track and intensity of typhoons for three SCS typhoons with different intensities and translate speeds. With the coupled model, the ocean thermodynamical responses to the typhoon forcing are also investigated through the analysis of latent heat flux as well as the upper 300 m layer during the passage of typhoons.

2 Datasets, models and methodology

2.1 Typhoon description

To analyze the impact of coupling in ocean-atmosphere model for typhoons over the SCS, we have simulated three typhoons with different translation speeds, shapes of track and intensities. The variations in the cyclones are chosen to check the capabilities of the coupled model in simulating typhoons. A brief description of these typhoons is given as follows.

Typhoon Mujigae formed at 12:00 UTC on 30th September 2015 as a tropical depression in the southeast Philippines. It became a tropical cyclone at 12:00 UTC on 1st October and made its first landfall over the Philippines at roughly 20:00 UTC on 2nd October. It further intensified over the SCS as it approached mainland China. The typhoon made landfall in Guangdong province of China at 06:10 UTC on 4th October 2015. During its strongest phase, it had a sustained 10-min wind speed over 160 kmph making it one of the strongest typhoons (category 4; with a wind speed of 17.5–24.5 m/s and a minimum central pressure of 937 hPa) of the year 2015.

Typhoon Merbok formed at 15:00 UTC on 10th June 2017 as a large-scale tropical depression west of Manila, Philippines. It slowly intensified over the SCS, reaching its peak at 12:00 UTC on June 12th with a 10-min sustained wind speed over 100 kmph and a minimum central pressure of 985 hPa. Merbok translated at a speed of 6 m/s, becoming one of the

fastest-moving typhoons over the SCS. It made landfall over Shenzhen at 14:00 UTC on 12th June 2017.

Typhoon Hato formed northeast of the Philippines by 03: 00 UTC on 20th August 2017. It is one of the strongest and fastest-moving (a translation speed of ~8 m/s) typhoons over the SCS. It intensified rapidly over the SCS and made landfall near Jinwan, China at 04:50 UTC on 23rd August. At its peak, it had a 10-min sustained wind speed over 160 kmph (a minimum central pressure of 948 hPa) and was classified as a category 3 typhoon.

2.2 Datasets

As for the initial and boundary conditions for the simulations, the atmospheric data are obtained from the European Centre for Medium-Range Weather Forecasts Re-Analysis project (ERA-Interim). The ERA-Interim data has a temporal resolution of 6 h and spatial resolution of 0.75°, which provides necessary parameters (i.e., potential temperature, pressure, wind components, heat fluxes, mixing ratios of water, rain, ice and snow, and surface skin temperature) for initializing and running the WRF model. The oceanic data are obtained from the Estimating the Circulation and Climate of the Ocean version 2 (ECCO2) dataset (Menemenlis et al., 2005, 2008). The ECCO2 data has a temporal resolution of 3 days and spatial resolution of 0.5°. It provides oceanic temperature, salinity, ocean currents, and sea level for the initial and lateral boundary conditions. The bottom boundary of the ocean grid is taken from the Etopo2 bathymetry data.

As for the simulation validation, the Joint Typhoon Warning Center (JTWC) data has been used for the information on the track and intensity of typhoons. The Group for High Resolution Sea Surface temperature (GHRSST) satellite products (Martin et al., 2012) have been used for validation of simulated SST.

2.3 Model configuration

The coupled ocean-atmosphere-wave-sediment transport (COAWST) model (Warner et al., 2010) includes Regional Ocean Modelling System (ROMS) and Weather Research and Forecasting (WRF) modelling system to simulate the ocean and atmosphere status simultaneously. ROMS is a high-resolution stretched terrain-following hydrostatic model (Haidvogel et al., 2000; Shchepetkin and McWilliams, 2005), which solves the momentum and other primitive equations using split-explicit time-stepping schemes over the ocean. Along the horizontal, the model solves the primitive equations on a staggered Arakawa C-grid. A sea/land mask is used to describe the coastal boundaries in the finite discretized grid. WRF is a fully compressible non–hydrostatic model (Skamarock et al., 2019) that solves the primitive equations over a terrain following hydrostatic pressure coordinates and also uses the staggered Arakawa C-grid. For the simulation of atmospheric variables, it also employs various time integration and advection schemes.

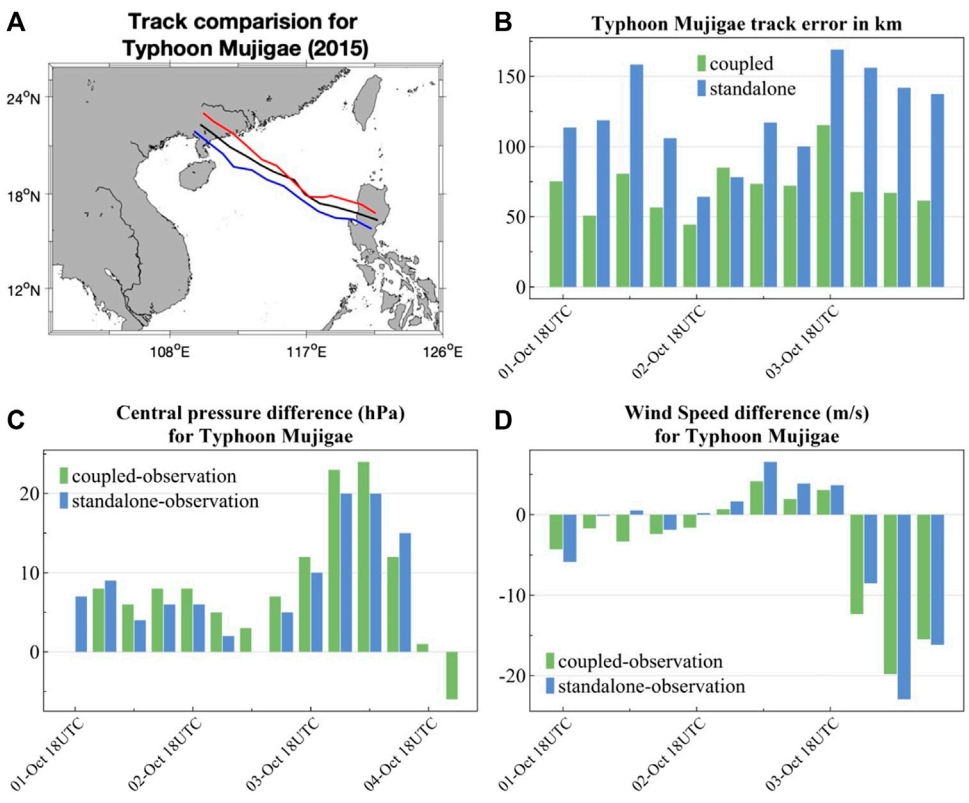

FIGURE 2
(A) The track of Typhoon Mujigae from JTWC observation (blue), the standalone WRF model (red), and the coupled model (black). Time series of **(B)** the simulated track bias, **(C)** the central pressure bias, and **(D)** the wind speed bias.

The outermost domain of the study is shown in Figure 1 and it ranges from 90°E to 135°E and 2°N to 35°N. The WRF model has an outermost domain with a 36-km horizontal resolution, a middle domain (d02) with a 12-km horizontal resolution, and the innermost domain (d03) with a 4-km horizontal resolution. All domains have 40 vertical levels with the top setting at the 50 hPa pressure level. WRF model utilizes the Rapid and Accurate Radiative Transfer (RRTM) (Mlawer et al., 1997) scheme for the Longwave Radiation estimation and Dudhia Scheme (Dudhia, 1989) for the shortwave radiation calculation. MYNN scheme (Nakanishi and Niino, 2006) is used for the calculations of the planetary boundary layer as recommended by previous studies in wind field simulation. NOAH land surface physics model and Kain-Fritsch cumulus convections scheme (Kain, 2004) are used for the simulations. Morrison 2-moment scheme (Morrison et al., 2009) is employed for estimating cloud microphysics. The ROMS model is configured with a single domain (12 km horizontal resolution and 32 sigma (vertical) levels) which is slightly larger than the outermost domain of WRF. The horizontal and vertical mixing schemes of the model are selected as K-Profile Parameterisation and Large-Maxwell-Doney scheme (Large et al., 1994). The model initialization as well as the lateral boundaries are provided from ERA-Interim and ECCO2 data, that is, interpolated to the model grid resolution. The model bathymetry is provided from the Etopo2 bathymetry data.

During the coupling process, the WRF model provides the zonal and meridional wind stress components, radiation, evaporation, and precipitation field to the ROMS model. The ROMS model receives the atmospheric model input every 20 min and computes the surface fluxes of momentum, sensible heat, and latent heat using the COARE (Coupled Ocean-Atmosphere Response Experiment) algorithm (Fairall et al., 2003). The ROMS model provides the sea surface temperature (SST) to the atmosphere model for typhoon simulations. Since both models have different horizontal resolutions, a weighted average intermediary grid is created over each grid to interpolate and transfer the data correctly. Both the coupled model and the standalone WRF model are initiated 1 day in advance of the cyclogenesis and run for 7 days.

2.4 Methodology

Since the eye of typhoon is not a direct output from the model, the typhoon track can be estimated as the movement of the lowest surface pressure between each time steps of simulations. The simulated cyclone tracks are compared with the observation from JTWC, and the deviations from the observation will be analyzed in Section 3.1. The track bias is the distance between the simulated typhoon center ($longitude_{sim}$; $latitude_{sim}$) and the corresponding JTWC record ($longitude_{JTWC}$; $latitude_{JTWC}$) at each time step, which can be expressed as $d = \sqrt{(longitude_{sim} - longitude_{JTWC})^2 + (latitude_{sim} - latitude_{JTWC})^2}$. Then the distance d was converted from a radian scale to a kilometer scale using 1° = 110 km. The precision of the recorded wind speed from JTWC is five knots (~2.5 m/s), while the one of the model derived values is 0.1 m/s. For the maximum wind validation, we first converted the unit

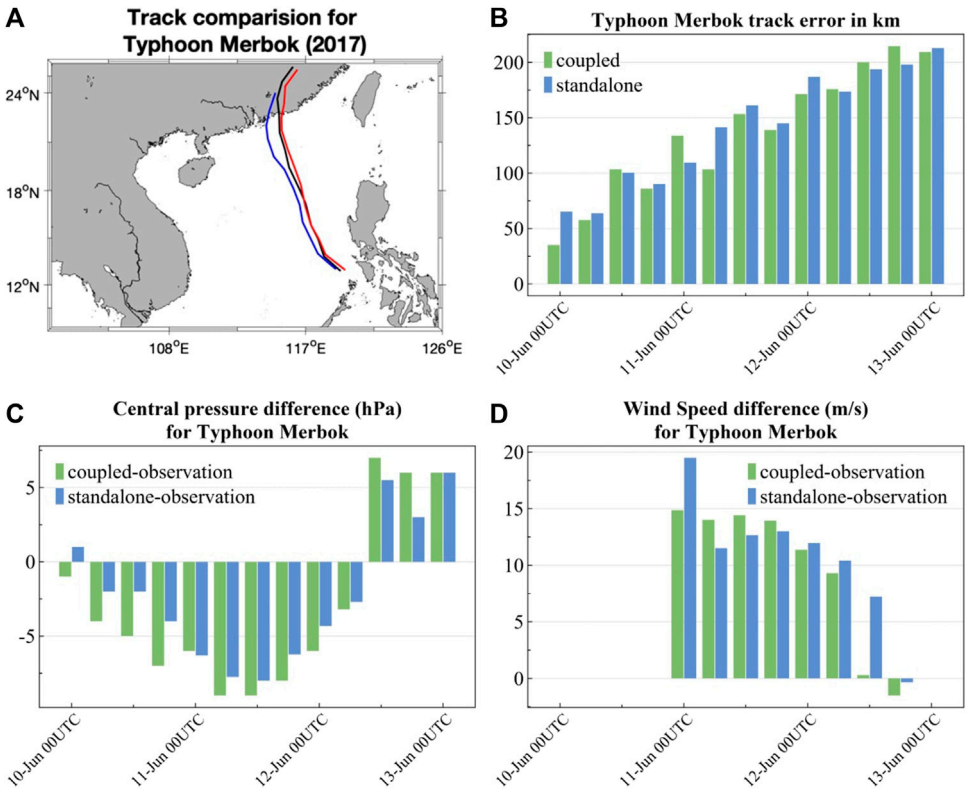

FIGURE 3
Similar to Figure 2 but for typhoon merbok.

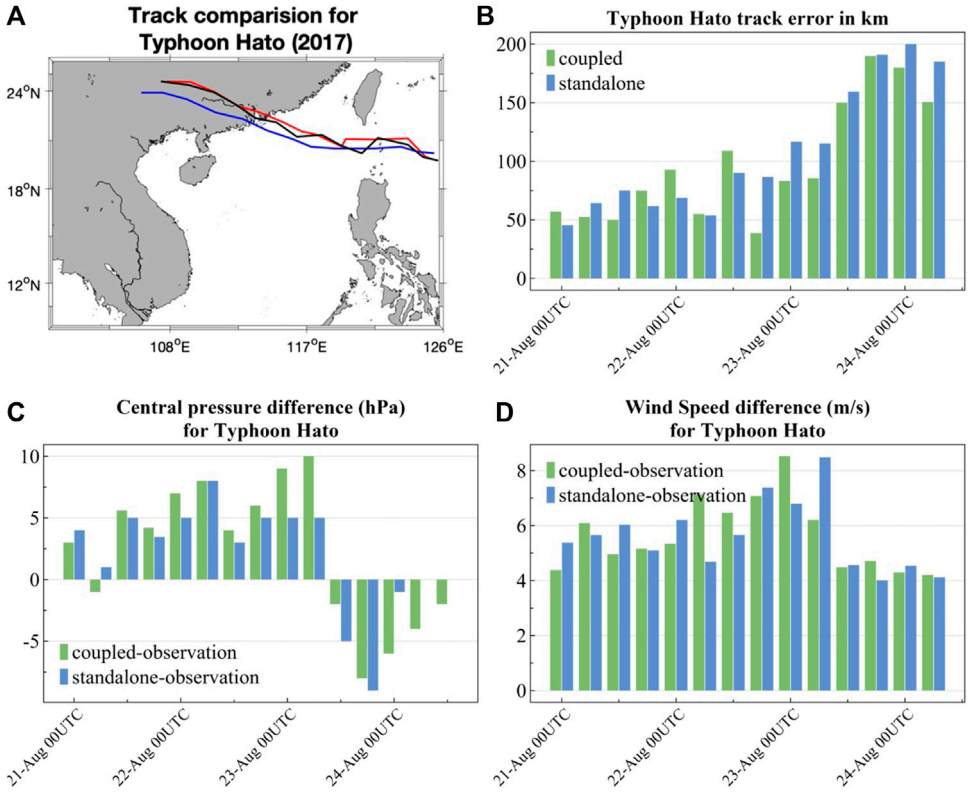

FIGURE 4
Similar to Figure 2 but for typhoon hato.

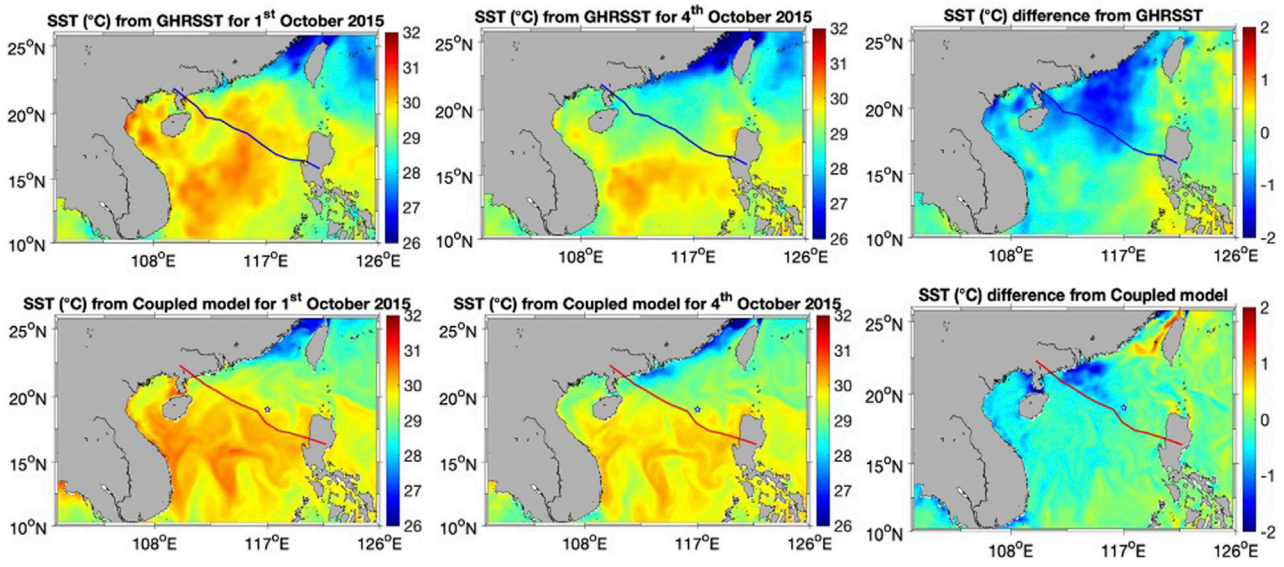

FIGURE 5
The SST change associated with Typhoon Mujigae. SST distribution on the day of (Left) typhoon genesis, and (middle) landfall. (Right) The SST difference between these two dates. (Top) GHRSST satellite data and (bottom) the coupled model output. The star symbols indicate the region of intensification in the coupled model which will be further investigated in Section 3.4.

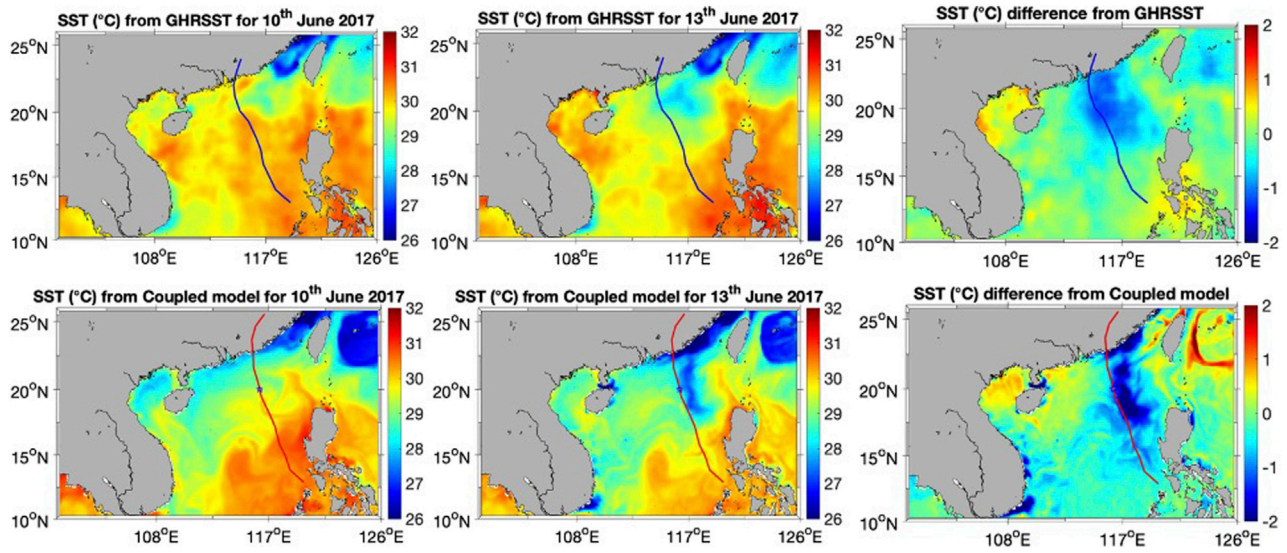

FIGURE 6
Similar to Figure 5 but for typhoon merbok.

from knots to m/s then analyzed the deviation. A positive bias indicates that the model overpredicts the parameters.

3 Results and discussions

3.1 Simulated tracks and intensity of typhoons

The simulated typhoon track, wind speed, and central pressure for the selected typhoons from both the coupled ocean-atmosphere model and the standalone WRF model, along with JTWC data, are provided in Figure 2, Figure 3, Figure 4.

The depression phase of Typhoon Mujigae started in the Pacific Ocean and it attained the cyclonic form over the Philippines islands. Therefore, the simulated typhoon was initialized over the islands as shown in Figure 2. Compared to the JTWC reported track, the standalone WRF model has an initial bias of 120 km, while the coupled model has a smaller one of 70 km (Figure 2B). Initial bias of the typhoon location can greatly affect the simulated track, which can even cause a significant intensity bias if there is any large thermodynamical pattern (e.g., ocean mesoscale eddies) on the simulated track. In both uncoupled and coupled simulations, the typhoon intensified over the SCS and moved northwestward, with the tracks lying to the north of the observational one. The average track biases are about 120 km for the standalone model and 70 km for the coupled model throughout the simulations which is almost same as the initialization bias. The simulation of tracks has improved up to 40% in the coupled model. The simulations produce a weaker typhoon, with the positive biases in central pressure and the negative biases in maximum wind speed. After 3rd October 2015 (Figures 2C, D), the biases of the simulated central pressure and wind speed increased. These biases can be attributed to the earlier landfall in the simulation, which makes the typhoon lose its intensity earlier than the observation.

Figure 3 shows the atmospheric parameters for Typhoon Merbok. The typhoon originated west of the Philippines and traversed northwards making landfall over mainland China. A typhoon with a translation speed above 20 km/h or 5.6 m/s is considered to be moving fast (e.g., Kim et al., 2020). Merbok was one of the fastest moving typhoons (~6 m/s) recorded in the SCS and yet the simulated Merbok traversed even faster (~7 m/s) than observation. The simulated and observational tracks are close to each other in the open sea (Figure 3A), with the initial bias of less than 50 km. The improvement in the track is significant up to 10% in the coupled model. The track biases become larger when the typhoon moved close to the land and made a slight curve at 19°N. The faster and more straight simulated tracks result in an earlier (18–22 h) landfall than the observation, with a 100 km location bias. The higher translational speed of the simulated typhoons resulted in making landfall earlier than the observation and the bias increased rapidly since then. The initial 50-km bias in the track increase to a 200-km bias as the typhoon weakened after landfall in the simulations (Figure 3B). The models produce a stronger typhoon, with a negative central pressure bias and a positive wind speed bias. The bias in the central pressure and wind speed reduced as the simulated typhoon over land lost its intensity (Figures 3C, D). Also, it is noticed that cyclones with a fast translational speed generally cannot get intensified into a strong typhoon as it spends less time over the warmer oceans and gains less energy from the sea-air interaction (Mei et al., 2012).

The validation of atmospheric parameters for Typhoon Hato is shown in Figure 4. Typhoon Hato had its genesis in the Pacific Ocean and moved westwards, and finally made landfall over China. Both the coupled and standalone models are able to capture the genesis spot and reproduce the track. The track biases stay lower than 50 km before landfall on 23rd August 2017 (Figure 4B). The bias of landfall location is

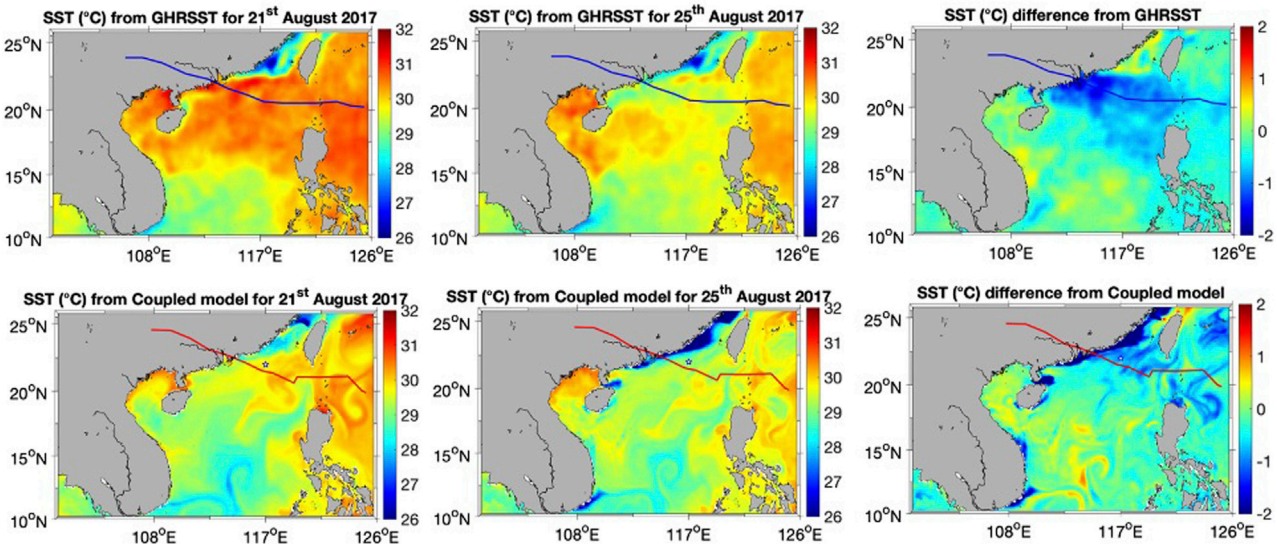

FIGURE 7
Similar to Figure 5 but for typhoon hato.

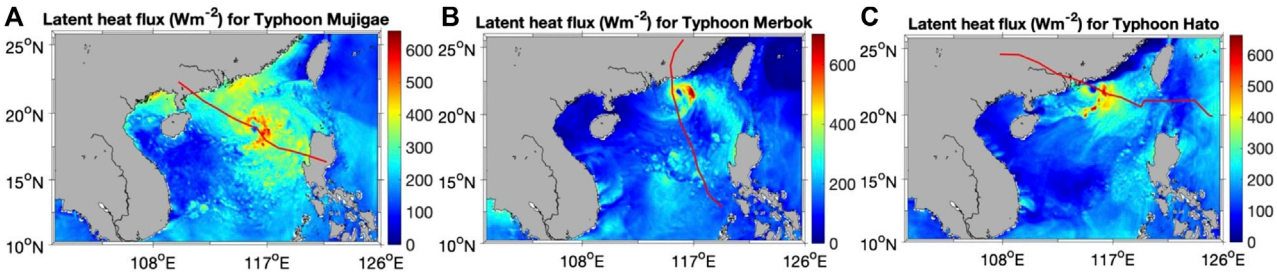

FIGURE 8
Maximum simulated latent heat release from ocean to atmosphere along with the simulated track during the passage of typhoons over the SCS. **(A)** Typhoon Mujigae, **(B)** Typhoon Merbok, and **(C)** Typhoon Hato.

less than 25 km in the coupled model but higher (75 km) in the standalone model. After landfall, the simulated typhoons followed a track with a bias of about 150 km from the observed track. Overall, the track error has reduced by 10% in the coupled model when compared to the standalone model. The central pressure biases are within 10 hPa throughout the simulation. The central pressure derived from the coupled model is higher than the standalone model as upper ocean cooling feedback in the coupled model is higher. The coupled model has a better performance in simulating the maximum wind speed, with a slightly lower bias of about 4–6 m/s.

We must confess that the improvement of the intensity simulation is not significant, or even worse. In general, the simulated typhoons have a weaker intensity. This is largely because the sea surface cooling caused by the typhoon will prevent the typhoon from further intensifying, which will be more significant in the coupled model. On the other hand, the validation of simulated intensity is more complicated than that of track simulation, for the development of typhoons in the simulation may be more or less different from the real one due to the model parameterization of subgrid physical processes.

3.2 Sea surface temperature

Previous studies have found that the coupling between ocean and atmosphere induces a substantial sea surface cooling and results in weaker simulated typhoons due to less heat enthalpy in the upper ocean (Zambon et al., 2014; Prakash and Pant, 2017; Guo et al., 2020). The main advantage of using a coupled model in the typhoon analysis is that we can understand the complex energy exchanges between the ocean and atmosphere and how the typhoon reacts to it. The analysis in Section 3.1 shows the coupled model performs better in simulating typhoon activity, so the following analysis will be based on the output from the coupled model.

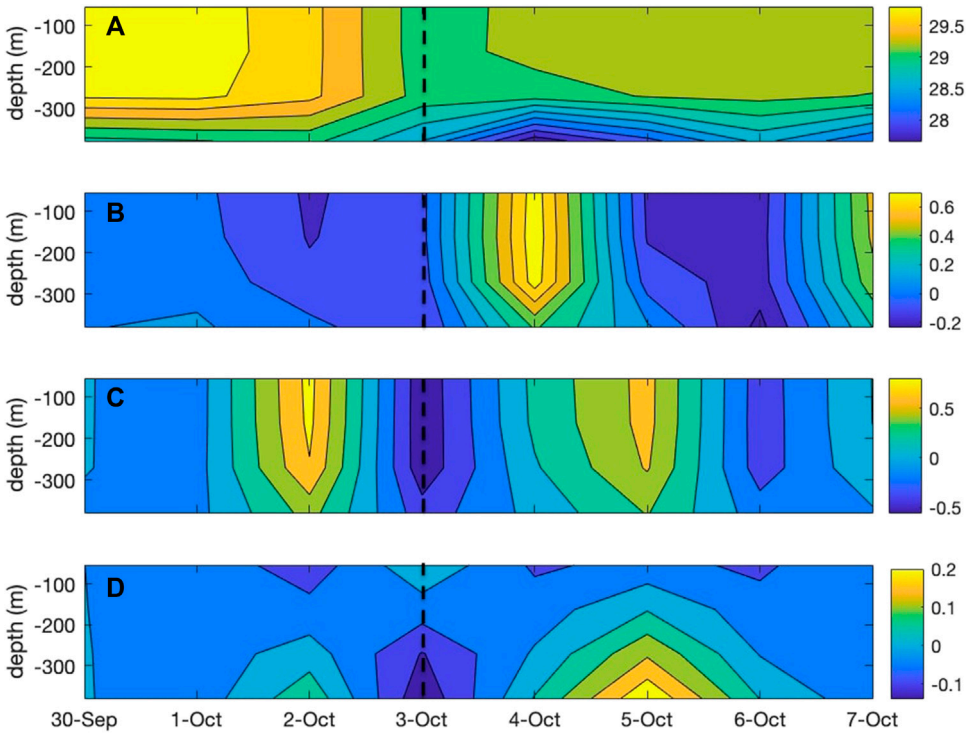

FIGURE 9
Time series of the vertical structure of the upper ocean in the region with maximum latent heat release for typhoon Mujigae. **(A)** Temperature in ˚C, **(B)** zonal velocity in m/s, **(C)** meridional velocity in m/s, and **(D)** the scaled vertical velocity in cm/s. Dotted line indicates the intensification date.

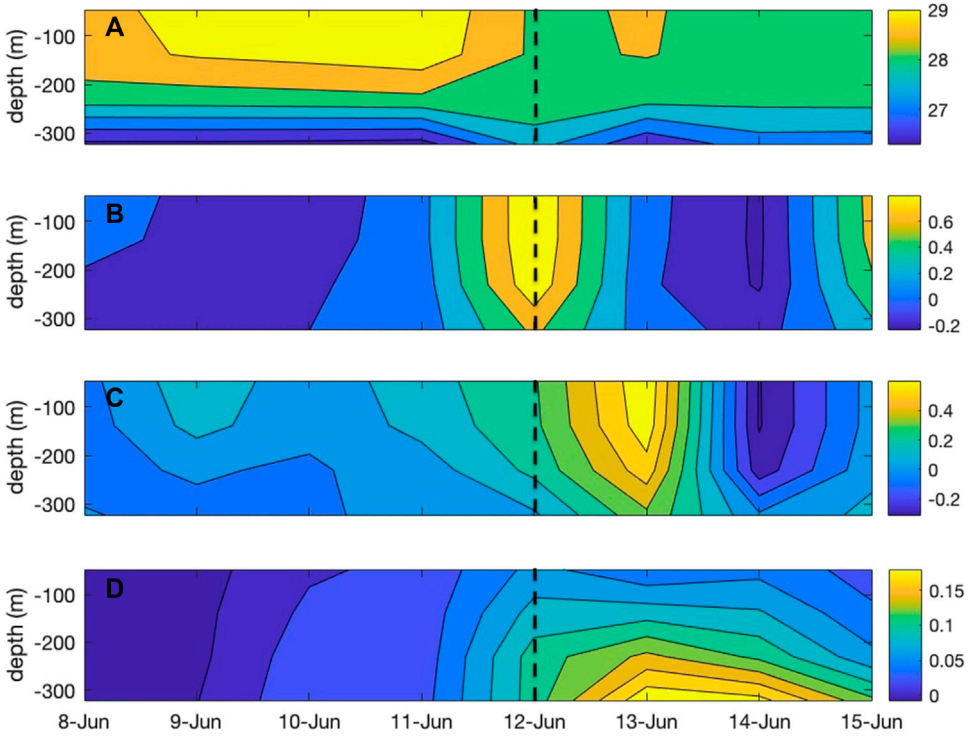

FIGURE 10
Similar to Figure 9 but for typhoon merbok.

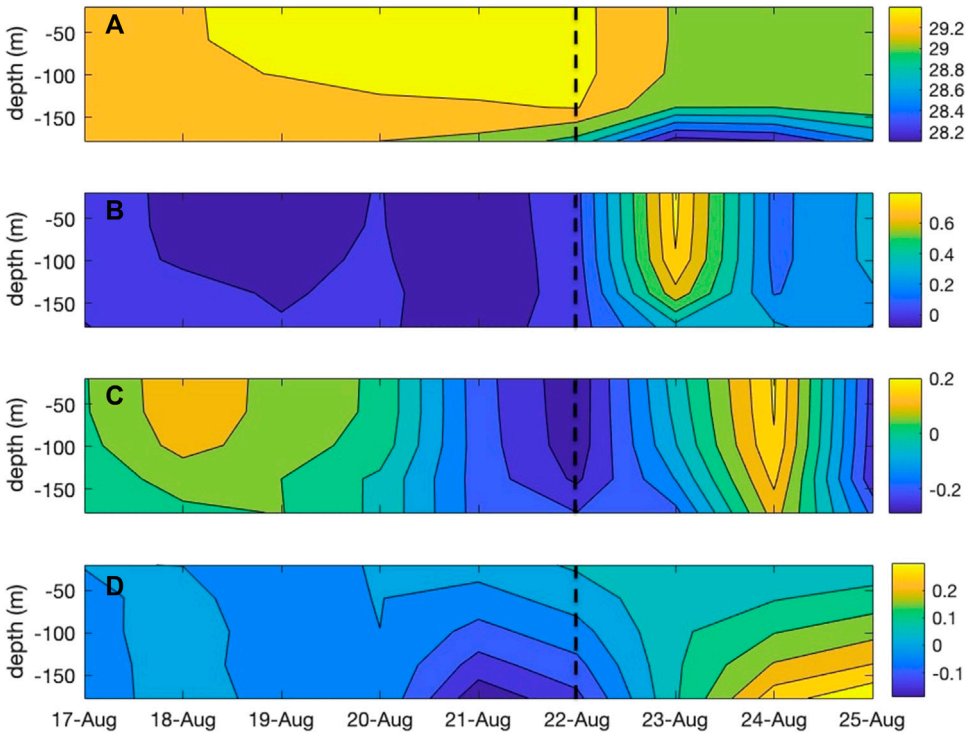

FIGURE 11
Similar to Figure 9 but for typhoon hato.

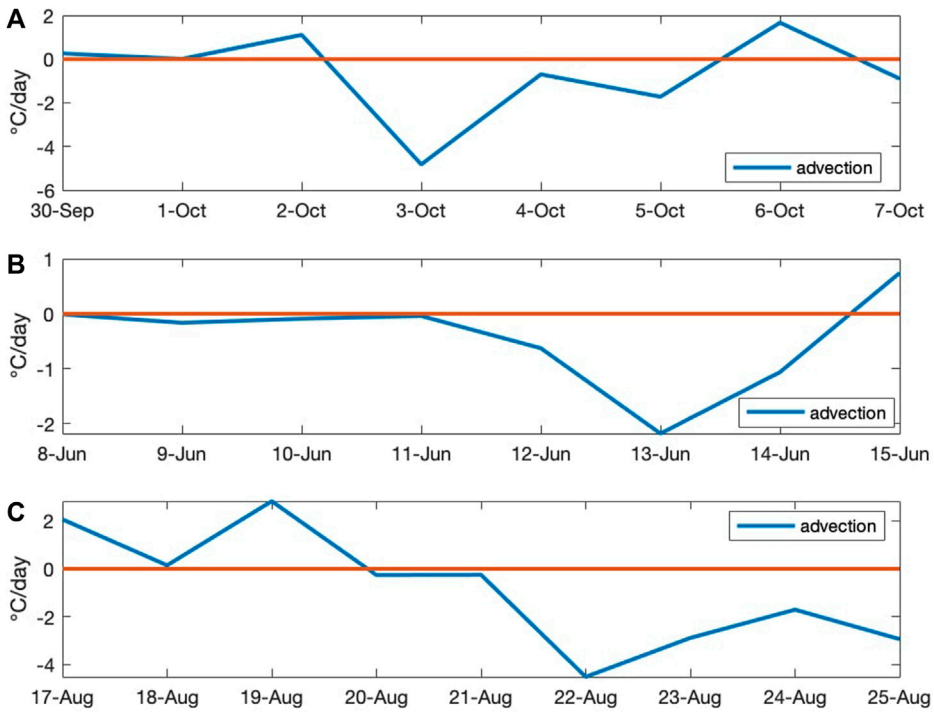

FIGURE 12
Contribution of advection terms to the heat budget averaged over the mixed layer in °C/day for **(A)** Typhoon Mujigae, **(B)** Typhoon Merbok, and **(C)** Typhoon Hato.

The simulated SST for the different typhoons from the coupled model is compared with GHRSST satellite observation as shown in Figure 5, Figure 6, Figure 7. Two dates are selected for comparison for each typhoon, with one at which the typhoon genesis and the other of landfall. As the typhoon extracts the energy from the ocean for its intensification, the surface temperature of the ocean decreases. This decrease in SST can be used as a proxy for the energy absorbed by the typhoon.

The SSTs for Typhoon Mujigae derived from the satellite observation and the coupled model are shown in Figure 5. The typhoon started intensifying on 1st October and made landfall on 4th October. In the simulation, there is an initial bias of about 0.25°C on the genesis day over the coastal South China yet the reduction in SST during landfall is captured well. The observed cooling is substantial along the coastal China where the typhoon absorbed heat energy from the ocean before making landfall. This energy transfer has been well captured by the coupled model but to a lesser extent. Observation shows SST cooling up to 2°C, while the coupled model shows up to 1.75°C. The reduction of SST has occurred along the right side of the typhoon track due to the increased Ekman pumping (e.g., Huang and Oey, 2015; Wei et al., 2018).

The SST variations for Typhoon Merbok from observation and simulation are shown in Figure 6. The genesis of Typhoon Merbok occurred on 10th June 2017 and it made landfall on the late night of 12th June 2017. The typhoon dissipated over land on 13th June. The observation shows that the passage of the typhoon over the SCS has reduced the SST up to 1.5°C. The simulated SST cooling is stronger than the observation, with a cooling up to 2°C. The stronger cooling in the simulated SST indicates that the simulated typhoon has absorbed more energy from the ocean surface. In addition, the typhoon moved much faster and made landfall earlier in the simulation.

Figure 7 shows the SST variations of Typhoon Hato from observation and simulations. The satellite observation shows that the SST is higher than 31°C covering the northern SCS, which provides a favorable condition for a typhoon genesis. The temperature difference shows that the SST cooling is above 1°C along the entire track, with the strongest cooling (2°C) near the coast. The coupled model can reproduce the SST cooling along the track and in the coastal region, with a stronger cooling by about 0.25°C (Figure 7).

It is well known that the strongest SST cooling caused by the typhoon, which coincides with the maximum energy extraction, has occurred on the right side of the track due to the strong Ekman pumping rather than on the track due to the strong wind stress (Schade and Emanuel, 1999; Jacob et al., 2000). The substantial cooling in the coupled model can reduce the typhoon intensification due to lower surface energy available for further intensifications.

3.3 Latent heat releasing from ocean surface

The typhoon intensity largely depends on the surface heat exchange (Emanual, 1986; Byran and Rotunno, 2009). Modelling and observational studies have showed that the typhoon intensification is accompanied by increases in the sea-to-air latent heat flux (e.g., Bell et al., 2008; Lin et al., 2014; Jaimes et al., 2015; Gao et al., 2017). Latent heat release in the atmosphere is the main source of energy keeping typhoons active. Latent heat supplies energy to the immense convections that occur in the eyewall and rain bands of the typhoon (Bister and Emanuel, 1998). Initially, a large-scale convection sets over the ocean under the warm upper ocean conditions. As the convection intensifies, it drags on more volume of moisture rich air from the surrounding region. This air rises and cools, thereby condensing the moisture and releasing the latent heat, which further expands the air at the center. This expansion of air creates a low-pressure region and more convergence occurs at the lower levels. This positive feedback intensifies the depression into a cyclone (Craig and Gray, 1996). As long as there is latent heat release and convergence occurs at the lower levels, the cyclone keeps on intensifying. Meanwhile, the heat releases from the upper ocean to the atmosphere, which results a cooling in the ocean surface and a warming the atmosphere boundary layer (Emanuel, 1986; Emanuel et al., 1994; Bister and Emanuel, 1998). Although the vertical mixing and Ekman pumping (Walker et al., 2005; Wada et al., 2009) are important mechanisms of SST cooling under a typhoon, the typhoon-induced heat fluxes can dominate the SST cooling in the near-coastal shallow ocean regions (Shen and Ginis, 2003). By knowing the amount of latent heat released, we can gain a better understanding of typhoon intensity changes and sea surface cooling. The simulated maximum amount of latent heat released from the ocean for all three typhoons ranges from 600 to 700 Wm^{-2}, occurring on the right side of the tracks (Figure 8). This is consistent with the substantial cooling found on the right of the tracks. The extent of higher latent heat release (>300 Wm^{-2}) spreads wider for Mujigae and Hato but was more concentrated for Merbok. The wider spread of latent heat release is the main reason for intensifying these two storms into category 4 and 3 typhoons, respectively.

3.4 Ocean mixed layer

The typhoon intensity largely depends on the ocean thermodynamics. The ocean must contain enough energy in the upper layers for typhoon intensification (Prasad and Hogan, 2007; Prakash and Pant, 2017; Zhang, 2022). Besides the high SST, the mixed layer (i.e., isothermal layer) needs to be warm and thick enough to substantially supply energy to the typhoon (Wu et al., 2007; Lin et al., 2008; Anandh et al., 2020) and retain itself under the destruction from typhoon impact (e.g., Lee and Chen, 2014). The simulated upper ocean thermodynamical characteristics (i.e., the temperature, the horizontal and vertical ocean currents) in the region where the typhoons intensified (as shown by star symbols in Figures 5–7) are provided in Figure 9, Figure 10, Figure 11.

The upper ocean state during the passage of Typhoon Mujigae is shown in Figure 9. The region of intensification is near 19°N and 117°E. The temperature within the upper 250 m stays above 29°C before typhoon. The typhoon passed over the region on 3rd October (black dashed lines in Figure 9), and its impact can be seen in the substantial variations of the sea surface as well as the layer beneath 300 m. The temperature has reduced up to 1.5°C compared to the previous days. The zonal and meridional surface velocities are shown in Figures 9B,C. The meridional velocity has changed direction in the previous 2 days of the

typhoon approach. As the typhoon approached from the south, northward movement of waters is expected. The reversion of the surface current is expected as the typhoon go through the region. The injection of cool waters from the deeper ocean can be seen as the typhoon passed (Figure 9A), which agrees well with the upwelling (Figure 9D). This upwelling is associated with the Ekman pumping caused by the strong typhoon wind stress.

Figure 10 shows the upper ocean state variation for Typhoon Merbok. The region of intensification is near 20°N and 116.25°E. The ocean surface during Typhoon Merbok (black dashed lines in Figure 10) was not as warm as that for Typhoon Mujigae, nor the mixed layer (50–75 m) was deeper. The typhoon came across the region on 12th June 2017, and caused a significant surface cooling up to 1°C (Figure 10A). The upwelling of the cold deeper ocean water was not significant in the temperature variation but can be seen in the vertical velocity field (Figure 10D). The horizontal velocity fields also captured the sudden surge in ocean waters when the typhoon entered this region.

The vertical thermal and dynamical structures of the upper ocean for Typhoon Hato are given in Figure 11 (black dashed lines in Figure 11). The region of intensification is near 22°N and 117°E. The mixed layer was deep (up to 140 m) when the typhoon approached. The typhoon passed over the region on 22nd August 2017 before landfall. The upwelling can be found in both temperature and vertical velocity fields. The temperature has reduced by 1°C as the typhoon passed.

As suggested by Zambon et al. (2014), the local change in temperature can be given by the heat budget equation as follows

$$\frac{\partial T}{\partial t} = -\left(u\frac{\partial T}{\partial x} + v\frac{\partial T}{\partial y} + w\frac{\partial T}{\partial z}\right) + \frac{\partial}{\partial x}\left(k\frac{\partial T}{\partial x}\right) + \frac{\partial}{\partial y}\left(k\frac{\partial T}{\partial y}\right) + \frac{\partial}{\partial z}\left(k\frac{\partial T}{\partial z}\right)$$

where $-(u\frac{\partial T}{\partial x} + v\frac{\partial T}{\partial y})$ is the horizontal advection and $-w\frac{\partial T}{\partial z}$ is the vertical advection (Prasad and Hogan, 2007; Zambon et al., 2014). The term $\frac{\partial}{\partial x}(k\frac{\partial T}{\partial x}) + \frac{\partial}{\partial y}(k\frac{\partial T}{\partial y})$ represent the horizontal diffusion and the term $\frac{\partial}{\partial z}(k\frac{\partial T}{\partial z})$ represents the vertical diffusion, with $k = 0.4$ is the diffusivity coefficient. Under a typhoon condition (i.e., the current speed of 1 m/s, and the temperature gradients of about 1 °C/day), the contribution of diffusion to the change in temperature (~0.01 °C/day) is two orders less than the temperature change due to the advection (~1 °C/day). Letting $f(z) = -(u(x,y,z)\frac{\partial T(x,y,z)}{\partial x} + v(x,y,z)\frac{\partial T(x,y,z)}{\partial y} + w(x,y,z)\frac{\partial T(x,y,z)}{\partial z})$, we can analyze the contribution of advection terms to the heat budget averaged over the mixed layer as $\frac{\int_{MLD}^{0} f(z)dz}{MLD}$, where MLD is the depth of mixed layer. Time series of the advection term contribution over the location of maximum latent heat flux (red shading regions in Figure 8) are shown in Figure 12. We can see that the maximum advection has occurred on the day of typhoon intensification and the integrated temperature change has reached up to 6 °C/day for the more intense typhoons Mujigae and Hato and up to 2°C/day for Typhoon Merbok. The strong advection has remained significant for 3–4 days after typhoon. From the time difference between the typhoon transit and advection, we can find that the stronger typhoons result in a quicker the upper ocean response due to the more intense wind stress. The oceanic vertical mixing and upwelling (Ekman pumping) are related to wind stress (Walker et al., 2005; Wada et al., 2009), which depends linearly on the near-surface (i.e., 10 m) wind speed (e.g., Hsu et al., 2017) and therefore is related to the typhoon's intensity. In other words, the wind stress in a stronger typhoon causes more vigorous turbulence and stronger upwelling and thus a quicker ocean response.

4 Discussion and conclusion

South China Sea has a high SST above 26°C throughout the year, which provides a favorable condition for typhoon formation and intensification. Previous numerical studies of typhoons have concentrated on atmospheric dynamics which cannot give a full picture of typhoon development. Here, the results show that the simulated track from the coupled model has improved from the standalone simulations. For Typhoon Mujigae, the track error has reduced up to 40% while for the other two typhoons, the track error has reduced by 10%. Note that the track errors increased during the typhoon's lifetime, related mainly to the different translation speeds from the simulations and the observations. The coupled simulations produced more accurate translational speeds than the standalone simulations (e.g., Mooney et al., 2019). The coupling between the ocean and atmosphere provides a more physically realistic representation of the interaction between the typhoon and ocean and, consequently, the accuracy of typhoon tracks.

The coupled model can also reproduce the upper ocean response to typhoons, with an SST cooling comparable to the satellite observation. The strongest cooling occurs on the right of the typhoon track. The maximum latent heat release reaching above 600 $-\mathrm{Wm}^{-2}$ can also be found on the right of the track, with a more intense latent heat release found in the stronger typhoon cases. The analysis of the latent heat suggests that the latent heat releasing from the ocean cools the sea surface and intensifies the typhoons. The intense latent heat release region is found to be larger for a slow-moving typhoon and concentrated for a fast-moving typhoon. Although wind-driven vertical mixing is the primary cause of SST cooling under a typhoon (Wada et al., 2009), the typhoon-induced heat fluxes dominate the SST cooling in the near-coastal shallow ocean regions (Shen and Ginis, 2003). The mixed layer analysis of output from the coupled model reveals the upwelling caused by the typhoon passage and the oscillations in zonal and meridional velocities. The well mixing of the ocean as well as the upper ocean cooling is noted in the vertical velocity. The heat budget analysis shows that the cooling of the upper ocean is mainly attributed to the advection associated with the typhoon forcing.

However, the simulation of typhoon intensity has not been improved (or even worse) by the coupled model. This worse performance in the simulation of intensity as well as the SST variation is closely related with the upper ocean thermodynamics. A thick and warm mixed layer can prevent the SST cooling too severe and provide more enthalpy for typhoon intensification. Hereafter, this intensified typhoon triggers a strong advection in the upper ocean, which in return destroys the original mixed layer. Perhaps the advection responses too fast in the strong typhoon cases, which impedes the mixed layer to provide enough energy for the typhoon intensification. Further improvements are needed for upper ocean simulation in order to better simulating the typhoon intensity.

These analyses show that the ocean response is an inevitable part of the numerical analysis of typhoons. The oceanic feedback to the atmosphere can be used to understand how the energy exchanges

happen and how the oceanic waters support typhoon development. The coupled ocean-atmosphere models can be a useful tool for typhoon forecasting and analysis.

Data availability statement

The original contributions presented in the study are included in the article/Supplementary Material, further inquiries can be directed to the corresponding authors.

Author contributions

AT: conceptualization, methodology, formal analysis, writing—original draft; TX: resources, writing—original draft, supervision; L-PW: conceptualization, supervision, project administration, funding acquisition. All authors contributed to the article and approved the submitted version.

Funding

This work has been supported by the National Natural Science Foundation of China (42075071, 11988102), Guangdong Provincial Key Laboratory of Turbulence Research and Applications (2019B21203001), Guangdong-Hong Kong-Macao Joint Laboratory for Data-Driven Fluid Mechanics and Engineering Applications (2020B1212030001), and Shenzhen Science and Technology Program (JCYJ20220530113005012, KQTD20180411143441009).

Acknowledgments

Computing resources are provided by the Center for Computational Science and Engineering of Southern University of Science and Technology.

Conflict of interest

The authors declare that the research was conducted in the absence of any commercial or financial relationships that could be construed as a potential conflict of interest.

Publisher's note

References

Adriano, B., Gokon, H., Mas, E., Koshimura, S., Liu, W., and Matsuoka, M. (2014). "Extraction of damaged areas due to the 2013 Haiyan typhoon using ASTER data," in 2014 IEEE Geoscience and Remote Sensing Symposium, Quebec City, QC, Canada, 13-18 July 2014 (IEEE), 2154–2157. doi:10.1109/IGARSS.2014.6946893

Anandh, T. S., Das, B. K., Kuttippurath, J., and Chakraborty, A. (2020). A coupled model analyses on the interaction between oceanic eddies and tropical cyclones over the Bay of Bengal. *Ocean. Dyn.* 70 (3), 327–337. doi:10.1007/s10236-019-01330-x

Bell, M. M., and Montgomery, M. T. (2008). Observed structure, evolution, and potential intensity of category 5 Hurricane Isabel (2003) from 12 to 14 September. *Mon. Weather Rev.* 136, 2023–2046. doi:10.1175/2007mwr1858.1

Bister, M., and Emanuel, K. A. (1998). Dissipative heating and hurricane intensity. *Meteorology Atmos. Phys.* 65 (3), 233–240. doi:10.1007/bf01030791

Bryan, G. H., and Rotunno, R. (2009). Evaluation of an analytical model for the maximum intensity of tropical cyclones. *J. Atmos. Sci.* 66, 3042–3060. doi:10.1175/2009jas3038.1

Craig, C. G., and Gray, S. L. (1996). CISK or WISHE as the mechanism for tropical cyclone intensification. *J. Atmos. Sci.* 53, 3528–3540. doi:10.1175/1520-0469(1996)053<3528:COWATM>2.0.CO;2

Davis, C., Wang, W., Chen, S. S., Chen, Y., Corbosiero, K., DeMaria, M., et al. (2008). Prediction of landfalling hurricanes with the advanced hurricane WRF model. *Mon. weather Rev.* 136 (6), 1990–2005. doi:10.1175/2007MWR2085.1

Di, Z., Gong, W., Gan, Y., Shen, C., and Duan, Q. (2019). Combinatorial optimization for WRF physical parameterization schemes: A case study of three-day typhoon simulations over the northwest Pacific ocean. *Atmosphere* 10 (5), 233. doi:10.3390/atmos10050233

Done, J., Davis, C. A., and Weisman, M. (2004). The next generation of NWP: Explicit forecasts of convection using the Weather Research and Forecasting (WRF) model. *Atmos. Sci. Lett.* 5 (6), 110–117. doi:10.1002/asl.72

Dudhia, J. (1989). Numerical study of convection observed during the winter monsoon experiment using a mesoscale two-dimensional model. *J. Atmos. Sci.* 46 (20), 3077–3107. doi:10.1175/1520-0469(1989)046<3077:nsocod>2.0.co;2

Emanuel, K. A. (1986). An air-sea interaction theory for tropical cyclones. Part I: Steady state maintenance. *J. Atmos. Sci.* 43, 585–605. doi:10.1175/1520-0469(1986)043<0585:aasitf>2.0.co;2

Emanuel, K. A. (2013). Downscaling CMIP5 climate models shows increased tropical cyclone activity over the 21st century. *Proc. Natl. Acad. Sci.* 110 (30), 12219–12224. doi:10.1073/pnas.1301293110

Emanuel, K. A., Neelin, J. D., and Bretherton, C. S. (1994). On large-scale circulations in convecting atmospheres. *Quart. J. Roy. Meteor Soc.* 120, 1111–1143. doi:10.1002/qj.49712051902

Emanuel, K. A. (1999). Thermodynamic control of hurricane intensity. *Nature* 401 (6754), 665–669. doi:10.1038/44326

Emanuel, K. (2003). Tropical cyclones. *Annu. Rev. earth Planet. Sci.* 31 (1), 75–104. doi:10.1146/annurev.earth.31.100901.141259

Fairall, C. W., Bradley, E. F., Hare, J. E., Grachev, A. A., and Edson, J. B. (2003). Bulk parameterization of air–sea fluxes: Updates and verification for the COARE algorithm. *J. Clim.* 16 (4), 571–591. doi:10.1175/1520-0442(2003)016<0571:bpoasf>2.0.co;2

Fisher, E. L. (1958). Hurricanes and the sea-surface temperature field. *J. Atmos. Sci.* 15 (3), 328–333. doi:10.1175/1520-0469(1958)015<0328:hatsst>2.0.co;2

Gao, S., Zhai, S., Chen, B., and Li, T. (2017). Water budget and intensity change of tropical cyclones over the Western North Pacific. *Mon. Weather Rev.* 145, 3009–3023. doi:10.1175/mwr-d-17-0033.1

Gettelman, A., Bresch, D. N., Chen, C. C., Truesdale, J. E., and Bacmeister, J. T. (2018). Projections of future tropical cyclone damage with a high-resolution global climate model. *Clim. Change* 146 (3), 575–585. doi:10.1007/s10584-017-1902-7

Gopalakrishnan, S. G., Goldenberg, S., Quirino, T., Zhang, X., Marks, F., Yeh, K. S., et al. (2012). Toward improving high-resolution numerical hurricane forecasting: Influence of model horizontal grid resolution, initialization, and physics. *Weather Forecast.* 27 (3), 647–666. doi:10.1175/WAF-D-11-00055.1

Guo, T., Sun, Y., Liu, L., and Zhong, Z. (2020). The impact of storm-induced SST cooling on storm size and destructiveness: Results from atmosphere-ocean coupled simulations. *J. Meteorological Res.* 34 (5), 1068–1081. doi:10.1007/s13351-020-0001-2

Haidvogel, D. B., Arango, H. G., Hedstrom, K., Beckmann, A., Malanotte-Rizzoli, P., and Shchepetkin, A. F. (2000). Model evaluation experiments in the north atlantic basin: Simulations in nonlinear terrain-following coordinates. *Dyn. Atmos. oceans* 32 (3-4), 239–281. doi:10.1016/S0377-0265(00)00049-X

Herbeck, L. S., Unger, D., Krumme, U., Liu, S. M., and Jennerjahn, T. C. (2011). Typhoon-induced precipitation impact on nutrient and suspended matter dynamics of a tropical estuary affected by human activities in Hainan, China. *Coast. Shelf Sci.* 93 (4), 375–388. doi:10.1016/j.ecss.2011.05.004

Huang, S. M., and Oey, L. Y. (2015). Right-side cooling and phytoplankton bloom in the wake of a tropical cyclone. *J. Geophys. Res. Oceans* 120 (8), 5735–5748. doi:10.1002/2015JC010896

Hsu, J., Lien, R., D'Asaro, E. A., and Sanford, T. B. (2017). Estimates of surface wind stress and drag coefficients in typhoon megi. *J. Phys. Oceanogr.* 47, 545–565. doi:10.1175/JPO-D-16-0069.1

Islam, T., Srivastava, P. K., Rico-Ramirez, M. A., Dai, Q., Gupta, M., and Singh, S. K. (2015). Tracking a tropical cyclone through WRF–ARW simulation and sensitivity of model physics. *Nat. Hazards* 76 (3), 1473–1495. doi:10.1007/s11069-014-1494-8

Jacob, S. D., Shay, L. K., Mariano, A. J., and Black, P. G. (2000). The 3D oceanic mixed layer response to Hurricane Gilbert. *J. Phys. Oceanogr.* 30 (6), 1407–1429. doi:10.1175/1520-0485(2000)030%3C1407:TOMLRT%3E2.0.CO;2

Jaimes, B., Shay, L. K., and Uhlhorn, E. W. (2015). Enthalpy and momentum fluxes during Hurricane Earl relative to underlying ocean features. *Mon. Weather Rev.* 143, 111–131. doi:10.1175/mwr-d-13-00277.1

Kain, J. S. (2004). The kain–fritsch convective parameterization: An update. *J. Appl. meteorology* 43 (1), 170–181. doi:10.1175/1520-0450(2004)043<0170:tkcpau>2.0.co;2

Kim, S. H., Moon, I. J., and Chu, P. S. (2020). An increase in global trends of tropical cyclone translation speed since 1982 and its physical causes. *Environ. Res. Lett.* 15 (9), 094084. doi:10.1088/1748-9326/ab9e1f

Kueh, M. T. (2012). Multiformity of the tropical cyclone wind–pressure relationship in the Western North Pacific: Discrepancies among four best-track archives. *Environ. Res. Lett.* 7 (2), 024015. doi:10.1088/1748-9326/7/2/024015

Large, W. G., McWilliams, J. C., and Doney, S. C. (1994). Oceanic vertical mixing: A review and a model with a nonlocal boundary layer parameterization. *Rev. Geophys* 32, 363–403. doi:10.1029/94rg01872

Le Mau, D., Vlasova, G., and Nguyen, D. T. T. (2021). Distribution features of the typhoons in the South China sea. *Russ. J. Earth Sci.* 21 (1), 1001–1008. doi:10.2205/2020ES000746

Lee, C. Y., and Chen, S. S. (2014). Stable boundary layer and its impact on tropical cyclone structure in a coupled atmosphere–ocean model. *Mon. Weather Rev.* 142 (5), 1927–1944. doi:10.1175/MWR-D-13-00122.1

Lin, I. I., Pun, I. F., and Lien, C. C. (2014). Category-6 supertyphoon Haiyan in global warming hiatus: Contribution from subsurface ocean warming. *Geophys. Res. Lett.* 41, 8547–8553. doi:10.1002/2014gl061281

Lin, I. I., Wu, C. C., Pun, I. F., and Ko, D. S. (2008). Upper-ocean thermal structure and the Western North Pacific category 5 typhoons. Part I: Ocean features and the category 5 typhoons' intensification. *Mon. Weather Rev.* 136 (9), 3288–3306. doi:10.1175/2008MWR2277.1

Ma, Z., Fei, J., Liu, L., Huang, X., and Cheng, X. (2013). Effects of the cold core eddy on tropical cyclone intensity and structure under idealized air–sea interaction conditions. *Mon. weather Rev.* 141 (4), 1285–1303. doi:10.1175/MWR-D-12-00123.1

Ma, Z., Zhang, Y., Wu, R., and Na, R. (2021). Statistical characteristics of the response of Sea Surface temperatures to westward typhoons in the South China sea. *Remote Sens.* 13 (5), 916. doi:10.3390/rs13050916

Martin, M., Dash, P., Ignatov, A., Banzon, V., Beggs, H., Brasnett, B., et al. (2012). Group for high resolution Sea Surface temperature (GHRSST) analysis fields inter-comparisons. Part 1: A GHRSST multi-product ensemble (gmpe). *Deep Sea Res. Part II Top. Stud. Oceanogr.* 77, 21–30. doi:10.1016/j.dsr2.2012.04.013

Mei, W., Pasquero, C., and Primeau, F. (2012). The effect of translation speed upon the intensity of tropical cyclones over the tropical ocean. *Geophys. Res. Lett.* 39 (7). doi:10.1029/2011GL050765

Menemenlis, D., Campin, J. M., Heimbach, P., Hill, C., Lee, T., Nguyen, A., et al. (2008). ECCO2: High resolution global ocean and sea ice data synthesis. *Mercat. Ocean. Q. Newsl.* 31, 13–21.

Menemenlis, D., Fukumori, I., and Lee, T. (2005). Using Green's functions to calibrate an ocean general circulation model. *Mon. weather Rev.* 133 (5), 1224–1240. doi:10.1175/MWR2912.1

Meng, C., Xu, W., Qiao, Y., Liao, X., and Qin, L. (2021). Quantitative risk assessment of population affected by tropical cyclones through Joint consideration of extreme precipitation and strong wind—a case study of hainan province. *Earth's Future* 9 (12), 2365. doi:10.1029/2021EF002365

Mlawer, E. J., Taubman, S. J., Brown, P. D., Iacono, M. J., and Clough, S. A. (1997). Radiative transfer for inhomogeneous atmospheres: RRTM, a validated correlated-k model for the longwave. *J. Geophys. Res. Atmos.* 102 (14), 16663–16682. doi:10.1029/97JD00237

Mooney, P. A., Mulligan, F. J., Bruyère, C. L., Parker, C. L., and Gill, D. O. (2019). Investigating the performance of coupled WRF-ROMS simulations of Hurricane Irene (2011) in a regional climate modeling framework. *Atmos. Res.* 215, 57–74. doi:10.1016/j.atmosres.2018.08.017

Morrison, H., Thompson, G., and Tatarskii, V. (2009). Impact of cloud microphysics on the development of trailing stratiform precipitation in a simulated squall line: Comparison of one-and two-moment schemes. *Mon. weather Rev.* 137 (3), 991–1007. doi:10.1175/2008MWR2556.1

Nakanishi, M., and Niino, H. (2006). An improved Mellor–Yamada level-3 model: Its numerical stability and application to a regional prediction of advection fog. *Boundary-Layer Meteorol.* 119 (2), 397–407. doi:10.1007/s10546-005-9030-8

Prakash, K. R., and Pant, V. (2017). Upper oceanic response to tropical cyclone Phailin in the Bay of Bengal using a coupled atmosphere-ocean model. *Ocean. Dyn.* 67 (1), 51–64. doi:10.1007/s10236-016-1020-5

Prasad, T. G., and Hogan, P. J. (2007). Upper-ocean response to hurricane ivan in a 1/25 nested gulf of Mexico HYCOM. *J. Geophys. Res. Oceans* 112 (C4), 04013. doi:10.1029/2006JC003695

Price, J. F. (1981). Upper ocean response to a hurricane. *J. Phys. Oceanogr.* 11 (2), 153–175. doi:10.1175/1520-0485(1981)011<0153:uortah>2.0.co;2

Schade, L. R., and Emanuel, K. A. (1999). The ocean's effect on the intensity of tropical cyclones: Results from a simple coupled atmosphere–ocean model. *J. Atmos. Sci.* 56 (4), 642–651. doi:10.1175/1520-0469(1999)056<0642:toseot>2.0.co;2

Shay, L. K., Ali, M. M., Barbary, D., D'Asaro, E. A., Halliwell, G., Doyle, J., et al. (2010). "Air–sea interface and oceanic influences," in *7th WMO international workshop on tropical cyclones (IWTC-VII)* (St. Gilles Les Bains, La Réunion, France: World Meteor Org). Avaliable At: http://www.wmo.int/pages/prog/arep/wwrp/tmr/otherfileformats/documents/1_3.pdf (Accessed August 20, 2021).

Shchepetkin, A. F., and McWilliams, J. C. (2005). The regional oceanic modeling system (ROMS): A split-explicit, free-surface, topography-following-coordinate oceanic model. *Ocean. Model.* 9 (4), 347–404. doi:10.1016/j.ocemod.2004.08.002

Shen, W., and Ginis, I. (2003). Effects of surface heat flux-induced sea surface temperature changes on tropical cyclone intensity. *Geophys Res. Lett.* 30 (18), 1933. doi:10.1029/2003GL017878

Shen, W., Song, J., Liu, G., Zhuang, Y., Wang, Y., and Tang, J. (2019). The effect of convection scheme on tropical cyclones simulations over the CORDEX East Asia domain. *Clim. Dyn.* 52 (7), 4695–4713. doi:10.1007/s00382-018-4405-y

Skamarock, W. C., Klemp, J. B., Dudhia, J., Gill, D. O., Liu, Z., Berner, J., et al. (2019). *A description of the advanced research WRF model version 4*. Boulder, CO, USA: National Center for Atmospheric Research, 145. doi:10.5065/1dfh-6p97

Tsou, C. H., Pei-Yu, H., Tu, C. Y., Cheng-Ta, C., Tzeng, T. P., and Cheng, C. T. (2016). Present simulation and future typhoon activity projection over Western north pacific and taiwan/east coast of China in 20-km HiRAM climate model. TAO: Terrestrial. *Atmos. Ocean. Sci.* 27 (5), 6. doi:10.3319/TAO.2016.06.13.04

Tsuboki, K., Yoshioka, M. K., Shinoda, T., Kato, M., Kanada, S., and Kitoh, A. (2015). Future increase of supertyphoon intensity associated with climate change. *Geophys. Res. Lett.* 42 (2), 646–652. doi:10.1002/2014GL061793

Wada, A., Cronin, M. F., Sutton, A. J., Kawai, Y., and Ishii, M. (2013). Numerical simulations of oceanic pCO2 variations and interactions between Typhoon Choiwan (0914) and the ocean. *J. Geophys. Res. Oceans* 118 (5), 2667–2684. doi:10.1002/jgrc.20203

Wada, A., Niino, H., and Nakano, H. (2009). Roles of vertical turbulent mixing in the ocean response to Typhoon Rex (1998). *J. Oceanogr.* 65, 373–396. doi:10.1007/s10872-009-0034-8

Wada, A., Uehara, T., and Ishizaki, S. (2014). Typhoon-induced Sea surface cooling during the 2011 and 2012 typhoon seasons: Observational evidence and numerical investigations of the sea surface cooling effect using typhoon simulations. *Prog. Earth Planet. Sci.* 1 (1), 11–25. doi:10.1186/2197-4284-1-11

Walker, N. D., Leben, R. R., and Balasubramanian, S. (2005). Hurricane-forced upwelling and chlorophyll a enhancement within cold-core cyclones in the Gulf of Mexico. *Geophys Res. Lett.* 32, 23716. doi:10.1029/2005GL023716

Wang, G., Su, J., Ding, Y., and Chen, D. (2007). Tropical cyclone Genesis over the South China sea. *J. Mar. Syst.* 68, 318–326. doi:10.1016/j.jmarsys.2006.12.002

Wang, K., Yang, Y., Reniers, G., and Huang, Q. (2021). A study into the spatiotemporal distribution of typhoon storm surge disasters in China. *Nat. Hazards* 108 (1), 1237–1256. doi:10.1007/s11069-021-04730-9

Wang, Y. Q., and Wu, C. C. (2004). Current understanding of tropical cyclone structure and intensity changes–a review. *Meteorology Atmos. Phys.* 87 (4), 257–278. doi:10.1007/s00703-003-0055-6

Warner, J. C., Armstrong, B., He, R., and Zambon, J. B. (2010). Development of a coupled ocean–atmosphere–wave–sediment transport (COAWST) modeling system. *Ocean. Model.* 35 (3), 230–244. doi:10.1016/j.ocemod.2010.07.010

Wei, J., Liu, X., and Jiang, G. (2018). Parameterizing sea surface temperature cooling induced by tropical cyclones using a multivariate linear regression model. *Acta Oceanol. Sin.* 37 (1), 1–10. doi:10.1007/s13131-018-1153-0

Wu, C. C., Lee, C. Y., and Lin, I. I. (2007). The effect of the ocean eddy on tropical cyclone intensity. *J. Atmos. Sci.* 64 (10), 3562–3578. doi:10.1175/JAS4051.1

Xiao, F., and Xiao, Z. (2010). Characteristics of tropical cyclones in China and their impacts analysis. *Nat. Hazards* 54 (3), 827–837. doi:10.1007/s11069-010-9508-7

Yao, C., Xiao, Z., Yang, S., and Luo, X. (2021). Increased severe landfall typhoons in China since 2004. *Int. J. Climatol.* 41, E1018–E1027. doi:10.1002/joc.6746

Zambon, J. B., He, R., and Warner, J. C. (2014). Investigation of hurricane Ivan using the coupled ocean–atmosphere–wave–sediment transport (COAWST) model. *Ocean. Dyn.* 64 (11), 1535–1554. doi:10.1007/s10236-014-0777-7

Zhang, C., Hu, C., Huang, G., Yao, C., Zheng, Z., Wang, T., et al. (2019). Perspective on landfalling frequency and Genesis location variations of southern China typhoon during peak summer. *Geophys. Res. Lett.* 46 (12), 6830–6838. doi:10.1029/2019GL083420

Zhang, H. (2022). Modulation of upper ocean vertical temperature structure and heat content by a fast-moving tropical cyclone. *J. Phys. Oceanogr.* 53, 493–508. doi:10.1175/JPO-D-22-0132.1

Frontiers in Earth Science

Investigates the processes operating within the major spheres of our planet

Advances our understanding across the earth sciences, providing a theoretical background for better use of our planet's resources and equipping us to face major environmental challenges.

Discover the latest Research Topics

See more →

Frontiers

Avenue du Tribunal-Fédéral 34
1005 Lausanne, Switzerland
frontiersin.org

Contact us

+41 (0)21 510 17 00
frontiersin.org/about/contact